Frequency-Dependent Resistivity for a Two-Dimensional Electron Gas with Electrostatic Modulation

by

Paula Fekete

A dissertation submitted to the Graduate Faculty in Physics
in partial fulfillment of the requirements for the degree of Doctor of Philosophy
The City University of New York
2007

UMI Number: 3245078

ProQuest Information and Learning Company
300 North Zeeb Road
P.O. Box 1346
Ann Arbor, MI 48106-1346

This manuscript has been read and accepted for the Graduate Faculty in Physics in satisfaction of the dissertation requirement for the degree of Doctor of Philosophy.

G. Gumbs

Date
Chair of Examining Committee

S. Catto

Date
Executive Officer

V. Fessatidis

G. Foster

N. Maitra

L. Massa

Supervisory Committee

THE CITY UNIVERSITY OF NEW YORK

Abstract

FREQUENCY-DEPENDENT RESISTIVITY FOR A TWO-DIMENSIONAL ELECTRON GAS WITH ELECTROSTATIC MODULATION

by Paula Fekete

Thesis supervisor: Professor Godfrey Gumbs

We present a model calculation for the photoconductivity of a two-dimensional electron gas (2DEG) in an ambient perpendicular magnetic field. An electrostatic modulation is also applied to produce quantum wires (QW), dots (QD) or antidots (QA) in the 2DEG. This system is then subjected to a weak radiation field with its frequency lying in the microwave range. The Landau eigenstates of the periodically modulated system are first found numerically and then used in the Kubo formula to obtain the frequency-dependent longitudinal (ρ_{xx}) and transverse (ρ_{xy}) resistivities. These quantum magnetotransport (QMT) coefficients are investigated in the low magnetic field region ($B < 0.3T$) over a range of frequencies (Ω) of the external, time-dependent radiation field. The effects of scattering are considered for square arrays of quantum dots and antidots, as well as one-dimensional (1D) quantum wires. The quantum dots, antidots, and wires are simulated by potential forms widely used in the relevant literature. The effect of changing the scatterer type and strength is investigated. The contribution to the QMT coefficients from states near and below the Fermi level is examined when the magnetic field strength and density of charge carriers is varied. The effect of sub-Landau level state formation on the QMT coefficients is also analyzed. The dependence of the QMT coefficients on commensurability effects in the magnetic field and scattering potential is described. Numerical investigations are conducted which show how the magnetic field strength, modulating potential intensity, lattice scattering, electron density, and radiation field frequency affect the AC longitudinal and Hall resistivities. The calculation is restricted to the low-frequency regime where the system is assumed to be in or close to equilibrium.

Contents

3 Eigenspectrum Dispersion and Fermi Energy Calculations 39

List of Figures

Chapter 1

Introduction and Background

The aim of this dissertation is to investigate the magnetotransport properties of a 2DEG in the presence of 1D and 2D periodic electrostatic potential modulations, and subject to radiation of finite frequency. I will refer to this problem as AC magnetotransport. This theoretical work is based on previous research completed at Hunter College by my thesis advisor, Professor Godfrey Gumbs, and his former graduate students and collaborators. They examined the magnetoresistance of a 2DEG subject to a weak lateral 1D and 2D superlattice potential, but without an incident radiation. I will refer to this subject as DC magnetotransport. Results for the DC magnetotransport were obtained for delta-function peak type impurities, as well as periodic potentials described by the N-th power of simple trigonometric functions (cosine for 1D and a cross-product of cosines for 2D). For large enough positive modulation strengths these functions can describe a 1D array of parallel quantum antiwires, or a 2D square array of antidots. For large negative values of the potential's strength they can depict a 1D array of parallel quantum wires, or a 2D array of quantum antidots. Previous results were presented in [47] by Gumbs and Park, as well as a series of papers by Gumbs and Huang [54] - [56]. The longitudinal and transverse conductivity and resistivity of a 2DEG with scattering by these dot and antidot type potentials was calculated in a perpendicular magnetic field. The same results were also presented for wire and antiwire type potentials. Gumbs and Huang used delta–function type scatterers in [48], whereas Gumbs and Park extended the formalism to scatterers of finite size by using the cosine-potential model at zero frequency. I extended these results, and applied the ensuing formalism to the AC magnetotransport problem, investigating the effect of incident radiation for several values of the incident radiation's frequency. As the effect due to impurity scattering was found to be weak in previous work ([54] - [56]), I did not take into account the contribution of impurities to the AC magnetotransport. Throughout my research I was constantly verifying my theory by comparing results obtained for the finite frequency case to those previously obtained for zero frequency. To check that the finite frequency results are correct, I verified that they reduce to those obtained for zero frequency by taking the limit of the modulation frequency going to zero, and comparing my results to those obtained in the DC case.

In the rest of this chapter I will present a short history of how our understanding of electrical conduction evolved, followed by a description of the concept of "mesoscopic physics", which is the physics I investigate. Then I describe some transport theories that shaped our understanding of transport on the mesoscopic scale. This is followed by a section presenting heterojunctions and superlattices. Finally, I present some experimental results obtained in the investigation of magnetotransport properties of the 2DEG, starting with some pioneering papers and ending with recent results.

1.1 Evolution of Conductivity Concepts

Our understanding of the conduction properties of different materials can be classified into three stages of evolution. The first stage dates back to the early 1800s when the resistance (R) (and the conductance (G)) of a sample were measured in two-terminal I-V measurements (i.e., current I, voltage V). The resistance (R) of a sample was determined using Ohm's law ($R = V/I$) as the potential difference (V) applied between the two ends of a sample divided by the current (I) passing through it, and the conductance (G) was defined as the reciprocal of the resistance ($G = 1/R$). Simple experiments demonstrated however, that the resistance (and conductance) was not a comprehensive enough physical property, as measurements on different sample shapes made of the same material resulted in different resistance (and conductance) values. It was shown that the resistance of a sample ($R = \rho L/A$) is directly proportional to its length (L) and inversely proportional to its cross-sectional area (A) the factor of proportionality being its resistivity (ρ). Correspondingly, the conductance ($G = \sigma A/L$) of a sample was found to be inversely proportional to its length (L) and directly proportional to its cross-sectional area (A). The coefficient of proportionality (σ) is the conductivity of the sample material. Introduction of the sample geometry independent, intrinsic material properties of conductivity (σ) and resistivity (ρ) marked the second level of our understanding of the conduction properties of materials. Their knowledge allowed the classification of the current-carrying capability of different conductors. As early as the beginning of the twentieth century it was realized that resistivity and conductivity were not fundamental material parameters either. Some materials, such as semiconductors for example, exhibited different values of conductivity (and resistivity), depending on how they were manufactured, moreover they displayed conduction properties for which the classical conductivity and resistivity concepts alone could not account. Using the classical concept of electrons as corpuscular objects one could explain the electrical properties of metals, such as the tungsten filament of a light bulb for example, but could not account for the unusual behavior exhibited by semiconductors.

Our understanding of the conduction properties of materials reached the third level when solid state devices (such as semiconductor diodes and transistors) were developed. It became clear that new physical quantities have to be identified to explain the remarkable new conduction phenomena discovered in this field. Carrier density (n) referring to the number of electrons per unit volume, and carrier mobility (μ) used to describe the ratio between the drift velocity of electrons in a conductor and the applied electric field was defined. The development of semiconductor diodes and transistors marked the beginning of a new chapter, called electronics, in the study of the transport properties of conductors. It became clear that to understand the conduction properties of these novel solid state devices one has to account for electrons behaving both as particles, and waves. Quantum mechanics was called for to solve the problem of electrical transport in their case.

1.2 Mesoscopic Physics

Questions arose along the previously outlined process of understanding conduction: Will the formula $G = \sigma A/L$ fail when the physical properties length (L) and/or area (A) of the sample are made arbitrarily small? Is there a limit at which the formula breaks down? How small do objects have to become so that their conductance will not only depend on the physical properties of the material they are made out of, but also on their specific shape, and even on the presence and placement of obstructions to current flow, such as the lattice and impurity atoms in the sample?

The answer is that the above simple proportionality formula no longer holds when the dimensions of the sample become small enough to allow coherent propagation of electrons across it. In the process of finding the above answer a new field of physics opened up, that of mesoscopic physics, describing current flow on a length scale where the quantum mechanical nature of conduction electrons becomes important. The term mesoscopic originates from the Greek word “mesos”, which means intermediate. The intermediate, or mesoscopic, conduction regime lies between the microscopic world of a few lattice spacings and the macroscopic world interpreted by classical physics. The new physics describing conductors consisting of a large number of atoms (on the order of $10^{10} - 10^{11}$) but small enough to allow coherent electron propagation expresses electron transport in terms of transmission coefficients rather than in terms of the Boltzmann transport equation.

Finding an exact length scale where the conductivity formula $G = \sigma A/L$ breaks down is actually not straightforward, because the answer is influenced by many factors. It was first thought that the quantum mechanical properties of conduction electrons become important when the length scale of a sample is reduced to just a few lattice spacings. This did not turn out to be the case. Development in lithographic techniques during the 1980s made a multitude of experimental devices in the submicron range available, allowing the experimental investigation of the question: “How small can we go?” leading to significant progress in our understanding of the meaning of resistance at the microscopic level. It was found that mesoscopic transport can be observed in conductors having a much larger length scale than initially thought, ranging from a few nanometers (the order of 10^{-9} m) to hundreds of microns (the order of 10^{-4}) corresponding to 100, 1,000 of even 10,000 times the lattice spacing. A wealth of novel quantum phenomena was observed in the mesoscopic size regime, and it was discovered that the laws governing the mesoscopic world are different from those governing the macroscopic one. Just to mention one example, the conductance of a wire of width on the order of the electron "size" becomes quantized in terms of e^2/h, where e is the elementary charge and h is the Planck constant. It is clear that conductance in the mesoscopic range strongly deviates from the predictions of classical physics.

1.3 Size Scales

Let us now return to a previously given example, that of a conduction electron moving in the tungsten filament of a light bulb, to explain what is meant by electron "size", and also to identify the size scales on which a conductor will show ohmic behavior. According to de Broglie's hypothesis the electron (as all matter) has a wave-like nature (wave-particle duality). The knowledge of the de Broglie wavelength ($\lambda_{dB} = h/p$) equal to the ratio of Planck's constant (h) and the electron's momentum (p), allows one to associate a typical size with any electron of known momentum. A simple calculation shows that the diameter of the tungsten filament in a light bulb is about ten million times larger than the de Broglie wavelength of the conduction electron. Since the length scales are so far removed from each other in this case, electrons in the filament can be described as classical particles. Their motion due to the voltage applied to the light bulb resembles a flow, much like the flow of a liquid in a pipe. There are two additional characteristic lengths that a conductor's size must significantly exceed for its conduction to be described by the laws of classical physics. These are the mean free path of its conduction electrons (l), which is the distance the electron travels before its initial momentum is destroyed, and the coherence length(l_c), which is the distance the electron travels before its initial phase is changed.

In conductors and electronic devices electron energies may vary from thousandths of electron-volts to several electron-volts, making the corresponding length scale associated with the electron range from a fraction of an Ångström to hundreds of Ångströms. Similarly, the size of the three characteristic lengths (de Broglie wavelength, mean free path, and coherence length) depends on the material, and it is strongly affected by external parameters such as temperature and applied external fields. At very low temperatures (in the milli-Kelvin range) the quantum mechanical nature of conduction electrons is strongly manifested in conductors on the nanometer scale. At such low temperatures the coherence length of electrons is on the order of a micron or more, therefore the quantum mechanical behavior of electrons dominates the physics under these circumstances. These tiny conductors have revealed sample-specific fluctuations in conductance which are surprisingly sensitive to variations in the applied magnetic field and/or the placement of impurities within the sample, and for these reasons their magnetotransport is intensely investigated.

1.4 Transport Theories

Until the second half of the twentieth century disordered electronic systems were regarded as too complex to be described by theoretical physicists. The first description of electron propagation in perfect crystalline solids is given by Bloch's theorem [1], which forms the foundation for our understanding of the problem. According to this theorem, the states (wavefunctions) of electrons moving in the periodic potential of the ions forming a crystal lattice are plane waves modulated by the periodic lattice potential. The concept of the Bloch wavefunction was developed by Felix Bloch in 1928.

A few decades later, in 1956, metallic conduction was described by Lev Landau [2], [3] in his theory of Fermi liquids. According to Landau, electrons form a Fermi sea, and are also described by plane waves modulated by the periodic lattice potential. Although the Coulomb interaction between electrons in metals is not weak (the kinetic and potential energy of such electrons has the same order of magnitude) still most properties of metals can be described by treating electrons as a weakly interacting fermionic liquid. According to Landau's Fermi-liquid theory, one can describe a strongly interacting Fermi system (even the strongly interacting conduction electrons in a metal) in terms of quasiparticles, which interact only weakly. Therefore, in Landau's theory the excitations of the interacting fermionic system can be described by single-particle wave-functions. Because electrons obey Fermi statistics, only a small fraction of them, those with energy within $k_B T$ of the Fermi energy, contribute to the electric conductivity. The theory's remarkable agreement with experimental results lead to becoming now well-accepted to describe the properties of metals by treating their electrons as a noninteracting gas of fermions.

It was assumed that the Fermi liquid theory also applies to systems with impurities. In the 1970s it became clear that in the limit of low temperatures not only interactions between the electrons and ions, but even those between electrons call for important corrections to the Fermi-liquid theory. At room temperature electrons are scattered by lattice vibrations, resulting in a loss of momentum leading to a nonzero resistivity $\rho\,(T)$. In the limiting case of zero temperature however, resistivity can be traced back to the scattering of electrons at the Fermi energy by static defects such as impurities or vacancies. This situation can also be described by a free-electron model, that is, a model in which the states at the Fermi energy are represented by single-particle wavefunctions.

One year after the publication of Landau's Fermi liquid theory, in 1957, Kubo [4] defined electric conductivity in a quantum mechanical version of the "fluctuation-dissipation" theorem, which relates the linear response conductance (a fluctuation) to the equilibrium noise current (a dissipation). His approach, allowing the calculation of a non-equilibrium property (like conductance) using the methods of equilibrium quantum statistical mechanics, has changed the approach to expressing the response properties of non-equilibrium systems close to equilibrium. Our understanding of electron transport was revolutionized when Kubo's formalism, a Green's function approach to the linear response theory of quantum systems, was applied to it.

Another useful formula of conductance, specifically applicable to mesoscopic systems, was also formulated in 1957 by Landauer [5]. This formula is based on the idea that electrons are in thermal equilibrium with various chemical potentials in the leads attached to the sample. This is reasonable because the resistivity of mesoscopic systems is due to scattering by static random potentials and inelastic collisions leading to dissipation which occurs mainly in the voltage and current contact pads outside the sample. Electrons, originating from the current leads, undergo scattering as they pass through the random potential of the sample, and the conductance (defined as the ratio of the current and the applied potential difference) is proportional to the transmission coefficient. Landauer's original formula was derived for a strictly one-dimensional geometry, but has been extended to the multichannel case by Marcus Büttiker [66]. This extended form of the formula is suitable to describe the resistance of nanoscale conductors, relating a non-equilibrium property, such as conductance, to a scattering problem.

To derive the frequency-dependent photoconductivity tensor in this work, we use a Kubo-type formula obtained using the linear-response approach following the work of Gumbs and Huang [48]. The ensuing Green's function expression of the longitudinal and Hall conductivities, which neglect electron-impurity interactions, will suffice to demonstrate the effect of finite frequency radiation on the QMT properties of two-dimensional electron systems.

1.5 Heterojunctions

As it was mentioned earlier, over the last few decades, mesoscopic structures have become the system of choice for studying transport. The gallium arsenide - aluminum gallium arsenide ($GaAs/AlGaAs$) system has been widely used in mesoscopic transport measurements, as it provides a high quality two-dimensional conduction channel, with mean free paths on the order of 10^{-5} m at low temperatures, and 10^{-7} m at room temperature. Advances in high resolution epitaxy techniques made possible the fabrication of a variety of structures in the mesoscopic range, such as quantum wells, tunneling barriers, and other ultra-thin layered structures, such as quantum dots and antidots, as well as quantum wires. As a result, the study of transport in a regime in which the Boltzmann equation is clearly invalid became easily accessible to experimentalists. Additionally, it became possible to create artificial potential profiles in mesoscopic structures, which can be used to control the quantum-mechanical motion of the conduction electrons. Transport in such systems is comparable to that in highly conducting disordered materials, as on the spatial scale of interest the material is non-uniform. Current lines distort due to the presence of the potential profiles, thus the current density becomes non-uniform spatially within the material. A variety of novel electronic properties were discovered in these systems, such as the integer and fractional quantum Hall effect (QHE), Shubnikov-de Haas (SdH) oscillations, and Weiss oscillations, which are important both in theoretical solid-state physics and in building advanced device applications.

As recent work on mesoscopic systems has largely been based on the $GaAs/AlGaAs$ heterojunction, it is worthwhile to present how the thin, two-dimensional conducting layer is formed at the interface between $GaAs$ and $AlGaAs$. The motivation to use multilayer devices is that electron mobilities in multilayers exceed those of the otherwise equivalent monolayers such as the *GaAs* structure. High mobilities are desired as novel phenomena can be experimentally observed in such devices at lower magnetic fields and higher temperatures. Most properties of *AlGaAs* are very similar to those of *GaAs*, but there are a few important differences. One is that the Fermi energy in the wide-gap *AlGaAs* layer is higher than in the narrow-gap *GaAs*. Moreover, if the *AlGaAs* layer is doped with shallow donors, then the Fermi level is shifted from the middle of the band gap of *AlGaAs* to the donor level. Another difference is that the *GaAs* conduction band edge lies lower in energy than the *AlGaAs* donor states, creating an abrupt discontinuity, called band offset, in the energy bands at the interface. These two factors cause electrons from the donor sites of *AlGaAs* to spill over into the *GaAs* region when the two materials are brought in contact, leaving behind positively charged donors. The *AlGaAs* layer is therefore depleted, as electrons flow from *AlGaAs* to *GaAs* in order to satisfy the requirement of a continuous Fermi level (E_F in Figure 1.1) throughout the structure. This electron transfer raises the electrostatic potential on the *AlGaAs* side of the interface region as the electrons leave behind numerous ionized donors. The ensuing space charge and electrostatic potential causes the valence and conduction bands to bend. Band bending, which is the bending of band edges at the interface between *AlGaAs* and *GaAs* is illustrated in Figure 1.1, which is an idealized sketch of the situation. Once the electrons have fallen into the lower energy *GaAs* states they are unable to gain enough energy to move back up to the *AlGaAs* conduction band. These electrons become confined to a thin layer of the *GaAs* near the interface and form the 2DEG. The confined electrons cannot move across the interface between the *GaAs* and *AlGaAs*, but they are free to move in the two spatial directions parallel to the interface.

Figure 1.1 shows the situation when five dissimilar semiconductor layers are brought into contact, assuming that the conduction and valence bands line-up in the z-

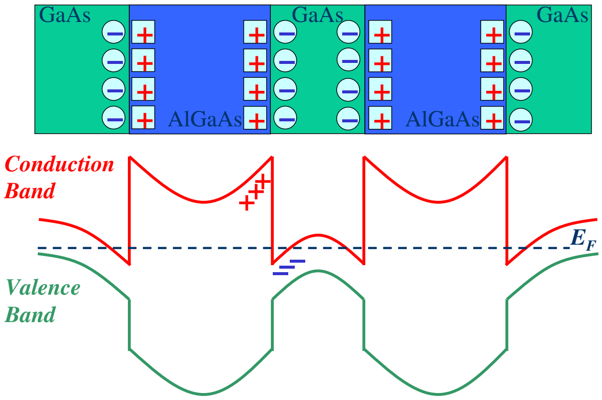

Figure 1.1: Energy band diagram for the $GaAs/AlGaAs$ heterostructure

direction. After equilibrium is established, the Fermi energy becomes the same throughout the entire structure (dashed line in the figure). The electron density is sharply peaked near the $GaAs/AlGaAs$ interface where the Fermi energy is inside the conduction band, forming the thin conducting layer, which is referred to as the two-dimensional electron gas. The carrier concentration in a 2DEG typically ranges from 2×10^{11} to 2×10^{12} electrons per cubic centimeter. The electrons are therefore free to propagate in the $x - y$ plane but are confined by some potential $U(z)$ in the z-direction. At low temperatures and low carrier densities only the lowest subbands are occupied and the higher subbands do not play any significant role in the conduction properties of the system. Therefore the z-dimension can be ignored altogether and the conducting layer can be simply treated as a two-dimensional electron system in the $x - y$ plane.

The electron confinement and mobility is enhanced if modulation doping is employed. Modulation doping was first proposed by Nobel laureate Horst L. Störmer et al. [9], and it is accomplished by growing the multilayer heterojunction in the presence of a calibrated doping source (such as Si), which can be switched on and off abruptly, in such a way that only the $AlGaAs$ layer is deliberately doped with silicon impurities. Using the modulation doping technique, very high carrier mobilities can be achieved ($10^6\ cm^2/Vs$ for $GaAs$) as the permanent separation of the conduction electrons from their parent donor impurity atoms also reduces the influence of ionized and neutral impurity scattering on the electron motion.

In such devices as the one described above, the 2DEG confined to the $GaAs/AlGaAs$ interface by the heterostructure band offset can be depleted by applying a negative voltage to a metallic gate deposited on the surface of the structure. As the gate voltage decreases, the constriction within the gap between the electrodes narrows, the carrier density within the constriction decreases, and steps or plateaus are observed in the conductance. The electron gas is dynamically two-dimensional because of the vertical confinement to within one electron wavelength that occurs near the hetero-interface due to the repulsive potential barrier associated with the conduction band offset and the attractive potential associated with the positively charged ionized donors. In addition to the vertical confinement, the electron gas is usually constricted laterally to the size of an electron wavelength using the electrostatic potential provided by split-gate electrodes. Devices with a lateral configuration using metallic electrodes on the 2DEG to implement potential barriers have the advantage that the applied back-gate voltage can change the electron density in the leads so that the current flow through the structure can be studied as a function of the equilibrium Fermi energy, which depends on the electron density.

Applying a static magnetic field on mesoscopic conductors has a profound effect on their electronic and transport properties. External application of magnetic fields of variable strength to nanostructures is an invaluable tool available to the experimentalist in probing the system. Magnetic fields give rise to new fundamental behavior not observed in bulk-like systems, as for example the quantum Hall effect. The fundamental quantity characterizing a magnetic field is the magnetic flux density B, which in mks units is measured in Teslas (T). In the study of semiconductor nanostructures, low field magnetotransport experiments usually correspond to fields less then 1 T, which is the regime in which experiments such as the classical Hall effect measurements are usually performed, and the low field regime is also the one in which we investigate the 2DEG. To observe the quantum Hall effect much higher magnetic fields are required (on the order of 30 T and higher).

When the magnetotransport of nanostructure systems such as quantum wells, wires and dots is investigated, two distinct cases are possible depending on the direction in which the magnetic field is applied. For the first, the magnetic field is parallel to one of the directions of free electron propagation; for the other the field is perpendicular to the free electron motion of the system. This second case is investigated in this work. Qualitatively, when free particles are subject to a magnetic field, they experience the Lorentz force:

$$\vec{F} = q\vec{v} \times \vec{B}, \tag{1.1}$$

where $\vec{v}$ is the velocity of the carrier. Since the force is always perpendicular to the direction of travel of the charged particle, its motion in the absence of other forces is circular, following closed loop cyclotron orbits, with angular frequency given by the cyclotron frequency:

$$\omega_c = \frac{eB}{m_c}, \tag{1.2}$$

where m_c is the cyclotron mass of the particle. For isotropic systems like those we consider, the cyclotron mass becomes simply the electron effective mass M^*. In the quantum mechanical picture, the circular orbits associated with the Lorentz force must be quantized (causing the electron to “interfere with itself”), which means that the electron’s wave character forces an integral number of de Broglie wavelengths to fit into the circumference of its orbital motion. This is in analogy to orbital quantization occurring about a central potential such as, for example, is the case of the electron’s motion around an atomic nucleus. It follows from the Bohr-Sommerfeld quantization condition that a restriction is also placed on the electron’s kinetic energy, which becomes quantized into a ladder of discrete levels, known as Landau levels. The Landau levels are equally spaced, separated by an energy given by Planck’s constant times the cyclotron frequency ($\hbar\omega_c$) and highly degenerate. The degeneracy of each level can be determined as follows. Applying periodic boundary conditions, the wave vectors in the y-direction are spaced by $\Delta k_y = 2\pi/L_y$. This means that the corresponding wave functions are spaced by $\Delta y_k = 2\pi\hbar/eBL_y$. The total number of states in each Landau band is therefore given by:

$$N_{2D} = \frac{L_x}{\Delta y_k} = \frac{eBL_xL_y}{h} = N_xN_y\Phi \tag{1.3}$$

where L_x is the sample length in the x-direction, L_y is the sample length in the y-direction, N_x and N_y are integers giving the number of unit cells in the x and y directions, a is the lattice constant, and $\Phi = Ba^2/\left(h/e\right)$ is the number of flux quanta per unit cell (also referred to as flux ratio).

1.6 Superlattices

In the past few decades it became possible to fabricate a new class of heterostructures with electrical conductivities mainly determined by a fixed arrangement of scatterers, which force the electrons to reside in predetermined positions. These scattering arrays are interesting to investigate because they show unusual transport properties caused by collective excitations of the 2DEG due to the strong modulation potential. The small-scale synthetic semiconductor structures that we presented thus far are usually referred to as superlattices. They can be classified into two main groups:

- multilayer *heterojunctions* consisting of alternate layers of two (or more) dissimilar semiconductors with nanometer thickness, with electron flow across the interfaces between layers, and

- monolayer *homojunctions* produced by a periodic alteration of doping in a single semiconductor layer, which may be part of a heterojunction, but with electron transfer restricted to a single layer and electron flow parallel to the interface.

The dynamics of conduction electrons in *heterojunctions* was first investigated theoretically in 1970 by Leo Esaki and Raphael Tsu [7]. They predicted the observation of novel quantum mechanical effects in these structures when the period of the superlattice is shorter than the electron mean free path. The novel effects were attributed to the formation of very narrow allowed and forbidden bands in the energy eigenvalue spectrum, and were associated with a drastic reduction of the Brillouin zone into a series of minizones. The combined effect of narrow energy bands and narrow wave-vector zones for electrons resulted in the appearance of portions of negative differential conductance in the current-voltage $(I - V)$ characteristics of these structures.

As early as 1974 such superlattices were successfully grown in 2D - as reported by Chang, Esaki, and Tsu [8]. Moreover, it became possible to fabricate multi-layers, and many other kinds of nanometer scale semiconductor structures due to advances in molecular beam epitaxy (MBE) growth techniques. This lead to important new discoveries in the field of magnetotransport, such as the integer and fractional quantum Hall effect. The magnetotransport properties of these superlattices are still intensely investigated both theoretically and experimentally.

1.7 Magnetoresistance

Since the discovery of the quantum Hall effect the magnetoresistance of a 2DEG was intensely investigated both theoretically and experimentally. Edwin Hall discovered the Hall effect in 1879. At that time the existence of the electron was not experimentally confirmed, and even the sign of charge carriers in a metallic conductor was uncertain. In a Hall measurement the resistivity of a current-carrying wire placed in a magnetic field is investigated. According to classical theory (the Drude model) the longitudinal resistance is independent of the variation of the magnetic field, while the transverse resistance increases linearly with B. In 1978, Klaus von Klitzing [40] found flat Hall plateaus in the transverse magnetoresistance, ρ_{xy}, while studying the Hall effect in semiconductors at very low temperatures and very high magnetic fields. His discovery is now known as the integer quantum Hall effect, and he won the Nobel Prize for the discovery in 1985. As the strength of the magnetic field was increased, oscillations of the longitudinal resistivity (ρ_{xx}), the Shubnikov-de Haas oscillations, were also observed. The period of these oscillations corresponds to the filling of the Landau levels. Whenever ρ_{xx} goes through a minimum, a new plateau appears in the transverse resistivity, ρ_{xy}. These plateaus correspond to quantized values of the Hall resistivity: $\rho_{xy} = \frac{h}{2e^2N}$, where h is Planck's constant, N is an integer, and e is the charge of the electron. The cause of this unusual behavior of the longitudinal and transverse magnetoresistances can be found in modifications of the density of states of a 2DEG placed in a magnetic field. The density of states breaks up into a sequence of equally spaced levels due to electrons being constrained to follow circular paths at frequency ω_c (the cyclotron frequency) which is determined by the intensity of the magnetic field, B. The wave character of the electron requires an integral number of de Broglie wavelengths to fit in the circumference of this orbit. As a consequence, the electrons' kinetic energy can only take certain quantized values resulting in a ladder of discrete allowed levels, called Landau levels (LL). The magnetic field must be high enough so that electrons are able to complete at least a few orbits before losing momentum due to scattering. This means that the condition $\omega_c \tau_m > 1$ must be satisfied between the cyclotron frequency and the momentum relaxation time, τ_m, otherwise the effect is washed out. These features are usually absent at room temperature, but evident when the temperature, T, is low enough so that $\hbar\omega_c > k_B T$, (where $\hbar$ is the Planck constant, h, divided by 2π, and k_B is the Boltzmann constant). The effect is important therefore, when the spacing of energy levels is large enough compared to $k_B T$.

As it was mentioned before, in addition to a magnetic field, one can also impose a modulation potential onto the heterostructure with the 2DEG layer. The ability to apply a controllable potential to the high mobility *GaAs/AlGaAs* 2DEG via a patterned gate with a grating constant of a few thousand Ångströms has allowed experimentalists to study magnetotransport properties over a wide range of modulation potentials. The modulation potential can be applied in two orthogonal directions or in only one direction. In the presence of a weak periodic modulation, the longitudinal magnetoresistance of such structures also exhibits oscillations associated with the filling of successive Landau levels. In addition to the SdH oscillations, a new kind of magnetoresistance oscillation was reported by Weiss et al. in 1988. [40] These oscillations in ρ_{yy} are known as Weiss oscillations, and are explained classically in terms of the commensurability between the superlattice period and the cyclotron radius. They were found both experimentally and theoretically to be 180° out of phase relative to, and much weaker than, the dominating oscillations in ρ_{xx}. The effect is shown to result from an oscillatory dependence of the bandwidth of the modulation-broadened Landau levels of the 2D electron system on the guiding center for each level [40]. The Weiss oscillations have been attributed to the formation of a Hofstadter type energy spectrum [11] - [34].

When the energy eigenspectrum of a 2DEG in a 2D lattice potential in the presence of an external magnetic field is investigated as a function of the flux ratio, $\Phi = \frac{\text{flux through unit cell}}{\text{flux quantum}}$, a fractal structure known as"Hofstadter's butterfly" is obtained. Historically, Hofstadter's butterfly spectrum was obtained in two cases. One of them treats the electrons in the tight-binding approximation (TBA) [11] (electrons confined in the presence of a strong 2D periodic lattice potential) and in the presence of a weak magnetic field, the other applies a weak 2D periodic perturbation potential to the Landau-quantized 2DEG [30] in a strong magnetic field.

Magnetoresistance oscillations as function of the magnetic field for a 2DEG subject to a weak 1D modulation have been reported [35], [36]. For a 2D periodic modulation potential, the magnetotransport properties of the 2DEG have also revealed some interesting features [37]. By varying the strength of the modulation, one can achieve a transition from weak density variations of the 2DEG to the extreme limit where some regions become devoid of electrons. This strong spatially modulated potential, which can be attained experimentally by etching an array of microscopic holes in a 2DEG, thereby creating quantum dots, leads to dramatic commensurability effects when the radius of the electron's orbit becomes comparable to the period of the quantum dot potential. Suppression of the commensurate Weiss oscillations, pronounced double peak structure in the magnetoresistance, presence of orbits commensurate with the lattice constant, as well as occurrence of negative and quenched Hall resistivities for low magnetic fields have been found for a square array of scatterers [38], [54].

Negative Hall resistivity and its quenching at low magnetic fields, as well as negative longitudinal resistivity have also been observed in a quantum-wire junction [47]. The low-field conductance of ideal QW-s was shown to be quantized, however in realistic QW-s some features were found to deviate from the ideal, giving rise to different regimes of conductance, depending on the geometry of the sample.

Magnetotransport coefficient calculations in a rectangular dot and antidot type superlattice at low magnetic fields in the presence of a controllable potential were published in the past [48], but the effect of a time-dependent periodic potential on such a system has just recently been examined.[50] Torres and Kunold investigate the microwave photoconductivity of a 2DEG in the presence of a magnetic field and a 2D electrostatic modulation. Their approach to the problem is not through the same Green's function method, such as employed in this work. They consider the periodic potential as a perturbation applied to the exactly solvable microwave driven Landau problem. They find that the total longitudinal conductivity and resistivity exhibit strong oscillations, which go through minima for certain values of the radiation field and cyclotron frequency ratio. For certain values of the electron mobility and microwave power intensity they find negative resistance states (NRSs). The negative resistance states appear only for certain values of the lattice parameter, which are commensurate with the magnetic length $L_H = \sqrt{\hbar/(eB)}$. They propose that NRSs arise due to the combined effect of the periodic modulation, perpendicular magnetic field, and microwave irradiation. They argue however, that for the experimental observation of these negative resistance states electron mobilities one order of magnitude higher than currently available are required.

As the problem of AC conductivity comes into the focus of theoretical interest, it is reasonable to ask the question whether the features of longitudinal and Hall conductivities published recently will be reproduced in our calculations making use of the Kubo formula, in which the matrix elements of the chosen modulation potentials are evaluated numerically using Hofstadter-type wavefunctions.

Chapter 2

Model Potentials

This chapter presents the theoretical model used to describe the periodic potential forms investigated, as well as the method applied to calculate the energy eigenvalue dispersion of a 2DEG in the presence of such periodic modulation potentials applied in both, or in only one spatial direction. Using nanolithographic techniques such one- or two-dimensional periodic potentials of different strength, period and shape can be imposed experimentally upon a two-dimensional electron system, such as that formed at the interface between $GaAs$ and $AlGaAs$. The modulating potentials can be imprinted in such way that their periods are much shorter than the electron mean free path, or phase coherence length, leading to the appearance of interesting quantum conduction phenomena. The potential forms investigated here are therefore either 2D square arrays of dots or antidots, or arrays of parallel 1D quantum wires or anti-wires. This chapter presents the equations needed to express the numerical values of energy eigenvalues and expansion coefficients entering the wavefunctions for the various potential types investigated.

We start the presentation of our model by writing the single-electron Hamiltonian for a one- or two-dimensional scattering array potential located in the $x-y$ plane and subject to a uniform perpendicular magnetic field $\vec{B} = B\hat{z}$ along the z direction. In *mks* units this Hamiltonian can be written as:

$$H_0 = \frac{1}{2M^*}\left[\vec{p} - q\vec{A}\left(\vec{x}\right)\right]^2 + U_L\left(\vec{x}\right) \tag{2.1}$$

The above Hamiltonian describes the motion of a particle of charge q in an electromagnetic field of scalar and vector potentials $\phi\left(\vec{x}\right)$ and $\vec{A}\left(\vec{x}\right) = (0, Bx, 0)$, respectively. The vector potential $\vec{A}\left(\vec{x}\right)$ is written in the Landau gauge. In equation (2.1) $U_L\left(\vec{x}\right) = q\phi\left(\vec{x}\right)$ represents the modulating potential energy. In this notation one should use $q = -e$ for electrons, where e is the positive elementary charge. M^* stands for the effective mass of the charge carriers, which are electrons in our case.

A modulation potential for an arbitrary rectangular scattering array has a Fourier expansion of the general form:

$$U_L\left(\vec{x}\right) = \sum_{\vec{G}} V_{\vec{G}} e^{i\vec{G}\cdot\vec{x}} \tag{2.2}$$

where $\vec{G} = (N_x k_x, N_y k_y)$, is a reciprocal lattice vector, with N_x and N_y being integers counting the number of dots in the x and y direction, respectively, while $a_x = 2\pi/k_x$ and $a_y = 2\pi/k_y$ are the scattering array lattice constants in the x and y direction. Explicit results will be given in this chapter for three simple cases of the modulation potential. For simplicity, the period of all two-dimensional potentials will be considered to be the same in the x and y directions ($a_x = a_y = a$).

The first modulation potential form considered is of a delta-function type, suitable to describe a two-dimensional lattice of strong scatterers, with a very steep lattice potential, and scattering center diameters much smaller than the lattice constant a, such as that used in reference [48]. Although this work is mainly concerned with the 1D and 2D cosine type modulation potentials, we also present the delta function plots for several reasons, which are given below. We acknowledge that a δ-function does not represent a realistic lattice potential, but its use is still justified for two reasons. One is that an array of δ-functions approximates well a lattice potential with very sharp peaks of small diameter, and the second is that its use vastly reduces the complexity of the calculations. This is the reasoning behind the use of the delta potential in the first place, but in addition to the previous argument it was also used as the basis of comparison with results obtained for the more complex, realistic lattice potential shapes. Mathematically, as well as in the programming process, the use of the delta potential was very convenient because integrals involved in the solution of the problem became trivial to calculate, thus no numerical integrations were needed, therefore it had great didactic value. In the case of the 1D or 2D cosine potentials however, only some of the integrals could be calculated analytically, while others had to be solved numerically.

2.1 Delta Potential

The delta-function modulation describes a 2D lattice of strong scatterers (arrays of antidots placed in the $x-y$ plane). It is a good approximation of a very steep lattice potential, having a lattice constant a that far exceeds the diameter of the scattering centers. The explicit form of the two-dimensional delta potential used is:

$$U_L\left(\vec{x}\right) = V_0 \sum_{i,j} \delta\left(\vec{x} - \vec{R}_{i,j}\right) \tag{2.3}$$

where the δ-function is two-dimensional, and $\vec{R}_{i,j} = (ia, ja)$ denotes a lattice vector, while V_0 represents the modulating potential's amplitude. For antidots the magnitude of V_0 has to be chosen to be positive. A modulation described by a sine or cosine function (or rather their sum or cross product raised to a certain power) will be a more realistic description of the modulation potential. As we intended to investigate the influence that changing the representation of the lattice potential brings, we also employed such periodic potentials in our calculations. These potential forms are presented in the following sections.

2.2 1D Periodic Potential

The second type of scattering potential that we consider is a one-dimensional potential, such as used in reference [47] (see Figure 2.1) corresponding to quantum wires and anti-wires.

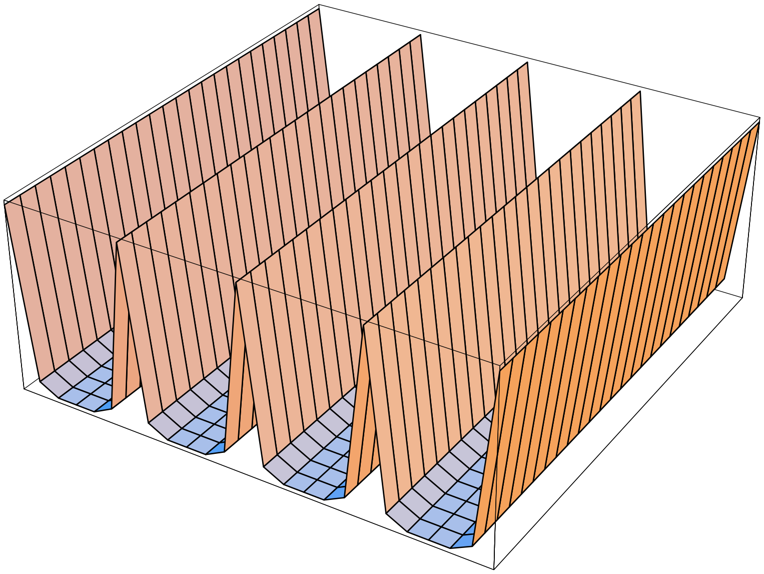

Figure 2.1: Set of short quantum wires with $V_0 = 10$ and $N = 10$

The 1D periodic potential that we investigate corresponds to a modulation in the x-direction, and it is expressed in the form:

$$U_L\left(\vec{x}\right) = V_0\left[\cos\left(\frac{2\pi x}{a}\right)\right]^{2N}. \tag{2.4}$$

When the modulation is in the y direction, we need to make the substitution $x \rightarrow y$. In equation (2.4) V_0 denotes the height of the potential barrier, a is the period of the potential, and N represents the steepness of the slope of the potential.

This 1D modulation introduces a Bloch-band structure in the x-direction, while in the y-direction we expect free-electron behavior. The potential form given in equation (2.4) describes an array of short quantum wires, when the parameter denoting the height of the potential barrier is $V_0 > 0$. The parameter N influences the steepness of the potential; the larger the N, the steeper the potential barrier, and consequently the wider the conduction channel for the charge carriers. If the value of V_0 is large enough, charge carriers become trapped by the potential, and this is why the model can be used to represent an array of quantum wires. If the value chosen for the potential's strength is $V_0 < 0$, the modulation corresponds to anti-wires.

2.3 2D Periodic Potential

Last but not least, we examine a two-dimensional periodic potential involving cross-products of cosine functions having the same period a in both the x and y direction, written in a form widely used in relevant literature (see references [48], [57], [58]) and specified by the equation:

$$U_L\left(\vec{x}\right) = V_0\left[\cos\left(\frac{2\pi x}{a}\right)\cos\left(\frac{2\pi y}{a}\right)\right]^{2N} \tag{2.5}$$

This potential depicts a two-dimensional square array of quantum dots (see Figure 2.2) if the value of V_0 is chosen to be negative. If however, the value of V_0 is positive

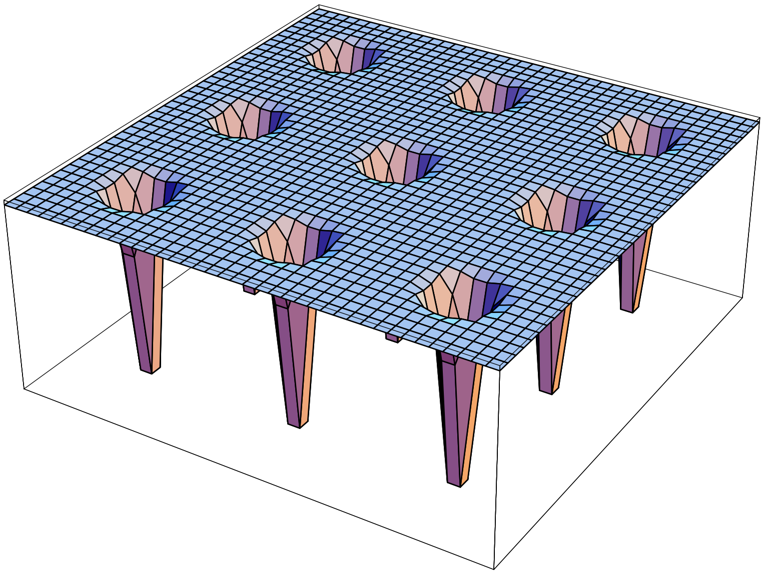

Figure 2.2: Quantum dot potential well with $V_0 = -25$ and $N = 10$

(see Figure 2.3) the potential describes quantum antidots. The magnitude of V_0 influences the dot (antidot) diameter and depth (height). The power N controls the steepness of the quantum dot (antidot) potential, and the reason for taking $2N$ in the exponent is to ensure negative (positive) potential when V_0 is taken as a negative (positive) value.

2.4 Expansion Coefficients and Eigenvalues

In this section we present the theory that leads to the equations which determine the eigenvalues $\varepsilon_j(X_0)$, and the expansion coefficients $C_n(j, X_0)$ (1D modulation), and $C_{n,m}(j, X_0)$ (2D modulation), appearing in the wavefunctions corresponding to the three modulation potential cases investigated. These coefficients also enter the expressions of the structure factors defined in Chapter 5. Both the energy eigenvalues, and the expansion coefficients are also needed in the calculation of the Fermi energy,

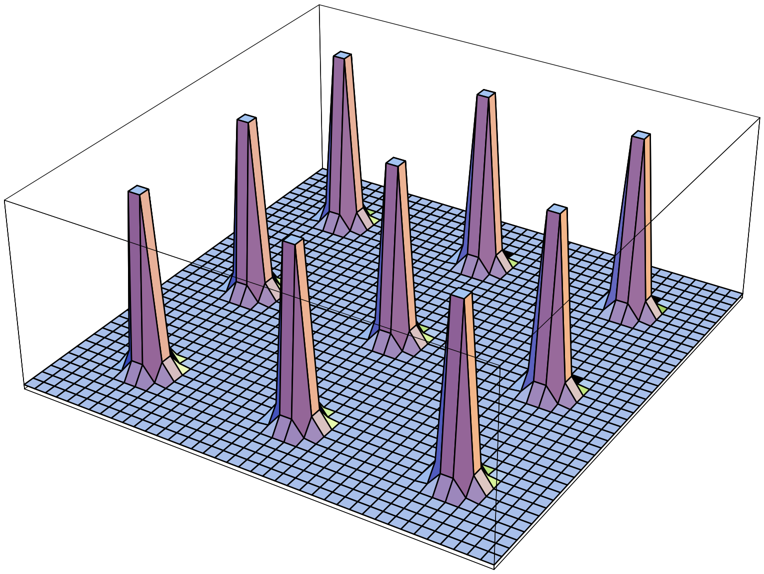

Figure 2.3: Quantum antidot potential
Quantum antidot potential with $V_0 = 100$ and $N = 20$

which at its turn, and together with the eigenvalues and expansion coefficients, is needed in the numerical calculation of the conductivity tensor.

2.4.1 Eigenfunctions

With a modulation in the x-direction only (1D modulation), and in the absence of impurities, the single-particle eigenfunctions of the Hamiltonian expressed in equation (2.1) are given by:

$$\psi_{j,X_0}\left(\vec{x}\right) = \sum_{n} C_n\left(j, X_0\right) \phi_{n,X_0}\left(\vec{x}\right) \tag{2.6}$$

where j is the subband index, $X_0 = k_y L_H^2$ is the guiding center of the cyclotron orbits, (with k_y a wave vector in the y direction and $L_H = \sqrt{\hbar/eB}$ the magnetic length), $n = 0, 1, 2, ...$ is the Landau-level index. The expansion coefficients $C_n\left(j, X_0\right)$ can be found by diagonalizing the Hamiltonian matrix (2.1). In the 1D modulation case the matrix elements of the perturbation are diagonal with respect to k_y, which means that k_y is a good quantum number. In equation (2.6) $\phi_{n,X_0}(\vec{x})$ are normalized, shifted harmonic oscillator eigenfunctions labeled by the Landau level index n and the wave vector k_y (which enters through the expression of X_0). These same eigenfunctions will also be used in calculating the band part of the longitudinal and transverse conductivities, when the matrix elements of the velocity operators presented in Chapter 5 will be expressed. The shifted harmonic oscillator eigenfunctions appearing in equation (2.6) have the explicit expression:

$$\begin{aligned} \phi_{n,X_0}(\vec{x}) &= \sqrt{\frac{1}{\pi^{1/2} L_y L_H 2^n n!}} \exp\left(-\frac{iX_0 y}{L_H^2}\right) \\ &\cdot \exp\left[-\frac{(x-X_0)^2}{2L_H^2}\right] H_n\left(\frac{x-X_0}{L_H}\right) \end{aligned} \tag{2.7}$$

In equation (2.7) $L_y = N_y a$ is the sample length in the y-direction and $H_n(x)$ is the nth order Hermite polynomial.

If additional modulation is introduced in the y-direction, the translational invariance in this direction is destroyed, and the matrix elements of the perturbation are no longer diagonal with respect to k_y. The physical meaning of this is that the additional modulation leads to additional Bragg scattering, and thus to a subband splitting of the Landau bands which are obtained in the 1D modulation case. With the vector potential expressed in the Landau gauge, and in the absence of impurities, the energy eigenstates for the 2D modulation case can be expressed by the wavefunctions:

$$\psi_{j,X_0}(\vec{x}) = \sum_{n,m} C_{n,m}(j, X_0)\, \phi_{n,X_0+mGL_H^2}(\vec{x}) \tag{2.8}$$

where j, X_0, n, and L_H are the same as in the 1D case, while $m = 0, \pm 1, \pm 2, ...$

stands for the umklapp scattering effect, and $G = 2\pi/a$ is a reciprocal lattice vector. Again, the expansion coefficients $C_{n,m}(j, X_0)$ can be found by diagonalizing the Hamiltonian matrix (2.1). In equation (2.8) the normalized, shifted harmonic oscillator wavefunctions $\phi_{n,X_0+mGL_H^2}(\vec{x})$ have the form:

$$\begin{aligned}\phi_{n,X_0+mGL_H^2}(\vec{x}) = \sqrt{\frac{1}{\pi^{1/2} L_y L_H 2^n n!}} \exp\left[-\frac{i\left(X_0 + mGL_H^2\right) y}{L_H^2}\right] \\ \cdot \exp\left[-\frac{\left(x - X_0 - mGL_H^2\right)^2}{2L_H^2}\right] H_n\left(\frac{x - X_0 - mGL_H^2}{L_H}\right)\end{aligned} \tag{2.9}$$

Again, these are the same eigenfunctions as those that we will use in Chapter 5 in the calculation of the band part of the 2D conductivities.

We calculate the effect of the modulation potential $U_L(\vec{x})$ on the eigenvalue spectrum by the diagonalization of the Hamiltonian in equation (2.1) in the two sets of basis functions given above, corresponding to 1D and 2D modulations. We are motivated to do this as we suspect to find correlations between the energy spectrum and the magnetotransport properties, as it was already proven previously by a large number of experimental and theoretical investigations of magnetotransport in lateral superlattices. Also, as mentioned earlier, we need the eigenenergies ε_j and eignevectors $C_n(j, X_0)$ (respectively $C_{n,m}(j, X_0)$ for the 2D modulation case) to express the conduction coefficients.

2.4.2 Equations Leading to Eigenvalues and Eigenvectors for the Delta Potential

The explicit form of the two-dimensional delta function type of modulating lattice potential used in our calculations is:

$$U_L\left(\vec{x}\right) = V_0 \sum_{k,l=-\infty}^{+\infty} \delta\left(x - la\right)\delta\left(y - ka\right) \tag{2.10}$$

(Its general form was given in equation (2.3).)

The influence of this 2D modulation potential on the energy eigenvalues of the 2DEG is calculated by diagonalizing the Hamiltonian (2.1) in the set of 2D basis functions (2.8). The equation leading to the expansion coefficients entering the wavefunctions are found by the solution of the following linear equation:

$$\left\{\left[\varepsilon_n^{(0)} - \varepsilon_j\left(X_0\right)\right]\delta_{n,n'}\delta_{m,m'} + \frac{V_0}{aL_H\pi^{1/2}}\sqrt{\frac{1}{2^{n+n'}n!n'!}}B_{n,n'}^{m,m'}\left(X_0\right)\right\}\sum_{n,m} C_{n,m}\left(j, X_0\right) = 0 \tag{2.11}$$

The same calculation leads to the secular equation determining the energy eigenvalues of the problem. For the delta potential case the equation, written in dimensionless variables is:

$$Det\left[\left(n + \frac{1}{2} - \frac{\varepsilon_j}{\hbar\omega_c}\right)\delta_{n,n'}\delta_{m,m'} + \frac{\bar{V}}{\sqrt{\Phi}}\sqrt{\frac{1}{2^{n+n'}n!n'!}}B_{n,n'}^{m,m'}\left(L\right)\right] = 0 \tag{2.12}$$

where the coefficient $B_{n,n'}^{m,m'}$ entering expression (2.12) are the matrix elements of the delta function type of potential, and it has the following expression:

$$B_{n,n'}^{m,m'}\left(L\right)=\sum_{l=-\frac{N_x}{2}}^{+\frac{N_x}{2}}\exp\left\{-\Phi\pi\left[\left(l-\frac{1}{\Phi}\left(\frac{L}{N_y}+m\right)\right)^2+\left(l-\frac{1}{\Phi}\left(\frac{L}{N_y}+m'\right)\right)^2\right]\right\}$$
$$\cdot H_n\left\{\sqrt{2\Phi\pi}\left[l-\frac{1}{\Phi}\left(\frac{L}{N_y}+m\right)\right]\right\}H_{n'}\left\{\sqrt{2\Phi\pi}\left[l-\frac{1}{\Phi}\left(\frac{L}{N_y}+m'\right)\right]\right\} \tag{2.13}$$

In equation (2.13) the following notation was used for the rescaled value of the modulation potential's magnitude:

$$\bar{V}=\frac{M^*V_0}{\pi\sqrt{2}\hbar^2} \tag{2.14}$$

2.4.3 Equations Leading to Eigenvalues and Eigenvectors for the 1D Periodic Modulation

The effect of the 1D modulation potential $U_L\left(\vec{x}\right)$ on the energy eigenvalues of our system is determined by the diagonalization of the Hamiltonian (2.1) in the set of basis functions (2.6):

$$H_0\psi_{j,X_0}\left(\vec{x}\right)+U_L\left(\vec{x}\right)\psi_{j,X_0}\left(\vec{x}\right)=\varepsilon_j\left(X_0\right)\psi_{j,X_0}\left(\vec{x}\right) \tag{2.15}$$

The same calculation also leads to the equation for the expansion coefficients (eigenvectors) $C_n\left(j,X_0\right)$, for the case of 1D modulation. The matrix equation determining these 1D expansion coefficients has the form:

$$\sum_n \left\{ \left[\varepsilon_n^{(0)} - \varepsilon_j\left(X_0\right)\right]\delta_{n,n'} + \frac{V_0}{\pi^{1/2}L_H}\sqrt{\frac{1}{2^{n+n'}n!n'!}}B_{n,n'}\left(X_0\right)_{\cos 1D} \right\} C_n\left(j,X_0\right) = 0 \tag{2.16}$$

The orthonormality condition satisfied by these expansion coefficients are also needed in the numerical calculation of the magnetotransport coefficients, and they can be written as:

$$\sum_n C_n\left(j,X_0\right)C_n\left(j',X_0'\right) = \delta_{j,j'}\delta_{X_0,X_0'} \tag{2.17}$$

The same calculation leads to the secular equation from which we can determine the energy eigenvalues $\varepsilon_j\left(X_0\right)$:

$$Det\left\{ \left[\varepsilon_n^{(0)} - \varepsilon_j\left(X_0\right)\right]\delta_{n,n'} + \frac{V_0}{\pi^{1/2}L_H}\sqrt{\frac{1}{2^{n+n'}n!n'!}}B_{n,n'}\left(X_0\right)_{\cos 1D} \right\} = 0 \tag{2.18}$$

In equation (2.18) $B_{n,n'}\left(X_0\right)_{\cos 1D}$ denotes the matrix element of the 1D modulation potential calculated in terms of the set of basis functions (2.6):

$$\begin{aligned} B_{n,n'}\left(X_0\right)_{\cos 1D} &= \left\langle \phi_{n',X_0}\left(\vec{x}\right)\right| U_L\left(\vec{x}\right)\left|\phi_{n,X_0}\left(\vec{x}\right)\right\rangle \\ &= \int_{-\infty}^{+\infty} dx \exp\left[-\frac{\left(x-X_0\right)^2}{2L_H^2}\right] H_{n'}\left(\frac{x-X_0}{L_H}\right) \\ &\cdot \left[\cos\left(\frac{2\pi x}{a}\right)\right]^{2N} \exp\left[-\frac{\left(x-X_0\right)^2}{2L_H^2}\right] H_n\left(\frac{x-X_0}{L_H}\right) \end{aligned} \tag{2.19}$$

Periodic boundary conditions are assumed in the sense that a translation in the x direction by L_x (which is the sample size in the x-direction) reproduces the same wave function. This assumption, and the fact that the modulating potential is also periodic in a, $U_L(x) = U_L(x+a)$, means that the energy eigenspectrum is periodic in a as well, $\varepsilon_j(X_0) = \varepsilon_j(X_0 + a)$, so that our investigation of the eigenspectrum can be restricted to the first Brillouin zone $-\pi/a \leq k_y \leq \pi/a$.

At this point in the discussion we "rescale" our equations to a set of new, dimensionless variables that we chose to use so that our numerical calculations are sensible. The magnetic field entering the problem determines the two "scales" that we work with: one is the magnetic length $L_H = \sqrt{\hbar/eB}$, which sets a length scale for the problem, while the cyclotron energy $\hbar\omega_c$, with $\omega_c = eB/M^*$ the cyclotron frequency, gives an energy scale. These energy scales will also be used in expressing the conductivity components in Chapter 5. We will now express the energy eigenvalues in the dimensionless variables using the two "scales" mentioned. In the new, rescaled variables, the matrix equation leading to the 2D expansion coefficients may be written as:

$$\sum_n \left\{ \left[\left(n + \frac{1}{2} \right) - \varepsilon_j(L) \right] \delta_{n,n'} + \frac{aV_0}{\pi^{1/2} L_H \hbar\omega_c} \sqrt{\frac{1}{2^{n+n'} n! n'!}} B_{n,n'}(L)_{\cos 1D} \right\} C_n(j,L) = 0 \tag{2.20}$$

The secular equation (2.18) leading to the energy eigenvalues is also expressed in terms of the new variables, and it becomes:

$$Det \left\{ \left[\left(n + \frac{1}{2} \right) - \varepsilon_j(L) \right] \delta_{n,n'} + \frac{aV_0}{\pi^{1/2} L_H \hbar\omega_c} \sqrt{\frac{1}{2^{n+n'} n! n'!}} B_{n,n'}(L)_{\cos 1D} \right\} C_n(j,L) = 0 \tag{2.21}$$

At this point we introduce the notation:

$$\frac{aV_0}{\pi^{1/2}L_H\hbar\omega_c} = \frac{\bar{V}}{\sqrt{\Phi}}, \tag{2.22}$$

In equation (2.22) $\bar{V}$ denotes the rescaled potential strength:

$$\bar{V} = \frac{a^2M^*V_0}{\pi\sqrt{2}\hbar^2} \tag{2.23}$$

Finally, the matrix element of the 1D modulating potential in rescaled variables can be explicitly written as:

$$\begin{aligned} B_{n,n'}\left(L\right)_{\cos 1D} = &\int\limits_{-\frac{N_x}{2}}^{+\frac{N_x}{2}} dl \exp\left[-\pi\Phi\left(l-\frac{1}{\Phi}\frac{L}{N_y}\right)^2\right] H_{n'}\left[\sqrt{2\pi\Phi}\left(l-\frac{1}{\Phi}\frac{L}{N_y}\right)\right] \\ &\cdot\left[\cos\left(2\pi l\right)\right]^{2N}\exp\left[-\pi\Phi\left(l-\frac{1}{\Phi}\frac{L}{N_y}\right)^2\right] H_{n}\left[\sqrt{2\pi\Phi}\left(l-\frac{1}{\Phi}\frac{L}{N_y}\right)\right] \end{aligned} \tag{2.24}$$

where $k_y = \frac{2\pi L}{N_y a}$. By adopting periodic boundary conditions L can take integer values ranging from, $-N_y/2$ to $(N_y/2)-1$, where $L_y = N_y a$ is the sample length in the y direction.

2.4.4 Equations Leading to Eigenvalues and Eigenvectors for the 2D Periodic Modulation

Now we would like to list equations leading to the energy eigenvalues and eigenvectors for the 2D periodic modulation potential. The expansion coefficients $C_{n,m}\left(j, X_0\right)$, are determined from the matrix equation:

$$\sum_{n,m}\left\{\left[\varepsilon_n^{(0)}-\varepsilon_j\left(X_0\right)\right]\delta_{n,n'}\delta_{m,m'}+\frac{V_0}{a^2\pi^{1/2}L_H}\sqrt{\frac{1}{2^{n+n'}n!n'!}}B_{n,n'}^{m,m'}\left(X_0\right)_{\cos 2D}\right\}C_{n,m}\left(j,X_0\right)=0 \tag{2.25}$$

These 2D expansion coefficients $C_{n,m}\left(j,X_0\right)$, also satisfy an orthonormality condition, which can be written as:

$$\sum_{n,m}C_{n,m}^{*}\left(j,X_0\right)C_{n',m'}\left(j',X_0'\right)=\delta_{j,j'}\delta_{X_0,X_0'} \tag{2.26}$$

Next we write the secular equation determining the energy eigenvalues for the 2D case:

$$Det\left\{\left[\left(n+\frac{1}{2}\right)\hbar\omega_c-\varepsilon_j\left(X_0\right)\right]\delta_{n,n'}\delta_{m,m'}\ +\frac{V_0}{a^2\pi^{1/2}L_H}\sqrt{\frac{1}{2^{n+n'}n!n'!}}B_{n,n'}^{m,m'}\left(X_0\right)_{\cos 2D}\right\}=0 \tag{2.27}$$

The matrix element of the 2D modulation potential $B_{n,n'}^{m,m'}\left(X_0\right)_{\cos 2D}$, appearing in equations (2.25) and (2.27) is written in rescaled variables as:

$$\begin{aligned}B_{n,n'}^{m,m'}\left(L\right)_{\cos 2D}&=\frac{2N!}{2^{2N}\left(N+\frac{m-m'}{2}\right)!\left(N-\frac{m-m'}{2}\right)!}\\&=\int_{-N_x/2}^{N_x/2}dl\exp\left\{-\Phi\pi\left[+\left(l-\frac{1}{\Phi}\left(\frac{L}{N_y}+m'\right)\right)^2\right]\right\}H_{n'}\left[\sqrt{2\Phi\pi}\left(l-\frac{1}{\Phi}\left(\frac{L}{N_y}+m'\right)\right)\right]\\&\cdot\left[\cos\left(2\pi l\right)\right]^{2N}\exp\left[-\Phi\pi\left(l-\frac{1}{\Phi}\left(\frac{L}{N_y}+m\right)\right)^2\right]H_n\left[\sqrt{2\Phi\pi}\left(l-\frac{1}{\Phi}\left(\frac{L}{N_y}+m\right)\right)\right]\end{aligned} \tag{2.28}$$

It can be verified that in the 2D case as well the energy eigenvalues are symmetric with respect to X_0, $\varepsilon_j(X_0) = \varepsilon_j(-X_0)$ and they satisfy the periodicity condition $\varepsilon_j(X_0 + a) = \varepsilon_j(X_0 + GL_H^2)$. It follows that the expansion coefficients $C_{n,m}(j, X_0)$ have the Bloch property. In addition, the matrix element of the perturbation expressed in equation (2.28) is unchanged if a simultaneous exchange of $m \to m + p$ and $m' \to m' + p'$ is performed. In consequence, each Landau level splits into p subbands in the case of the 2D modulation. This is an important observation, as it will be seen that the energy eigenspectrum dispersion for the 2D modulation potentials will be quite different from that corresponding to the 1D case. The explanation for the different shape of the two groups of graphs (1D and 2D) is exactly this subband splitting introduced by the modulation in the second direction.

Now we write the dimensionless form of equations (2.25) and (2.28), as these are needed to be able to perform numerical calculations. The secular equation (2.25) is written in dimensionless variables as:

$$Det\left\{\left[n + \frac{1}{2} - \bar{\varepsilon}_j(L)\right]\delta_{n,n'}\delta_{m,m'} + \frac{\bar{V}}{\sqrt{\Phi}}\sqrt{\frac{1}{2^{n+n'}n!n'!}}B_{n,n'}^{m,m'}(L)_{\cos 2D}\right\} = 0 \qquad (2.29)$$

The expansion coefficients $C_{n,m}(j, L)$, can be determined from the following equation, written in the new variables:

$$\sum_{n,m}\left\{\left[n + \frac{1}{2} - \varepsilon_j(L)\right]\delta_{n,n'}\delta_{m,m'} + \frac{\bar{V}}{\sqrt{\Phi}}\sqrt{\frac{1}{2^{n+n'}n!n'!}}B_{n,n'}^{m,m'}(L)_{\cos 2D}\right\}C_{n,m}(j, L) = 0 \qquad (2.30)$$

In equations (2.29) and (2.30) the notation $\bar{V} = \frac{a^2 M^* V_0}{\pi\sqrt{2}\hbar^2}$ was introduced, while the rest of the dimensionless variables are the same as previously used in the case of the 1D equations.

Finally, we give the equation of the matrix element of the 2D modulation potential written in the "rescaled" variables:

$$
\begin{aligned}
B_{n,n'}^{m,m'}\left(L\right)_{\cos 2D} &= \frac{2N!}{2^{2N}\left(N+\frac{m-m'}{2}\right)!\left(N-\frac{m-m'}{2}\right)!} \\
&\cdot \int\limits_{-N_x/2}^{N_x/2} dl \exp\left\{-\pi\Phi\left[l-\frac{1}{\Phi}\left(\frac{L}{N_y}+m'\right)\right]^2\right\} H_{n'}\left\{\sqrt{2\pi\Phi}\left[l-\frac{1}{\Phi}\left(\frac{L}{N_y}+m'\right)\right]\right\} \\
&\cdot \exp\left\{-\pi\Phi\left[l-\frac{1}{\Phi}\left(\frac{L}{N_y}+m\right)\right]^2\right\} H_{n}\left\{\sqrt{2\pi\Phi}\left[l-\frac{1}{\Phi}\left(\frac{L}{N_y}+m\right)\right]\right\} \left[\cos\left(2\pi l\right)\right]^{2N}
\end{aligned}
\tag{2.31}
$$

In equation (2.31) the integration variable is a dimensionless variable, for which the notation $l = x/a$ was used. It can be seen that in equation (2.31) of the matrix element of the 2D modulation potential the y-integration was performed analytically, but the x-integration will have to be done numerically.

Chapter 3

Eigenspectrum Dispersion and Fermi Energy Calculations

In this chapter we present numerical results of the energy eigenvalues versus the wave vector (energy eigenvalue dispersion) plots for the three different potential modulation cases, as well as energy eigenvalue plots as a function of the variation of the flux ratio Φ. We start with the 1D potential followed by the 2D delta-function and 2D cosine modulation cases. It is important to remember that for no modulation the energy eigenvalue dispersion spectra would consist of thin, equally spaced, horizontal lines separated by $\hbar\omega_c$, which correspond to unperturbed Landau levels. Thus in the unmodulated case the energy eigenvalues retain a constant value upon a variation of the wave vector or of the magnitude of the magnetic field. The Landau levels are degenerate, more then one electron occupies the same energy level, corresponding to the different possible wave vectors that these electrons may have. In the presence of a modulation, this degeneracy is lifted. The applied magnetic field enters our formalism through the flux ratio $\Phi = Ba^2/\phi_0$, where $\phi_0 = h/e$ is the flux quantum (h stands for the Planck constant and e for the elementary charge). It is clear that the flux ratio is directly proportional to the magnitude of the applied magnetic field B, thus the magnetic field-dependence of the plots is always shown through the flux ratio-dependence. As it will be shown, in the presence of a modulation potential, the Landau levels will no longer be independent of the variation of the wave vector, or the applied magnetic field. We will also illustrate the modification in the eigenvalue dispersion plots caused by changing the sample size in the case of the delta potential, respectively those brought by changing the exponential power of the periodic terms in the case of the 1D and 2D cosine potentials. Some general features of the figures are common for all three of the potential types investigated, and they can be described in advance, without the need of repeating them in each of the individual cases. For weak modulation amplitudes and strong magnetic fields the eigenenergy spectra show degenerate, but distinguishable Landau levels, while for strong modulation amplitudes and weak magnetic fields a mixing of the Landau levels can be seen. This confirms the explicit influence of the modulation potential and magnetic field strength on the energy level distribution. The bandwidth increases with the increase of the Landau level indices. The larger the magnitude of the modulation potential strength, the higher the topmost value of the energy eigenvalues (for negative potentials the lower the bottom value). Different Landau levels do not at all (or only weekly) overlap for small values of the modulation potential strength, the overlap becomes more significant as the magnitude of the modulation potential is increased. For the same modulation potential, lower Landau levels have smaller overlap then the higher ones. Also confirmed by the three different types of potential forms investigated is that the eigenenergy dispersion shows the characteristics of the Hofstadter spectrum. In this chapter we also present some sketches of the periodic (cosine type) modulating potential shapes, to illustrate the influence of changing the exponent of the periodic function(s) entering the expression of the quantum wire and dot/antidot potentials.

3.1 Eigenspectrum Dispersion for the 1D Modulation

The energy eigenvalue dispersion plots in the case of 1D modulation are somewhat different from the corresponding plots obtained for the 2D delta potential or 2D cosine type periodic modulations. This is due to the fact that in the 1D modulation case we do not see a subband splitting of the Landau levels and also the mixing of the LL is observed at much higher magnitudes of the modulation potential strength as compared to the delta potential case, however the large bandwidth oscillations are still present, and they are proportional to the strength of the modulation potential applied.

3.1.1 Dependence of the Eigenspectrum Versus $\bar{k}_y$ Graphs on the Strength of Modulation

The dependence on the strength of the modulation potential $\bar{V}$, of four energy eigenspectra obtained for the one-dimensional cosine modulation potential are shown as a function of the rescaled wave vector $\bar{k}_y$ in Figure 3.1. Figures 3.1 (a) and (b) represent the eigenspectra of a 1D quantum wire array (a sketch of which is shown in Figure 2.1) while (c) and (d) are the eigenspectra for an antiwire potential. In all four of the plots in Figure 3.1 it can be seen that the 1D modulation broadens the Landau levels into bands of oscillatory width. The modulation potential lifts the degeneracy of the Landau levels, and yields eigenstates which carry current in the y direction. If the periodic potential is along the x axis, it will cause the k_y dispersion of the originally discrete Landau levels, i.e. leads to the appearance of Landau bands.

In Figure 3.1 the power of the cosine term in the modulation potential of equation

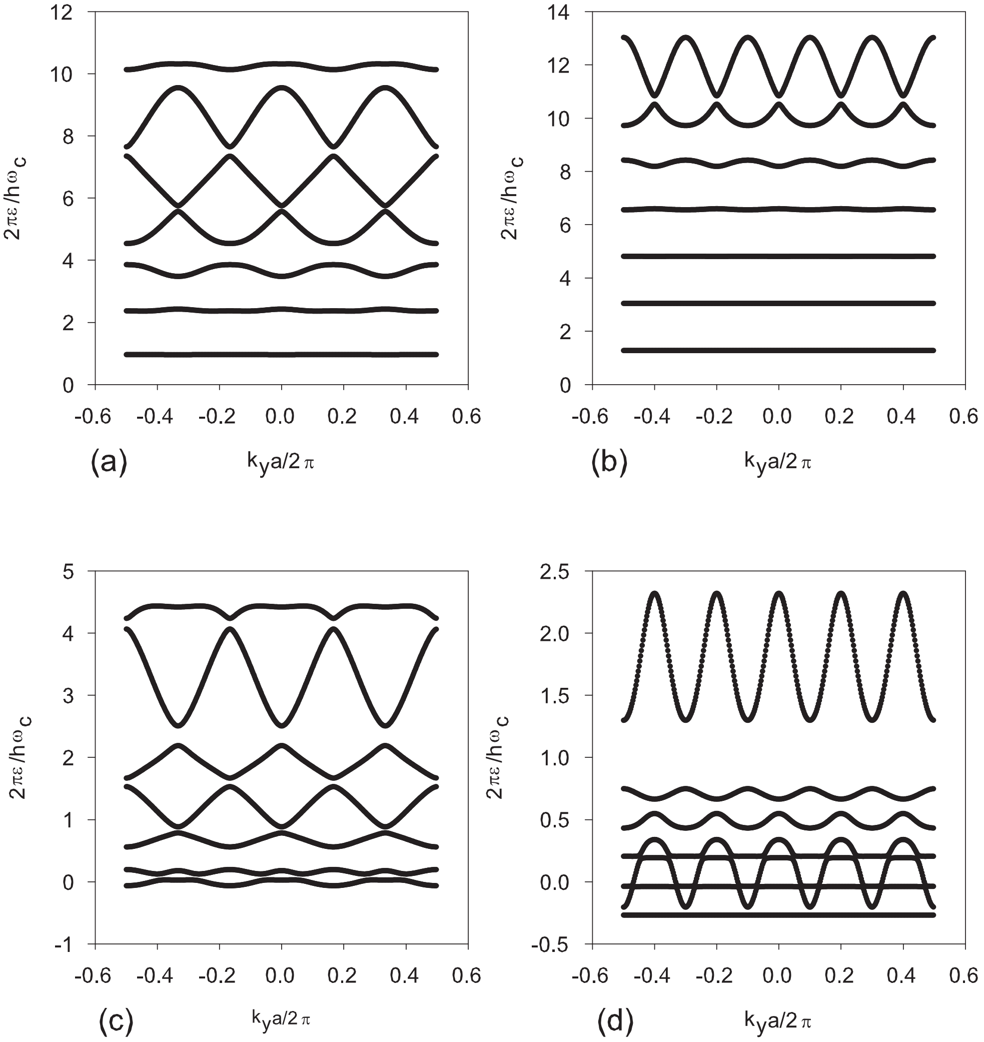

Figure 3.1: Plot of the dimensionless energy eigenvalues $\varepsilon/\hbar\omega_c$ vs. $\bar{k}_y = k_y a/2\pi$ for a 1D quantum wire and antiwire potential. The power of the modulation potential is $N = 10$, the scattering strength is $\bar{V} = 1.235$ for (a) and (b) and $\bar{V} = -1.235$ for (c) and (d). The flux ratio is $\Phi = 2/3$ for (a) and (c) and $\Phi = 2/5$ for (b) and (d).

(2.4) is 20 (which corresponds to $N = 10$, thus $2N = 20$) and this means that the potential peaks are steep, with a wide conduction channel produced between the peaks (See Figure 3.2 to follow how the shape of the 1D potential changes with an increase of N).

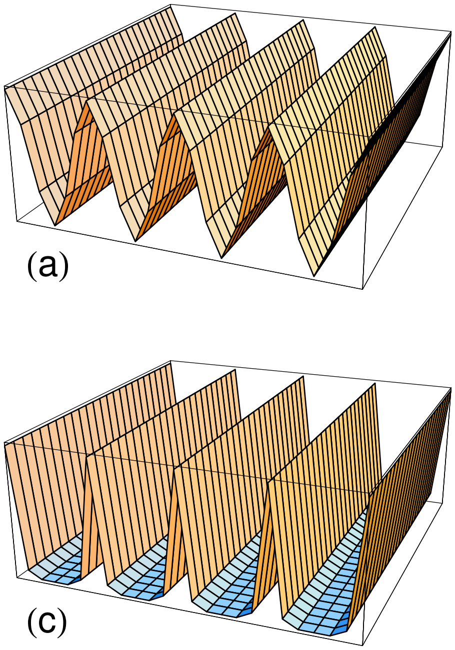

Figure 3.2: Sketch of the modulation potential for the 1D quantum wire array case. The four diagrams are drawn for $\bar{V} = 10$, $a = 0.5$. The power of the modulation potential is varied: (a) $N = 1$, (b) $N = 5$, (c) $N = 10$, (d) $N = 20$.

The strength of the scattering potential is chosen to be a small positive value of $\bar{V} = 1.235$ in Figures 3.1 (a) and (b) to model our one-dimensional quantum wire, and a negative value of $\bar{V} = -1.235$ for (c) and (d), which would correspond to an antiwire type potential. The values of the flux ratio are $\Phi = 2/3$ for (a) and (c) and $\Phi = 2/5$ for (b) and (d). Figure 3.1 illustrates how the energy eigenvalues deviate from the well-known Landau levels $\hbar\omega_c\left(n + \frac{1}{2}\right)$ of a homogeneous 2DEG with no modulation.

It can be seen that in the 1D quantum wire/antiwire modulation potential case there is a broadening of the Landau levels into bands of oscillatory width, but no subband formation can be observed. In the absence of modulation the eigenvalue dispersion would look like thin, straight, horizontal lines similar to the energy levels of a periodic oscillator potential. When a 1D modulation potential is present, the LL width depends on the values taken by $\bar{k}_y$ in an oscillatory manner, and this is a consequence of the scattering introduced by the potential. Figure 3.1 illustrates it well that the dispersion of the LLs becomes more significant with increasing band index n. The lowest LLs are still almost perfectly flat because the strength of the modulation is small, but the highest levels are very much affected by scattering, the broadening of these bands is very pronounced. For negative $\bar{V}$ some of the lowest energy eigenvalues become negative. The negativity of the low energy levels is more pronounced in Figure 3.1 (d), for which the value of the flux ratio is lower ($\Phi = 2/5$) than for Figure 3.1 (c). A lower flux ratio means a lower magnetic field (as $\Phi = Ba^2/\phi_0$, with $\phi_0 = \hbar/e$ the flux quantum and a the lattice constant), and in this lower magnetic field the highest energy level shows a larger band width oscillation as compared to the corresponding energy levels in the higher magnetic field. The explanation of this behavior is found in the large cyclotron orbit of electrons with high Landau level index n. Such electrons follow large radius circular paths, therefore the probability of them to be scattered by the walls of the quantum wires is larger.

These features of the energy eigenvalue dispersion plots can be explained by investigating how the electron's cyclotron orbit radius changes with the magnitude of the applied magnetic field and the value of the Landau level index n. The radius of the cyclotron orbit can be expressed as $r_c = \sqrt{(n+1)\,(\hbar/eB)}$, thus it is inversely proportional to the magnitude of the applied magnetic field, and directly proportional to the Landau level index n. It is reasonable then to find that in higher magnetic fields the

Landau levels will have a lesser widening, as an electron on a smaller cyclotron orbit will undergo less scattering. Also, electrons on higher Landau levels have a higher index n, and this means that they will follow larger orbits, with increased probabilities of undergoing scattering, as they encounter more collisions with the walls of the wires. Thus the higher LLs are more broad. For the small magnitudes of the modulation potential amplitude such as used in plotting Figure 3.1, there is no strong overlap between different Landau levels for the case of 1D modulation. In fact, as opposed to the case of 2D modulation that follows, with increased scattering strength magnitude the bands will become more widely separated from each other and do not overlap significantly. Also, the Hofstadter property of the eigenvalue dispersion plots is present for certain values of the flux ratio (such as the ones shown in Figure 3.1). It can be seen that in Figures 3.1 (a) and (c) there are three complete periods present in the first Brillouin zone corresponding to $\Phi = p/q = 2/3$ (i.e. there are $q = 3$ periods), while in Figures 3.1 (b) and (d) there are five periods, corresponding to $q = 5$.

For other rational values (such as $\Phi = 4/3$, $\Phi = 4/5$, $\Phi = 4/7$ for example) the Hofstadter type of periodicity is washed out, although the bands still show wide bandwidth oscillations, but the number of periods no longer matches up with the value of q. This is due to a commensurability effect between the radius of the electron's cyclotron orbit and the period of the 1D quantum wire modulation potential. For such values of the potential, the large number of scattering events that the electrons undergo lead to the disappearance of the periodicity. As the value of the flux ratio Φ increases (Φ is directly proportional to the applied magnetic flux B), the cyclotron radius of the electron decreases (for example, an electron moving in a magnetic field of flux ratio of $\Phi = 2/3$ will describe a circle with twice as large of a radius as the same identical electron moving in a magnetic field of flux ratio $\Phi = 4/3$) and an electron moving on a small circular orbit inside of a quantum wire may not even

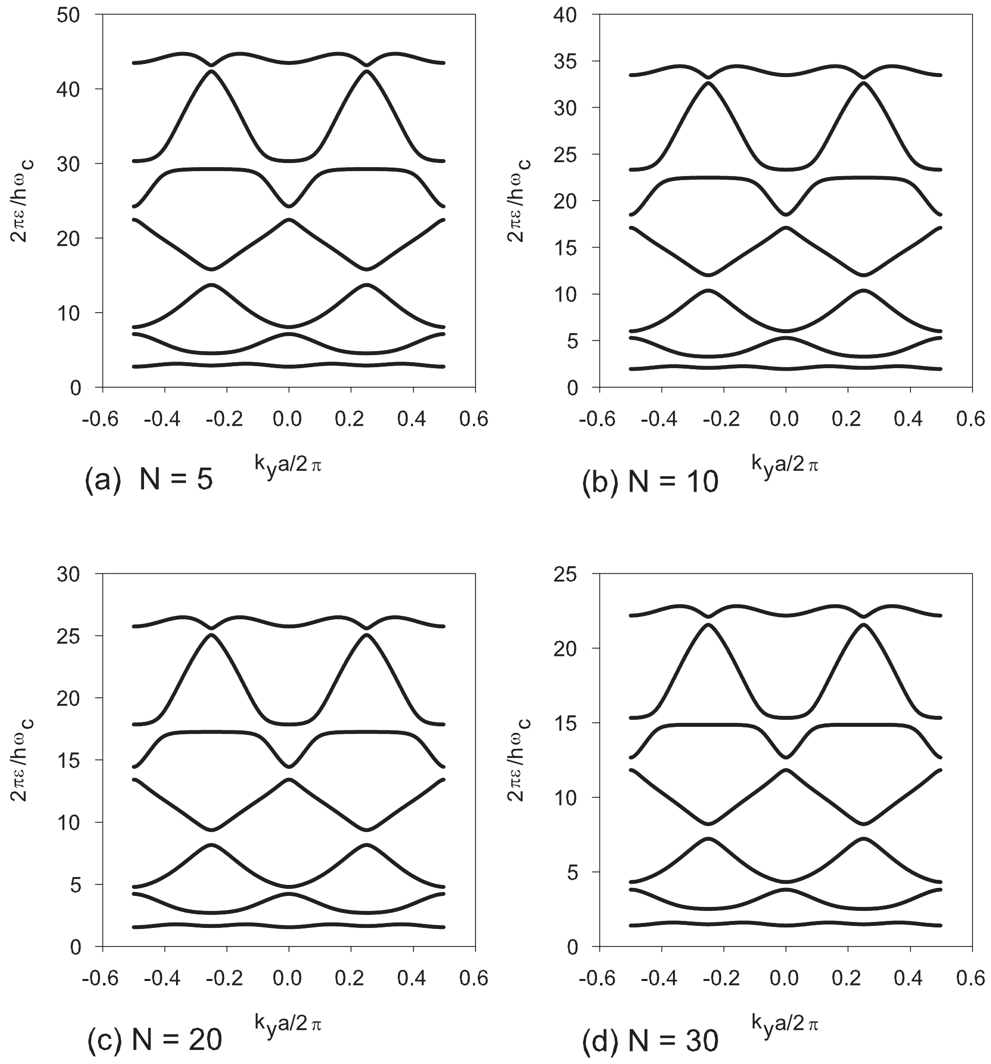

(a) N = 5

(b) N = 10

(c) N = 20

(d) N = 30

Figure 3.3: Plot of the energy eigenvalues $\varepsilon/\hbar\omega_c$ vs. $\bar{k}_y = k_y a/2\pi$ for a 1D quantum wire potential for different powers, N, of the modulation potential $U_L(\vec{x}) = \bar{V}\left[\cos\left(\frac{2\pi x}{a}\right)\right]^{2N}$. Other parameters are kept the same in all four figures: $\bar{V} = 12.35$, $\Phi = 1.0$, $N_x = 10$.

"feel" the influence of the potential if its radius of motion is small enough (i.e. will undergo no scattering off the potential).

3.1.2 Dependence of the 1D QW/QA Eigenspectrum on the Power of the Potential for Given Modulation Strength

Figure 3.3 shows the energy eigenvalue spectrum for four different values of the power of the periodic term entering the 1D modulation potential for the positive potential (QW) case. Figure (a) was obtained for the value of $N = 5$, (b) for $N = 10$, (c) for $N = 20$ and (d) for $N = 30$. The four energy eigenspectra are identical in shape, as all the other parameters in the numerical calculations were kept the same. Namely, the size of the sample was chosen such as to include $N_x = 10$ periods of the modulation potential (corresponding to 10 parallel quantum wires), the flux ratio had an integer value of $\Phi = 1$, while the strength of the modulation potential was $\bar{V} = 12.35$. The only difference in the four spectra is the amount of upward shift of the modulation-widened Landau bands. Thus for the smallest value of the exponent (Figure 3.3 (a)), the highest eigenvalues are as high as $\varepsilon/\hbar\omega_c = 45$ on the rescaled energy axis, while in Figure 3.3 (d) (which corresponds to the highest value of the periodic term's exponent) the highest eigenvalues are found around $\varepsilon/\hbar\omega_c = 23$. When the value of N is increased, the width of the quantum wires is increased (as it can be see in Figure 3.2). As the steepness of the quantum wire "walls" is increased, the space between them also increases, and more electrons can move freely in the enlarged space between the scattering potentials. For this reason, the upward shift of the LLs is decreased, when N is increased.

3.1.3 Dependence of the 1D QW/QA Eigenspectrum on the Flux Ratio for Given Modulation Strength

Figure 3.4 contains four plots of the energy eigenvalues as a function of the flux ratio for increasing values of the modulation potential amplitude. The values of the potential amplitude $\bar{V} = 0.235$ for plot (a), $\bar{V} = 1.235$ for plot (b), $\bar{V} = 5.235$ for plot (c), and $\bar{V} = 5.235$ for plot (d) were selected to show what modification to the energy levels occupied by electrons does an increase in the potential amplitude bring. Thus in Figure 3.4 (a), which corresponds to the smallest value of the potential, the LLs are not overlapping at all. In the same plot it can be seen that in the large magnetic field region (large values of Φ) the LLs behave like those expected for the unmodulated system (equally spaced, thin, horizontal lines). In the low magnetic field region however, the Landau levels are broadened, and show some oscillations. This behavior in the low magnetic field region can be explained by the fact that the cyclotron radius of the electron's path is large, thus the probability for the electron to undergo a collision is larger, as the larger the radius of the orbit, the larger the probability for the electron to undergo a collision with the walls of the constricting wires. Reversely, when the magnetic field has a large value, the cyclotron orbit of the electron is small, and it is therefore more probable that the electron will not collide with the walls of the quantum wire as it moves along it. This is why the right-hand side of plot (a) looks so much like unperturbed Landau levels. Now let us return to the role played by the modulation potential. Looking at the difference between plot (a) and plot (d) of Figure 3.4 one can see that a higher modulation potential amplitude leads to larger bandwidth oscillations of the Landau levels, which is caused by a stronger potential leading to more collisions of the electrons propagating through it. It is reasonable to think that when electrons travel along a system of shallow wires,

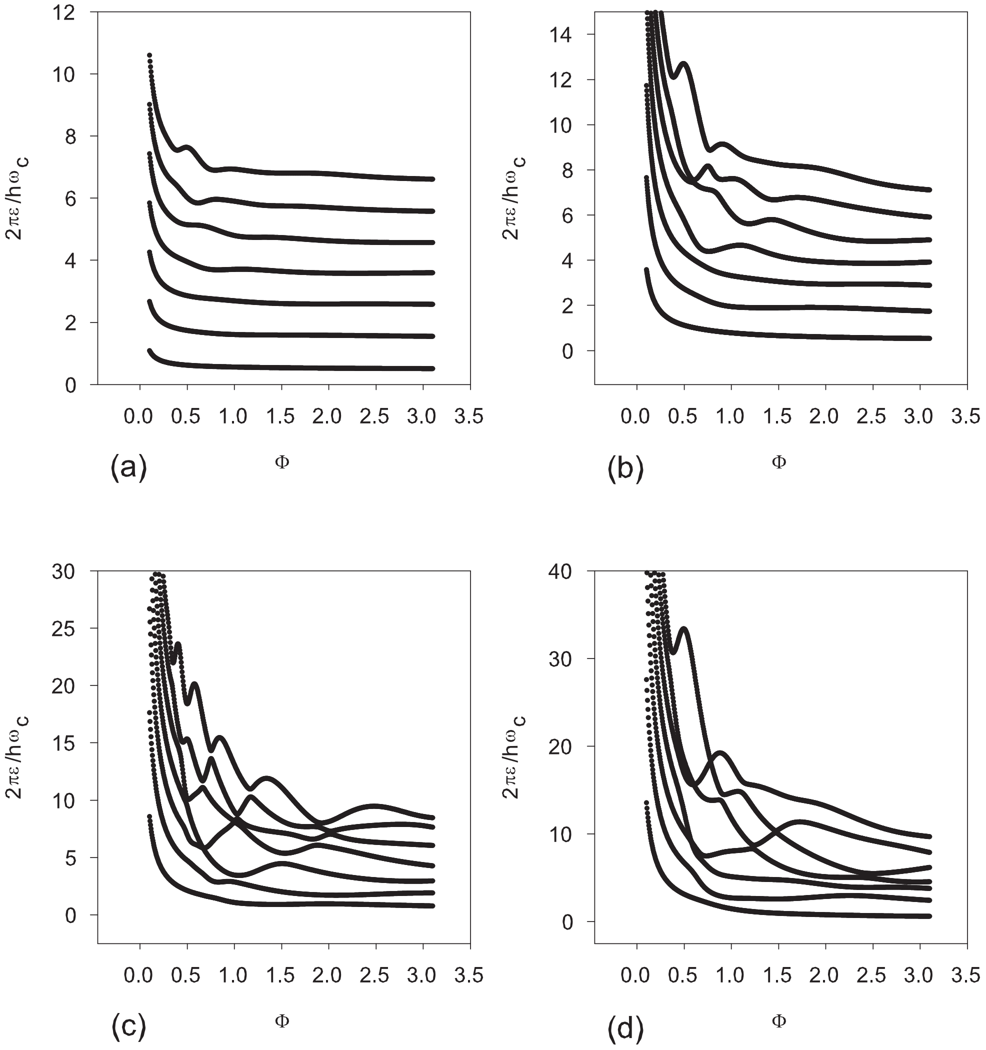

Figure 3.4: Plot of the energy levels $\varepsilon/\hbar\omega_c$ vs. the flux ratio $\Phi = Ba^2/\phi_0$ for a 1D quantum wire potential. The power of the modulation potential is $N = 10$. The scattering strength is $\bar{V} = 0.235$ for (a); $\bar{V} = 1.235$ for (b); $\bar{V} = 3.235$ for (c); and $\bar{V} = 5.235$ for (d). The plots were obtained for the following $k_y a/2\pi$ values: $k_y a/2\pi = -0.15$ for (a), (b), and (d); $k_y a/2\pi = 0.5$ for (c).

the probability of the electron scattering off the walls of the wire is small, and therefore the behavior of the 2DEG in this regime is not far from that of a free electron gas with no applied modulation potential. Plot (b) of Figure 3.4 depicts a situation that is intermediary between cases (a) and (c) or (d). There is definitely more mixing of the LLs in plot (b) than in plot (a), but in the large magnetic field region, where the electron describes small circles, there is a small probability for them to undergo a collision, as the combination of small orbiting radius and relatively weak modulation potential amplitude leads to a behavior of these charge carriers that is similar to that of the unmodulated system.

3.2 Eigenspectrum Dispersion Versus $\bar{k}_y$ for the 2D Delta Potential

In the following two subsections, we present numerical results for the eigenvalue dispersion curves for the delta potential expressed in equation (2.10). Figures 3.5 and 3.6 are energy eigenvalue dispersion spectra obtained numerically for the delta potential modulation through the solution of the secular equation (2.12).

3.2.1 The Influence of Changing Sample Size on the Eigenspectrum Dispersion for Delta Potential

In Figure 3.5 we present six eigenvalue dispersion diagrams obtained for the delta potential. The three figures on the left (labeled by (a), (c) and (e)) were obtained for a sample size of $N_x = N_y = 10$, while the three figures on the right (labeled (b), (d), and (f)) are for a larger sample, corresponding to $N_x = N_y = 20$ (i.e. the area of the sample for Figures 3.5 (b), (d), (f) is four times larger than those in (a), (c), (e)). All

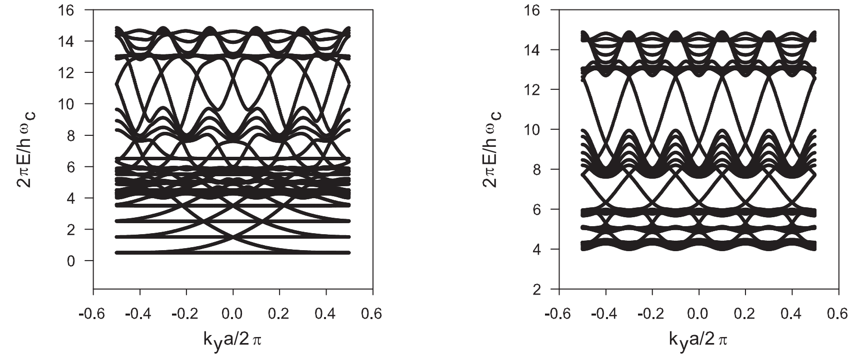

(a) $N_x = N_y = 10$ (b) $N_x = N_y = 20$

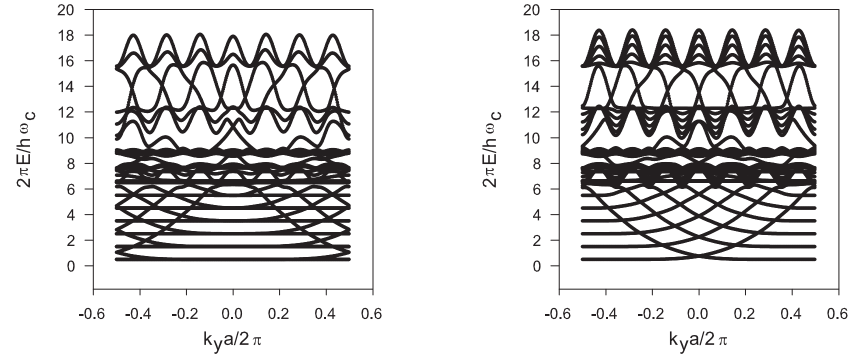

(c) $N_x = N_y = 10$ (d) $N_x = N_y = 20$

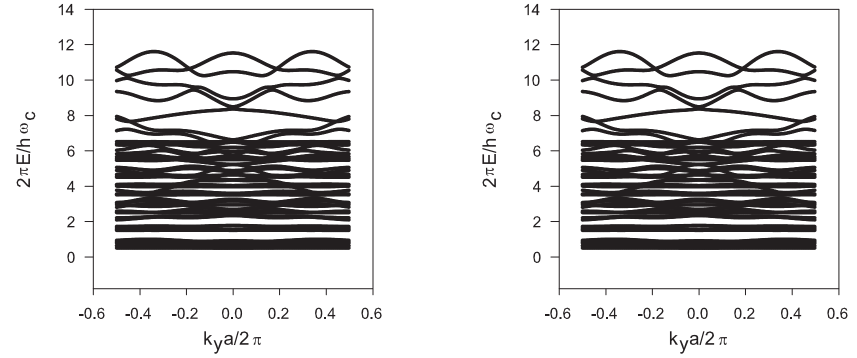

(e) $N_x = N_y = 10$ (f) $N_x = N_y = 20$

Figure 3.5: Influence of sample-size and variation of magnetic flux ratio $\Phi = Ba^2/\phi_0$, on the delta function modulation energy eigenspectrum versus $k_y a/2\pi$. The modulation potential is $V_0 = 1.235$ in all six cases shown. The figures on the left ((a), (c), and (e)) are for $N_x = N_y = 10$, while those on the right for $N_x = N_y = 20$. In figures (a) and (b) the rational value of the flux ratio is $\Phi = 1/5$, in (b) and (c) $\Phi = 1/7$, while in (d) and (e) $\Phi = 4/3$. In all of the plots, the same positive value of the modulation potential magnitude of $\bar{V} = 1.235$ was used.

six of the diagrams are obtained for the same, positive value of the modulation potential magnitude of $\bar{V} = 1.235$, thus they model a square array of strong, very steep and narrow antidot type of scatterers.

The pair of Figures 3.5 (a) and (b) are obtained for the same rational value of the flux ratio of $\Phi = 1/5$. Similarly, Figures 3.5 (c) and (d) also share the same rational value of the flux ratio of $\Phi = 1/7$. Finally the last pair of Figures 3.5 (e) and (f) are plotted for the common value of the flux ratio equal to $\Phi = 4/3$. By looking at these numerical values of the flux ratio, it can be observed that the first two pairs of diagrams (Figures 3.5 (a), (b), (c), and (d)) are obtained for relatively small values of the flux ratio, while the last pair of spectra (Figures 3.5 (e) and (f)) for a relatively large value. There are two important features that set apart the diagrams with smaller values of the flux ratio from those obtained for larger values. Both of these features can be explained with the same reasoning. The first feature is not as pronounced as the second one. Namely, it can be seen that for smaller values of the flux ratio, the eigenvalue spectra have a more significant upward shift then for the lower values. The second feature is that the first two pairs of graphs are not at all identical (although obtained for the same exact values of the parameters, except the sample size), while the last pair is identical (although these, too, were obtained for different sample sizes). These characteristics of the eigenvalue dispersion plots can be explained by investigating the influence that changing the magnitude of the applied magnetic field has on the electron's cyclotron orbit. The radius of the electron's orbit is inversely proportional to the applied magnetic field ($r_c = \sqrt{(n+1)\,(\hbar/eB)}$). Therefore, when the applied magnetic field is small (corresponding to the small values of the flux ratio Φ selected in Figures 3.5 (a), (b), (c), and (d)) the electron's orbit is large. This means that in its large radius orbiting motion the electron may

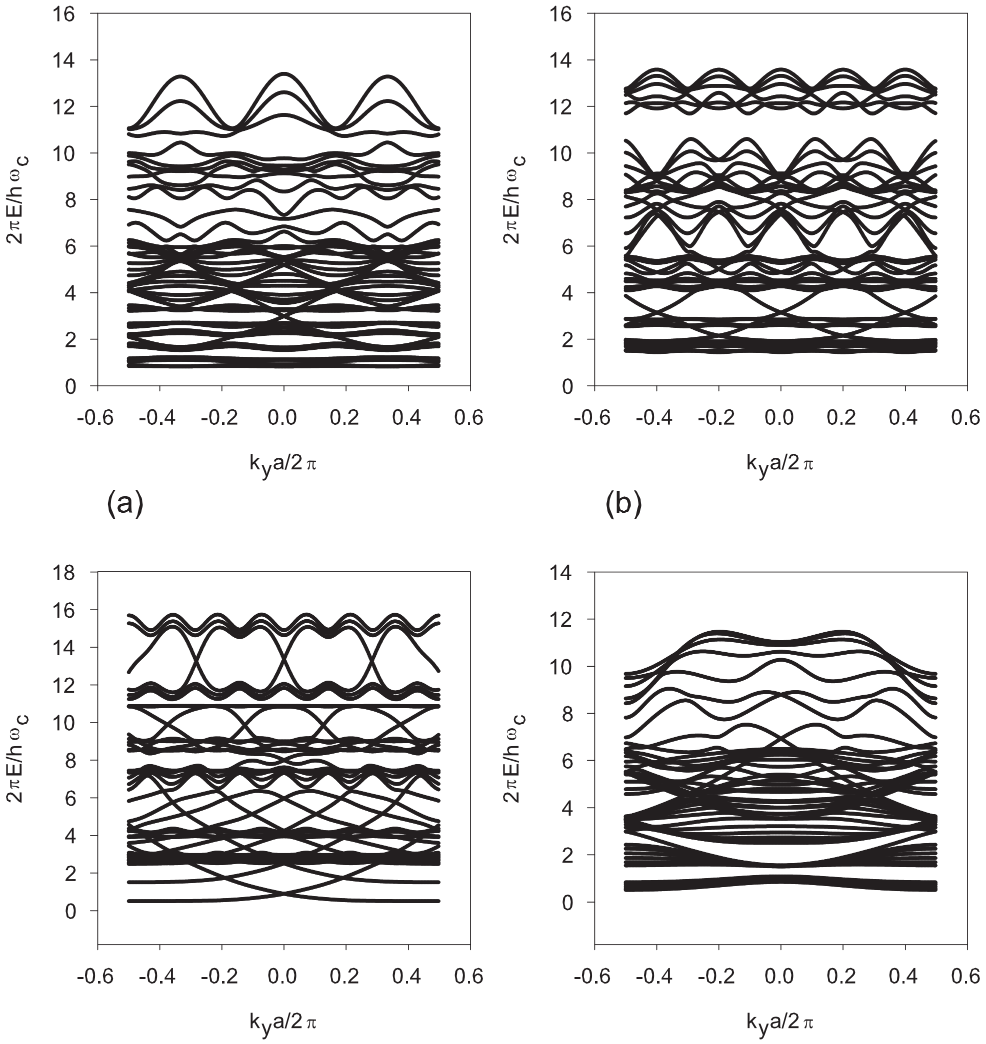

(a) (b)

(c) (d)

Figure 3.6: Influence on the eigenvalue dispersion plots of choosing rational vs. integer values of the flux ratio for the delta potential. The three different, rational values of the flux ratio are as follows: in (a) $\Phi = 2/3$, in (b) $\Phi = 2/5$, and in (c) $\Phi = 2/7$. The fourth plot (d) is shown for comparison, and it is obtained for the integer value of $\Phi = 1$. The modulation potential strength is $\bar{V} = 1.235$, and the sample size $N_x = N_y = 10$ for all four cases shown.

encounter many antidots, therefore making the probability of it being scattered larger than in the opposite case (larger value of the flux ratio Φ, such as selected for Figures 3.5 (e) and (f) corresponding to smaller cyclotron radii). When the cyclotron radius is small, the electron's orbit encircles only a few antidots, leading therefore to a much lower probability of being scattered. Therefore the highest energy eigenvalues lie lower than for the case of small applied magnetic fields. By selecting a different sample size the highest value attained by the energy eigenvalues stays the same, but the shape of the spectrum is different. When the sample is larger, including more antidots, electrons have a different probability to undergo scattering.

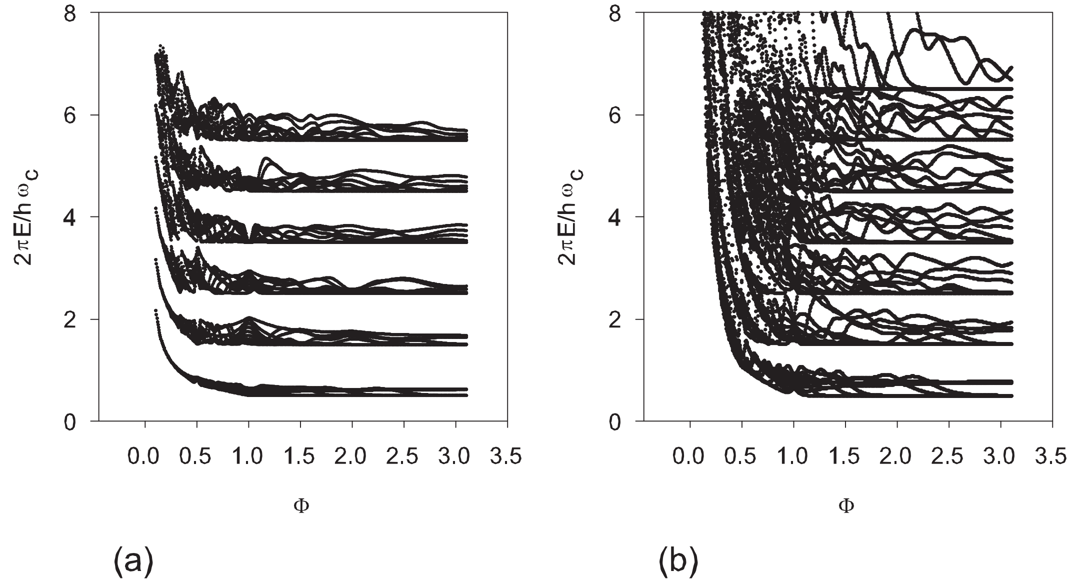

Figure 3.7: Energy eigenvalues versus the flux ratio $\Phi = Ba^2/\phi_0$ for two different values of the delta function modulation potential strength $\bar{V} = 0.235$ for (a) and $\bar{V} = 1.235$ for (b). Other parameters used in the plots are: $n = 5, m = 3, \bar{k}_y = -0.5$ for (a) and $n = 6, m = 4, \bar{k}_y = -0.25$for (b).

Figures 3.5 and 3.6 also illustrate the presence of Hofstadter-type periodicity in the wave-vector dispersion diagrams of the energy levels.

In Figure 3.6 (a) corresponding to $\Phi = p/q = 2/3$ the lowest Landau level is split into $p = 2$ subbands and there are $q = 3$ periods in the Brillouin zone. In Figure 3.6 (b), which was plotted for to $\Phi = p/q = 2/5$ there are $q = 5$ periods in the Brillouin zone, while in figure Figure 3.6 (c) there are $q = 7$ periods, corresponding to $\Phi = p/q = 2/7$. In the last of the Figures 3.6, which is Figure (d), there is no periodicity present in the Brillouin zone, as this figure corresponds to a value of $\Phi = 1.0$ (this is an integer value of the flux ratio, not a rational fraction). The periodic nature of the energy eigenvalue dispersion versus $\bar{k}_y$ plots can also be observed in Figure 3.5. Although the main reason for including this figure was to demonstrate the influence of increasing the sample size, the periodicity can be clearly seen on these diagrams as well.

3.2.2 Eigenvalues Versus Flux Ratio for 2D Delta Potential

When the magnitude of the scattering potential is small, the eigenvalue versus flux ratio plots show large bandwidth oscillations for the delta potential modulation case, as it can be seen in Figure 3.7. For weak scattering potential magnitude there is no overlap between different Landau levels, except for very small values of the flux ratio Φ. Even in the case of such weak scattering however, the coupling between Landau eigenstates cannot be ignored even for larger values of the flux ratio, values for which no mixing in the Landau levels can be seen in the plots. This can be deduced from the values obtained numerically for the expansion coefficients $C_{n,m}(j, X_0)$. These expansion coefficients result from the diagonalization of the matrix in equation (2.11). The coefficients $C_{n,m}(j, X_0)$ couple the Landau levels by entering the expression of the group velocities (calculated in Chapter 5). When the magnitude of the modulation potential is increased, the Landau levels overlap.

3.3 Energy Eigenvalue Plots for the 2D QD/QA Modulation

In this section we present energy eigenvalue plots that were obtained numerically for a 2D quantum dot/antidot array, modeled by the potential form given in equation (2.5). The energy eigenvalues are again investigated both as a function of the rescaled wave vector $\bar{k}_y$, and the flux ratio Φ, just as it was done in the case of the delta potential modulation, and the one-dimensional periodic cosine potential. We also investigated the influence that changing the power of the 2D periodic potential in equation (2.5) would have in the shape of the eigenspectrum dispersion.

3.3.1 Eigenvalue Dispersion for 2D QA Modulation

Figure 3.8 presents the wave-vector dispersion in the first Brillouin zone of the energy eigenvalues for the 2D quantum antidot potential. This means that the values of $\bar{V}$ are chosen to be positive in equation (2.5). Figure 3.8 was obtained for the following values of the parameters. For all six figures, the sample size was chosen to be the same ($N_x = N_y = 10$), as well as was the power of the product of the periodic terms in the expression of the potential ($N = 10$). The six different graphs correspond to three different positive values of the modulation potential magnitude, namely Figure 3.8 (a) was obtained for a small value of the modulation potential magnitude ($\bar{V} = 1.235$), Figure (b) was obtained for an intermediary value of this parameter ($\bar{V} = 12.350$), while Figures 3.8 (c)-(f) were obtained for the value of $\bar{V} = 50.000$, for which the Landau levels deviate considerably from the unperturbed case. Figure 3.8 (a) is showing only a portion of the full graph, to allow presenting more detail. This way the features of the three lowest Landau bands are magnified, so that their structure

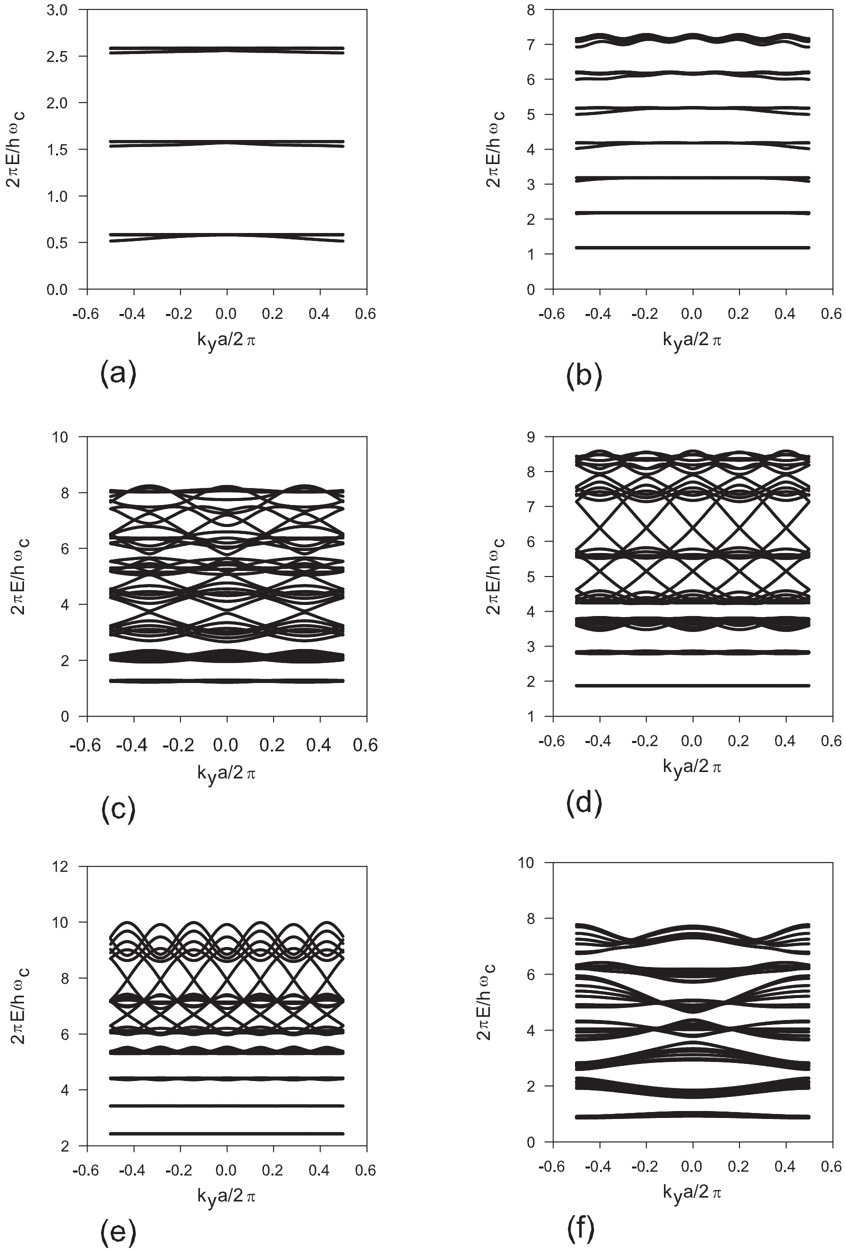

Figure 3.8: Plot of the energy eigenvalues $\varepsilon/\hbar\omega_c$ vs. $\bar{k}_y = k_y a/2\pi$ for 2D quantum antidot potentials. The modulation potential values used are as follows: in plot (a) $\bar{V} = 1.235$, in plot (b) $\bar{V} = 12.350$, while in plots (c)-(f) $\bar{V} = 50.000$. The sample size is $N_x = N_y = 10$, and the other parameters are kept the same in all six figures ($n = 6$, $m = 3$). The values of the flux ratio are chosen as follows: $\Phi = 1/3$ in (a), $\Phi = 2/5$ in (b), $\Phi = 4/3$ in (c), $\Phi = 4/5$ in (d), $\Phi = 4/7$ in (e), $\Phi = 2$ in (f).

can be seen. If the whole graph was shown, it would be impossible to tell these slightly broadened energy bands apart from those corresponding to the unperturbed case (unmodulated 2DEG).

In all six figures it can be seen that the width of the Landau levels is increased in the presence of modulation. The width increase is more pronounced for higher values of the modulation potential magnitude. Also, it can be seen that the amplitude of the oscillation increases with the increase of the Landau level index n (higher Landau levels have wider oscillations). The lowest Landau levels are almost completely flat, thus the potential does not completely lift their degeneracy. Landau levels with higher indices are more affected by the perturbation, thus their bandwidth oscillates much more significantly. Also, it can be seen that the LLs are split into subbands in a way that is similar to what was seen in the case of the delta potential scatterers, but not for the 1D modulation case (no subband structure was seen in the 1D periodic potential modulation). The widening and splitting of the Landau levels into bands is first of all directly proportional to the magnitude of the applied modulating potential. Also, it is directly proportional to the Landau level index. This can be explained again (just as in the case of delta and 1D modulation) by the fact that the cyclotron radius is directly proportional to the LL index and inversely proportional to the applied magnetic field. When the magnitude of the applied magnetic field is low, the electrons will describe large circular orbits. This means that the probability of the electron to being scattered by the modulation potential is large, therefore one expects that for smaller values of the magnetic field the width of the Landau level dispersion will be larger. The reverse is also true: for large magnetic fields (corresponding to larger values of Φ), electrons will describe orbits of smaller cyclotron radius, therefore it will be less probable that they would undergo collisions with the scattering centers introduced by the modulation potential. Also it is important to note the periodicity of the energy eigenvalue dispersion plots with the rational values of the flux ratio. In Figure 3.8 (b) the choice of $\Phi = p/q = 2/5$ causes the highest Landau level to have $q = 5$ periods, $\Phi = p/q = 4/3$ in (c) shows a periodicity of $q = 3$, $\Phi = p/q = 4/5$ in (d) displays $q = 5$ periods, $\Phi = p/q = 4/7$ in (e) has $q = 7$ periods, while for the integer value of $\Phi = 2$ in (f), there is no periodicity present. These results correspond to the “fingerprints” of the Hofstadter type eigenenergy spectrum.

3.3.2 Eigenvalue Dispersion for 2D QD Modulation

Shown in Figure 3.9 are the eigenenergy dispersion curves within the first Brillouin zone for the negative 2D periodic potential modeling quantum dots. The potential values chosen for the plot are $\bar{V} = -25.000$ for figures (a) and (b) and $\bar{V} = -50.000$ for (c) and (d). It is seen in the graphs that the Landau level width oscillates periodically for negative values of the modulation potential as well. The bandwidth oscillations are wider for smaller magnetic fields. As $\Phi = 2/3$ in figures (a) and (c) is smaller than $\Phi = 4/5$ in figures (b) and (d) the oscillations are wider in figures (a) and (c) as compared to those seen in (b) and (d). Also, the oscillating width of the Landau levels with higher index is much larger than those of the lower ones. Some of the lower Landau levels are almost unperturbed, so these potentials cannot completely lift the degeneracy of the lowest laying LLs. The explanation for these wider width oscillations is the same as presented in the quantum antidot case. The oscillation width is influenced by the size of the electron’s cyclotron orbit, which is directly proportional to the Landau level index and inversely proportional to the applied magnetic field. The presence of a Hofstadter type spectrum is evident in the case of the quantum dot modulation, too. It can be seen that the spectra displayed in Figures 3.9 (a) and (c) have three complete periods, corresponding to $q = 3$ (a rational value

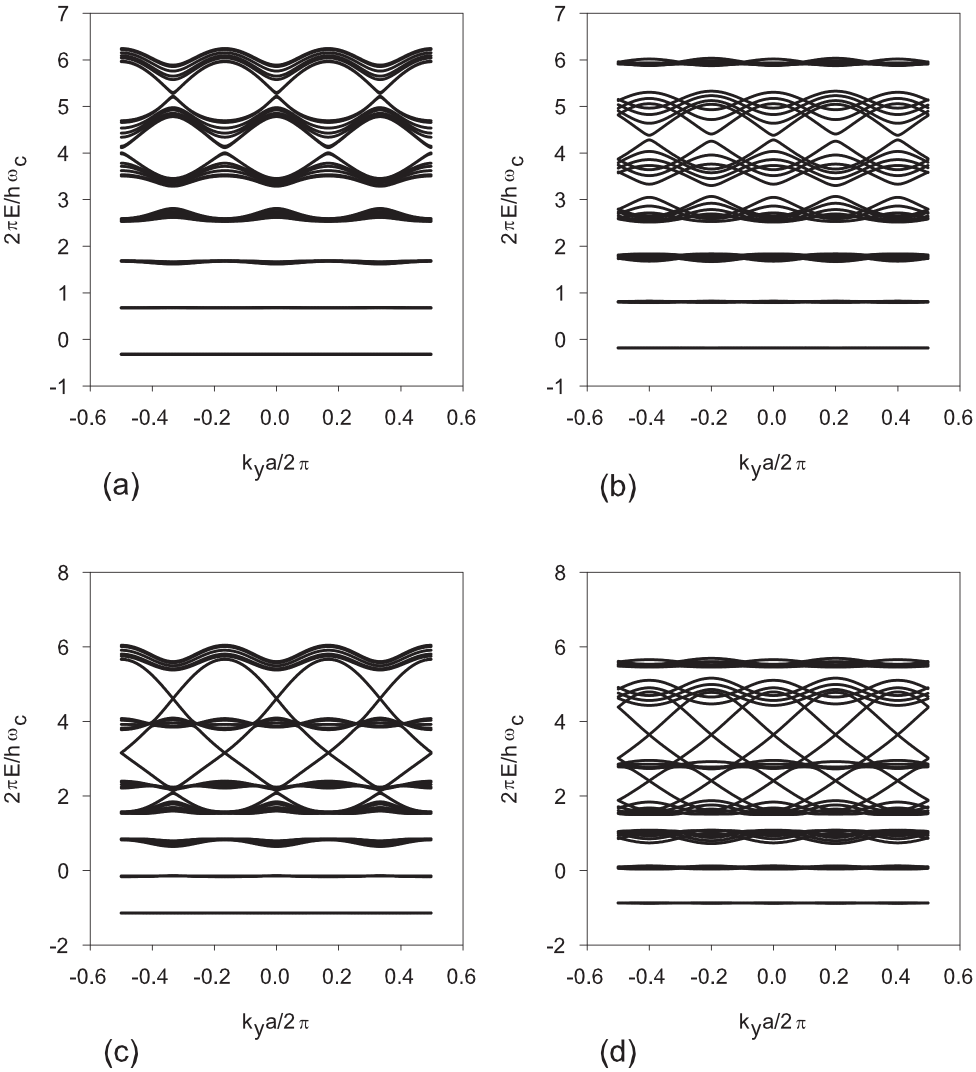

Figure 3.9: Plot of the energy eigenvalues $\varepsilon/\hbar\omega_c$ vs. $\bar{k}_y = k_y a/2\pi$ for a 2D quantum dot potential for different negative values of the modulation amplitudes, $\bar{V}$, and for two different rational values of the flux ratio Φ. In plots (a) and (b) $\bar{V} = -25.000$, while in (c) and (d) $\bar{V} = -50.000$. The sample size chosen was $N_x = N_y = 10$. Other parameters are kept the same in all six figures ($n = 6$, $m = 3$). The values of the flux ratio are chosen as follows: $\Phi = 2/3$ in (a) and (c), $\Phi = 4/5$ in (b) and (d).

of the flux ratio of $\Phi = p/q = 2/3$ was chosen in these two graphs), while the spectra displayed in Figures (b) and (d) includes a number $q = 5$ of complete oscillation corresponding to $\Phi = p/q = 4/5$. The influence of the magnitude of the modulation potential strength on the spectra can be seen by looking at values of the lowest energy levels: for the larger absolute value of the modulation potential $\bar{V} = -50.000$ (Figures (c) and (d)) the lowermost levels lie below those seen in figures (a) and (b), which were obtained for the value of the potential $\bar{V} = -25.000$.

3.3.3 Eigenvalues Versus Flux Ratio for 2D QA Potential

The dependence of the energy eigenvalues on the flux ratio Φ is shown in Figure 3.10 for quantum antidots. Three different values of the modulation potential strength were chosen to illustrate how the eigenvalue dispersion is influenced by changing the strength of modulation. As it was expected, when $\bar{V}$ increases, the Landau levels are shifted upward. On the left-hand side of the spectra, where the magnetic field is small, there is strong mixing of the Landau levels, especially for the higher values of the modulation potential. On the high magnetic field end of the plots (right-hand side) where there is no mixing of the Landau levels for the chosen values of the modulation potential strength, there is more broadening of the Landau levels for larger values of the modulation strength than for lower values. The explanation for this lies in the physical fact that for larger values of the modulation potential there will be more scattering, thus the Landau levels will be more broadened. For higher values of the modulation, mixing of the Landau levels would be seen even in the high magnetic field portion of the spectrum. In strong modulation (values of $\bar{V}$ exceeding 50.000) the Landau levels will overlap. This range of the potential is illustrated in the next subsection for the quantum dot potential case.

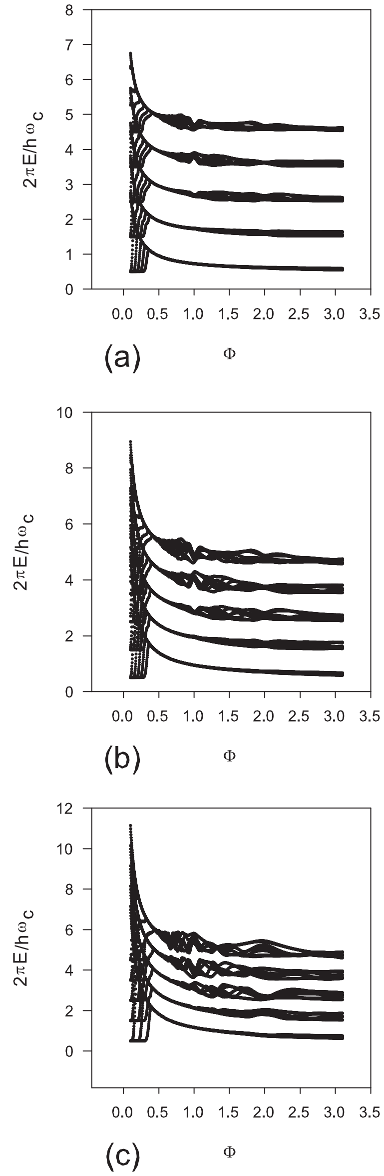

Figure 3.10: Plot of the energy eigenvalues $\varepsilon/\hbar\omega_c$ vs. Φ for a 2D quantum antidot potential for different positive values of the modulation amplitudes, $\bar{V}$, and for the same value of the wave vector $\bar{k}_y = 0.25$. The values of the modulation potential magnitude are $\bar{V} = 10.235$ in figure (a), $\bar{V} = 20.235$ in figure (b), and $\bar{V} = 30.235$ in figure (c). The sample size chosen was $N_x = N_y = 10$. Other parameters are kept the same in all six figures ($n = 4$, $m = 3$).

3.3.4 Eigenvalues Versus Flux Ratio for 2D QD Potential

Figure 3.11 shows the dependence of energy eigenvalue spectra on the variation of the magnitude of the modulation potential for negative values, which corresponds to quantum dots. The values of the potential in this case were chosen to have large absolute values, to illustrate the mixing of the Landau levels for large values of the potential. In all three graphs we can see that there is a large negative shift in eigenvalues for small values of the magnetic flux Φ. This is due to two reasons: first of all a large negative perturbation will lift the degeneracy of the Landau levels considerably, and secondly, for small values of the applied magnetic field the electrons are on larger cyclotron orbits, which increases their probability of undergoing scattering. Also it is seen that these eigenvalues corresponding to the smallest values of the applied magnetic field are strongly shifted down into the negative domain (the lowest energy eigenvalues are omitted from the plots, except Figure (a), to show more detail of the LL mixing in the upper portion of the spectrum). This is due to a combined effect of the negative potential and the applied magnetic field. Because a negative potential is applied to the 2DEG, some electrons, which may have small enough cyclotron orbits may be trapped inside the quantum dots, which means that their energy eigenvalues will be negative. The negativity of the eigenvalue spectrum is actually influenced by three factors. All of these are related to the feasibility of the electron being trapped inside the quantum dot. There will be large probability for an electron to be trapped inside the quantum dot if the diameter of the dot is large (this translates into a small value of the exponential of the periodic terms, thus N should be small), if the applied, negative modulation potential magnitude is large, and if the cyclotron orbit's diameter is small enough. As it will be seen in the next subsection, the dependence of the eigenvalues on the power of the periodic term is as expected (the smaller the

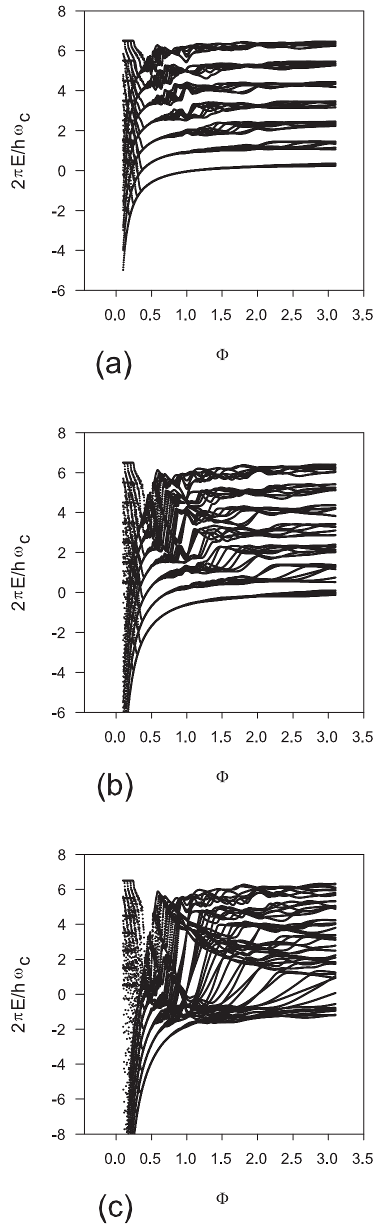

Figure 3.11: Plot of the energy eigenvalues $\varepsilon/\hbar\omega_c$ vs. Φ for a 2D quantum dot potential for different negative values of the modulation amplitudes, $\bar{V}$, and for the same value of the wave vector $\bar{k}_y = 0.25$. Large values of the modulation potential magnitudes were selected such as $\bar{V} = -25.000$ in figure (a), $\bar{V} = -50.000$ in figure (b), and $\bar{V} = -100.000$ in figure (c). The sample size chosen was $N_x = N_y = 10$. Other parameters are kept the same in all six figures ($n = 6$, $m = 3$).

value of N, the more negative the lowest energy eigenvalues become when all other parameters are the same). Figure 3.11 (a) corresponds to the smallest magnitude of the modulation potential $\bar{V} = -25.000$. It can be seen that LL mixing occurs mainly on the left-hand side of the plot, which corresponds to small values of the magnetic field. On the higher magnetic field end of the spectrum there is no LL mixing, but a subband structure can be seen, which is due to the fact that the potential lifts the degeneracy of these levels. In figure (b), which was obtained for the value $\bar{V} = -50.000$, there is more mixing of the LLs, even for some intermediate values of the magnetic field. In the left-hand side of the spectrum however, where the magnetic field is large, the Landau bands are only split into bands, but do not mix. For the third plot in the figure (c), which corresponds to the largest absolute value of the modulation potential $\bar{V} = -100.000$, there is mixing of LLs in every portion of the spectrum. For most part of the plot, the energy eigenlevels do not retain any resemblance to the thin, parallel, horizontal lines, which are characteristics of the unperturbed 2DEG. It has to be admitted that this last value of the modulation potential is in the very high range, which would not likely correspond to a "real" lattice potential.

3.3.5 Dependence of Eigenvalue Versus $\bar{k}_y$ Plots on the Power of the Cosine Terms for the 2D QD Potential

In the final part of the section analyzing the eigenvalue spectra, we present Figure 3.12 which is a plot of the energy eigenvalues versus the wave vector $\bar{k}_y$ obtained for several different values of the exponent of the cosine terms in the 2D periodic potential corresponding to negative modulation potentials (quantum dots). First of all, it is important to point out what modifications in the eigenvalue spectrum does the variation of the power of the periodic function cause in these spectra, as compared to Figure 3.3 in the 1D periodic modulation case. As opposed to the 1D modulation case, the quantum dot energy eigenvalue spectra are not identical in shape for the four different values of the modulation potential power, such as the case was for 1D modulation. All four of the spectra are different, although certain trends carry over from the lower values of the exponent N to the next higher value. What is important to notice is that we can follow how the negativity of the lowermost energy eigenvalues changes as a function of the power of the cosine terms, as it was described in the previous subsection. First of all, in all four spectra, the highest energy eigenvalues are located around the same value of 6. Thus the higher end of the energy spectrum is not drastically influenced by a change of the exponents. The change is more significant at the negative end of the spectrum. In Figure 3.12 (a), the lowest energy eigenvalues can be found around the value of -6, for Figure (b) around -3, for (c) around -1, while for Figure (d) around -0.5. It should be noted that other than changing the power of the periodic terms, all four of the spectra were obtained for identical values of the rest of the parameters. The modulation potential had a value of $\bar{V} = -50.000$, the sample size was $N_x = N_y = 10$, and the flux ratio $\Phi = 1/3$. The difference in shape, and in the lowest energy eigenvalue observed in the different spectra can be explained by the influence that the increase of the exponent has on the sizes of the quantum dots created. When the exponent is small, the diameter of the quantum dot is large. This means that electrons with even slightly larger cyclotron orbits can be trapped inside the dot, and therefore the energy eigenvalue spectrum shifts towards negative values. As the value of the exponent is increased, the diameter of the quantum dots decreases, and so does the negativity of the bottom part of the eigenvalue spectrum.

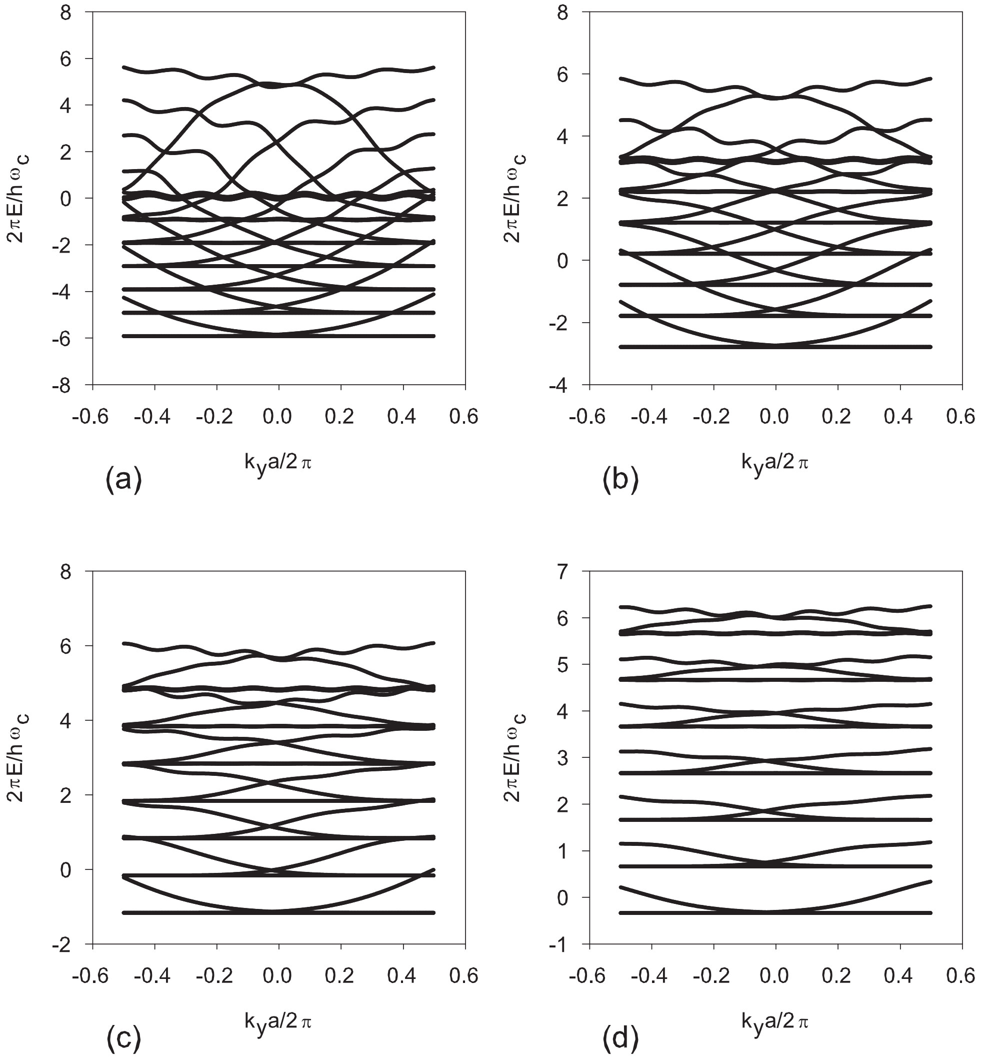

Figure 3.12: Plot of the energy eigenvalues $\varepsilon/\hbar\omega_c$ vs. $\bar{k}_y = k_y a/2\pi$ for 2D quantum dot potentials of different powers, N, of the modulation $U_L(\vec{x}) = \bar{V}\left[\cos\left(\frac{2\pi x}{a}\right)\cos\left(\frac{2\pi y}{a}\right)\right]^{2N}$. In Figure (a) $N = 5$, in (b) $N = 10$, in (c) $N = 20$, while in (d) $N = 40$ was the value chosen for the exponent of the periodic terms in the potential. Other parameters are kept the same in all four figures: $\bar{V} = -50.000$, $\Phi = 1/3$, sample size $N_x = N_y = 10$. This plot was obtained for the values $n = 6$, $m = 3$.

3.4 Variation of the Fermi Energy with the Applied Magnetic Field

In the final part of this chapter we will present numerical results obtained for the calculation of the Fermi energy for the three different potential forms investigated. The Fermi energy was obtained by the numerical solution of the equation:

$$n_{2D} = \frac{2N_y\Phi}{A}\sum_j \int_{-\frac{GL_H^2}{2}}^{\frac{GL_H^2}{2}} \frac{dX_0}{a} \int_{-\infty}^{\infty} d\varepsilon f\left(\varepsilon - \varepsilon_F\right) D_{j,X_0}\left(\varepsilon\right) \tag{3.1}$$

where n_{2D} is the carrier density of our sample, f stands for the Fermi-Dirac distribution function, and $D_{j,X_0}\left(\varepsilon\right)$ is the partial density of states. Obtaining plots for the variation of the Fermi energy as a function of the applied magnetic field was an important step in our numerical calculations, which followed after the eigenspectrum dispersion results were attained. The combined results of the eigenspectrum dispersion and Fermi energy plots were needed to calculate the conductance coefficients.

3.4.1 Fermi Energy for the Delta Potential

In Figure 3.13 the Fermi energy is plotted as a function of the flux ratio Φ for the positive delta function scattering potential for four different values of the modulation potential amplitude. As it is shown in this figure, the position of the Fermi energy depends on two parameters that can be modified experimentally. One is the magnitude of the flux ratio Φ, and the other is the strength of the scattering potential $\bar{V}$. In terms of the values taken by the parameter Φ the presented plots show that the Fermi energy varies as follows: for small values of the flux ratio (which corresponds to low magnetic fields) the Fermi energy is high, while for large values of the flux ratio (large magnetic fields) the Fermi energy is low. Thus the value taken by the Fermi energy is changing inversely with the increase of the applied magnetic field. As a function of the modulation potential magnitude $\bar{V}$, the shape of the Fermi energy graphs will be different for different modulation strengths for the same potential type, and it will also behave differently for the different potential types investigated, i.e. the variation of the Fermi energy for a positive quantum antidot system will be different than its variation for a system of negative quantum dots. Another interesting feature of the variation of the Fermi energy that can be seen in Figure 3.13 is the appearance of "steps" in its variation for larger values of the magnetic field. These steps can be explained with the following reasoning. As the Landau levels are degenerate, more than one electronic state can lie on each of these levels. Thus each level can be occupied by a certain number of electrons, and this number is determined by the value of the density of states, which is influenced by the magnitude of the applied magnetic field. As the magnitude of the applied magnetic field increases, more and more electrons can be placed into each Landau level, but the Fermi energy only changes to the next lower Landau level when the magnetic field's value is large enough so that all the states can be accommodated by the lower lying Landau levels. Thus a higher lying Landau level is gradually "depopulated" as the magnetic field increases, until even the last electron leaves this upper level, when the Fermi energy jumps to the next lower lying Landau level. This behavior of the Fermi energy is known as the "pinning of the Fermi energy at Landau levels" [54].

The second important parameter influencing the placement of the Fermi energy is the magnitude of the applied modulation potential $\bar{V}$. It can be seen in Figure 3.13 that the higher the magnitude of the modulation potential, the higher the value of the Fermi energy. This is a straightforward dependence of the Fermi energy on the applied modulation strength, as the stronger the modulation potential, the more

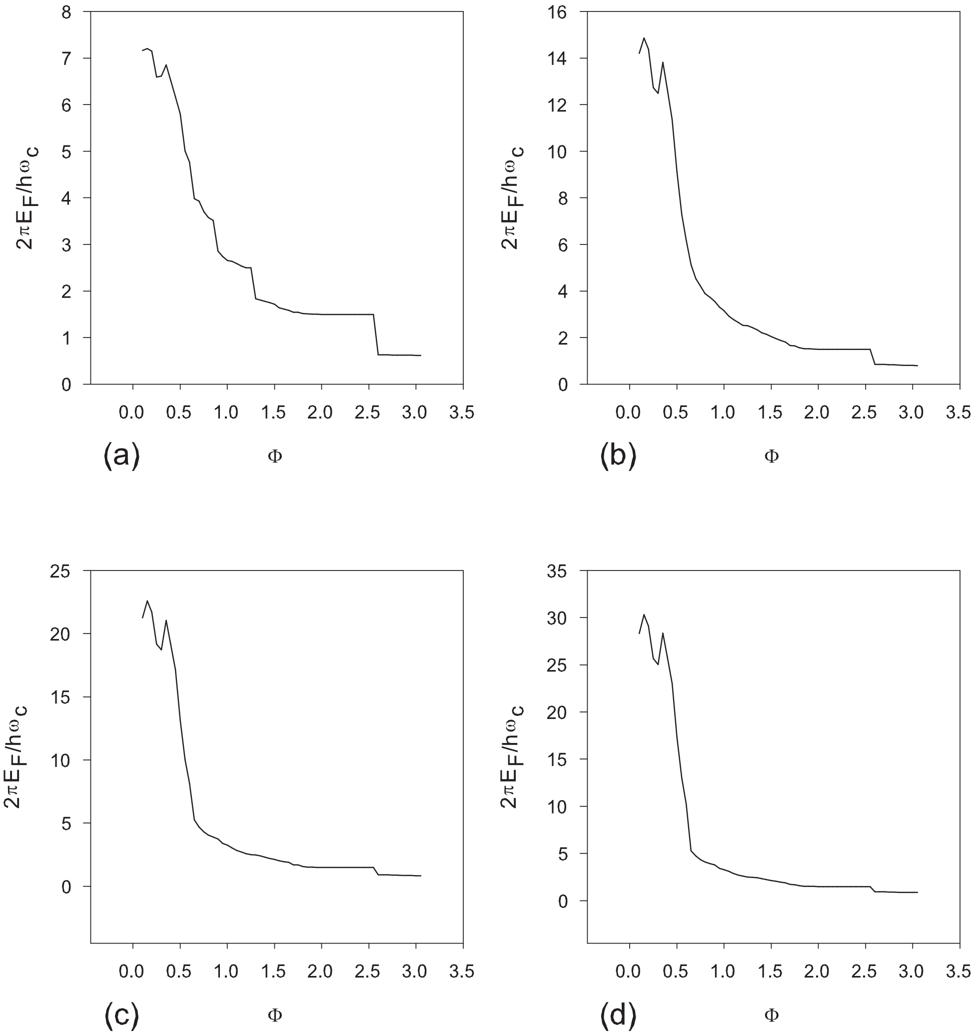

Figure 3.13: Plots of the Fermi energy as a function of the magnetic flux ratio Φ for the positive delta potential for different modulation strengths. Parameters used electron density $n_{2D}a^2 = 1.00$ and sample size $N_x = N_y = 20$ are the same for all four Figures. The modulation potential strength is $\bar{V} = 0.235$ in Figure (a), $\bar{V} = 1.235$ in Figure (b), $\bar{V} = 2.235$ in Figure (c), and $\bar{V} = 3.235$ in Figure (d).

likely it is that electrons undergo scattering.

3.4.2 Fermi Energy for 2D Periodic Potentials

Figure 3.14 includes six plots of the Fermi energy's variation with respect to the flux ratio Φ for the 2D dot (negative) and antidot (positive) periodic potential. The first two figures ((a) and (b)) are obtained for the negative, quantum dot potential, while the rest of the figures are the result of quantum antidot calculations (positive modulation). There is a marked difference between the behavior of the Fermi energy for the quantum dot type of potential (negative modulation), and that obtained for quantum antidots (positive modulation strength). This difference is in the profile of the steps (or plateaus) for the negative potential, as compared to the positive ones. The negative potential plateaus observed in the variation of the Fermi energy in Figure 3.14 start from a slightly lower value, then rise slightly. Meanwhile the positive potential plateaus start from a slightly higher value, and then fall slightly. For both the positive and negative potential the Fermi energy maintains its constant value along the plateaus while the applied magnetic field is increasing, until at a certain value of the magnetic field the Fermi energy abruptly changes, by jumping to the next lower lying plateau. This behavior is repeated several times until the lowest Landau level is reached for a threshold value of the magnetic field below which no more steps are observed in the variation of the Fermi energy. After this threshold value is exceeded the 2D electron system behaves as a homogeneous electron gas. For these large values of the magnetic field the orbits described by electrons are so small that scattering by the potential is unlikely, the electrons describe circular orbits between the potential peaks, without being scattered by the potential, thus they behave as an unperturbed 2DEG. The slight difference between the shape of the plateaus of

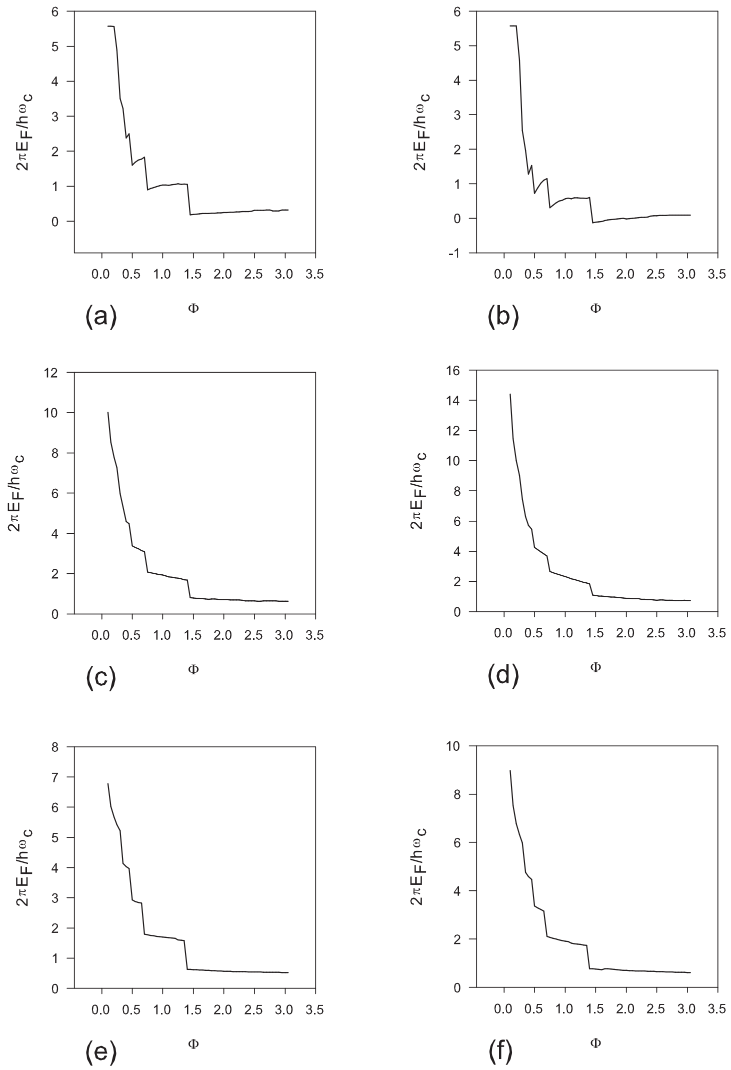

Figure 3.14: Plots of the Fermi energy as a function of the magnetic flux ratio Φ for the quantum dot and antidot potentials for different (positive and negative) modulation strengths. Parameters common to all six figures are: the electron density $n_{2D}a^2 = 1.00$, the sample size $N_x = N_y = 10$, and the power of the cross product of cosine function term $N = 10$. In Figure (a), (b), (c), and (d) the number of states is determined by $n = 5$, $m = 3$, while in Figures (e) and (f) the highest value taken by Landau level index was decreased by one, thus $n = 4$, $m = 3$. The values of the modulation potential strength are $\bar{V} = -20.235$ in Figure (a), $\bar{V} = -40.235$ in Figure (b), $\bar{V} = 20.235$ in Figure (c), $\bar{V} = 40.235$ in Figure (d), $\bar{V} = 10.235$ in Figure (e) and $\bar{V} = 20.235$ in Figure (f).

the Fermi energy variation with respect to the applied magnetic field permits one to differentiate between the two distinct models investigated (positive or negative potentials) not only by looking at their eigenvalue dispersion curves (discussed at the beginning of this Chapter) but also from the shape of their Fermi energy plots.

It is reasonable to find that plots for the negative potential would look differently than the positive potential ones (a difference in the Fermi energy versus applied magnetic field plots for the negative and positive potential modulation is also found in the 1D case as will be seen in the next subsection). The difference between the positive and negative modulation potentials is due to the different interaction between the electrons and the antidots or dots. In the positive modulation case the energy of electrons is altered by scattering by the antidots, while in the negative potential case electron energies are altered because trapping inside the dots. The capturing of electrons by dots is more significant for large absolute values of the modulation potential. As it can be seen in Figure 3.14 (b) for a part of the plot corresponding to values of Φ in the middle of the range shown, the Fermi energy takes negative values. This is not true for Figure 3.14 (a), which corresponds to a lower absolute value of the modulation potential. Thus we can conclude that the variation of the Fermi energy is quite distinct for the two different modulation cases for the 2D potential, although there also are certain similarities.

3.4.3 Fermi Energy for 1D Periodic Potentials

Figure 3.15 shows three Fermi energy versus flux ratio plots for the 1D modulation potential. All three of the plots was obtained for the same positive value of the modulation potential, but the other parameters were varied. Although the strength of modulation was the same in each of the plots, the variation of the Fermi energy

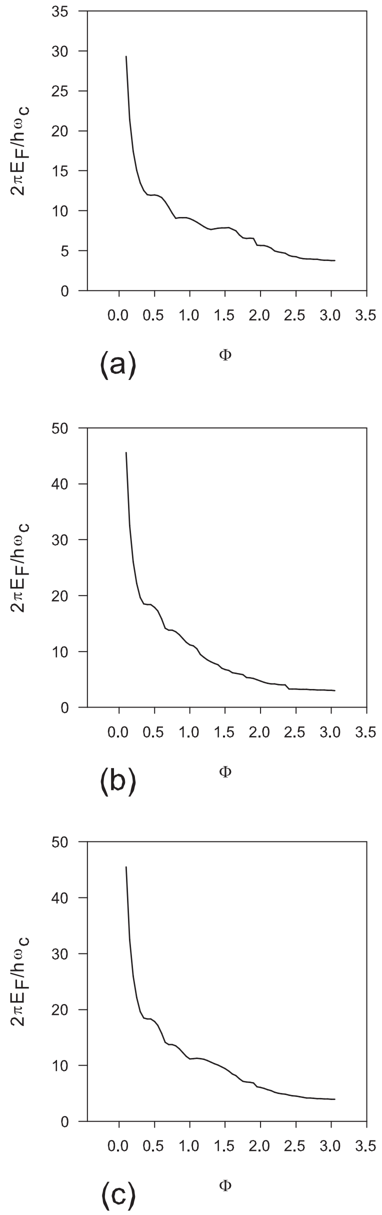

Figure 3.15: Dependence of the Fermi energy on the magnetic flux ratio Φ for the one-dimensional positive modulation potential for different values of the electron density. Parameters common to all three figures are the magnitude of the modulation potential strength $\bar{V} = 2.235$ and the power of the cosine term $N = 10$. In Figure (a) the highest value of the Landau level index is $n = 5$, while in Figures (b) and (c) it is $n = 6$. The electron density is $n_{2D}a^2 = 0.50$ in Figure (a), $n_{2D}a^2 = 0.75$ in Figure (b), and $n_{2D}a^2 = 1.00$ in Figure (c). Sample size is $N_x = N_y = 20$ in Figure (a) and $N_x = N_y = 10$ in Figures (b) and (c).

(including the maximum value taken) changes from graph to graph due to the change in the values selected for the other parameters. In Figure 3.13 (a) the electron density is the lowest of the three plots, and the total number of states is also lower, as the Landau level index selected in plotting this graph was $n = 5$.

By comparing Figures 3.14 and 3.15 one can see that the general characteristics of the Fermi level variation mentioned in the case of the 2D periodic cosine potential are also found in the 1D cosine type modulation case, namely the value of the Fermi energy is higher for lower values of the applied magnetic field, lower for higher values of the applied magnetic field, it shows the “pinning at Landau levels” behavior for higher values of the magnetic field, and it is higher for higher modulation potential magnitudes (this statement was verified numerically during our investigation, although no plots are shown to demonstrate this in Figure 3.15).

By looking at the values taken by the Fermi energy in the 1D plot of Figure 3.15 it can be seen that the highest value taken by E_F in Figure (a) is lower than in the other two plots (b) and (c), but the maximum values obtained in (b) and (c) are nearly the same. Figures 3.15 (b) and (c) were obtained for the same maximum value of the Landau level index ($n = 6$), which means that the total number of states is the same in both of these figures, but the electron density was chosen to be different. The difference in the variation of the Fermi energy for the last two figures (b) and (c) can be found in the portion of the graphs obtained for larger values of the magnetic field (right end of the Φ axis). In the region of lower magnetic fields, the Fermi energy goes through several steps in both of the plots. The difference between the two plots can be found in the higher magnetic field region. Namely between $\Phi = 2.2$ and $\Phi = 2.4$ in Figure (b) one can see the appearance of the last longer plateau in the variation of the Fermi energy. This plateau is again due to the “pinning” of the Fermi energy at a Landau level, just as it was explained in the previous two modulation cases. The corresponding last long plateau in Figure (c), which was drawn for a larger value of the carrier density ($n_{2D}a^2 = 1.0$ as compared to $n_{2D}a^2 = 0.75$ in Figure (b)) can be found between the values of Φ between 1.7 and 2.0. After the above-mentioned values of the magnetic field are exceeded in the two graphs, the electron gas under 1D modulation also starts behaving as a homogeneous 2DEG, as the threshold value of the magnetic field, for which the cyclotron orbits become so small that the electrons are no longer scattered by the potential, was exceeded.

3.4.4 Matching up the Variation of Fermi Energy to the Variation of Eigenvalues for the Three Model Potentials

In the final subsection of this chapter Figure 3.16 shows the variation of the Fermi energy with the applied magnetic field for the three different potential modulations (delta potential, 1D and 2D cosine potentials) placed over the variation of the energy eigenvalues with respect to the same variable. This figure was included to show the variation of the Fermi energy with respect to the modulation broadened Landau levels of the energy eigenvalue versus Φ plots. It is another way of illustrating the phenomenon of pinning of the Fermi energy at the different Landau levels. It can be seen in the figure that with the increase of the magnetic field, the Fermi energy decreases, but the decrease does not happen smoothly, but in steps, and these steps follow the profile taken by the modulation-broadened Landau levels. For low values of the magnetic field electrons follow large cyclotron orbits, thus there is a large probability for them to be scattered by the potential, and both the energy eigenvalues and the Fermi energy take large values in this domain. There are no steps seen in the decrease of the Fermi energy in this region. In the high magnetic field portion of the eigenvalue versus flux ratio (Φ) plots the bandwidth oscillations of the Landau

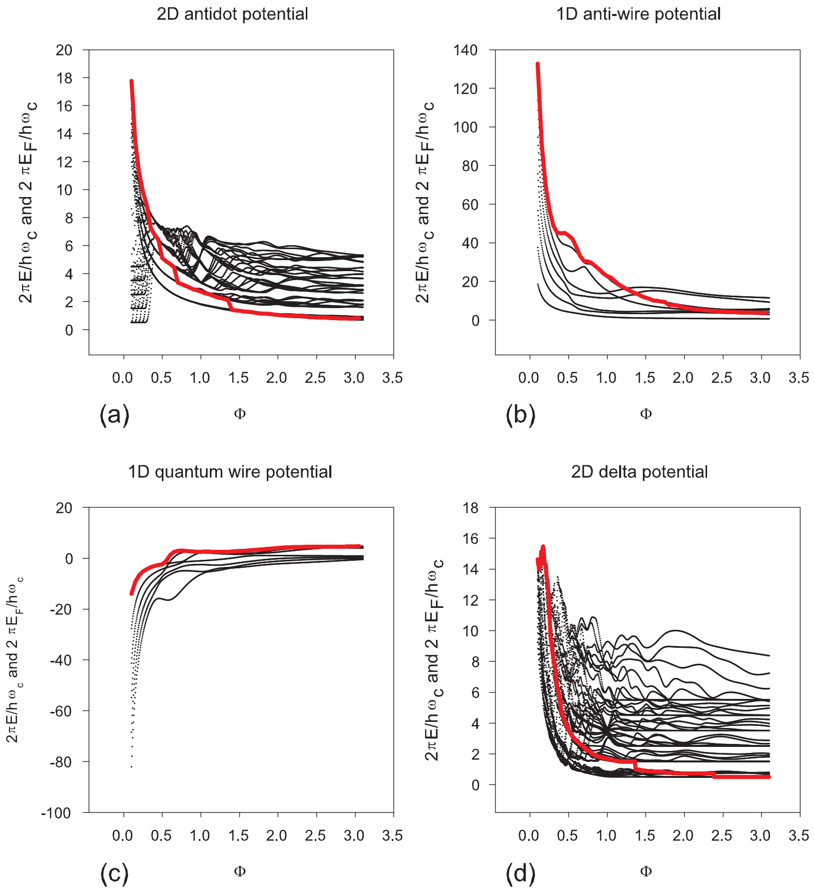

Figure 3.16: Fermi energy versus the magnetic flux ratio Φ plots placed on top of the corresponding eigenenergy dispersions for the three different potential forms investigated. The thick (red) line indicates the Fermi energy. Figure (a) corresponds to the 2D periodic quantum dot potential, Figure (b) is a one-dimensional quantum antiwire, Figure (c) is a one-dimensional quantum wire potential, while Figure (d) is a plot of the delta potential scatterers. Parameters used in the plots are as follows: Figure (a) sample size $N_x = N_y = 10$, the modulation potential magnitude is $\bar{V} = 60.235$, while its exponent is $N = 10$. The eigenvalue dispersion plot was obtained for the fixed value of the rescaled wavevector of $\bar{k}_y = 0.25$, while the Fermi energy plot was calculated for an electron density of $n_{2D}a^2 = 1.0$. In Figure (b) $N_x = N_y = 20$, $\bar{V} = 7.235$, $N = 10$, $\bar{k}_y = 0.05$, $n_{2D}a^2 = 1.0$. In Figure (c) $N_x = N_y = 20$, $\bar{V} = -8.235$, $\bar{k}_y = 0.05$, $n_{2D}a^2 = 1.0$. In Figure (d) $N_x = N_y = 10$, $\bar{V} = 1.235$, $\bar{k}_y = 0.25$, $n_{2D}a^2 = 1.0$.

levels are substantially reduced as compared to the low field region. For these larger magnetic field values the scattering effect is reduced, the Landau bandwidth has smaller oscillations, and the pinning phenomenon is more evident and easier to follow. This is the most easily seen in the 1D modulation case for which both a positive modulation potential plot, Figure 3.16 (b), and a negative modulation potential plot, Figure 3.16 (c) is shown, which also includes the variation of the Fermi energy, as these graphs do not have a subband structure associated with the broadening of the Landau levels.

At the conclusion of this section it needs to be mentioned that different characteristics of the variation of the Fermi energy with the applied magnetic field were illustrated for different types of modulation potential (to avoid repeating the same properties), but basically all of the general features mentioned are found in each of the plots, regardless of the type of modulation used.

Chapter 4

Quantum Magnetotransport Theory

4.1 Linear Response Theory for the Current

The AC current response of a disordered multiprobe conductor is found at temperature $T \cong 0$. The Kubo formula for the linear response tensor (LRT) $L(\Omega)$, is not assumed, but is calculated from first principles using the density-matrix formulation of the many-particle Schrödinger equation. In the first part of developing the theory the expression of the frequency-dependent nonlocal response function $\sigma(\vec{x}, \vec{x}', \Omega)$, is derived in terms of the exact eigenstates of the unperturbed Hamiltonian. We assume that the eigenfunctions of the unperturbed Hamiltonian, H_0, are known and they are solutions to the time-independent Schrödinger equation:

$$H_0 \psi_\alpha(\vec{x}) = \varepsilon_\alpha \psi_\alpha(\vec{x}) \tag{4.1}$$

Above H_0 stands for the single-particle Hamiltonian in a one- or two-dimensional scattering array potential located in the $x - y$ plane and a uniform perpendicular magnetic field $\vec{B} = B\hat{z}$ along the z direction. It is therefore assumed that H_0 has a known, complete, orthonormal set of eigenstates.

H_0 can be written explicitly using mks units as:

$$H_0 = \frac{1}{2M^*}\left[\vec{p} - q\vec{A}\left(\vec{x}\right)\right]^2 + U_L\left(\vec{x}\right) \tag{4.2}$$

Equation (4.2) is the Hamiltonian of a particle of charge q moving in an electromagnetic field of scalar and vector potentials $\phi\left(\vec{x}\right)$ and $\vec{A}\left(\vec{x}\right) = (0, Bx, 0)$, respectively. The vector potential above is written in the Landau gauge. In equation (4.2) $U_L\left(\vec{x}\right) = q\phi\left(\vec{x}\right)$ represents the lattice potential energy. For electrons, one should use $q = -e$, where e is the positive elementary charge. An effective mass, M^*, is used in calculations instead of the rest mass of the electron, because an electron in an electron gas with a prescribed background potential repels other electrons, thus becoming surrounded by a screening cloud. The electron plus the screening cloud constitutes a “quasi electron”, which can be described by an effective mass that differs from the rest mass of the electron. The effective interaction between two quasi electrons is a screened interaction that is weaker (shorter range) than the original Coulomb interaction.

We assume that the external perturbation may be written as a separable function of space and time. Thus, we place our array in a time-dependent periodic potential of the form:

$$V\left(\vec{x}, t\right) = V\left(\vec{x}\right)\cos\left(\Omega t\right)e^{-\gamma|t|} \tag{4.3}$$

In equation (4.3) Ω is the frequency of the perturbation, and γ is the rate at which the perturbation is turned on, while t is the time.

In order to have the frequency Ω well defined, it is assumed that the experiment is run for a long enough time $1/\gamma$. This means that the experimentally controllable parameters Ω and γ are chosen in such a way that $\Omega \gg \gamma$. Time scales are considered relative to other relevant physical times, such as the scattering time.

Following the usual linear response approach our aim is to find the current response of the system to first order in the external potential $V\left(\vec{x}, t\right)$. We use the equation of motion for the single-particle density matrix $\hat{\rho}\left(t\right)$:

$$i\hbar\frac{d\hat{\rho}\left(t\right)}{dt} = \left[H, \hat{\rho}\left(t\right)\right] \tag{4.4}$$

In the above equation we set $\hat{\rho}\left(t\right) = \hat{\rho}_0 + \hat{\rho}_1\left(t\right)$ and $H\left(t\right) = H_0 + H_1\left(t\right)$, thus the equation of motion of the single-particle density matrix can be written to first order in the perturbation as:

$$i\frac{d\left(\hat{\rho}_1\right)_{\alpha\beta}}{dt} \simeq -\frac{\varepsilon_{\beta\alpha}\left(\hat{\rho}_1\right)_{\alpha\beta}}{\hbar} + \frac{e\, f_{\beta\alpha}V_{\alpha\beta}}{\hbar}\cos\left(\Omega t\right)e^{-\gamma|t|} \tag{4.5}$$

where

$$\varepsilon_{\beta\alpha} \equiv \varepsilon_\beta - \varepsilon_\alpha \tag{4.6}$$

is the difference in energy eigenvalues, and

$$f_{\beta\alpha} \equiv f_\beta - f_\alpha \tag{4.7}$$

is the difference in Fermi functions, with the notation

$$f\left(\varepsilon_\alpha\right) = f_\alpha \tag{4.8}$$

standing for the well-known Fermi-Dirac distribution function:

$$f_\alpha \equiv \langle N\left(\varepsilon_\alpha\right)\rangle = \frac{1}{\exp\left[\frac{\left(\varepsilon_\alpha - \varepsilon_F\right)}{k_B T}\right] + 1} \tag{4.9}$$

with ε_F denoting the Fermi energy, and finally

$$V_{\alpha\beta} = \int d\vec{x}\psi_\alpha^*\left(\vec{x}\right)V\left(\vec{x}\right)\psi_\beta\left(\vec{x}\right) \tag{4.10}$$

standing for the matrix element of the potential in terms of eigenstates of the unperturbed Hamiltonian (4.1).

Equation (4.5) can be solved, and its solution yields the first-order correction to the density matrix:

$$\left[\hat{\rho}_1\left(t<0\right)\right]_{\alpha\beta} = \frac{e\,f_{\beta\alpha}\,V_{\alpha\beta}}{2}e^{\gamma t}\left(\frac{e^{i\Omega t}}{\varepsilon_{\alpha\beta} - \hbar\Omega + i\hbar\gamma} + \frac{e^{-i\Omega t}}{\varepsilon_{\alpha\beta} + \hbar\Omega + i\hbar\gamma}\right) \tag{4.11}$$

Now one can write the matrix element of the current density operator as:

$$\left[\hat{J}_{op}\left(\vec{x}\right)\right]_{\beta\alpha} = -\frac{ie\hbar}{2M^*}\left[\psi_\beta^*\left(\vec{x}\right)\overleftrightarrow{D}\psi_\alpha\left(\vec{x}\right)\right] \equiv -\frac{ie\hbar}{2M^*}\hat{W}_{\beta\alpha}\left(\vec{x}\right) \tag{4.12}$$

where $\hat{W}_{\beta\alpha}\left(\vec{x}\right)$ is the reduced current density operator, and $\overleftrightarrow{D}$ is the double-sided derivative operator whose action on two arbitrary functions f and g is defined as:

$$f\overleftrightarrow{D}g = f\left(\vec{x}\right)Dg\left(\vec{x}\right) - g\left(\vec{x}\right)\,D^*f\left(\vec{x}\right) = -g\overleftrightarrow{D}^*f \tag{4.13}$$

In equation (4.13) $D = \vec{\nabla} + \frac{ei}{\hbar}\vec{A}\left(\vec{x}\right)$ is the gauge-invariant derivative operator.

We would like to write the statistical current as:

$$\hat{J}\left(\vec{x},t\right) = \hat{J}_0\left(\vec{x}\right) + \hat{J}_1\left(\vec{x},t\right) \tag{4.14}$$

where

$$\hat{J}_0\left(\vec{x}\right) = Tr\left[\hat{\rho}_0\hat{J}_{op}\left(\vec{x}\right)\right] \tag{4.15}$$

and

$$\hat{J}_1\left(\vec{x},t\right) = Tr\left[\hat{\rho}_1\left(t\right)\hat{J}_{op}\left(\vec{x}\right)\right] \tag{4.16}$$

We note that $\hat{J}_0\left(\vec{x}\right)$ can be neglected in further calculations since it does not contribute to the transport current. This is due to the fact that it can be shown that $\nabla \cdot \hat{J}_0\left(\vec{x}\right) = 0$. The result can be derived using:

$$\vec{\nabla} \cdot \hat{W}_{\alpha\beta}\left(\vec{x}\right) = -\frac{2M^*}{\hbar^2}\varepsilon_{\beta\alpha}\psi^*_\alpha\left(\vec{x}\right)\psi_\beta\left(\vec{x}\right) \tag{4.17}$$

An expression for the current density results from combining the formula for the current density operator (4.12) with the equation satisfied by the density matrix (4.11) to give:

$$\begin{aligned}\hat{J}_1\left(\vec{x},t<0,\Omega,\gamma\right) &= Tr\left[\hat{\rho}_1\left(t\right)\ \hat{J}_{op}\left(\vec{x}\right)\right] = \sum_{\alpha,\beta}\left[\hat{\rho}_1\left(t\right)\right]_{\alpha,\beta}\left[\hat{J}_{op}\left(t\right)\right]_{\alpha,\beta} \\ &= -\frac{ie^2\hbar}{4M^*}\sum_{\alpha,\beta} f_{\beta\alpha}\,V_{\alpha\beta}\,\hat{W}\left(\vec{x}\right)\,e^{\gamma t}\left(\frac{e^{i\Omega t}}{\varepsilon_{\alpha\beta}-\hbar\Omega+i\hbar\gamma}+\frac{e^{-i\Omega t}}{\varepsilon_{\alpha\beta}+\hbar\Omega+i\hbar\gamma}\right)\end{aligned} \tag{4.18}$$

To make further progress, take the limit as $\gamma \rightarrow 0$ and make use of Dirac's formula:

$$\lim_{\gamma \to 0} \frac{1}{x \pm i\gamma} = P\left(\frac{1}{x}\right) \mp i\pi\delta\left(x\right) \tag{4.19}$$

In equation (4.19) P indicates the principal-value integral and δ is the Dirac delta function. Using (4.19) we can rewrite expression (4.18) as:

$$\begin{aligned}
&\hat{J}_1\left(\vec{x}, t < 0, \Omega\right) = -\frac{ie^2\hbar}{4M^*} \sum_{\alpha,\beta} f_{\beta\alpha} V_{\alpha\beta} \hat{W}_{\beta\alpha}\left(\vec{x}\right) \\
&\cdot \left\{ \cos\left(\Omega t\right) \left[-i\pi\delta\left(\varepsilon_{\beta\alpha} - \hbar\Omega\right) - i\pi\delta\left(\varepsilon_{\beta\alpha} + \hbar\Omega\right) + P\left(\frac{1}{\varepsilon_{\beta\alpha} - \hbar\Omega}\right) + P\left(\frac{1}{\varepsilon_{\beta\alpha} + \hbar\Omega}\right) \right] \right. \\
&\left. + i\sin(\Omega t) \left[-i\pi\delta\left(\varepsilon_{\beta\alpha} - \hbar\Omega\right) - i\pi\delta\left(\varepsilon_{\beta\alpha} + \hbar\Omega\right) + P\left(\frac{1}{\varepsilon_{\beta\alpha} - \hbar\Omega}\right) - P\left(\frac{1}{\varepsilon_{\beta\alpha} + \hbar\Omega}\right) \right] \right\}
\end{aligned} \tag{4.20}$$

Equation (4.20) is a generalization of the first order current response for the finite frequency case.

4.2 Frequency-Dependent Conductance Coefficients

Now rewrite the matrix element of the potential $V_{\alpha\beta}$ as an integral over the electric field $\vec{E}\left(\vec{x}\right) = -\vec{\nabla} V\left(\vec{x}\right)$. Equation (4.20) can be rewritten as:

$$\begin{aligned}
&\hat{J}_1\left(\vec{x}, t, \Omega\right) = \frac{ie^2\hbar^3}{8M^{*2}} \sum_{\alpha,\beta} \hat{W}_{\beta\alpha}\left(\vec{x}\right) \frac{f_{\beta\alpha}}{\varepsilon_{\beta\alpha}} \int_A d\vec{x}' \, \hat{W}_{\alpha\beta}\left(\vec{x}'\right) \cdot \vec{E}\left(\vec{x}'\right) \\
&\cdot \left\{ \cos\left(\Omega t\right) \left[-i\pi\delta\left(\varepsilon_{\beta\alpha} - \hbar\Omega\right) - i\pi\delta\left(\varepsilon_{\beta\alpha} + \hbar\Omega\right) + P\left(\frac{1}{\varepsilon_{\beta\alpha} - \hbar\Omega}\right) + P\left(\frac{1}{\varepsilon_{\beta\alpha} + \hbar\Omega}\right) \right] \right. \\
&\left. + i\sin\left(\Omega t\right) \left[-i\pi\delta\left(\varepsilon_{\beta\alpha} - \hbar\Omega\right) + i\pi\delta\left(\varepsilon_{\beta\alpha} + \hbar\Omega\right) + P\left(\frac{1}{\varepsilon_{\beta\alpha} - \hbar\Omega}\right) - P\left(\frac{1}{\varepsilon_{\beta\alpha} + \hbar\Omega}\right) \right] \right\}
\end{aligned} \tag{4.21}$$

We can now identify the frequency-dependent nonlocal response function $\sigma\left(\vec{x}, \vec{x}', \Omega\right)$, using the expression relating the current density to the applied external field:

$$\hat{J}_1\left(\vec{x}, \Omega\right) = \int d\vec{x}' \sigma\left(\vec{x}, \vec{x}', \Omega\right) \cdot \vec{E}\left(\vec{x}'\right) \tag{4.22}$$

We will use equation (4.22) to put the current density in a more convenient form, by rewriting the general expression of the first order current response as:

$$\hat{J}_1(\vec{x}, t, \Omega) = \int d\vec{x}' \left[\cos\left(\Omega t\right) \sigma_+\left(\vec{x}, \vec{x}', \Omega\right) + i \sin\left(\Omega t\right) \sigma_-\left(\vec{x}, \vec{x}', \Omega\right)\right] \vec{E}\left(\vec{x}'\right) \tag{4.23}$$

The following notations are used in equation (4.23):

$$\sigma_+\left(\vec{x}, \vec{x}', \Omega\right) \equiv \sigma_1\left(\vec{x}, \vec{x}', \Omega\right) + \sigma_2\left(\vec{x}, \vec{x}', \Omega\right) \tag{4.24}$$

and

$$\sigma_-\left(\vec{x}, \vec{x}', \Omega\right) \equiv \sigma_1\left(\vec{x}, \vec{x}', \Omega\right) - \sigma_2\left(\vec{x}, \vec{x}', \Omega\right) \tag{4.25}$$

The result obtained above in equation (4.23) leaves us with a current response that is composed of a dissipative term that oscillates as $\cos\left(\Omega t\right)$ and a reactive term that oscillates as $\sin\left(\Omega t\right)$. As we are interested in the real part of the linear response, we will investigate the properties of the dissipative term. A similar calculation can be conducted for the reactive term. Thus we will write $\sigma_+\left(\vec{x}, \vec{x}', \Omega\right)$ of equation (4.23) explicitly:

$$\sigma_+\left(\vec{x},\vec{x}',\Omega\right)=\frac{ie^2\hbar^3}{8M^{*2}}\sum_{\alpha,\beta}\frac{f\left(\varepsilon_\beta\right)-f\left(\varepsilon_\alpha\right)}{\varepsilon_\beta-\varepsilon_\alpha}\hat{W}_{\beta\alpha}\left(\vec{x}\right)\hat{W}_{\alpha\beta}\left(\vec{x}'\right)$$
$$\cdot\left[-i\pi\delta\left(\varepsilon_\beta-\varepsilon_\alpha-\hbar\Omega\right)-i\pi\delta\left(\varepsilon_\beta-\varepsilon_\alpha+\hbar\Omega\right)+P\left(\frac{1}{\varepsilon_\beta-\varepsilon_\alpha-\hbar\Omega}\right)+P\left(\frac{1}{\varepsilon_\beta-\varepsilon_\alpha+\hbar\Omega}\right)\right] \tag{4.26}$$

In the above equation we will separate terms containing delta-functions, which are even under an interchange of the indices α and β (and call this the *symmetrical part of the nonlocal response function*), from those including principal-value terms, which are odd under the interchange of the indices α and β (and call this the *asymmetrical part of the nonlocal response function*). The nonlocal response function can therefore be written as:

$$\sigma_+\left(\vec{x},\vec{x}',\Omega\right)=\sigma_s\left(\vec{x},\vec{x}',\Omega\right)+\sigma_{as}\left(\vec{x},\vec{x}',\Omega\right) \tag{4.27}$$

We also note here that in equation (4.26) the delta-function terms pick out the real part of the product of the reduced current density operators, $\hat{W}\left(\vec{x}\right)$, while the principal-value terms pick out the imaginary part.

The symmetric and asymmetric terms can be written explicitly as follows:

- Symmetrical part of the nonlocal response function:

$$\sigma_s\left(\vec{x},\vec{x}',\Omega\right)=\frac{\pi e^2\hbar^3}{8M^{*2}}\sum_{\alpha,\beta}\frac{f\left(\varepsilon_\beta\right)-f\left(\varepsilon_\alpha\right)}{\varepsilon_\beta-\varepsilon_\alpha}\hat{W}_{\alpha\beta}\left(\vec{x}'\right)\hat{W}_{\beta\alpha}\left(\vec{x}\right)$$
$$\cdot\left[\delta\left(\varepsilon_\beta-\varepsilon_\alpha-\hbar\Omega\right)+\delta\left(\varepsilon_\beta-\varepsilon_\alpha+\hbar\Omega\right)\right] \tag{4.28}$$

- Asymmetrical part of the nonlocal response function:

$$\begin{aligned}\sigma_{as}\left(\vec{x},\vec{x}',\Omega\right) = \frac{ie^2\hbar^3}{8M^{*2}}\sum_{\alpha,\beta}\frac{f\left(\varepsilon_\beta\right)-f\left(\varepsilon_\alpha\right)}{\varepsilon_\beta-\varepsilon_\alpha}\hat{W}_{\alpha\beta}\left(\vec{x}'\right)\hat{W}_{\beta\alpha}\left(\vec{x}\right)\\ \cdot\left[P\left(\frac{1}{\varepsilon_\beta-\varepsilon_\alpha-\hbar\Omega}\right)+P\left(\frac{1}{\varepsilon_\beta-\varepsilon_\alpha+\hbar\Omega}\right)\right]\end{aligned} \tag{4.29}$$

The conductance coefficients can now be expressed in terms of the exact eigenfunctions of the unperturbed system using the definition of $\hat{W}_{\alpha\beta}$ introduced in equation (4.12) in terms of the double-sided derivative operators as:

$$\begin{aligned}\sigma_s\left(\vec{x},\vec{x}',\Omega\right) = -\frac{\pi e^2\hbar^3}{8M^{*2}}\sum_{\alpha,\beta}\frac{f\left(\varepsilon_\beta\right)-f\left(\varepsilon_\alpha\right)}{\varepsilon_\beta-\varepsilon_\alpha}\psi_\alpha\left(\vec{x}\right)\psi_\alpha^*\left(\vec{x}'\right)\overleftrightarrow{D}^*\overleftrightarrow{D}'\psi_\beta\left(\vec{x}'\right)\psi_\beta^*\left(\vec{x}\right)\\ \cdot\left[\delta\left(\varepsilon_\beta-\varepsilon_\alpha-\hbar\Omega\right)+\delta\left(\varepsilon_\beta-\varepsilon_\alpha+\hbar\Omega\right)\right]\end{aligned} \tag{4.30}$$

and:

$$\begin{aligned}\sigma_{as}\left(\vec{x},\vec{x}',\Omega\right) = -\frac{ie^2\hbar^3}{8M^{*2}}\sum_{\alpha,\beta}\frac{f\left(\varepsilon_\beta\right)-f\left(\varepsilon_\alpha\right)}{\varepsilon_\beta-\varepsilon_\alpha}\psi_\alpha\left(\vec{x}\right)\psi_\alpha^*\left(\vec{x}'\right)\overleftrightarrow{D}^*\overleftrightarrow{D}'\psi_\beta\left(\vec{x}'\right)\psi_\beta^*\left(\vec{x}\right)\\ \cdot\left[P\left(\frac{1}{\varepsilon_\beta-\varepsilon_\alpha-\hbar\Omega}\right)-P\left(\frac{1}{\varepsilon_\beta-\varepsilon_\alpha+\hbar\Omega}\right)\right]\end{aligned} \tag{4.31}$$

4.3 Green's Function Representation

We would like to transform equations (4.30) and (4.31), and write them using the retarded (G_ε^+) and advanced (G_ε^-) single-particle Green's functions:

$$G_\varepsilon^\pm\left(\vec{x},\vec{x}'\right) = \int d\alpha\frac{\psi_\alpha\left(\vec{x}\right)\psi_\alpha^*\left(\vec{x}'\right)}{\varepsilon-\varepsilon_\alpha\pm i\eta} \tag{4.32}$$

Let us introduce the following notations for the difference and the sum of the retarded and advanced Green's functions:

$$\Delta G_{\varepsilon}\left(\vec{x},\vec{x}'\right) \equiv G_{\varepsilon}^{+} - G_{\varepsilon}^{-} = -2\pi i \int d\alpha \psi_{\alpha}\left(\vec{x}\right) \psi_{\alpha}^{*}\left(\vec{x}'\right) \delta\left(\varepsilon - \varepsilon_{\alpha}\right) \tag{4.33}$$

$$\Sigma G_{\varepsilon}\left(\vec{x},\vec{x}'\right) \equiv G_{\varepsilon}^{+} + G_{\varepsilon}^{-} = 2 \int d\alpha \psi_{\alpha}\left(\vec{x}\right) \psi_{\alpha}^{*}\left(\vec{x}'\right) P\left(\frac{1}{\varepsilon - \varepsilon_{\alpha}}\right) \tag{4.34}$$

Using the notations introduced above in relations (4.33) and (4.34) the symmetric and antisymmetric part of the conductance coefficients may be expressed in terms of Green's functions as:

$$\begin{aligned}
\sigma_{s}\left(\vec{x},\vec{x}',\Omega\right) = & -\frac{e^{2}\hbar^{3}}{32\pi\hbar\Omega M^{*2}} \int\limits_{-\infty}^{\infty} d\varepsilon f\left(\varepsilon\right) \\
& \cdot \Big\{ \Delta G_{\varepsilon}\left(\vec{x},\vec{x}'\right) \overleftrightarrow{D}^{*} \overleftrightarrow{D}' \left[\Delta G_{\varepsilon+\hbar\Omega}\left(\vec{x}',\vec{x}\right) - \Delta G_{\varepsilon-\hbar\Omega}\left(\vec{x}',\vec{x}\right)\right] \\
& + \left[\Delta G_{\varepsilon+\hbar\Omega}\left(\vec{x},\vec{x}'\right) - \Delta G_{\varepsilon-\hbar\Omega}\left(\vec{x},\vec{x}'\right)\right] \overleftrightarrow{D}^{*} \overleftrightarrow{D}' \Delta G_{\varepsilon}\left(\vec{x}',\vec{x}\right) \Big\}
\end{aligned} \tag{4.35}$$

for the symmetrical part, and:

$$\begin{aligned}
\sigma_{as}\left(\vec{x},\vec{x}',\Omega\right) = & -\frac{e^{2}\hbar^{3}}{32\pi\hbar\Omega M^{*2}} \int\limits_{-\infty}^{\infty} d\varepsilon f\left(\varepsilon\right) \\
& \cdot \Big\{ \Delta G_{\varepsilon}\left(\vec{x},\vec{x}'\right) \overleftrightarrow{D}^{*} \overleftrightarrow{D}' \left[\Sigma G_{\varepsilon-\hbar\Omega}\left(\vec{x}',\vec{x}\right) - \Sigma G_{\varepsilon+\hbar\Omega}\left(\vec{x}',\vec{x}\right)\right] \\
& - \left[\Sigma G_{\varepsilon-\hbar\Omega}\left(\vec{x},\vec{x}'\right) - \Sigma G_{\varepsilon+\hbar\Omega}\left(\vec{x},\vec{x}'\right)\right] \overleftrightarrow{D}^{*} \overleftrightarrow{D}' \Delta G_{\varepsilon}\left(\vec{x}',\vec{x}\right) \Big\}
\end{aligned} \tag{4.36}$$

for the asymmetrical part.

We can now obtain the *total nonlocal conductivity* at finite frequency by adding relations (4.35) and (4.36). We substitute the explicit form of the sum and difference of the retarded and advanced Green's functions using their definition given in (4.33) and (4.34) to obtain our final result for the total nonlocal response function:

$$
\begin{aligned}
\sigma\left(\vec{x},\vec{x}',\Omega\right) = &-\frac{e^2\hbar^3}{16\pi\hbar\Omega M^{*2}}\int\limits_{-\infty}^{\infty} d\varepsilon f\left(\varepsilon\right) \\
&\cdot\Big\{\Delta G_{\varepsilon}\left(\vec{x},\vec{x}'\right)\overset{\leftrightarrow}{D}^{*}\overset{\leftrightarrow}{D}' \left[-G^{-}_{\varepsilon+\hbar\Omega}\left(\vec{x}',\vec{x}\right)+G^{-}_{\varepsilon-\hbar\Omega}\left(\vec{x}',\vec{x}\right)\right] \\
&+\left[G^{+}_{\varepsilon+\hbar\Omega}\left(\vec{x},\vec{x}'\right)-G^{+}_{\varepsilon-\hbar\Omega}\left(\vec{x},\vec{x}'\right)\right]\overset{\leftrightarrow}{D}^{*}\overset{\leftrightarrow}{D}'\Delta G_{\varepsilon}\left(\vec{x}',\vec{x}\right)\Big\}
\end{aligned}
\tag{4.37}
$$

This expression generalizes the result obtained by Baranger and Stone [51] in the zero frequency case. When the $\Omega \to 0$ limit is taken in equation (4.37) the results of Baranger and Stone are found. We will make use of this generalized expression to obtain the averaged Ω-dependent conductivity, which is the central theoretical result of this thesis. Equation (4.37) is the Kubo formula for the response function generalized to finite frequency.

4.4 Frequency-Dependent Kubo Formula

After obtaining an expression for the total nonlocal response tensor, $\sigma\left(\vec{x},\vec{x}',\Omega\right)$, we would like to apply the finite frequency formalism obtained thus far to derive an expression for the frequency-dependent linear response tensor, $L\left(\Omega\right)$. Taking this step is motivated by the fact that previous linear response calculations in magnetic field have also expressed L using either impurity averaging [52] or spatial averaging [4]. Following the method introduced by Smrčka and Středa [53] we can define the frequency-dependent linear response tensor, $L(\Omega)$, as follows. We start by relating the spatially averaged current density to a constant applied electric field, $\vec{E}$, by the relation:

$$\frac{1}{S}\int_{A} d\vec{x} J(\vec{x},\Omega) \equiv L \cdot \vec{E} \tag{4.38}$$

In the above equation S is the “length” of the two-dimensional region A along the direction of current flow. Based on equation (4.38) the relationship between the linear response tensor L, and the nonlocal conductivity tensor, $\sigma(\vec{x},\vec{x}')$, can be expressed as:

$$L = \int_{A} d\vec{x} \int_{A} d\vec{x}'\, \sigma(\vec{x},\vec{x}') \tag{4.39}$$

We make use of equation (4.39) to define the frequency-dependent linear response tensor, which we write as:

$$L(\Omega) = \int_{A} d\vec{x} \int_{A} d\vec{x}'\, \sigma(\vec{x},\vec{x}',\Omega) \tag{4.40}$$

This is a very important expression obtained in the development of the theory thus far, since we can use it to do numerical calculations. We now need to express the linear response tensor of equation (4.40) in a form that is suitable for conducting the numerical investigation of the problem.

Next, we use the definition given by equation (4.40) to obtain the contribution of the asymmetric part of the nonlocal response function to the linear response tensor. Substituting the relationship for $\sigma_{as}(\vec{x},\vec{x}',\Omega)$ given by equation (4.36) into (4.40) we obtain:

$$
\begin{aligned}
L_{as}(\Omega) = &-\frac{e^2\hbar^3}{32\pi\hbar\Omega M^{*2}} \int\limits_{-\infty}^{\infty} d\varepsilon\, f(\varepsilon) \int\limits_A d\vec{x} \int\limits_A d\vec{x}' \\
&\cdot \Big\{ \Delta G_\varepsilon(\vec{x},\vec{x}')\, \overleftrightarrow{D}^{*} \overleftrightarrow{D}' \left[\Sigma G_{\varepsilon-\hbar\Omega}(\vec{x}',\vec{x}) - \Sigma G_{\varepsilon+\hbar\Omega}(\vec{x}',\vec{x})\right] \\
&- \left[\Sigma G_{\varepsilon-\hbar\Omega}(\vec{x},\vec{x}') - \Sigma G_{\varepsilon+\hbar\Omega}(\vec{x},\vec{x}')\right] \overleftrightarrow{D}^{*} \overleftrightarrow{D}'\, \Delta G_\varepsilon(\vec{x}',\vec{x}) \Big\}
\end{aligned}
\tag{4.41}
$$

When averaged over the sample, the asymmetric part of the nonlocal response function $\sigma_{as}(\vec{x}',\vec{x},\Omega)$, reduces to zero, thus only the symmetric part contributes to the linear response tensor, so the response of the system to the external perturbation is dominated only by the symmetric part of the nonlocal response function.

We now write the Green's functions in equation (4.35) in their explicit forms and also introduce complete sets:

$$
\int d\vec{r}_i \,|\vec{r}_i\rangle \langle \vec{r}_i| = \hat{1} \tag{4.42}
$$

so that we may write the linear response tensor L, as a trace:

$$
\begin{aligned}
L(\Omega) = &-\frac{\hbar}{4\pi\hbar\Omega} \int\limits_{-\infty}^{\infty} d\varepsilon\, f(\varepsilon) \int\limits_A d\vec{x} \int\limits_A d\vec{x}' \\
&\cdot Tr\left\{ J(\vec{x}) \left[G^{+}_{\varepsilon+\hbar\Omega} - G^{+}_{\varepsilon-\hbar\Omega}\right] J(\vec{x}')\, \Delta G_\varepsilon - J(\vec{x})\, \Delta G_\varepsilon J(\vec{x}') \left[G^{-}_{\varepsilon+\hbar\Omega} - G^{-}_{\varepsilon-\hbar\Omega}\right]\right\}
\end{aligned}
\tag{4.43}
$$

Next, we express the difference in the advanced and retarded Green's function, ΔG_ε, in terms of the Hamiltonian operator through the relation:

$$
\Delta G_\varepsilon = -2\pi i \delta(\varepsilon - H) \tag{4.44}
$$

Using relation (4.44) equation (4.43) can be written as:

$$L\left(\Omega\right)=\frac{i\hbar}{2\hbar\Omega}\int\limits_{-\infty}^{\infty}d\varepsilon f\left(\varepsilon\right)\int\limits_{A}d\vec{x}\int\limits_{A}d\vec{x}'$$
$$\cdot\, Tr\left\{J\left(\vec{x}\right)\left[G^{+}_{\varepsilon+\hbar\Omega}-G^{+}_{\varepsilon-\hbar\Omega}\right]J\left(\vec{x}'\right)\delta\left(\varepsilon-H\right)-J\left(\vec{x}\right)\delta\left(\varepsilon-H\right)J\left(\vec{x}'\right)\left[G^{-}_{\varepsilon+\hbar\Omega}-G^{-}_{\varepsilon-\hbar\Omega}\right]\right\} \tag{4.45}$$

In the following section we express the linear response tensor of (4.45) in terms of the velocity operator.

4.5 Kubo Formula in Terms of Velocity Operators

The next step of the calculation is to rewrite the trace over the current-density operator as a trace over the velocity operator. Use the following relationship between the trace of the product of the current density operator and an arbitrary operator, and the trace of the velocity operator times the same operator:

$$\int d\vec{x}\,Tr\left[\hat{J}_{op}\left(\vec{x}\right)\hat{A}_{op}\left(\vec{x}\right)\right]=eTr\left(\hat{v}_{op}\hat{A}_{op}\right) \tag{4.46}$$

The use of relation (4.46) greatly simplifies the result (4.45) obtained for the frequency dependent linear response tensor $L\left(\Omega\right)$:

$$L\left(\Omega\right)=\frac{i\hbar e^{2}}{2\hbar\Omega}\int\limits_{-\infty}^{\infty}d\varepsilon f\left(\varepsilon\right)Tr\left[v\left(G^{+}_{\varepsilon+\hbar\Omega}-G^{+}_{\varepsilon-\hbar\Omega}\right)v\delta\left(\varepsilon-H\right)\ -v\delta\left(\varepsilon-H\right)v\left(G^{-}_{\varepsilon+\hbar\Omega}-G^{-}_{\varepsilon-\hbar\Omega}\right)\right] \tag{4.47}$$

Equation (4.47) is the explicit form of the linear response tensor generalized to the frequency-dependent case as defined in relation (4.40) but written in terms of velocity operators.

4.6 Component Form of the Linear Response Tensor Per Unit Area

We would now like to express the linear response tensor per unit area in a component form and eliminate the trace from expression (4.47). In component form the linear response tensor may be written as:

$$\begin{aligned} L_{\mu\nu}(\Omega) &= \frac{i\hbar e^2}{2\hbar\Omega A}\int_{-\infty}^{\infty} d\varepsilon f(\varepsilon) \\ &\cdot Tr\left[v_\mu G^+_{\varepsilon+\hbar\Omega} v_\nu \delta(\varepsilon - H) - v_\mu G^+_{\varepsilon-\hbar\Omega} v_\nu \delta(\varepsilon - H)\right. \\ &\left. - v_\mu \delta(\varepsilon - H) v_\nu G^-_{\varepsilon+\hbar\Omega} + v_\mu \delta(\varepsilon - H) v_\nu G^-_{\varepsilon-\hbar\Omega}\right] \end{aligned} \tag{4.48}$$

A lengthy, but straightforward, calculation leads to the explicit expression of the linear response tensor per unit area in component form:

$$\begin{aligned} L_{\mu\nu}(\Omega) &= \frac{i\hbar e^2}{2\hbar\Omega A}\int_{-\infty}^{\infty} d\varepsilon f(\varepsilon) \sum_{M,N} v_\mu^{NM} v_\nu^{MN} \\ &\cdot \left\{ \left[\frac{\delta(\varepsilon - \varepsilon_N)}{\varepsilon + \hbar\Omega - \varepsilon_M + i\eta} - \frac{\delta(\varepsilon - \varepsilon_N)}{\varepsilon - \hbar\Omega - \varepsilon_M + i\eta} \right] \right. \\ &\left. - \left[\frac{\delta(\varepsilon - \varepsilon_M)}{\varepsilon + \hbar\Omega - \varepsilon_N - i\eta} - \frac{\delta(\varepsilon - \varepsilon_M)}{\varepsilon - \hbar\Omega - \varepsilon_N - i\eta} \right] \right\} \end{aligned} \tag{4.49}$$

Equation (4.49) can also be written in terms of the Green's functions as:

$$\begin{aligned} L_{\mu\nu}(\Omega) = {} & \frac{i\hbar e^2}{2\hbar\Omega A}\int\limits_{-\infty}^{\infty} d\varepsilon f(\varepsilon)\sum_{M,N} v_\mu^{NM} v_\nu^{MN} \\ & \cdot\left\{\left[G_M^+(\varepsilon+\hbar\Omega)-G_M^+(\varepsilon-\hbar\Omega)\right]\delta(\varepsilon-\varepsilon_N)\right. \\ & \left. -\delta(\varepsilon-\varepsilon_M)\left[G_N^-(\varepsilon+\hbar\Omega)-G_N^-(\varepsilon-\hbar\Omega)\right]\right\} \end{aligned} \tag{4.50}$$

The subscripts used on the Green's functions in the above equation only serve "book-keeping purposes", so that one can easily identify the functions over which one performs the composite summation denoted by indices N and M. The energy eigenvalue-dependent relation (4.50) is an important new result involving velocity-velocity correlations, which generalizes the findings of Gumbs and Huang [48] to the case of frequency-dependent modulation. It is the general expression that allows us to express the longitudinal, L_{xx}, and transverse L_{yx}, conductivities.

Chapter 5

Band Part of the Conductivity for 2D and 1D Modulation Potentials

In the rest of the analytical calculations performed here we investigate the band part of the frequency-dependent conductivity tensor, as written in equation (4.50). In our final expression we will neglect electron-electron interactions, as we would like to focus our attention at describing the effects of lattice scattering introduced by the potential forms investigated in this dissertation. This approximation is reasonable, because in the low magnetic field region which we investigate, it is known that many-particle interactions do not have an important influence on the magnetotransport properties of a homogeneous 2DEG, so we assume that the same holds in the presence of modulation. We also neglect small perturbative effects from the voltage or current leads attached to the sample, thus considering the electric field over the whole sample to be uniform. As the sample size is extremely small in our case, this approximation is justified because the electric field varies over a larger length scale than our sample size. We are considering the case of weak applied magnetic fields and low temperatures (on the order of milli-Kelvins), so that the zero temperature limit of the Fermi-Dirac distribution could be used as a good approximation for our system's distribution function. Therefore, we neglect contributions resulting from changes in the electron distribution function due to many-particle interactions. As we assume that experimental measurements would be carried out on very pure samples of high mobility, we find it reasonable to neglect the effect of impurity scattering as compared to lattice scattering, and this is the motivation to focus our attention on effects caused only by the scattering due to the applied electrostatic modulation potential.

Thus we rewrite equation (4.50) using a superscript "(0)", and we will refer to this quantity as the band part of the conductivity in what follows:

$$\begin{gathered} L_{\mu\nu}^{(0)}(\Omega) = \frac{i\hbar e^2}{2\hbar\Omega A} \int\limits_{-\infty}^{\infty} d\varepsilon f(\varepsilon) \sum_{M,N} v_{\mu}^{NM} v_{\nu}^{MN} \\ \cdot \left\{ \left[G_M^{(0)+}(\varepsilon + \hbar\Omega) - G_M^{(0)+}(\varepsilon - \hbar\Omega) \right] \delta(\varepsilon - \varepsilon_N) \right. \\ \left. -\delta(\varepsilon - \varepsilon_M) \left[G_N^{(0)-}(\varepsilon + \hbar\Omega) - G_N^{(0)-}(\varepsilon - \hbar\Omega) \right] \right\} \end{gathered} \tag{5.1}$$

We would now like to write the longitudinal and transverse components of the band part of the frequency-dependent conductivity for the 1D and 2D cosine-type periodic potentials. We assume our 2DEG to be located in the $x - y$ plane, and the applied magnetic field to be in the z direction, thus the x velocity components used in our calculations can be expressed in the form $v_x = \frac{p_x}{M^*}$, while the y-component can be written as $v_y = \frac{p_y}{M^*} + \frac{eBx}{M^*}$.

5.1 Band Part of Conductivity for 2D Modulation

The eigenfunctions used to calculate the matrix elements v_{μ}^{NM} and v_{ν}^{MN} in equations (5.1) for the 2D modulation are as follows:

$$|N\rangle = \psi_{j,X_0}(\vec{x}) = |j, X_0\rangle = \sum_{n,m} C_{n,m}(j, X_0)\phi_{n,X_0+mGL_H^2}(\vec{x}) \tag{5.2}$$

Where,

j labels the energy eigenvalues,

$X_0 = k_y L_H^2$ is the guiding center of the cyclotron orbits,

k_y is a wave vector in the y direction,

$L_H = \sqrt{\frac{\hbar}{eB}}$ is the magnetic length,

$n = 0, 1, 2, ...$ is the Landau-level index,

$m = \pm 1, \pm 2, ...$ is the magnetic band index (umklapp scattering effect),

$G = \frac{2\pi}{a}$ is a reciprocal lattice vector.

In equation (5.2) the function $\phi_{n,X_0+mGL_H^2}(\vec{x})$ denotes the following:

$$\begin{aligned}\phi_{n,X_0+mGL_H^2}(\vec{x}) &= \frac{1}{\sqrt{L_y}} \exp\left[-\frac{i\left(X_0 + mGL_H^2\right)y}{L_H^2}\right]\sqrt{\frac{1}{\pi^{1/2}L_H 2^n n!}} \\ &\cdot \exp\left[-\frac{\left(x - X_0 - mGL_H^2\right)^2}{2L_H^2}\right] H_n\left(\frac{x - X_0 - mGL_H^2}{L_H}\right)\end{aligned} \tag{5.3}$$

where,

$L_y = N_y a$ is the sample length in the y direction, and

H_n is a Hermite polynomial of order n.

Therefore, we may write the xx element of the frequency-dependent conductivity, $L_{xx}^{(0)}(\Omega)$, using equation (5.1) and making the following substitution for the generalized summation notation over states N and M:

$$\sum_{N,M} \rightarrow \left(\frac{L_y}{2\pi L_H^2}\right)^2 \sum_{j,j'} \int_{-\frac{G}{2}L_H^2}^{\frac{G}{2}L_H^2} dX_0 \int_{-\frac{G}{2}L_H^2}^{\frac{G}{2}L_H^2} dX_0' \tag{5.4}$$

We will proceed by giving the results for the frequency-dependent 2D magnetoconductivity coefficients obtained after performing the above-mentioned generalized summation, followed by the same coefficients determined for the 1D modulation case.

5.1.1 2D Longitudinal Conductivity, L_{xx}

After a lengthy, but straightforward calculation, which is presented in some detail in Appendix A, the band part of the longitudinal conductivity is obtained in the form:

$$\begin{aligned} L_{xx}^{(0)}(\Omega) = {} & \frac{i\hbar^3 e^2 L_y}{4\pi\hbar\Omega A L_H^2 M^{*2}} \int\limits_{-\infty}^{\infty} d\varepsilon f(\varepsilon) \sum_{j,j'} \int\limits_{-\frac{G}{2}L_H^2}^{\frac{G}{2}L_H^2} dX_0 \left(F^{(2)}_{j,X_0;j',X_0}\right)^2 \\ & \cdot \left\{ \left[\frac{\delta\left[\varepsilon-\varepsilon_{j'}(X_0)\right]}{\varepsilon+\hbar\Omega-\varepsilon_j(X_0)+i\eta} - \frac{\delta\left[\varepsilon-\varepsilon_{j'}(X_0)\right]}{\varepsilon-\hbar\Omega-\varepsilon_j(X_0)+i\eta} \right] \right. \\ & \left. - \left[\frac{\delta\left[\varepsilon-\varepsilon_j(X_0)\right]}{\varepsilon+\hbar\Omega-\varepsilon_{j'}(X_0)-i\eta} - \frac{\delta\left[\varepsilon-\varepsilon_j(X_0)\right]}{\varepsilon-\hbar\Omega-\varepsilon_{j'}(X_0)-i\eta} \right] \right\} \end{aligned} \tag{5.5}$$

where the notation $F^{(2)}_{j,X_0;j',X_0}$ is used for one of the structure factors introduced by Gumbs and Huang in [48] for the zero frequency case. These structure factors play an important role in the calculation, as they determine the group velocities. The structure factor used in equation (5.5) has the following definition:

$$\begin{aligned} F^{(2)}_{j,X_0;j',X_0} = -F^{(2)*}_{j',X_0;j,X_0} = & \int\limits_A d\vec{x}\psi^*_{j,X_0}(\vec{x})\frac{\partial}{\partial x}\psi_{j',X_0}(\vec{x}) \\ = \frac{1}{\sqrt{2}L_H}\sum_{n,m} C_{n,m}(j,X_0) & \left[\sqrt{n+1}C^*_{n+1,m}(j',X_0) - \sqrt{n}C^*_{n-1,m}(j',X_0)\right] \end{aligned} \tag{5.6}$$

An important symmetry property upon the interchange of indices j and j' of this structure factor, shown in equation (5.6), is proved in Appendix A. Using the Dirac formula to express the denominators of the terms in curly brackets at the end of equation (5.5), we separate the principal value integral terms from the Dirac delta-function terms, and investigate their behavior when the double summation over j and j' is performed. It turns out that the principal value integral terms cancel when the summation is performed, therefore only the Dirac delta-function terms survive. The frequency-dependent longitudinal conductivity formula becomes:

$$L_{xx}^{(0)}(\Omega) = \frac{\pi\hbar^2 e^2 N_y \Phi}{\Omega A M^{*2}} \int\limits_{-\infty}^{\infty} d\varepsilon \sum_{j,j'} \int\limits_{-\frac{G}{2}L_H^2}^{\frac{G}{2}L_H^2} \frac{dX_0}{a} \left(F_{j,X_0;j',X_0}^{(2)}\right)^2$$
$$\cdot D_{j',X_0}(\varepsilon) \left\{\left[f(\varepsilon - \hbar\Omega) - f(\varepsilon)\right] D_{j,X_0}(\varepsilon - \hbar\Omega) - \left[f(\varepsilon + \hbar\Omega) - f(\varepsilon)\right] D_{j,X_0}(\varepsilon + \hbar\Omega)\right\} \tag{5.7}$$

In equation (5.7) we used the following notations for the partial densities of states:

$$D_{j',X_0}(\varepsilon) = \delta\left[\varepsilon - \varepsilon_{j'}(X_0)\right] \tag{5.8}$$

$$D_{j,X_0}(\varepsilon - \hbar\Omega) = \delta\left[\varepsilon - \hbar\Omega - \varepsilon_j(X_0)\right] \tag{5.9}$$

$$D_{j,X_0}(\varepsilon + \hbar\Omega) = \delta\left[\varepsilon + \hbar\Omega - \varepsilon_j(X_0)\right] \tag{5.10}$$

In the limit as $\hbar\Omega \rightarrow 0$, equation (5.7) reduces to the result obtained by Gumbs and Huang in [48] for the zero frequency case. To be able to use equation (5.7) in numerical calculations it has to be rewritten in terms of dimensionless variables. The details of how this was done are given in Appendix B.

We just give the final formula used in the numerical investigation, as we would like to show that it is inversely proportional to the frequency of the applied radiation field, as this is a determining factor of the shape of the longitudinal conductivity graphs that we obtained.

$$\begin{aligned}
&L_{xx}^{(0)}\left(\bar{\Omega}\right)=\frac{e^2}{h}\cdot\frac{\pi}{\Phi\bar{\Omega}N_x}\sum_{j,j'}\int\limits_{-\frac{1}{2}}^{\frac{1}{2}}d\bar{k}_y\\
&\left\{\sum_{n,m}C_{n,m}\left(j,\bar{k}_y\right)\left[\sqrt{n+1}C_{n+1,m}^{*}\left(j',\bar{k}_y\right)-\sqrt{n}C_{n-1,m}^{*}\left(j',\bar{k}_y\right)\right]\right\}^2\\
&\cdot\left\{\left\{\theta\left[\bar{\varepsilon}_F-\bar{\varepsilon}_{j'}\left(\bar{k}_y\right)+\bar{\Omega}\right]-\theta\left[\bar{\varepsilon}_F-\bar{\varepsilon}_{j'}\left(\bar{k}_y\right)\right]\right\}\delta\left[\bar{\varepsilon}_j\left(\bar{k}_y\right)-\bar{\varepsilon}_{j'}\left(\bar{k}_y\right)+\bar{\Omega}\right]\right.\\
&\left.-\left\{\theta\left[\bar{\varepsilon}_F-\bar{\varepsilon}_{j'}\left(\bar{k}_y\right)-\bar{\Omega}\right]-\theta\left[\bar{\varepsilon}_F-\bar{\varepsilon}_{j'}\left(\bar{k}_y\right)\right]\right\}\delta\left[\bar{\varepsilon}_j\left(\bar{k}_y\right)-\bar{\varepsilon}_{j'}\left(\bar{k}_y\right)-\bar{\Omega}\right]\right\}
\end{aligned}\tag{5.11}$$

5.1.2 2D Hall Conductivity, L_{yx}

The band part of the Hall conductivity, $L_{yx}^{(0)}\left(\Omega\right)$ can be obtained following a very similar method as that applied in obtaining the longitudinal component. Details of the calculation are given in Appendix C. The main difference in the procedure is that the velocity operators appearing in the Hall conductivity are not the same as in the longitudinal case. When the 2DEG is placed in the $x-y$ plane and the applied magnetic field is pointing in the z–direction the velocity components can be expressed as $v_x=\frac{p_x}{M^*}$ which was already used in calculating the longitudinal conductivity. The y-component of the velocity is $v_y=\frac{p_y}{M^*}+\frac{eBx}{M^*}$.

Thus to express $L_{yx}^{(0)}\left(\Omega\right)$ we need to calculate the following velocity matrix elements:

$$\left\langle N\right|v_y\left|M\right\rangle=\left\langle N\right|\frac{p_y}{M^*}\left|M\right\rangle+\left\langle N\right|\frac{eBx}{M^*}\left|M\right\rangle\tag{5.12}$$

and

$$\langle M|\, v_x \,|N\rangle = \langle M|\, \frac{p_x}{M^*} \,|N\rangle \tag{5.13}$$

In equations (5.12) and (5.13) above $|N\rangle$ and $|M\rangle$ are the same eigenstates as used in the case of the longitudinal conductivity (see equations (5.2) and (5.3)). For some details of the calculation go to Appendix C. Here we only give the final formula:

$$\begin{aligned} L_{yx}^{(0)}(\Omega) = &-\frac{\hbar^3 e^2 L_y}{\pi A M^{*2} L_H^2} \sideset{}{'}\sum_{j,j'} \int\limits_{-\frac{G}{2}L_H^2}^{\frac{G}{2}L_H^2} dX_0 \\ &\cdot \left\{ \frac{1}{L_H^2} \mathrm{Re}\left[F^{(1)}_{j',X_0;j,X_0} F^{(2)}_{j,X_0;j',X_0}\right] + \mathrm{Re}\left[F^{(3)}_{j',X_0;j,X_0} F^{(2)}_{j,X_0;j',X_0}\right] \right\} \\ &\cdot \frac{1}{\left[\varepsilon_{j'}(X_0) - \varepsilon_j(X_0)\right]^2 - (\hbar\Omega)^2} \int\limits_{-\infty}^{\infty} d\varepsilon f(\varepsilon) D_{j',X_0}(\varepsilon) \end{aligned} \tag{5.14}$$

In equation (5.14) the following notation is introduced for another structure factor, which was originally defined by Gumbs and Huang for the zero frequency case [48]:

$$\begin{aligned} F^{(1)}_{j,X_0;j',X_0} &= F^{(1)*}_{j',X_0;j,X_0} = \int\limits_A d\vec{x}\psi^*_{j,X_0}(\vec{x}) x \psi_{j',X_0}(\vec{x}) \\ &= \frac{L_H}{\sqrt{2}} \sum_{n,m} C_{n,m}(j,X_0) \left(\sqrt{n+1} C^*_{n+1,m}(j',X_0) + \sqrt{n} C^*_{n-1,m}(j',X_0) \right) \end{aligned} \tag{5.15}$$

The symmetry property of this structure factor upon an interchange of the indices j and j', given in equation (5.15), is also verified in Appendix C. It can be seen that in equation (5.15) the structure factor previously introduced in the longitudinal conductivity calculation (see equation (5.6)) also appears. The third structure factor appearing in equation (5.15) is defined as:

$$\begin{aligned} F^{(3)}_{j,X_0;j',X_0} &= F^{(3)*}_{j',X_0;j,X_0} = -i\int\limits_A d\vec{x}\psi^*_{j,X_0}\left(\vec{x}\right)\frac{\partial}{\partial y}\psi_{j',X_0}\left(\vec{x}\right) \\ &= -G\sum_{n,m} mC^*_{n,m}\left(j,X_0\right)C_{n,m}\left(j',X_0\right) - \frac{X_0}{L_H^2}\delta_{j,j'} \end{aligned} \tag{5.16}$$

Its symmetry property upon an interchange of the indices j and j' can also be found in Appendix C.

The prime notation in equation (5.14) over the summation sign means that the summation will be performed only for those values of the indices j and j' for which $\left|\varepsilon_j\left(X_0\right) - \varepsilon_{j'}\left(X_0\right)\right| \neq \hbar\Omega$. When the $\Omega \to 0$ limit is taken, this equation reduces to the result obtained by Gumbs and Huang in [48] for the zero frequency case. This is the final form of the Hall conductivity for the 2D cosine modulation. A modified form of this equation, written in dimensionless variables, is used in the numerical calculations. We present this dimensionless form here, as it will become important to know the form it takes in the analysis of the conduction coefficients in Chapter (6). Some details of the calculation leading to the dimensionless form are shown in Appendix H.

$$\begin{aligned}
L_{yx}\left(\Omega\right) = &-\frac{e^2}{h}\frac{2}{N_x\Phi}\sum_{j,j'}\int\limits_{-\frac{1}{2}}^{\frac{1}{2}} d\bar{k}_y \frac{\theta\left[\bar{\varepsilon}_F-\bar{\varepsilon}_j\left(\bar{k}_y\right)\right]}{\left[\bar{\varepsilon}_j\left(\bar{k}_y\right)-\bar{\varepsilon}_{j'}\left(\bar{k}_y\right)\right]^2-\left(\bar{\Omega}\right)^2} \\
&\cdot\left\{\sum_{n,m} C_{n,m}\left(j,\bar{k}_y\right)\left[\sqrt{n+1}C^*_{n+1,m}\left(j',\bar{k}_y\right)+\sqrt{n}C^*_{n-1,m}\left(j',\bar{k}_y\right)\right]\right. \\
&\cdot\sum_{l,k} C_{l,k}\left(j',\bar{k}_y\right)\left[\sqrt{l+1}C^*_{l+1,k}\left(j,\bar{k}_y\right)-\sqrt{l}C^*_{l-1,k}\left(j,\bar{k}_y\right)\right] \\
&+2\sqrt{\frac{\pi}{\Phi}}\sum_{n,m} C_{n,m}\left(j,\bar{k}_y\right)\left[\sqrt{n}C^*_{n-1,m}\left(j',\bar{k}_y\right)+\sqrt{n+1}C^*_{n+1,m}\left(j',\bar{k}_y\right)\right] \\
&\left.\cdot\sum_{k,l} C_{l,k}\left(j',\bar{k}_y\right)\left[\sqrt{l+1}C^*_{l+1,k}\left(j,\bar{k}_y\right)-\sqrt{l}C^*_{l-1,k}\left(j,\bar{k}_y\right)\right]\right\}
\end{aligned} \tag{5.17}$$

5.1.3 2D Resistivities

To calculate the resistivities we need to perform the tensor inversion of the conductivity matrix. The general formulas leading to the elements of the resistivity matrix are shown below:

$$\rho^{(0)}_{xx}\left(\Omega\right) = \frac{L^{(0)}_{yy}\left(\Omega\right)}{L^{(0)}_{yy}\left(\Omega\right)L^{(0)}_{xx}\left(\Omega\right)+\left[L^{(0)}_{yx}\left(\Omega\right)\right]^2} \tag{5.18}$$

$$\rho^{(0)}_{xy}\left(\Omega\right) = -\rho^{(0)}_{yx}\left(\Omega\right) = \frac{L^{(0)}_{yx}\left(\Omega\right)}{L^{(0)}_{yy}\left(\Omega\right)L^{(0)}_{xx}\left(\Omega\right)+\left[L^{(0)}_{yx}\left(\Omega\right)\right]^2} \tag{5.19}$$

$$\rho^{(0)}_{yy}\left(\Omega\right) = \frac{L^{(0)}_{xx}\left(\Omega\right)}{L^{(0)}_{yy}\left(\Omega\right)L^{(0)}_{xx}\left(\Omega\right)+\left[L^{(0)}_{yx}\left(\Omega\right)\right]^2} \tag{5.20}$$

These formulas can be used to calculate resistivities for the 1D modulation case as well. Due to the symmetry of the potential upon an interchange of x and y in the 2D cosine modulation case, we have the following identities satisfied by the conductivity coefficients:

$$L^{(0)}_{xx}(\Omega) = L^{(0)}_{yy}(\Omega) \tag{5.21}$$

$$L^{(0)}_{yx}(\Omega) = -L^{(0)}_{xy}(\Omega) \tag{5.22}$$

The use of these symmetry properties allows some simplifications in the resistivity formulas listed above for the 2D case. In the 1D case however, the potential lacks the symmetry present in the 2D potential case, so the general formulas (5.18)–(5.20) must be used when calculating resistivities.

5.2 Band Part of Conductivity for 1D Modulation

In this section we present similar formulas to those obtained in the case of 2D modulation for the longitudinal and Hall components of the band part of the frequency-dependent conductivity, but for the 1D cosine-type periodic potential. Again, we assume that the 2DEG is located in the $x-y$ plane, and the applied magnetic field is in the z direction. Because the modulation potential contains only an x-dependent term, the longitudinal conductivity does no longer satisfy the symmetry property given in equation (5.21). Thus we need to express three different components of 1D conductivities, two longitudinal ones, and one transverse. The velocity components are still given by $v_x = \frac{p_x}{M^*}$ for the x-component, while the y-component can be written as $v_y = \frac{p_y}{M^*} + \frac{eBx}{M^*}$. In the following three subsections we list the three 1D conductivity components obtained. The main difference between the results obtained for the 1D and 2D cases, other than the lack of symmetry in the problem, is that the eigenfunctions by which the matrix elements of the velocity operators are expressed are different in the 1D case, they have a much simpler form, which was already used in the calculation of the eigenenergy spectrum (equations (2.6) and (2.7)). Therefore, the structure factors for the 1D case will also be different, and will have a simpler form than in the 2D case. As the procedure followed to obtain these conductivity components and structure factors is so similar to the 2D case, we only list our final results in what follows. We start with the L_{xx} component.

5.2.1 1D Transverse Conductivity, L_{xx}

The transverse conductivity (along the modulation direction) formula obtained has the form:

$$\begin{aligned} L_{xx}^{(0,1D)}(\Omega) = {} & \frac{\hbar^3 e^2 L_y}{4\hbar\Omega A M^{*2} L_H^2} \int\limits_{-\infty}^{\infty} d\varepsilon \sum_{j,j'} \int\limits_{-\frac{G}{2}L_H^2}^{\frac{G}{2}L_H^2} dX_0 \left(F_{j,X_0;j',X_0}^{(2,1D)} \right)^2 \\ & \cdot \delta\left[\varepsilon - \varepsilon_{j'}(X_0)\right] \left\{ \left[f(\varepsilon - \hbar\Omega) - f(\varepsilon)\right] \delta\left[\varepsilon - \hbar\Omega - \varepsilon_j(X_0)\right] \right. \\ & \left. - \left[f(\varepsilon + \hbar\Omega) - f(\varepsilon)\right] \delta\left[\varepsilon + \hbar\Omega - \varepsilon_j(X_0)\right] \right\} \end{aligned} \tag{5.23}$$

In equation (5.23) the following notation is used for one of the 1D structure factors:

$$\begin{aligned} F_{j,X_0;j',X_0}^{(2,1D)} & = \int\limits_A d\vec{x} \psi_{j,X_0}^*(\vec{x}) \frac{\partial}{\partial x} \psi_{j',X_0}(\vec{x}) \\ & = \frac{1}{\sqrt{2} L_H} \sum_n C_n(j, X_0) \left[\sqrt{n+1} C_{n+1}^*(j', X_0) - \sqrt{n} C_{n-1}^*(j', X_0) \right] \end{aligned} \tag{5.24}$$

The delta functions appearing in equation (5.23) are denoting the following partial densities of states:

$$D_{j',X_0}\left(\varepsilon\right)=\delta\left[\varepsilon-\varepsilon_{j'}\left(X_0\right)\right] \tag{5.25}$$

$$D_{j,X_0}\left(\varepsilon-\hbar\Omega\right)=\delta\left[\varepsilon-\hbar\Omega-\varepsilon_{j}\left(X_0\right)\right] \tag{5.26}$$

$$D_{j,X_0}\left(\varepsilon+\hbar\Omega\right)=\delta\left[\varepsilon+\hbar\Omega-\varepsilon_{j}\left(X_0\right)\right] \tag{5.27}$$

Using notations (5.24) – (5.26) equation (5.22) may be written as:

$$L_{xx}^{(0,1D)}\left(\Omega\right)=\frac{\hbar^3e^2L_y}{4\hbar\Omega AM^{*2}L_H^2}\int\limits_{-\infty}^{\infty}d\varepsilon\sum_{j,j'}\int\limits_{-\frac{G}{2}L_H^2}^{\frac{G}{2}L_H^2}dX_0\left(F_{j,X_0;j',X_0}^{(2,1D)}\right)^2$$
$$D_{j',X_0}\left(\varepsilon\right)\left\{\left[f\left(\varepsilon-\hbar\Omega\right)-f\left(\varepsilon\right)\right]D_{j,X_0}\left(\varepsilon-\hbar\Omega\right)-\left[f\left(\varepsilon+\hbar\Omega\right)-f\left(\varepsilon\right)\right]D_{j,X_0}\left(\varepsilon+\hbar\Omega\right)\right\} \tag{5.28}$$

Now we rewrite the coefficient in front of the first integration in equation (5.28) in a more convenient form:

$$\frac{\hbar^3e^2L_y}{2\hbar\Omega AL_H^2M^{*2}}=\frac{\pi\hbar^3e^2N_y\Phi}{a\hbar\Omega AM^{*2}} \tag{5.29}$$

Using the results (5.29) equation (5.28) can be written as:

$$L_{xx}^{(0,1D)}(\Omega) = \frac{\pi\hbar^3 e^2 N_y \Phi}{\hbar\Omega A M^{*2}} \int\limits_{-\infty}^{\infty} d\varepsilon \sum_{j,j'} \int\limits_{-\frac{G}{2}L_H^2}^{\frac{G}{2}L_H^2} \frac{dX_0}{a} \left(F_{j,X_0;j',X_0}^{(2,1D)}\right)^2$$
$$\cdot D_{j',X_0}(\varepsilon)\left\{\left[f(\varepsilon-\hbar\Omega)-f(\varepsilon)\right]D_{j,X_0}(\varepsilon-\hbar\Omega)-\left[f(\varepsilon+\hbar\Omega)-f(\varepsilon)\right]D_{j,X_0}(\varepsilon+\hbar\Omega)\right\} \tag{5.30}$$

Finally, we write the 1D transverse conductivity, L_{xx}, in terms of dimensionless variables, which is the form used in numerical calculations:

$$\begin{aligned} L_{xx}^{(0,1D)}(\Omega) &= \frac{e^2}{h}\cdot\frac{\pi}{\Phi\bar{\Omega}N_x N_y}\sum_{j,j'}\int\limits_{-\frac{1}{2}}^{\frac{1}{2}} d\bar{k}_y \\ &\cdot\left\{\sum_n C_n\left(j,\bar{k}_y\right)\left[\sqrt{n+1}C_{n+1}^*\left(j',\bar{k}_y\right)-\sqrt{n}C_{n-1}^*\left(j',\bar{k}_y\right)\right]\right\}^2 \\ &\cdot\left\{\left\{\theta\left[\bar{\varepsilon}_F-\bar{\varepsilon}_{j'}\left(\bar{k}_y\right)+\bar{\Omega}\right]-\theta\left[\bar{\varepsilon}_F-\bar{\varepsilon}_{j'}\left(\bar{k}_y\right)\right]\right\}\delta\left[\bar{\varepsilon}_j\left(\bar{k}_y\right)-\bar{\varepsilon}_{j'}\left(\bar{k}_y\right)+\bar{\Omega}\right]\right. \\ &\left.-\left\{\theta\left[\bar{\varepsilon}_F-\bar{\varepsilon}_{j'}\left(\bar{k}_y\right)-\bar{\Omega}\right]-\theta\left[\bar{\varepsilon}_F-\bar{\varepsilon}_{j'}\left(\bar{k}_y\right)\right]\right\}\delta\left[\bar{\varepsilon}_j\left(\bar{k}_y\right)-\bar{\varepsilon}_{j'}\left(\bar{k}_y\right)-\bar{\Omega}\right]\right\} \end{aligned} \tag{5.31}$$

In equation (5.31) the definition of the dimensionless variables is the same as in the 2D case.

5.2.2 1D Longitudinal Conductivity, L_{yy}

The longitudinal conductivity formula for 1D modulation is:

$$\begin{aligned}
L_{yy}^{(0,1D)}(\Omega) &= \frac{\hbar^3 e^2 N_y \Phi}{2\Omega A M^{*2}} \int\limits_{-\infty}^{\infty} d\varepsilon \sum_{j,j'} \int\limits_{-\frac{G}{2}L_H^2}^{\frac{G}{2}L_H^2} \frac{dX_0}{a} \\
&\cdot \left[\frac{1}{L_H^4} \left(F_{j',X_0;j,X_0}^{(1,1D)} \right)^2 + \frac{2}{L_H^2} F_{j',X_0;j,X_0}^{(1,1D)} F_{j',X_0;j,X_0}^{(3,1D)} + \left(F_{j',X_0;j,X_0}^{(3,1D)} \right)^2 \right] \\
&\cdot D_{j',X_0}(\varepsilon) \left\{ \left[f(\varepsilon - \hbar\Omega) - f(\varepsilon) \right] D_{j,X_0}(\varepsilon - \hbar\Omega) - \left[f(\varepsilon + \hbar\Omega) - f(\varepsilon) \right] D_{j,X_0}(\varepsilon - \hbar\Omega) \right\}
\end{aligned} \tag{5.32}$$

The following notation is introduced for another one of the 1D structure factors:

$$\begin{aligned}
F_{j,X_0;j',X_0}^{(1,1D)} &= F_{j',X_0;j,X_0}^{(1,1D)*} = \int\limits_A d\vec{x} \psi_{j,X_0}^*(\vec{x}) x \psi_{j',X_0}(\vec{x}) \\
&= \frac{L_H}{\sqrt{2}} \sum_n C_n(j, X_0) \left(\sqrt{n+1} C_{n+1}^*(j', X_0) + \sqrt{n} C_{n-1}^*(j', X_0) \right)
\end{aligned} \tag{5.33}$$

while the third structure factor for the 1D case is given by the expression:

$$F_{j,X_0;j',X_0}^{(3,1D)} = F_{j',X_0;j,X_0}^{(3,1D)*} = -\frac{X_0}{L_H^2} \delta_{j,j'} \tag{5.34}$$

We also give the 1D longitudinal conductivity L_{yy} in terms of dimensionless variables, which is the form that will be used in numerical calculations:

$$\begin{aligned} L_{yy}^{(0,1D)}\left(\Omega\right) = {} & \frac{e^2}{h}\frac{\pi}{\bar{\Omega} N_x N_x \Phi}\sum_{j,j'}\int\limits_{-\frac{1}{2}}^{\frac{1}{2}} d\bar{k}_y \\ & \cdot \left[\left(F^{(1,1D)}_{j',\bar{k}_y;j,\bar{k}_y}\right)^2 + 4\sqrt{\frac{\pi}{\Phi}}F^{(1,1D)}_{j',\bar{k}_y;j,\bar{k}_y}F^{(3,1D)}_{j',\bar{k}_y;j,\bar{k}_y} + \frac{4\pi}{\Phi}L_H^2\left(F^{(3,1D)}_{j',\bar{k}_y;j,\bar{k}_y}\right)^2\right] \\ & \cdot \left\{\left[f\left(\bar{\varepsilon}_{j'}\left(\bar{k}_y\right)-\bar{\Omega}\right) - f\left(\bar{\varepsilon}_{j'}\left(\bar{k}_y\right)\right)\right]\delta\left[\bar{\varepsilon}_{j'}\left(\bar{k}_y\right)-\bar{\Omega}-\bar{\varepsilon}_j\left(\bar{k}_y\right)\right]\right. \\ & \left. - \left[f\left(\bar{\varepsilon}_{j'}\left(\bar{k}_y\right)+\bar{\Omega}\right) - f\left(\bar{\varepsilon}_{j'}\left(\bar{k}_y\right)\right)\right]\delta\left[\bar{\varepsilon}_{j'}\left(\bar{k}_y\right)+\bar{\Omega}-\bar{\varepsilon}_j\left(\bar{k}_y\right)\right]\right\} \end{aligned} \tag{5.35}$$

5.2.3 1D Hall Conductivity, L_{yx}

Finally, we list the theoretical and dimensionless forms of the Hall conductivity for the 1D modulation potential:

$$\begin{aligned} L_{yx}^{(0,1D)}\left(\Omega\right) = {} & -\frac{\hbar^3 e^2 L_y}{\pi A M^{*2} L_H^2}\sum_{j,j'}{}' \int\limits_{-\frac{G}{2}L_H^2}^{\frac{G}{2}L_H^2} dX_0 \\ & \cdot \left\{\frac{1}{L_H^2}\mathrm{Re}\left[F^{(1,1D)}_{j',X_0;j,X_0}F^{(2,1D)}_{j,X_0;j',X_0}\right] + \mathrm{Re}\left[F^{(3,1D)}_{j',X_0;j,X_0}F^{(2,1D)}_{j,X_0;j',X_0}\right]\right\} \\ & \cdot \frac{1}{\left[\varepsilon_{j'}\left(X_0\right)-\varepsilon_j\left(X_0\right)\right]^2 - \left(\hbar\Omega\right)^2}\int\limits_{-\infty}^{\infty} d\varepsilon f\left(\varepsilon\right) D_{j',X_0}\left(\varepsilon\right) \end{aligned} \tag{5.36}$$

In equation (5.36) the structure factors are defined as follows: equation (5.33) is used for the first structure factor, $F^{(1,1D)}_{j,X_0;j',X_0}$, equation (5.24) for the second one, $F^{(2,1D)}_{j,X_0;j',X_0}$, while equation (5.34) for the third one, $F^{(3,1D)}_{j,X_0;j',X_0}$. In the conclusion of this subsection we give the dimensionless form of the Hall conductivity equation for the 1D periodic modulation case:

$$L_{yx}^{(0,1D)}\left(\Omega\right)=-\frac{e^{2}}{h}\frac{2}{N_{x}N_{y}\Phi}\sum_{j,j'}{}^{'}\int\limits_{-\frac{1}{2}}^{\frac{1}{2}}d\bar{k}_{y}\frac{\theta\left[\bar{\varepsilon}_{F}-\bar{\varepsilon}_{j}\left(\bar{k}_{y}\right)\right]}{\left[\bar{\varepsilon}_{j'}\left(\bar{k}_{y}\right)-\bar{\varepsilon}_{j}\left(\bar{k}_{y}\right)\right]^{2}-\left(\bar{\Omega}\right)^{2}} \cdot\left\{\mathrm{Re}\left[F_{j',\bar{k}_{y};j,\bar{k}_{y}}^{(1,1D)}F_{j,\bar{k}_{y};j',\bar{k}_{y}}^{(2,1D)}\right]+2\sqrt{\frac{\pi}{\Phi}}\mathrm{Re}\left[F_{j',\bar{k}_{y};j,\bar{k}_{y}}^{(3,1D)}F_{j,\bar{k}_{y};j',\bar{k}_{y}}^{(2,1D)}\right]\right\} \tag{5.37}$$

This concludes the section presenting 1D conductivity coefficients, and the chapter presenting the conductivity and resistivity coefficients. The resistivities for the 1D cosine modulation case are also given by equations (5.18) – (5.20) listed for the 2D case. Their form is unchanged in the 1D modulation case, only the symmetry properties used at the 2D modulation case cannot be applied to simplify these formulas in the numerical calculations. In the following chapter the numerical results obtained for the conductivity and resistivity of the 2D and 1D cosine type periodic modulation are presented.

Chapter 6

Effect of 2D Modulation and Finite Frequency on Magnetotransport

This chapter explores the longitudinal and transverse magnetotransport of a 2DEG subjected to a 2D periodic electrostatic modulation potential in the presence of finite frequency radiation. As it was mentioned earlier, the two-dimensional potentials considered could replicate 2D square arrays of dots and antidots, for sufficiently strong modulation.

The investigation of this problem was motivated by our knowledge of the presence of interesting commensurability oscillations found in the magnetoresistance of the 2DEG in heterostructures such as $GaAs/AlGaAs$. The magnetoresistance of a 2DEG with modulation has been intensely investigated since 1976, when Hofstadter published a paper [11] drawing attention to interesting band structure effects which might affect transport and optical properties. A 2D modulation potential applied to the 2DEG in a magnetic field lifts the degeneracy of the Landau levels, and leads to the appearance of Landau bands of finite width. In the tight-binding model of a simple cubic lattice, the energy spectrum is known as "Hofstadter's butterfly" [11], [45],

[46]. Since Hofstadter's original work was published, the 2D motion of electrons in a periodic potential and a perpendicular magnetic field has been intensely studied and it revealed a series of other interesting commensurability effects. In our investigation of the eigenvalue dispersion we found evidence supporting the presence of some commensurability effects, such as the periodic oscillation of the modulation-broadened Landau level bandwidth, when rational values of the magnetic flux were applied to the unit cell (see Chapter 3).

In a strong magnetic field (much larger than 1 T) and at low temperature ($\sim 4K$) magnetoresistance oscillations, known as Shubnikov-de Haas oscillations, are observed in the longitudinal direction for a homogeneous 2DEG. Meanwhile the tranverse resistivity exhibits a series of plateaus known as the integral quantum Hall effect. The quantum mechanical explanation for the high magnetic field behavior was found in the so-called Laughlin states [12]. The resistivity steps of the integral quantum Hall effect can be explained in terms of single-particle states with the Fermi energy in the gap between successive Landau levels.

Even in the absence of a modulation potential the magnetoconductivity of a 2DEG under the influence of a frequency-dependent electric field in the RF, microwave, and IR frequency range has lead to interesting results. Abundant availability of high-mobility samples produced by submicrometer lithography certainly makes the experimental investigation of the problem possible. The low-magnetic field behavior of the magnetoresistance can be explained using a classical treatment. Recent experimental results obtained by two different groups [13],[14] drew attention to the significant consequences that the irradiation of a 2DEG with a frequency-dependent electric field has on the transport properties at low magnetic fields. In this low magnetic field region the Hall resistivity is not quantized, and the longitudinal resistivity exhibits giant oscillations. We give a brief description of the experimental results obtained by the two experimentalist groups. The first is related to the observation of some peculiar effects in the 2DEG in high mobility $GaAs/AlGaAs$ heterostructures under strong microwave radiation, such as the disappearance of the diagonal conductivity without Hall resistance quantization at low temperatures and low magnetic fields [16]. These so called zero resistance states (ZRSs) may originate from negative resistance states first predicted in the pioneering work of Ryzhii [15]. Also, Shubnikov-de Haas-like oscillations in the millimeter wave photoconductivity of a high-mobility 2DEG were observed[13]. These giant oscillations in amplitude occur in a weak magnetic field and their period is determined by the ratio of the millimeter wave to the cyclotron frequency.

The dynamical conductivity of a 2DEG in very high mobility $GaAs/AlGaAs$ heterostructures was also determined from the attenuation and velocity of surface acoustic waves (SAWs). The determination is possible because SAWs in piezoelectric crystals are affected by the electrical properties of nearby conductors. Broad conductivity resonances were found in the low-temperature and high magnetic field limit [17]. A relation that reflects the frequency and wavevector-dependent electrical conductivity of the 2DEG was also obtained by Simon [18]. SAWs also play an important role in the study of composite fermions for which Halperin, Lee, and Read [19] obtained the nonlocal conductivity at half filling.

The 2DEG edge electronic structure can be studied by another experimental technique. This is based on the observation of low-frequency edge magnetoplasmons propagating along the electrostatically confined edge of the 2DEG. 2D edge magnetoplasmons were studied in the quantum Hall regime at radio frequencies [20], [21]. The method provides quantitative information about the applied electrostatic potential and the spatial structure of the edge channels. There have also been measurements of the microwave photoconductivity of $GaAs/AlGaAs$ heterostructures for which resonant responses were obtained corresponding to collective plasmon excitations in a perpendicular magnetic field [22]-[25], [27].

The conductivity of a 2DEG in low magnetic fields, where the usual Shubnikov-de Haas oscillations do not appear, was calculated in the semiclassical regime within the framework of the Boltzmann transport equation. Since the fabrication of periodic artificial scatterers in a highly mobile 2DEG at the interface of a $GaAs/AlGaAs$ heterostructure became possible, many experimentalists have studied their QMT properties for a variety of imposed scatterers [26],[28],[38],[43]. A class of novel effects was discovered. For example, for a square array of antidots formed by strong repulsive scatterers embedded in a 2DEG, the introduction of spatially modulated 2D potentials leads to dramatic commensurability effects at low magnetic fields and temperatures such as the suppression of the commensurate Weiss oscillations, and negative and quenched Hall resistivities. Other unusual effects are the pronounced resistance peaks and the double peak feature, which is manifested when a cyclotron orbit circumscribes a group of antidots in the square array [38]. As the electrostatic modulation potentials modeling antidots were continuously varying functions, the cyclotron orbits are distorted. Non-circular cyclotron orbits have been demonstrated in transport measurements of the cyclotron frequency [26]. Microwave photoconductivity measurements in the range of 60-400 GHz on an antidot array revealed that the resonant signals were shifted to higher magnetic fields with increasing frequency [28].

The experimental investigation of our problem, the magnetoconductivity of a 2DEG under the influence of a periodic electrostatic modulation potential and a frequency-dependent electric field has also been pursued [29]. The photocurrent measurements performed in a $GaAs/AlGaAs$ superlattice placed in a parallel magnetic field, and exposed to THz radiation, revealed the presence of a new channel for electric conduction. Electrons in one quantum well were photo-excited to tunnel resonantly into the neighboring wells without intrasubband relaxation.

6.1 2D Magnetotransport

In the rest of this chapter, we present the numerical results obtained for the variation of the AC and DC magnetotransport coefficients in the presence of a 2D electrostatic modulation. A perpendicular magnetic field, B, is also applied to the sample. Results are given for various frequencies of an external radiation field, Ω. We present the conductance coefficients versus magnetic field in the presence of the radiation field and compare them to their respective values obtained without radiation. Our calculations were carried out for both negative and positive modulation potentials.

6.1.1 2D $L_{xx}^{(0)}(\Omega)$ for $\bar{V} < 0$

Figure 6.1 shows our numerical results for the longitudinal conductivity, $L_{xx}^{(0)}(\Omega)$ for a negative 2D electrostatic modulation potential of strength $\bar{V} = -40.235$. The absolute value of this potential is large as compared to relevant energy scales present in the problem ($|V_0| \gg \hbar\omega_c$) and in fact all of the following graphs are obtained for the strong modulation case. We are using these large values of the modulation potential since we know that our model potential approaches quantum dot (antidot) behavior for large positive (negative) values of the potential strength. We analyze the regime in which the following conditions are met by the parameters entering the problem: the temperature is small compared to the strength of the periodic potential ($k_BT/\hbar\omega_c < \bar{V}$) and the frequency of the incoming radiation is correlated with the value of the Fermi energy $\hbar\omega_c \sim E_F$.

Figure 6.1 illustrates the effect that the electromagnetic radiation has on the longitudinal conductivity $L_{xx}^{(0)}(\Omega)$. In the inset (corresponding to the absence of radiation,

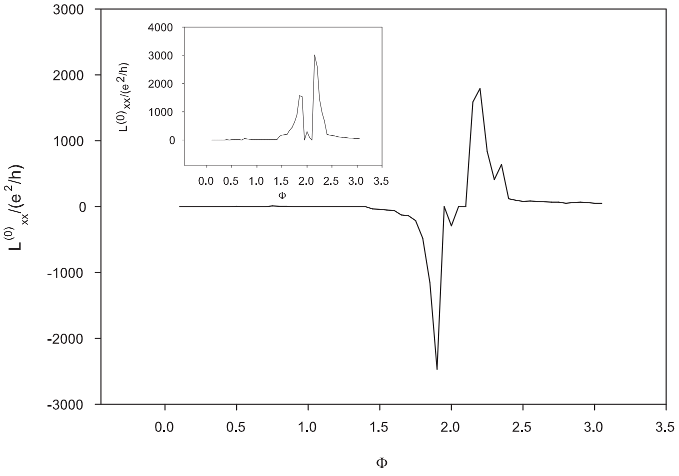

Figure 6.1: Longitudinal conductivity with and without (inset) radiation field for negative 2D electrostatic modulation. Sample size $N_x = N_y = 10$, modulation potential strength $\bar{V} = -40.235$, while its exponent $N = 10$. Other parameters used are $n = 5$, $m = 3$, electron density $n_{2D}a^2 = 1.0$, and power of the periodic term $N = 10$. For the frequency of the radiation the value $\hbar\Omega = E_F$ was used.

$\Omega = 0$) it can be seen that the longitudinal conductivity goes through a series of positive oscillations as the value of the applied magnetic field increases. In the presence of radiation however, a large amplitude negative oscillation appears. In the low magnetic field portion of the plot, the longitudinal conductivity maintains a constant value around zero in both plots (with or without electromagnetic radiation). This is due to the fact that in the low magnetic field region the Lorentz force acting on the electrons has a dominant effect. Under its influence, electrons describe large radius cyclotron orbits, with diameters that can become larger than the spacing between potential peaks. Consequently, electrons could describe several closed orbits without becoming affected by the potential. When the magnetic field is increased, the longitudinal conductivity shows a series of oscillations, which are due to the commensurability of the cyclotron radius and the period of the modulation potential. On the other end of the Φ axis, that corresponding to large values of the magnetic field, we see again a decrease in the longitudinal conductivity. This time the effect is caused by a different mechanism. When the magnetic field is strong, the radius of the cyclotron orbit is small. The 2DEG returns to its homogeneous behavior. As the electrons are following their tiny circular orbits, they no longer "feel" the effect of the modulation. There is no more mixing of the Landau orbits present, as these orbits become decoupled for large values of the magnetic field. Figure 6.1 displays a large negative "dip" in $L_{xx}^{(0)}$ when $\Omega \neq 0$. This means that there is backscattering in the presence of a radiation field. No backscattering can be seen in the $L_{xx}^{(0)}$ plot when $\Omega = 0$ (inset).

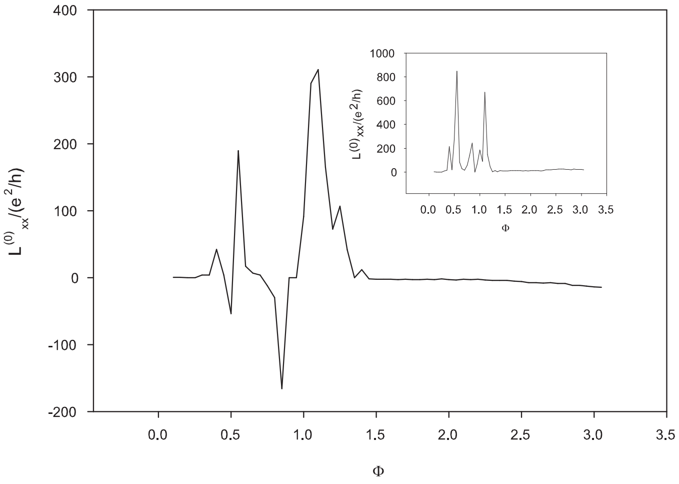

Figure 6.2: Longitudinal conductivity with and without (inset) radiation field for negative 2D electrostatic modulation. Sample size $N_x = N_y = 10$, modulation potential strength $\bar{V} = -60.235$, while its exponent $N = 10$. Other parameters used are $n = 5$, $m = 3$, electron density $n_{2D}a^2 = 1.0$, and power of the periodic term $N = 10$. For the frequency of the radiation the value $\hbar\Omega = E_F$ was used.

A similar situation can be seen in Figure 6.2, in which the negative 2D modulation potential is increased to $\bar{V} = -60.235$. Again, in the absence of radiation the longitudinal conductivity $L_{xx}^{(0)}(\Omega)$ goes through a series of large amplitude oscillations, but these are all in the positive region. In the presence of the radiation the longitudinal conductivity also shows large oscillations, but some have a negative amplitude. In the large magnetic field portion of the plot the values taken by the longitudinal conductivity become small after a threshold value of Φ is exceeded, because electrons return to the homogeneous 2DEG behavior. The Landau levels are decoupled, there is no more mixing of the Landau orbits. By a comparison of Figures 6.1 and 6.2, it can be concluded that for a stronger negative potential the commensurability oscillations of the longitudinal conductivity take place at lower magnetic fields.

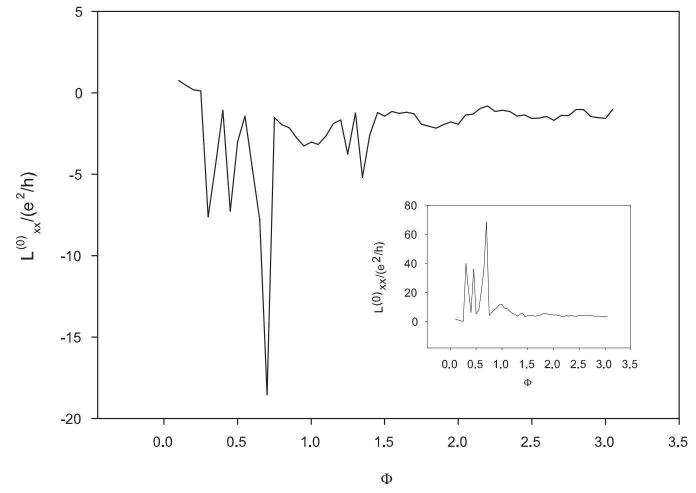

Figure 6.3: Longitudinal conductivity with and without (inset) radiation field for negative 2D electrostatic modulation. Sample size $N_x = N_y = 10$, modulation potential strength $\bar{V} = -80.235$, while its exponent $N = 10$. Other parameters used are $n = 5$, $m = 3$, electron density $n_{2D}a^2 = 1.0$, and power of the periodic term $N = 10$. For the frequency of the radiation the value $\hbar\Omega = E_F$ was used.

The reason for this is that the electrostatic potential dominates the Lorentz force starting at lower values of the applied magnetic field. On the other end of the Φ axis, that corresponding to high values of the magnetic field, the homogeneous 2DEG behavior starts at smaller values of the magnetic field. Thus the threshold value is smaller for the stronger negative potential.

In Figure 6.3, the absolute value of the modulation potential is further increased.

This leads to a drastic change in the shape of the longitudinal conductivity plots in the presence of radiation as compared to the previous two cases shown. The inset shows no qualitative change in the behavior of the longitudinal conductivity in the absence of irradiation as compared to the previous two cases presented. It still shows large amplitude positive oscillations. In the presence of the electromagnetic field however, all the oscillations are in the negative region of the plot. There are no more positive oscillations in the longitudinal conductivity, as in the previous cases, which means that the combined effect of this even stronger (than in the previous two cases) value of the modulation potential and the radiation field is that most of the electrons are backscattered.

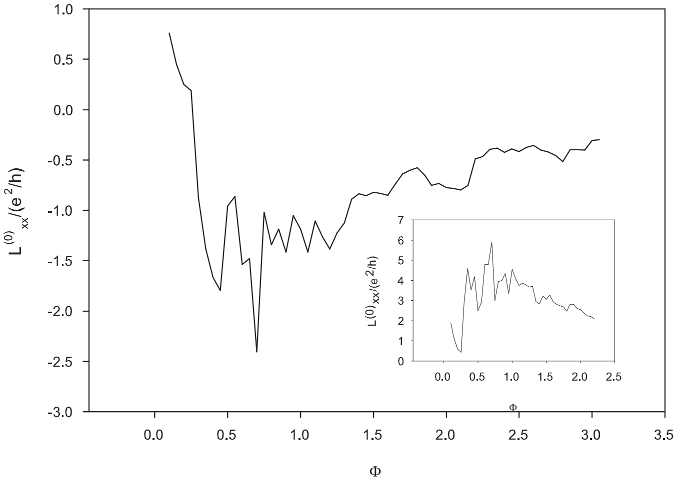

Figure 6.4: Longitudinal conductivity with and without (inset) radiation field for negative 2D electrostatic modulation. Sample size $N_x = N_y = 10$, modulation potential strength $\bar{V} = -100.235$, while its exponent $N = 10$. Other parameters used are $n = 5$, $m = 3$, electron density $n_{2D}a^2 = 1.0$. For the frequency of the radiation the value $\hbar\Omega = E_F$ was used.

Figure 6.4 was obtained for the largest negative strength of modulation potential that we investigated. Again, as it can be seen in the inset, when there is no radiation present, the longitudinal conductivity shows oscillatory behavior. These oscillations do not have a definite period, but they extend over a larger range of Φ values than those seen for the cases of lower modulation potential strengths (Figures 6.1, 6.2, and 6.3) and there is a larger number of oscillations present in the plot. The amplitude of these oscillations is lower for higher values of the magnetic field, as electrons on small cyclotron orbits are affected in a lesser degree by the negative potential, but the conductivity no longer returns to homogeneous 2DEG behavior for large values of the applied magnetic field in the range of magnetic fields investigated. Next we present a series of four plots which compare the variation of the longitudinal conductivity for various frequency values of the external radiation field. Each of these plots, which are shown in Figure 6.5, was obtained for four different values of the frequency Ω. The largest positive to negative conductivity oscillations are obtained for the smallest value of the frequency chosen in the Figure, which is $\Omega = 0.25 E_F/\hbar$. In the plots, this corresponds to the large dashed (green) line. The next largest oscillation amplitudes (which are much smaller than those for $\Omega = 0.5 E_F/\hbar$) are obtained for those values of the frequency for which $\Omega = 0.5 E_F/\hbar$. These are represented by the solid (red) line in the figure. The dotted (black) line corresponds to frequency values of $\Omega = E_F/\hbar$. For the largest value of the frequency chosen in the figure ($\Omega = 1.5 E_F/\hbar$) the conductivity oscillations are further reduced in amplitude, especially for the two largest values of the modulation potential strength shown, Figures 6.5 (c) and (d). The influence of the choice of the incoming radiation frequency on the variation of the longitudinal conductivity can be seen by looking back at the theoretical formula used to generate these graphs. In equation (5.11) the argument of the step function depends on both the value of the Fermi energy and that of the radiation frequency. The step functions "pick out" the electronic eigenstates that lie within a range of $\pm\hbar\Omega$ of E_F, thus only these eigenstates contribute to the longitudinal conductivity, while in the zero frequency case only eigenenergies equal to the Fermi energy contribute. Moreover,

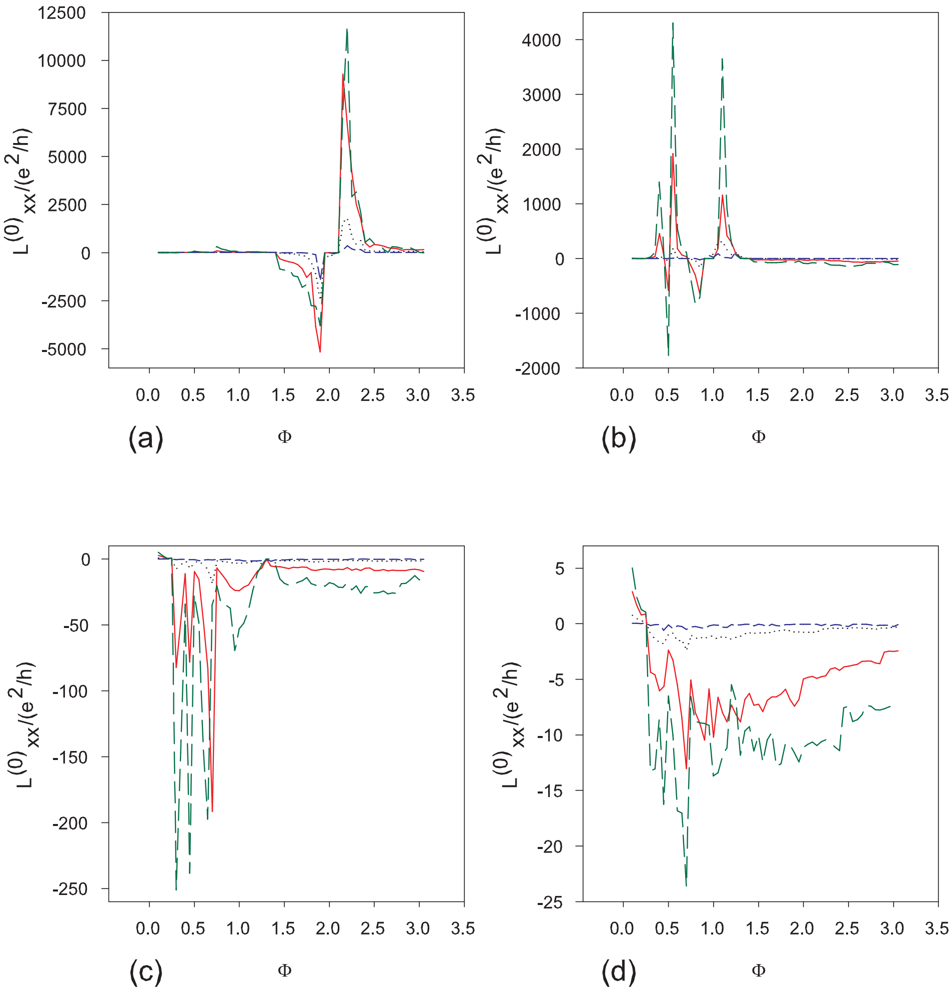

Figure 6.5: Longitudinal conductivity for different values of the frequency of the radiation field. The large dashed (green) line corresponds to those values of the frequency for which $\hbar\Omega = 0.25E_F$, the solid (red) line corresponds to $\hbar\Omega = 0.5E_F$, the dotted (black) line corresponds to $\hbar\Omega = E_F$, while the short dashed (blue) line is for $\hbar\Omega = 1.5E_F$. Other parameters used in the figure are sample size $N_x = N_y = 10$, 2D modulation potential strength $\bar{V} = -40.235$ for (a), $\bar{V} = -60.235$ for (b), $\bar{V} = -80.235$ for (c), and $\bar{V} = -100.235$ for (d). The exponent of the periodic term $N = 10$, while $n = 5$, $m = 3$, and electron density $n_{2D}a^2 = 1.0$.

the multiplicative factor at the beginning of this longitudinal conductivity formula is inversely proportional to the incoming radiation frequency. Thus, with the increase of this frequency, the amplitude of the oscillations is reduced. The green (large dashed) line, which corresponds to the lowest value of the frequency, has the largest amplitude oscillations, while the blue (short dashed) line, which corresponds to the highest frequency, shows the lowest amplitude ones. As conduction is due mainly to electrons within a small range of the Fermi energy, the effect of the radiation is established through the step functions entering formula (5.11) "picking out" the energy eigenvalues over which the summations are performed.

6.1.2 2D $L_{yx}^{(0)}(\Omega)$ for $\bar{V} < 0$

We start this section by presenting a comparison of the Hall magnetoconductivity coefficient plots in the presence of the electromagnetic radiation to those obtained with no irradiation.

Figure 6.6 is a plot of the tranverse (or Hall) conductivity obtained for two large values of 2D modulation potential strength ($\bar{V} = -80.235$ and $\bar{V} = -100.235$). There are a few important observations to be made. The first is that the Hall conductivity obtained for negative $\bar{V}$ with no incident radiation applied shows large amplitude negative oscillations as the strength of the applied magnetic field increases. These oscillations are negative because of the negative sign entering their definitions (not listed in this work). It should be noted that the band part of the zero frequency Hall conductivity transforms according to the relation $L_{yx}^{(0)}(0) = -L_{xy}^{(0)}(0)$ upon an interchange of x and y, while the corresponding finite frequency formula is $L_{yx}^{(0)}(\Omega) = -L_{xy}^{(0)}(\Omega)$. In the presence of radiation, the band part of the Hall conductivity also shows oscillations, but these occur mostly in the positive region, with very few large

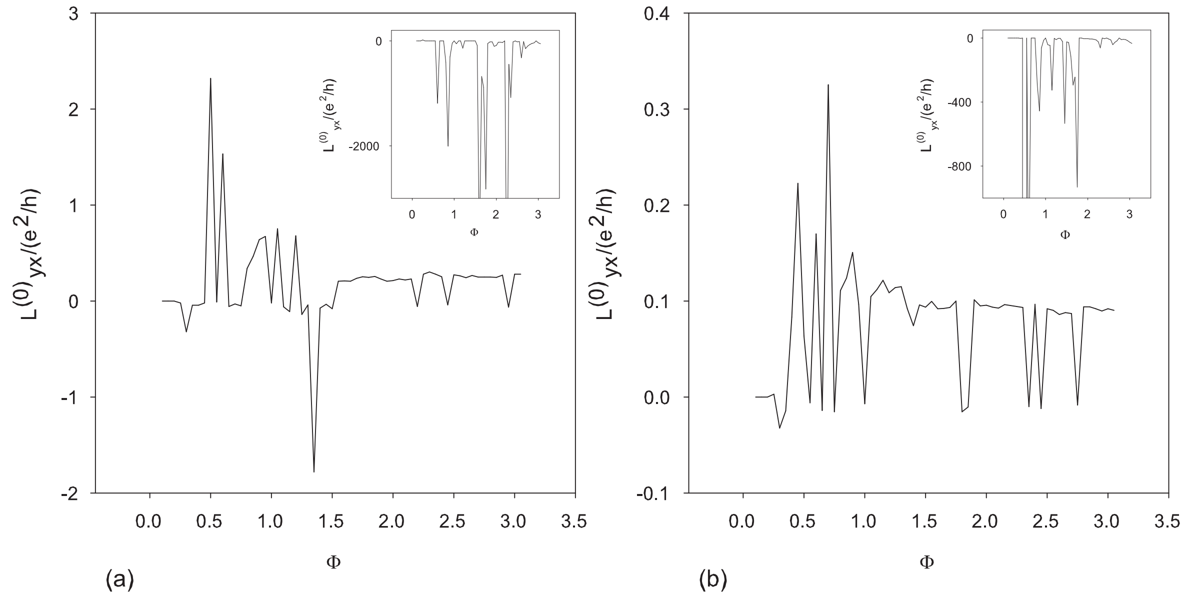

(a) (b)

Figure 6.6: Hall conductivities with and without (inset) radiation field for negative 2D electrostatic modulation. Sample size $N_x = N_y = 10$, modulation potential strength $\bar{V} = -80.235$ in (a) and $\bar{V} = -100.235$ in (b), while the exponent of the periodic term $N = 10$. Other parameters used are $n = 5$, $m = 3$, electron density $n_{2D}a^2 = 1.0$. For the frequency of the radiation the value $\hbar\Omega = E_F$ was used.

amplitude negative oscillations, despite the negative sign in their definition given in equation (5.17).

There is some similarity between the zero-frequency longitudinal conductivity's large-amplitude oscillations and those of the zero-frequency Hall conductivity. This similarity is that they also occur in the small-field region of the graphs. The amplitude of the oscillations in the insets of both plots of Figure 6.6 diminishes in the large magnetic field region, especially in plot (b).

To understand the behavior of the Hall conductivity upon the variation of the applied magnetic field, one should look at equation (5.17). In this equation the step function "picks out" only the electronic eigenstates that lie below E_F, thus only these eigenstates contribute to the Hall conductivity (this is true for both the zero and finite frequency formulas, but the zero frequency formula is not listed explicitly).

Therefore, only the lower-lying eigenstates (below the Fermi level) are contributing to the Hall conductivity. Although there is some similarity between the behavior of the Hall conductivity with and without irradiation, such as that the amplitude of the oscillations decrease upon an increase of the modulation potential strength, there also are important differences.

The most important difference is that the oscillations of the band part of the Hall conductivity are mostly positive when the sample is irradiated. With an increase of the modulation potential strength the negative oscillations diminish, as the single negative amplitude oscillation in plot (a) of Figure 6.6, corresponding to the lower value of the modulation potential strength, disappears in plot (b), which was obtained for a larger modulation potential strength.

Figure 6.7 presents the influence that changing the frequency of the incident radiation has on the tranverse conductivity for the negative 2D electrostatic modulation. As it can be seen from the plots, the Hall conductivity shows some large amplitude positive to negative oscillations for the various values of the external radiation frequency. The amplitude of these oscillations is larger for the smaller values of the radiation frequency, thus the increasing frequency reduces the conductivity. The large dashed (green) line in the figure corresponds to $\Omega = 0.25E_F/\hbar$, which is the lowest value of the frequency that was investigated. The largest amplitude oscillations are found for this value of the frequency of the incoming radiation in all four of the plots. The next largest oscillation amplitudes are obtained for the frequency value of $\Omega = 0.5E_F/\hbar$, which corresponds to the solid (black) line in the plots of Figure 6.7. The amplitude of the oscillations diminishes for the two higher values of the radiation field frequency, which are $\Omega = E_F/\hbar$ shown by a dotted (black) line, and $\Omega = 1.5E_F/\hbar$ represented by a short dashed (blue) line in the plots. It can also be seen in Figure 6.7, that for large values of the magnitude of the 2D modulation

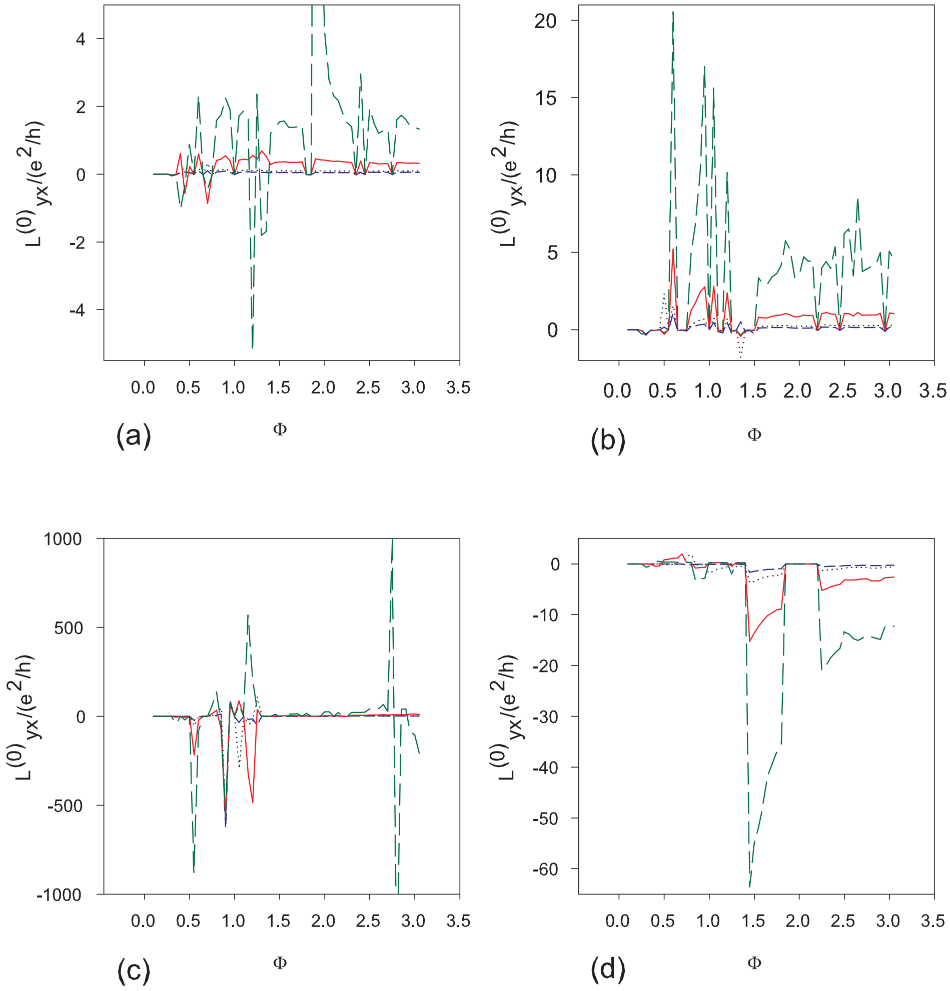

Figure 6.7: Hall conductivities for negative values of the modulation potential and different frequencies of the radiation field for the negative 2D electrostatic modulation. The long dashed (green) line corresponds to those values of the frequency for which $\hbar\Omega = 0.25E_F$, the solid (red) line corresponds to $\hbar\Omega = 0.5E_F$, the dotted (black) line corresponds to $\hbar\Omega = E_F$, while the short dashed (blue) line is for $\hbar\Omega = 1.5E_F$. Other parameters used in this Figure are sample size $N_x = N_y = 10$, modulation potential strength $\bar{V} = -100.235$ for (a), $\bar{V} = -80.235$ for (b), $\bar{V} = -60.235$ for (c), and $\bar{V} = -20.235$ for (d). The exponent of the periodic term $N = 10$, while $n = 5$, $m = 3$, and electron density $n_{2D}a^2 = 1.0$.

potential, $\bar{V}$ the large amplitude positive to negative conductivity oscillations are found all through the magnetic field range investigated (plots (a) and (b)), while for smaller potential strengths they are limited to a certain range of magnetic field values (plots (c) and (d)).

6.1.3 2D $\rho_{xx}^{(0)}(\Omega)$ for $\bar{V} < 0$

In this subsection, we present the numerical results for the longitudinal resistivities $\rho_{xx}^{(0)}(\Omega)$ for a two-dimensional electrostatic modulation potential with various strengths. As the modulation potential is symmetric with respect to the x and y directions, the longitudinal conductivity is obtained from a modified form of equation (5.18) in which the symmetry of the conductivity tensor is used ($L_{xx}^{(0)}(\Omega) = \text{Ł}_{yy}^{(0)}(\Omega)$).

In Figures 6.8 and 6.9, the values of the longitudinal resistivity are shown for four different values of the 2D modulation potential amplitude, and for four values of the frequency of the radiation field for each of the plots. The four plots share a common feature: for low values of the magnetic field, the longitudinal resistivity shows a large peak.

Another interesting feature of the graphs, which is evident especially in Figures 6.8 (a) and (b), obtained for the largest strengths of the modulation potential ($\bar{V} = -100.235$ for (a) and $\bar{V} = -80.235$ for (b)) is that the value of the longitudinal resistivity is decreasing with an increase of the magnetic field. Also in these two figures, it can be seen that most of the values of the longitudinal resistivity are negative, which means that we are dealing with negative resistance states (NRS) which in the past few years became the topic of intense theoretical and experimental research.

Although these states were not yet found experimentally, their existence is ex-

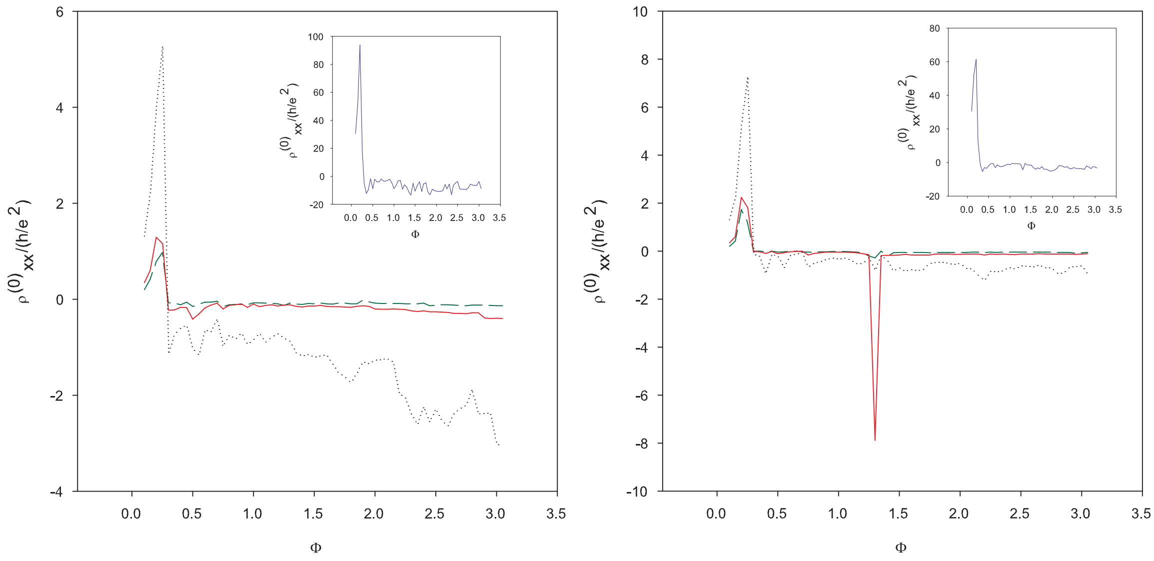

(a) (b)

Figure 6.8: Longitudinal resistivities for different values of the frequency of the radiation field and two values of the modulation potential strength. The large dashed (green) line corresponds to those values of the frequency for which $\hbar\Omega = 0.25E_F$, the solid (red) line corresponds to $\hbar\Omega = 0.5E_F$, the dotted (black) line corresponds to $\hbar\Omega = E_F$, while the inset (blue line) is for $\hbar\Omega = 1.5E_F$. Other parameters used in the figure are sample size $N_x = N_y = 10$, 2D modulation potential strength $\bar{V} = -100.235$ for (a) and $\bar{V} = -80.235$ for (b). The exponent of the periodic term $N = 10$, while $n = 5$, $m = 3$, and electron density $n_{2D}a^2 = 1.0$.

plained theoretically by several different mechanisms. One mechanism is disorder assisted absorption and emission of the incident electromagnetic radiation, which means that the NRS are caused by an impurity scattering mechanism [50]. Another possible mechanism leading to the appearance of a negative resistivity is resonant scattering of electrons from coherent rebounding orbits. For the values of the magnetic field for which resonant scattering occurs, the net scattering force overcomes the Lorentz force, producing a negative Hall voltage [49].

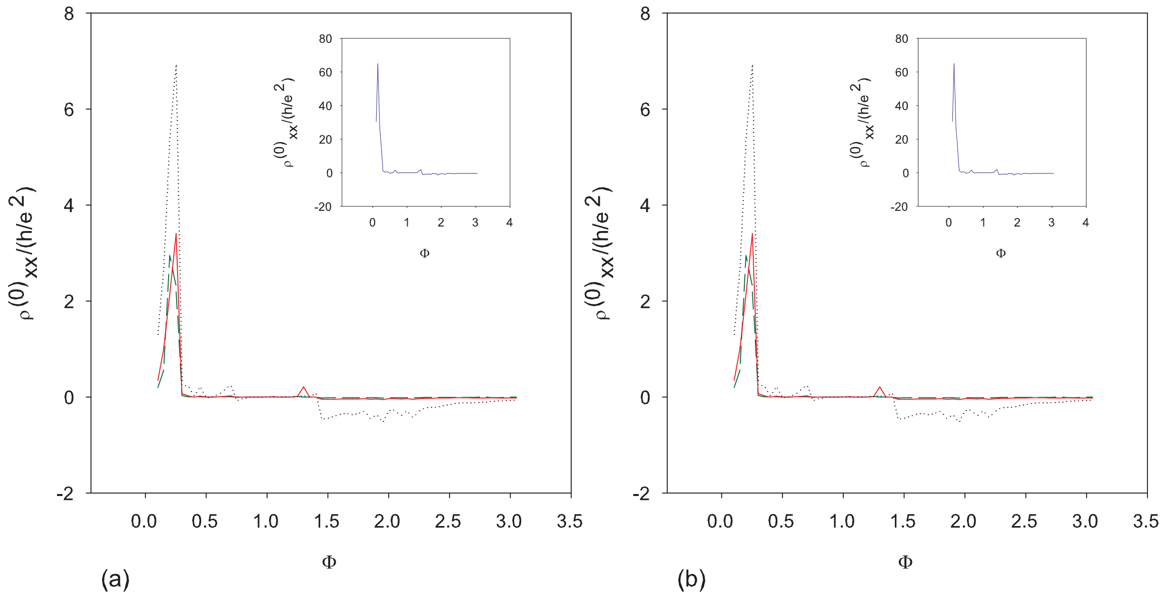

Figure 6.9: Longitudinal resistivities for different values of the frequency of the radiation field and two values of the 2D modulation potential strength. The large dashed (green) line corresponds to those values of the frequency for which $\hbar\Omega = 0.25E_F$, the solid (red) line corresponds to $\hbar\Omega = 0.5E_F$, the dotted (black) line corresponds to $\hbar\Omega = E_F$, while the inset (blue line) is for $\hbar\Omega = 1.5E_F$. Other parameters used in the figure are sample size $N_x = N_y = 10$, modulation potential strength $\bar{V} = -60.235$ for (a) and $\bar{V} = -40.235$ for (b). The exponent of the periodic term $N = 10$, while $n = 5$, $m = 3$, and electron density $n_{2D}a^2 = 1.0$.

6.1.4 2D $\rho^{(0)}_{xy}(\Omega)$ for $\bar{V} < 0$

Figure 6.10 shows the variation of the Hall resistivity for two different values of the 2D modulation potential $\bar{V} = -100.235$ and $\bar{V} = -80.235$ for 2D negative electrostatic modulation. These Hall resistivities corresponding to the negative 2D electrostatic modulation also show large amplitude negative oscillations corresponding to negative resistance states. The amplitudes of oscillation are now larger for the largest value of the external radiation frequency, $\Omega = E_F/\hbar$ (green long dashed line in the figures). This is opposite of the behavior seen in the case of the conductances (which had larger oscillations for the smaller value $\Omega = 0.5E_F\hbar$). This is a reasonable behavior of the resistivity, considering that its values are obtained by performing the inversion of the conductivity matrix. Thus if the values of the conductivity decrease when the frequency of the applied radiation increases, then the resistivities should increase when the frequency increases.

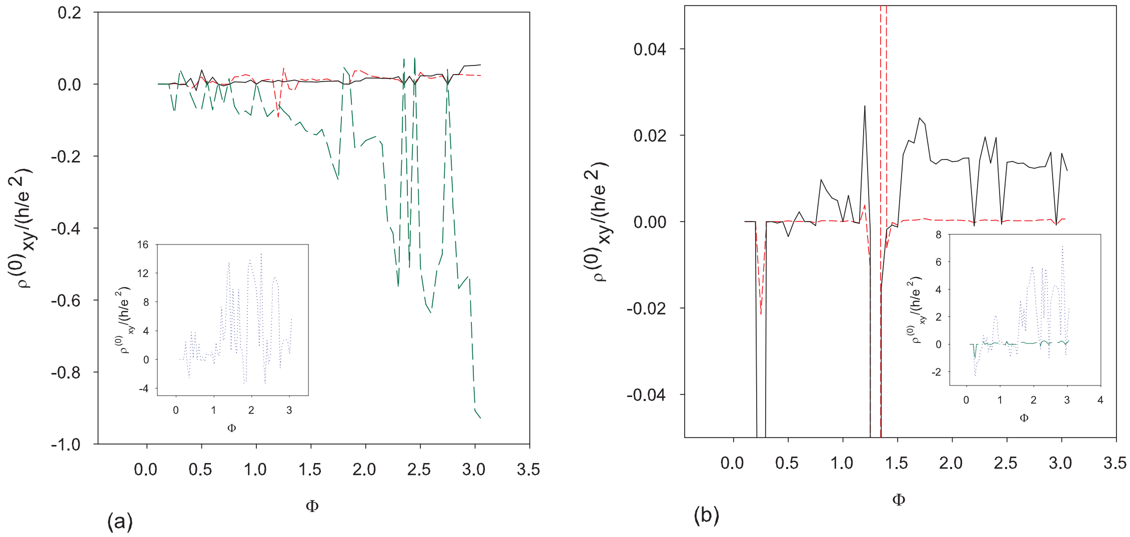

Figure 6.10: Hall resistivities for different values of the frequency of the radiation field and two negative values of the 2D modulation potential. The short dashed (red) line corresponds to those values of the frequency for which $\hbar\Omega = 0.25E_F$, the solid (black) line corresponds to $\hbar\Omega = 0.5E_F$, the long dashed (green) line corresponds to $\hbar\Omega = E_F$, while the dotted (blue) line is for $\hbar\Omega = 1.5E_F$. Other parameters used in the figure are sample size $N_x = N_y = 10$, modulation potential strength $\bar{V} = -100.235$ for (a) and $\bar{V} = -80.235$ for (b). The exponent of the periodic term $N = 10$, while $n = 5$, $m = 3$, and electron density $n_{2D}a^2 = 1.0$.

6.1.5 2D $L^{(0)}_{xx}(\Omega)$ for $\bar{V} > 0$

The scattering mechanism for the case of the positive electrostatic modulation is different than in the case when $\bar{V} < 0$. This is because when $\bar{V}$ is large, the potential peaks may only scatter electrons, there is no possibility for electrons to be "captured", as it was the case discussed in the case of negative $\bar{V}$. In the beginning of this subsection we present a series of longitudinal conductivity graphs in the presence of a radiation field, and compare them to those obtained for the zero frequency limit (no

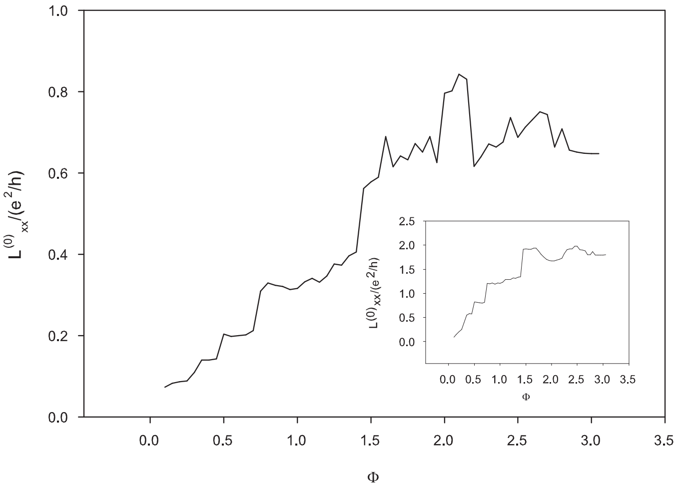

Figure 6.11: Longitudinal conductivity with and without (inset) radiation field for positive 2D electrostatic modulation. Sample size $N_x = N_y = 10$, modulation potential strength $\bar{V} = 60.235$, while its exponent $N = 10$. Other parameters used are $n = 5$, $m = 3$, electron density $n_{2D}a^2 = 1.0$. For the frequency of the radiation the value $\hbar\Omega = E_F$ was used.

radiation field). In Figure 6.11, the result of a longitudinal conductivity calculation for a strong negative 2D electrostatic potential is presented. The strength of the modulation potential is again chosen much larger than the highest value of the Fermi energy (about three times as large) in the plot, as we are interested in the oscillations introduced in the magnetotransport coefficients by the scattering potential, and want to avoid any influence on the magnetotransport coefficients introduced by changes in the electron density due to the variation of the magnetic field. Figure 6.11 illustrates that unlike the Hall conductance of the negative 2D electrostatic modulation potential, those corresponding to positive potential do not show a qualitative change in the presence of the radiation as compared to the zero frequency case which is shown in the inset, but the magnitude of the conductivity is reduced when $\Omega \neq 0$.

The shape of the two curves is similar, the main difference between them being that the order of magnitude of the conductance is reduced in the presence of the

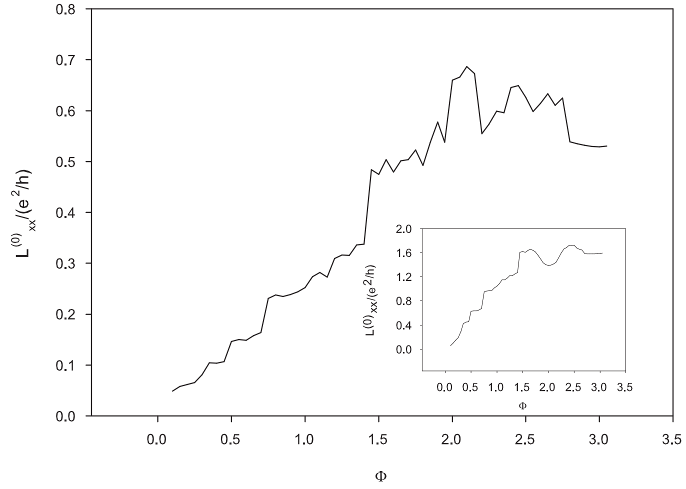

Figure 6.12: Longitudinal conductivity with and without (inset) radiation field for positive 2D electrostatic potential. Sample size $N_x = N_y = 10$, modulation potential strength $\bar{V} = 80.235$, while its exponent $N = 10$. Other parameters used are $n = 5$, $m = 3$, electron density $n_{2D}a^2 = 1.0$. For the frequency of the radiation the value $\hbar\Omega = E_F$ was used.

radiation. This is expected (as it was also mentioned in the case of the quantum dot type scatterers), as the longitudinal conductivity formula has a multiplicative factor which is inversely proportional to the applied radiation field frequency, as it can be seen in equation (5.11). In the large magnetic field region (second half of the Φ axis in the figure) the frequency dependent conductivity shows a series of oscillations, which are absent in the zero frequency case. These oscillations of the longitudinal conductivity for large values of the magnetic field are a general characteristic of the magnetoconductivity of antidots in the presence of radiation, as similar behavior can be observed for other values of the modulation potential. To illustrate this point we also show the longitudinal conductivity plot obtained for a larger value of the 2D modulation potential in Figure (6.12), which was obtained for $\bar{V} = 100.235$. In this figure, the conductivity plot in the presence of radiation has almost identical shape with that obtained without radiation up to the value of $\Phi = 1.5$. After this value

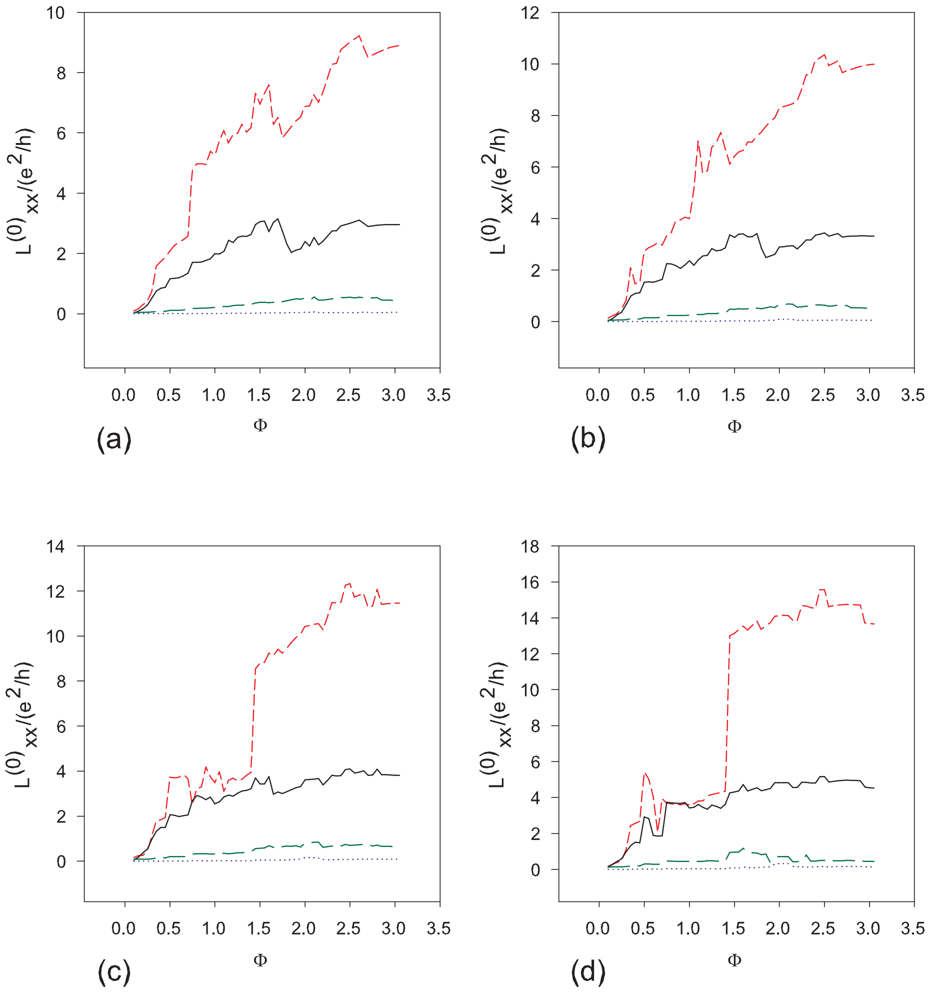

Figure 6.13: Longitudinal conductivity for different values of the frequency of the radiation field for the positive 2D electrostatic potential. The short dashed (red) line corresponds to those values of the frequency for which $\hbar\Omega = 0.25E_F$, the solid (black) line corresponds to $\hbar\Omega = 0.5E_F$, the long dashed (green) line is drawn for $\hbar\Omega = E_F$, while the dotted (blue) line is for $\hbar\Omega = 1.5E_F$. Other parameters used in the figure are sample size $N_x = N_y = 10$, modulation potential strength $\bar{V} = 100.235$ for (a), $\bar{V} = 80.235$ for (b), $\bar{V} = 60.235$ for (c), and $\bar{V} = 40.235$ for (d). The exponent of the periodic term $N = 10$, $n = 5$, $m = 3$, electron density $n_{2D}a^2 = 1.0$.

of the flux ratio is exceeded, the longitudinal conductivity in the presence of the finite frequency radiation shows oscillations which cannot be seen in the absence of radiation. At high magnetic fields the cyclotron radius of the electron is small, so it is less likely that it would undergo scattering. Thus the oscillatory effect must be due to the applied radiation field. The two presented graphs illustrate this well. However, for positive values of the modulation potential no negative resistivity states arise. To support this argument we also present four plots of the longitudinal conductivity of the antidot type scatterers obtained for four different values of the radiation field frequency. The four plots displayed in Figure 6.13, were obtained for the following values of the incident radiation frequency. In all of the plots the longitudinal conductivity shows an increase with the increase of the applied magnetic field. Therefore there are no negative values taken by the longitudinal conductivity of the antidots. Similar to the longitudinal conductivity of the quantum dots, the plots corresponding to larger values of the radiation frequency show lower amplitude oscillations than those obtained for lower values, and this is due to the multiplicative factor present in the formula of the longitudinal conductivity, which is inversely proportional to the frequency of the applied radiation field (equation (5.11)). In Figure 6.13, the short dashed (red) line is drawn for the incident radiation frequency taking the value of $\Omega = 0.25E_F/\hbar$, the solid (black) line corresponds to $\Omega = 0.5E_F/\hbar$, the long dashed (green) line is drawn for frequency values of $\Omega = E_F/\hbar$, while the dotted (blue) line is obtained when the frequency is $\Omega = 1.5E_F/\hbar$.

6.1.6 2D $L_{yx}^{(0)}(\Omega)$ for $\bar{V} > 0$

The Hall conductivity coefficients for the positive 2D modulation potential show some interesting features. For lower values of the modulation potential ($\bar{V} = 20.235$ and

$\bar{V} = 40.235$) their value becomes negative for a small portion the applied magnetic field. For both of the potentials mentioned above, the sudden drop in magnetoconductivity occurs for the same range of Φ around the value 2.0, the explanation for their occurrence is quenching. The cause is the formation of collimated states when electrons are backscattering off the lattice sites when the cyclotron orbit and potential period become commensurate (see Figures 6.15 and 6.14). This means that the electron's orbit diameter becomes equal to the spacing of scatterers, and electrons can undergo backward scattering off the potential peaks leading to negative values of the conductivity coefficients. In this case the effect of the Lorentz force is overcome by the backward scattering effect. For the smaller values of the potential the effect is not as pronounced as for the higher values, as higher potential strengths are more likely to cause backward scattering as illustrated in Figures 6.14 (a) and 6.15 (a), then lower potential values such as those of Figures 6.14 (b) and 6.15 (b).

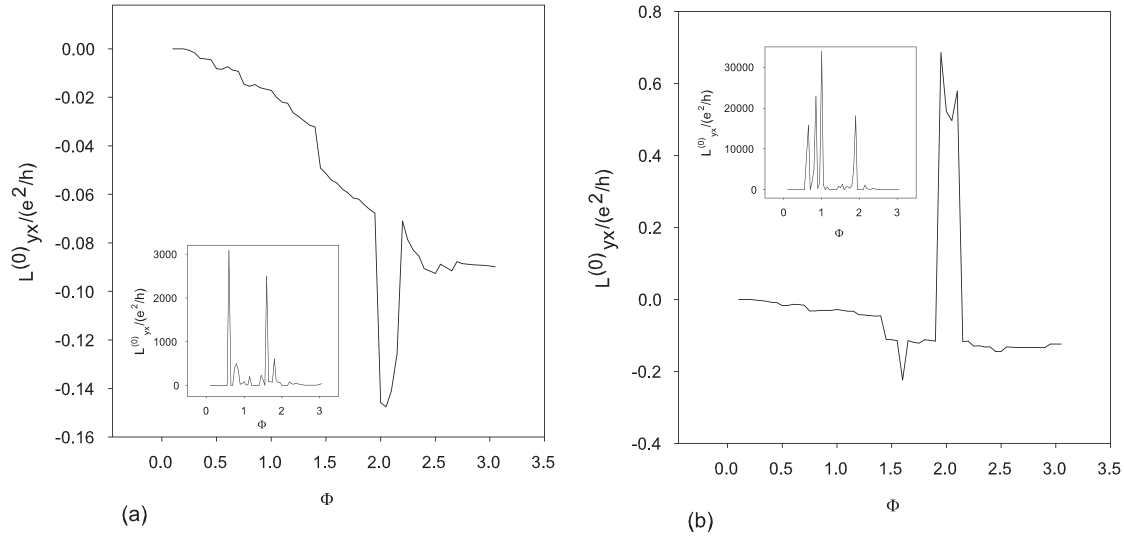

Figure 6.14: Hall conductivity with and without (inset) radiation field for positive 2D electrostatic potential. Sample size $N_x = N_y = 10$, modulation potential strength $\bar{V} = 80.235$ in (a) and $\bar{V} = 40.235$ in (b), while its exponent $N = 10$. Other parameters used are $n = 5$, $m = 3$, electron density $n_{2D}a^2 = 1.0$. For the frequency of the radiation the value $\hbar\Omega = E_F$ was used. The graphs in the insets are obtained for the same parameters, but correspond to the case of no applied radiation.

When the strength of the modulation potential is lower ($\bar{V} = 20.235$ and $\bar{V} = 40.235$) the negative dip in tranverse conductivity disappears, and instead a large amplitude positive "jump" occurs at roughly the same values of the applied magnetic field (see Figures 6.14 (b) and 6.15 (b)).

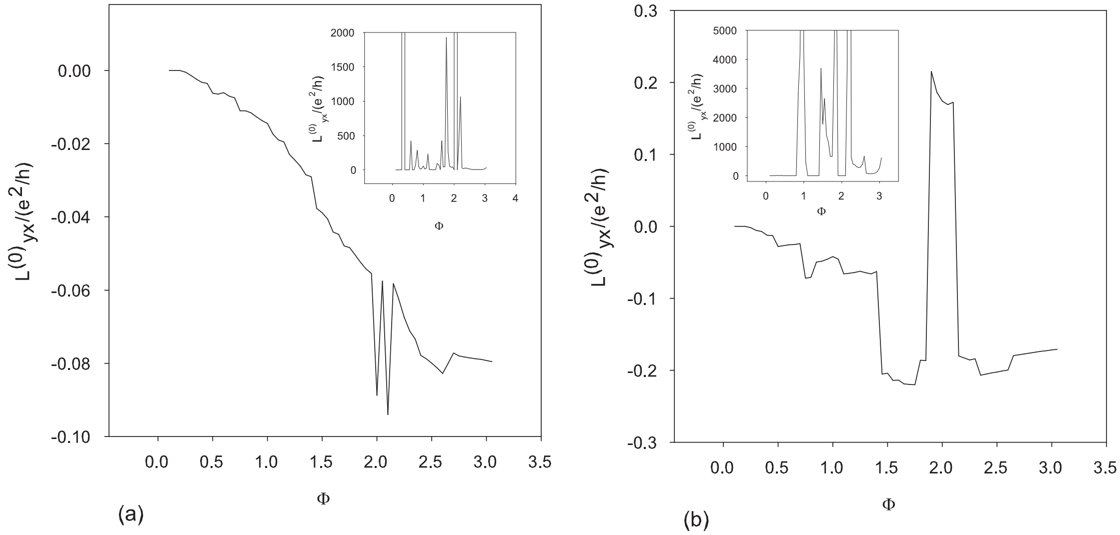

Figure 6.15: Hall conductivity with and without (inset) radiation field for positive 2D electrostatic modulation potential. Sample size $N_x = N_y = 10$, modulation potential strength $\bar{V} = 100.235$ in (a) and $\bar{V} = 20.235$ in (b), while its exponent $N = 10$. Other parameters used are $n = 5$, $m = 3$, electron density $n_{2D}a^2 = 1.0$. For the frequency of the radiation the value $\hbar\Omega = E_F$ was used. The graphs in the insets are obtained for the same parameters, but correspond to the case of no applied radiation.

The four plots of tranverse conductivity for the positive 2D electrostatic modulation potential illustrate that the presence of radiation has an important effect on these conduction coefficients, as the shape of the plots in the presence of radiation is quite different from those obtained in the dark and shown in the insets.

In the final part of this subsection, we present a series of plots showing the dependence of the Hall conductivity for positive 2D electrostatic modulation potential with respect to the variation of the strength of the potential and for four different values of the incident radiation frequency. For the smallest value of the incident radiation

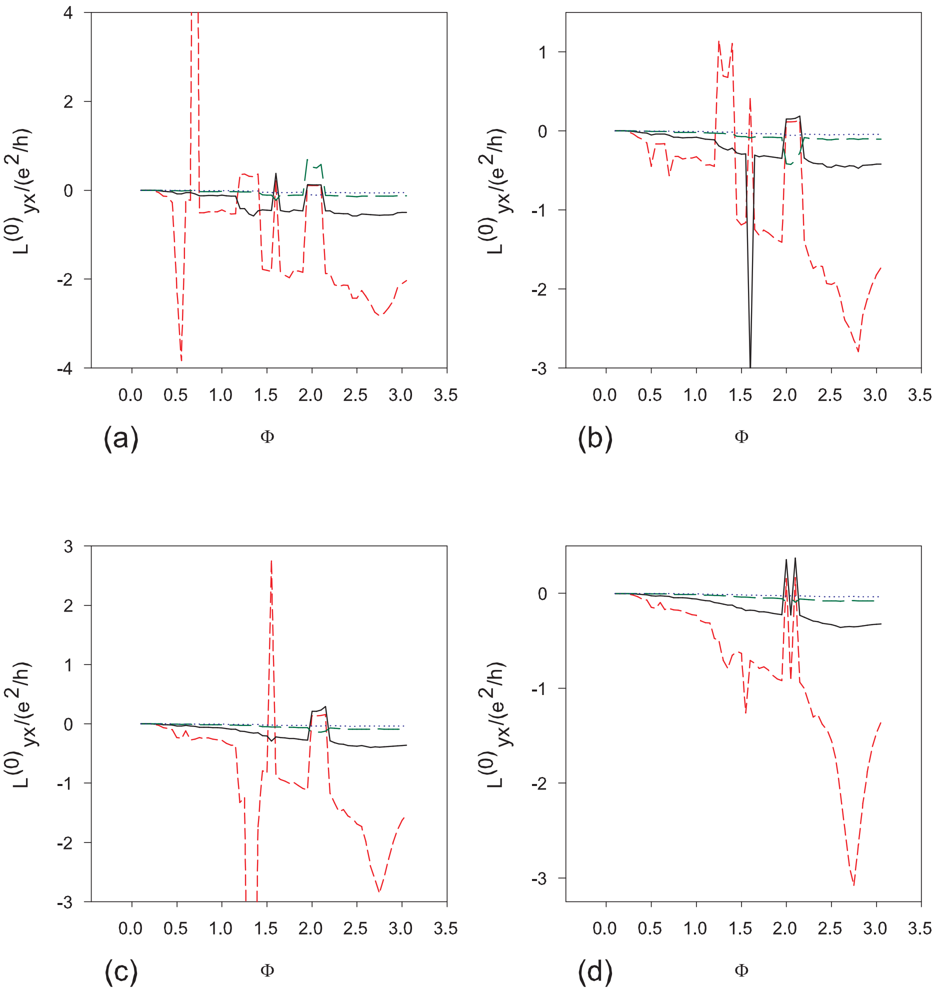

Figure 6.16: Hall conductivity for four different values of the incident radiation frequency for positive 2D electrostatic modulation potential. The short dashed (red) line corresponds to those values of the frequency for which $\hbar\Omega = 0.25E_F$, the solid (black) line corresponds to $\hbar\Omega = 0.5E_F$, the long dashed (green) line corresponds to frequencies for which $\hbar\Omega = E_F$, and the dotted (blue) line corresponds to the frequencies for which $\hbar\Omega = 1.5E_F$. Other parameters used in the figure are sample size $N_x = N_y = 10$, modulation potential strength $\bar{V} = 40.235$ for (a), $\bar{V} = 60.235$ for (b), $\bar{V} = 80.235$ for (c), and $\bar{V} = 100.235$ for (d). The exponent of the periodic term $N = 10$, $n = 5$, $m = 3$, electron density $n_{2D}a^2 = 1.0$.

frequency, $\Omega = 0.25E_F/\hbar$ (short dashed red line in the Figure) the tranverse magnetoconductivity shows the largest negative values and the largest amplitude positive to negative oscillations. As the frequency increases the amplitude of the oscillations decreases just as it did in the quantum dot case. For the larger values of the radiation frequency ($\Omega = E_F/\hbar$ and $\Omega = 1.5E_F/\hbar$) the amplitude of the oscillations is diminished.

6.1.7 2D $\rho_{xx}^{(0)}(\Omega)$ for $\bar{V} > 0$

Figure 6.17 shows the variation of the longitudinal resistivity for positive modulation potential strengths. As it can be seen from the Figure there are no negative oscillations observed in the longitudinal resistivity for positive values of the modulation potential.

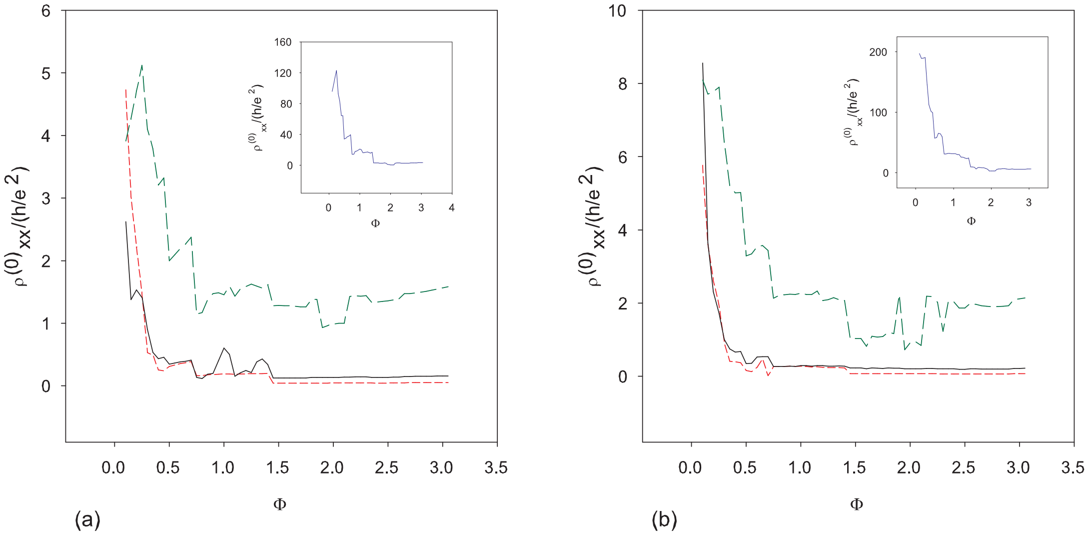

Figure 6.17: Longitudinal resistivity for four values of the incident radiation frequency for positive 2D electrostatic modulation potential. The short dashed (red) line corresponds to those values of the frequency for which $\hbar\Omega = 0.25E_F$, the solid (black) line to $\hbar\Omega = 0.5E_F$, the long dashed (green) line is for $\hbar\Omega = E_F$, while the inset (blue line) corresponds to $\hbar\Omega = 1.5E_F$. Sample size $N_x = N_y = 10$, modulation potential strength $\bar{V} = 20.235$ in plot (a), $\bar{V} = 40.235$ in plot (b), while the exponent of the periodic term in the potential $N = 10$. Other parameters used are $n = 5$, $m = 3$, and electron density $n_{2D}a^2 = 1.0$.

When the frequency of the applied radiation field increases, the magnitude of the resistivity decreases. In Figure 6.17, the short dashed (red) line corresponds to the value $\Omega = 0.25E_F/\hbar$ of the frequency, the solid (black) line corresponds to $\Omega = 0.5E_F/\hbar$, the green (long dashed) line is for $\Omega = E_F/\hbar$, and the inset (blue line) corresponds to the frequency of $\Omega = 1.5E_F/\hbar$. For the smaller values of the radiation frequency and for large magnetic fields, the longitudinal resistivity becomes a constant, which is in good agreement with the classical result. In the left-hand portion of the graphs, corresponding to small values of the applied magnetic field however, large-amplitude oscillations are observed. This feature is not only found in the present work, as other conductivity calculations also led to these so-called “giant low field magnetoresistance oscillations”. These magnetoresistance oscillations also appeared in the longitudinal resistivity for the quantum dots presented earlier, where it was explained to be a result of the scattering of the electrons off the sample boundaries for small magnetic fields, for which the electrons perform large radius cyclotron motion.

6.1.8 2D $\rho_{xy}^{(0)}(\Omega)$ for $\bar{V} > 0$

Finally, in the conclusion of the part discussing the 2D magnetotransport properties, we present plots of the Hall resistivity for the positive 2D electrostatic modulation potential. A total of four plots are shown to demonstrate the dependence of the resistivity on the modulation potential amplitude and the frequency of the incident radiation. Figure 6.18 (a) corresponds to the smallest value of $\bar{V} = 20.235$, followed by Figure 6.18 (b) with $\bar{V} = 40.235$. Then Figure 6.19 (a) presents the variation of the Hall resistivity for $\bar{V} = 60.235$, and finally Figure 6.19 (b) is for $\bar{V} = 80.235$.

It can be seen that the change of the strength of the modulation potential has a

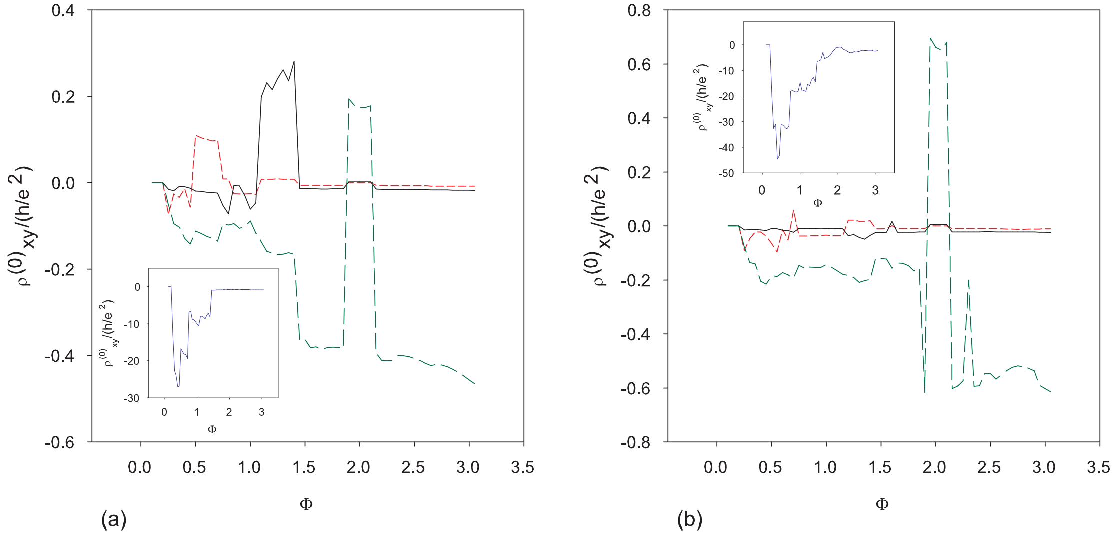

Figure 6.18: Hall resistivity for four values of the incident radiation frequency for positive 2D electrostatic modulation potential. The short dashed (red) line corresponds to those values of the frequency for which $\hbar\Omega = 0.25E_F$, the solid (black) line to $\hbar\Omega = 0.5E_F$, the long dashed (green) line is for $\hbar\Omega = E_F$, while the inset (blue line) corresponds to $\hbar\Omega = 1.5E_F$. Sample size $N_x = N_y = 10$, modulation potential strength $\bar{V} = 20.235$ in plot (a), $\bar{V} = 40.235$ in plot (b), while the exponent of the periodic term in the potential $N = 10$. Other parameters used are $n = 5$, $m = 3$, and electron density $n_{2D}a^2 = 1.0$.

strong influence on the range of values taken by the Hall resistance. Although the highest positive values attained are of the same order of magnitude, the lowest negative values strongly depend on the value taken by the modulation potential strength, and especially by the frequency of the incoming radiation. The largest negative oscillations correspond to the lowest value of the applied field frequency. These negative values appear mostly in the low magnetic field regime. The Hall magnetoresistivity is quenched at high magnetic fields. In Figures 6.18 and 6.19, the short dashed (red) line corresponds to frequency values of $\Omega = 0.25E_F/\hbar$, the solid (black) line corresponds to $\Omega = 0.5E_F/\hbar$, the long dashed (green) line is for $\Omega = E_F/\hbar$, while the inset (blue line) corresponds to $\Omega = 1.5E_F/\hbar$.

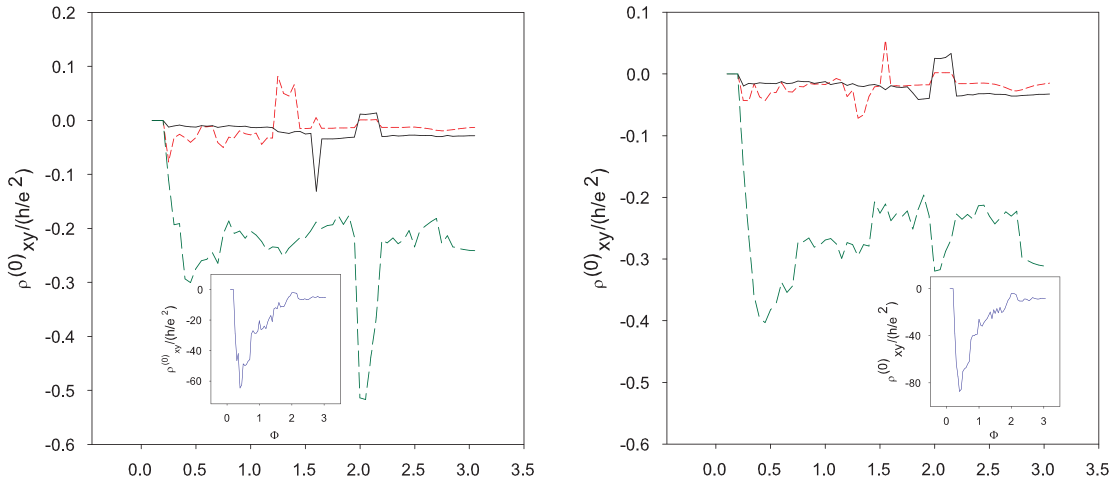

(a) (b)

Figure 6.19: Hall resistivity for four values of the incident radiation frequency for positive 2D electrostatic modulation potential. The short dashed (red) line corresponds to those values of the frequency for which $\hbar\Omega = 0.25E_F$, the solid (black) line to $\hbar\Omega = 0.5E_F$, the long dashed (green) line is for $\hbar\Omega = E_F$, while the inset (blue line) corresponds to $\hbar\Omega = 1.5E_F$. Sample size $N_x = N_y = 10$, modulation potential strength $\bar{V} = 60.235$ in plot (a), $\bar{V} = 80.235$ in plot (b), while the exponent of the periodic term in the potential $N = 10$. Other parameters used are $n = 5$, $m = 3$, and electron density $n_{2D}a^2 = 1.0$.

6.1.9 AC versus DC Magnetotransport with 2D Modulation. Comparison of Results.

The problem of DC magnetotransport with periodic 2D electrostatic modulation was the topic of the dissertation published less then ten years ago by a former graduate student of my adviser, Professor Godfrey Gumbs, by the name of Tae-ik Park.[59] In his dissertation, Park investigated the quantum magnetotransport coefficients of a 2DEG in a perpendicular magnetic field for positive and negative, 1D and 2D periodic electrostatic modulation using potentials of the same form as those used in this work. At the end of this chapter it seems appropriate to compare results obtained by Park in the absence of radiation to the results obtained for finite frequency magnetotransport. The main features of the magnetoresistivity coefficients obtained by Park for the 2D periodic modulation potential are:

-Oscillations in $L_{xx}^{(0)}(0)$ and $L_{yx}^{(0)}(0)$ which are associated with the filling of the Landau levels for low periodic modulation potential strengths.

-Distinct behavior of the longitudinal and Hall magnetotransport coefficients for positive and negative values of the periodic modulation potential strength. This is attributed to different scattering mechanisms for positive and negative modulation potential strengths.

-A double-peak feature in the longitudinal resistivity for large, positive periodic modulation potential strengths.

-Negative values and quenching of the Hall resistivity for positive and negative modulation potentials.

-Large positive to negative oscillations in the longitudinal and Hall resistivities for strong positive periodic modulation potentials.

In his dissertation, Park focused attention on determining how the magnetotransport coefficients for different periodic modulation potentials investigated are influenced by the potential strength as well as the steepness of the potential walls determined by the power of the cosine terms in equations (2.4) and (2.5). The focus of the current project is different, since it seeks to determine the influence of incident radiation on magnetotransport coefficients (i.e. the role played by radiation of different frequencies). Nevertheless, some comparisons can be made.

In accord with the results of Park, distinct behavior of the longitudinal conductivities was found for positive versus negative periodic modulation potential strengths in the absence of radiation. For positive modulation strengths, and no irradiation, the longitudinal conductivity shows small amplitude positive oscillations, and there is an increase in longitudinal conductivity values for increasing magnetic fields. The longitudinal conductivity for negative modulation potential strengths and no irradiation behaves differently. It is quenched for very low values of the magnetic field, then shows large amplitude positive oscillations in the intermediate magnetic field region, returning to homogeneous 2DEG behavior for large values of the magnetic field.

In the presence of finite frequency radiation, and for positive modulation potential strengths the longitudinal conductivity also shows small amplitude positive oscillations. There is also an increase in longitudinal conductivity values as the magnetic field increases. Also for positive modulation potential strengths, the smaller the values of the incident radiation frequency, the larger the values attained by the longitudinal conductivity for the same magnetic field and modulation potential strength. For the largest values of positive modulation potential strengths investigated, the increase in longitudinal conductivity is 15-fold for a 6-fold increase of the irradiation frequency. There is a remarkable difference between the behavior of the longitudinal conductivity for large negative values of the modulation potential strength with and without radiation. In the presence of radiation, the longitudinal conductivity becomes negative for large negative modulation potential strengths, and it shown large amplitude negative oscillations, while in the absence of radiation the longitudinal conductivity stays positive, and it displays positive oscillations. For the same magnetic field and modulation potential strengths, the AC longitudinal conductivity for negative modulation potentials also takes larger absolute values for smaller values of the incident radiation frequency. (In this case the actual values are negative.)

The Hall conductivity also shows different behavior in the absence of irradiation for positive and negative modulation potential strengths. For positive modulation potentials and no irradiation the Hall conductivity shows giant positive oscillations, while for negative modulation potential strengths the giant oscillations are negative.

In the presence of finite frequency radiation there is a drastic reduction in the size of oscillations of the Hall magnetoconductivity. For the lowest modulation potential strength the double peak feature is observed in the Hall conductivity for positive modulation potential strengths. Also for small positive modulation potential strengths the Hall conductivity becomes negative. This negative Hall conductivity is due to resonant scattering of electrons forming coherent rebounding orbits. In this case, the scattering force becomes stronger than the Lorentz force, which leads to a negative Hall voltage. For larger positive modulation strengths the negative Hall conductivity shows large amplitude positive oscillations in the high magnetic field region. In the case of positive modulation potential strengths, the Hall conductivity becomes positive in the presence of irradiation and it shows positive oscillations. For certain values of the magnetic field a few large amplitude, negative oscillations appear. As for the influence of the frequency of the incident radiation, for the same magnetic field and modulation potential strengths, the Hall conductivity shows larger absolute values for both negative and positive modulation potential strengths, when the frequency of the incident radiation is lower.

As far as the 2D longitudinal and Hall resistivities are concerned, there are several features of these magnetotransport coefficients that may be compared in the AC and DC case. The longitudinal resistivity for negative 2D modulation takes large values for small magnetic fields both in the AC and DC case. As the magnetic field increases, the longitudinal resistivity values decrease drastically in both cases. In the presence of radiation, and especially for strong modulation potential strengths, the longitudinal resistivity becomes negative, and it shows oscillations. As the modulation potential decreases, the amplitude of these negative oscillations decreases. The Hall resistivity in the negative modulation case also shows negative oscillations. The negativity of the Hall resistivity is explained by the net scattering force by the potential overcoming the magnetic force, and leading to the appearance of a negative Hall voltage.

For the positive 2D modulation case, the longitudinal resistivity shows similar characteristics as for the negative modulation case. It takes large values for small magnetic fields, and it decreases as the magnetic field decreases. In the presence of radiation, the values of the longitudinal resistivity are increased. The larger the frequency of the incident radiation, the higher the values taken by the longitudinal resistivity. The Hall resistivity for positive 2D modulation takes giant negative values for high values of the incident radiation frequency, and for low magnetic field values.

Chapter 7

Effect of 1D Modulation and Finite Frequency on Magnetotransport

Historically, successes attained in understanding the magnetotransport properties of 2D heterostructures with periodic modulation prompted to the application of the technique to reducing the dimensionality of such heterostructures to 1D, resulting in systems known as quantum wires (QW), or quantum antiwires (AW). The low magnetic field conductance of ideal QWs was shown to be quantized, and equal to e^2/h times the number of current-carrying channels [60]. The conductance of realistic QWs deviates from the ideal behavior. One reason for this is that real QW are not infinitely long, thus they do not have perfect translational symmetry. Real QWs operate in different regimes determined by their dimensions and parameters, such as their length, width and the elastic mean free path of charge carriers in the conduction channel(s). When the width of a QW is comparable, or larger than the mean free path, charge carriers do not "see" the wire as being one-dimensional. The conduction regime in this case will be similar to that observed in a weakly 2D modulated 2DEG. In the opposite limit, when the width of the wire is much less than the mean free path, charge carriers are affected by the boundaries of the QW, and quantum states extending from one end of the wire to the other will appear. These quantum channels carry current from one end of the wire to the other, resulting in ballistic transport. The electrical resistance of such wires loses its classical meaning, as they act as waveguides for charge carriers in the conduction channel. The electrical resistivity of these structures due to scattering by atoms or impurities will become unimportant. Their transport properties are mainly dependent on the boundary conditions, therefore transport in such conductors strongly depends on sample geometry [61]. Some of the interesting features of this ballistic conduction regime in 1D are the quenching of the transverse conductivity at low magnetic fields, and the occurrence of negative transverse resistivity states [61]-[66].

7.1 1D Magnetoresistance

We now present numerical results for the longitudinal, transverse, and Hall QMT coefficients for 1D modulation in the x direction. The theoretical part of the calculation is presented starting with Section 5.2. The main difference between the cases of 1D and 2D modulation is that for 2D modulation potentials there is a symmetry between the x and y directions, because the potential is symmetric. In the 1D case, however, choosing the modulation potential along the x-direction breaks this symmetry. Thus we will present numerical results for the following conduction coefficients: transverse conductivities, $L_{xx}^{(0)}$, along the modulation direction, Hall conductivities, $L_{yx}^{(0)}$, longitudinal conductivities, $L_{yy}^{(0)}$, along the quantum wire channel, transverse resistivities, $\rho_{xx}^{(0)}$, along the modulation potential, Hall resistivities, $\rho_{xy}^{(0)}$, and longitudinal conductivities, $\sigma_{yy}^{(0)}$, along the QW.

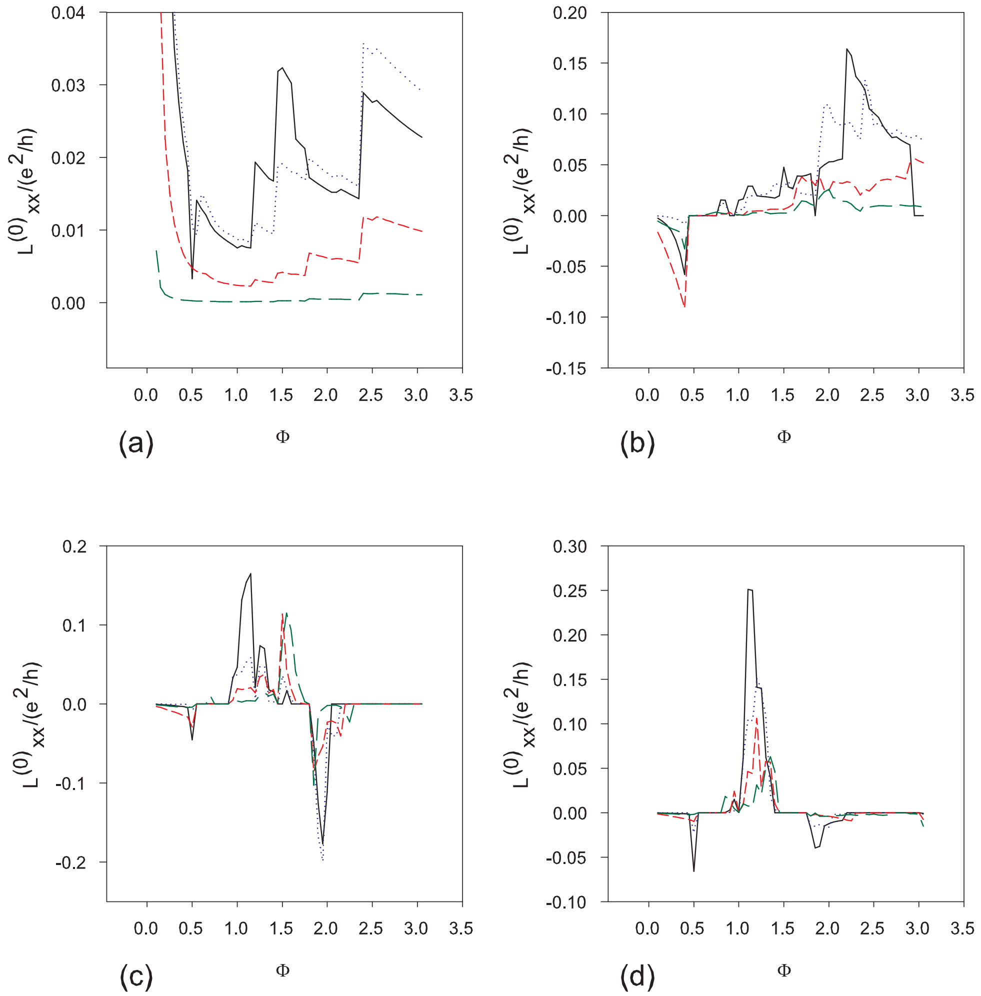

Figure 7.1: Transverse conductivities, L_{xx}, for several negative values of the 1D modulation potential and different frequencies of the incident radiation field. The solid (black) line corresponds to those values of the frequency for which $\hbar\Omega = 0.25E_F$, the dotted (blue) line corresponds to $\hbar\Omega = 0.5E_F$, the short dashed (red) line corresponds to $\hbar\Omega = E_F$, while the long dashed (green) line is for $\hbar\Omega = 1.5E_F$. Other parameters used in this Figure are sample size $N_x = N_y = 10$, modulation potential strength $\bar{V} = -0.235$ for (a), $\bar{V} = -3.235$ for (b), $\bar{V} = -7.235$ for (c), and $\bar{V} = -10.235$ for (d). Exponent of the periodic term $N = 10$, $n = 6$, and electron density $n_{2D}a^2 = 0.75$.

7.1.1 1D $L_{xx}^{(0)}(\Omega)$ for $\bar{V} < 0$

Figure 7.1 presents numerical results obtained for the transverse conductivities, $L_{xx}^{(0)}(\Omega)$, for four different, negative values of the 1D modulation potential. A wide range of modulation potential values was investigated to show the difference between the influence of incident radiation on a weakly modulated 2DEG (corresponding to the potential strength of $\bar{V} = -0.235$) all the way to the strong modulation case ($\bar{V} = -10.235$). We know that the latter potential strength corresponds to strong modulation because in Chapter 3, where the eigenvalue spectrum was investigated, strong mixing of the Landau bands was obtained for this value of the 1D potential, which is an indication of strong modulation. Each one of the graphs contains four plots obtained for different values of the incident radiation frequency. In all of the graphs of this Chapter a solid (black) line corresponds to those values of the incident radiation frequency for which $\hbar\Omega = 0.25E_F$, a dotted (blue) line corresponds to frequencies for which $\hbar\Omega = 0.5E_F$, a short dashed (red) line corresponds to $\hbar\Omega = E_F$, while a long dashed (green) line is used for those values of the frequency for which $\hbar\Omega = 1.5E_F$. Also in all of the graphs presented for the 1D modulation case the electron density used was $n_{2D}a^2 = 0.75$.

Figure 7.1 (a), which is obtained for the lowest absolute value of the modulation potential strength, has a different shape than the other three plots presented on the same Figure ((b), (c) and (d)). Namely, the transverse conductivity takes higher values in the low magnetic field region, and it monotonically decreases as the magnetic field is increased to a value of about $\Phi = 1.0$. This is the same behavior of the transverse conductivity as shown by the one-dimensionally modulated 2DEG in the absence of radiation [59]. The similarity with the zero frequency case is most pronounced for the incident radiation frequency value of $\Omega = 1.5E_F/\hbar$. As the magnetic field further increases, the finite frequency transverse conductivity deviates from the zero frequency behavior. As the magnetic field increases to values higher than $\Phi = 1.0$, $L_{xx}^{(0)}(\Omega)$ starts increasing, and then decreasing again, through a series of steps. The lower the frequency of the incident radiation, the higher the magnitude of these steps. For the next value of the modulation potential of $\bar{V} = -3.235$ that is presented in Figure 7.1 (b), the transverse conductivity plots have a different shape than those seen in Figure (a). In the low magnetic field region $L_{xx}^{(0)}(\Omega)$ starts from negative values, reaching a minimum and then it increases, going through a series of positive oscillations. In the large magnetic field region the oscillations have the largest amplitude. In the other two plots of Figure 7.1 (corresponding to the strong modulation case as $\bar{V} = -7.235$ in (c) and $\bar{V} = -10.235$ in (d)) the transverse conductivity shows yet a different behavior. For low magnetic fields $L_{xx}^{(0)}(\Omega)$ takes near-zero values, then it goes through a series of positive and negative oscillations, while in the high magnetic field region it returns to the unmodulated 2DEG behavior (it becomes zero). This latter behavior is due to the fact that as the magnetic field becomes large, the cyclotron orbit radii become small, and the electrons do not feel the effect of modulation as they follow their tiny circular orbits through the sample. The negative values taken by the transverse conductivity can be explained by the effect of the Lorentz force being overcome by the backward scattering effect.

7.1.2 1D $L_{yx}^{(0)}(\Omega)$ for $\bar{V} < 0$

Figure 7.2 shows two plots of the Hall conductivity obtained for negative modulation potentials in the presence of radiation. Both plots show that the Hall conductivity is quenched (it becomes zero) in the low magnetic field portion of the plots. Figure 7.2 (a), which was obtained for the lowest absolute value of the negative modulation potential strength shows different behavior than plots obtained for the Hall conductivity for higher values of the same parameter (also see Figure 7.3). In Figure (a) the Hall conductivity shows a monotonically decreasing behavior, going through several steps. The lower the incident radiation frequency, the larger the steps. An exception is the plot presented in the inset of Figure 7.3 (a) in which the Hall conductivity goes through a negative minimum followed by a positive peak in the range of magnetic fields investigated.

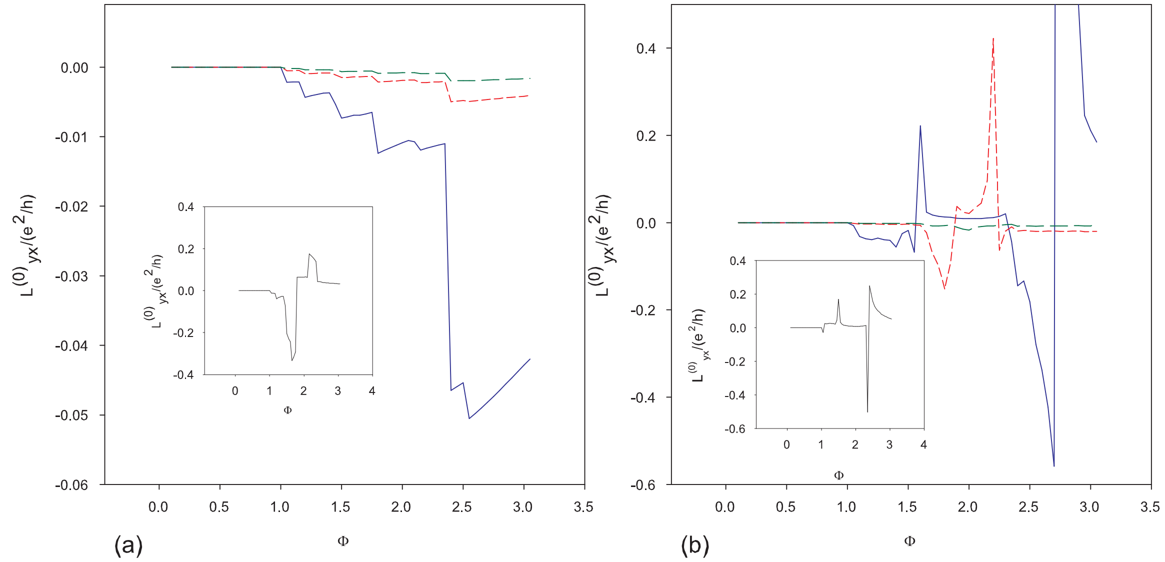

Figure 7.2: Hall conductivities for various negative values of the 1D modulation potential and different frequencies of the incident radiation field. The solid (black) line corresponds to those values of the frequency for which $\hbar\Omega = 0.25E_F$, the dotted (blue) line corresponds to $\hbar\Omega = 0.5E_F$, the short dashed (red) line corresponds to $\hbar\Omega = E_F$, while the solid (green) line in the inset is for $\hbar\Omega = 1.5E_F$. Other parameters used in this Figure are sample size $N_x = N_y = 10$, modulation potential strength $\bar{V} = -0.235$ for (a), and $\bar{V} = -3.235$ for (b). Exponent of the periodic term $N = 10$, $n = 6$, and electron density $n_{2D}a^2 = 0.75$.

Figure 7.3 shows the behavior of the Hall conductivity for two large negative modulation potential strengths. $L^{(0)}_{yx}(\Omega)$ goes through large negative to positive oscillations. The oscillations take place for mid-range values of the investigated magnetic fields. For the lowest and highest magnetic field values investigated, the oscillations die out, or their amplitude is reduced. All through the range of modulation potential values investigated, the low-magnetic field portion of the Hall conductivity is zero. This is in agreement with experimental and theoretical results previously obtained [61]-[66]. Although it is not trivial to give an explanation, based on single-particle transport theory, for the quenching of the Hall resistivity that appears for low magnetic field values, the phenomenon was observed experimentally [61]. It is customarily explained theoretically by the collimation of electrons. The collimated electrons are preferentially transmitted through the wire, quenching the Hall voltage. As in our case the Hall resistivity is calculated using equation (5.19), which has $L^{(0)}_{yx}(\Omega)$ in its numerator, at least we can clearly trace it back the quenching of the Hall resistivity to the quenching of the Hall conductivity.

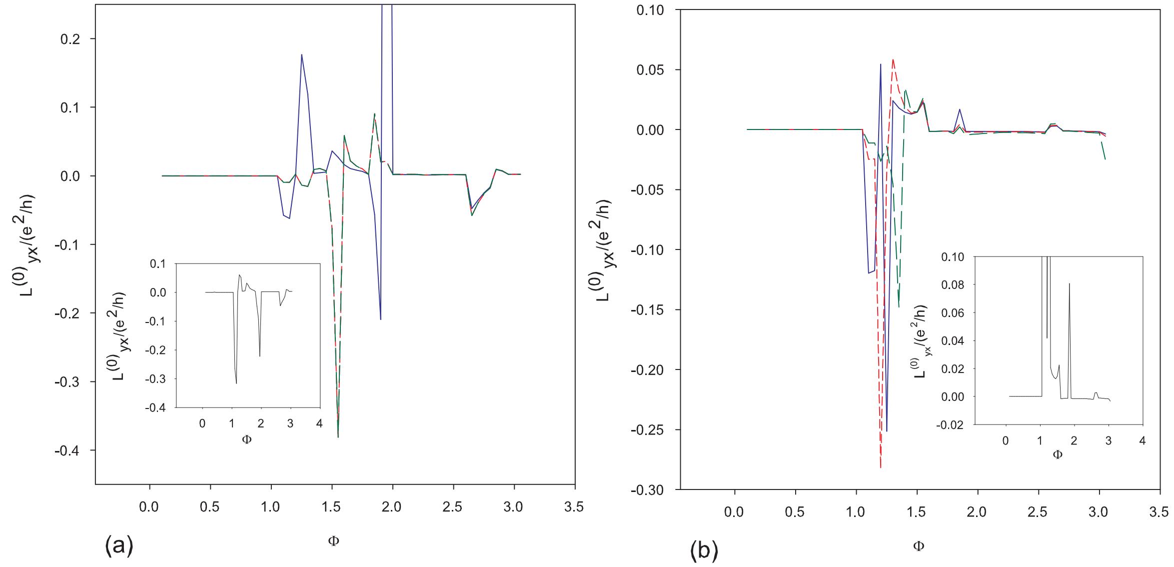

Figure 7.3: Hall conductivities for two negative values of the 1D modulation potential and different frequencies of the incident radiation field. The solid (black) line corresponds to those values of the frequency for which $\hbar\Omega = 0.25E_F$, the dotted (blue) line corresponds to $\hbar\Omega = 0.5E_F$, the short dashed (red) line corresponds to $\hbar\Omega = E_F$, while the solid (green) line in the inset is for $\hbar\Omega = 1.5E_F$. Other parameters used in this Figure are sample size $N_x = N_y = 10$, modulation potential strength $\bar{V} = -7.235$ for (a), and $\bar{V} = -10.235$ for (b). Exponent of the periodic term $N = 10$, $n = 6$, and electron density $n_{2D}a^2 = 0.75$.

7.1.3 1D $L_{yy}^{(0)}(\Omega)$ for $\bar{V} < 0$

Numerical data obtained for the longitudinal conductivity (along the quantum wire direction) is shown in Figure 7.4 for four different values of the modulation potential strength and four values of the incident radiation frequency. Figure 7.4 (a) corresponds to the lowest absolute value of the modulation potential strength ($\bar{V} = -0.235$) For this low value, the longitudinal conductivity is monotonically decreasing with increasing applied magnetic field. Changing the frequency of the incident radiation in this low modulation case does not introduce "steps" as those seen for the transverse conductivity $L_{xx}^{(0)}(\Omega)$. The lower the frequency of the incident radiation, the higher the maximum value from which the longitudinal conductivity decreases, but the minimum values attained for large magnetic fields is the same, nearly zero value. This is due to the fact that at high magnetic fields the electrons do not "feel" the effect of modulation, as they describe cyclotron orbits with such small radius, that it is unlikely that they would be scattered by the potential, i.e. the sample shows homogeneous 2DEG behavior. As the modulation strength is increased (Figure 7.4 (b)), the behavior of the longitudinal conductivity changes. For small magnetic field values the longitudinal conductivity is negative in this Figure, and with an increase of the magnetic field its values become positive. With the increase of the magnetic field, the longitudinal conductivity shows positive oscillations. After the initial negative values in the lowest magnetic field range investigated, the longitudinal conductivity does not have any more negative oscillations. This situation is changed in the strong modulation case. Although in both Figures 7.4 (c) and (d) $L_{yy}^{(0)}(\Omega)$ starts from negative values, similarly to Figure (b), the difference in the strong modulation case is that there are negative oscillations in the large magnetic field region as well. In fact in the large magnetic field region, the longitudinal

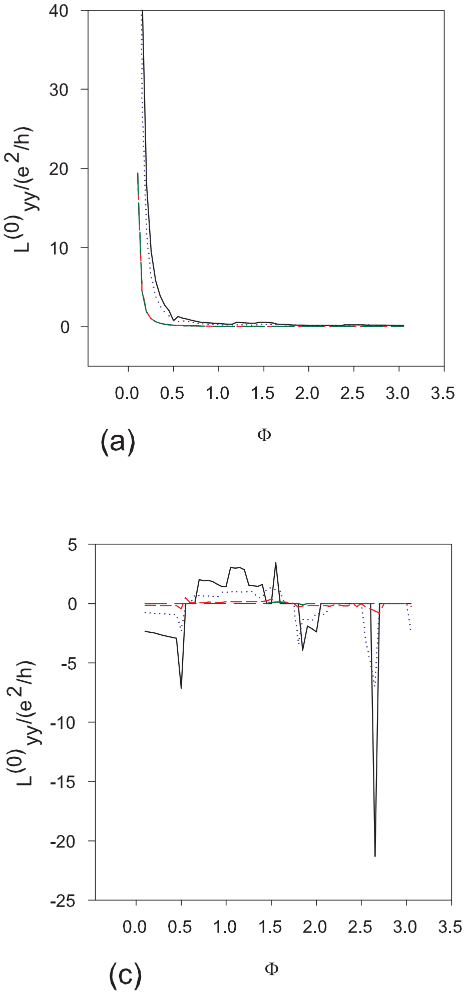

Figure 7.4: Longitudinal conductivities, L_{yy}, for several negative values of the 1D modulation potential and different frequencies of the incident radiation field. The solid (black) line corresponds to those values of the frequency for which $\hbar\Omega = 0.25E_F$, the dotted (blue) line corresponds to $\hbar\Omega = 0.5E_F$, the short dashed (red) line corresponds to $\hbar\Omega = E_F$, while the long dashed (green) line is for $\hbar\Omega = 1.5E_F$. Other parameters used in this Figure are sample size $N_x = N_y = 10$, modulation potential strength $\bar{V} = -0.235$ for (a), $\bar{V} = -3.235$ for (b), $\bar{V} = -7.235$ for (c), and $\bar{V} = -10.235$ for (d). Exponent of the periodic term $N = 10$, $n = 6$, and electron density $n_{2D}a^2 = 0.75$.

conductivity is either negative, or nearly zero for both of the strong modulation potential cases. In all four of the Figures 7.4, the larger the incident radiation frequency, the lower the amplitude of oscillations.

7.1.4 1D $\rho_{xx}^{(0)}(\Omega)$ for $\bar{V} < 0$

Figure 7.5 shows transverse resistivity plots obtained for negative 1D modulation potentials in the presence of incident radiation.

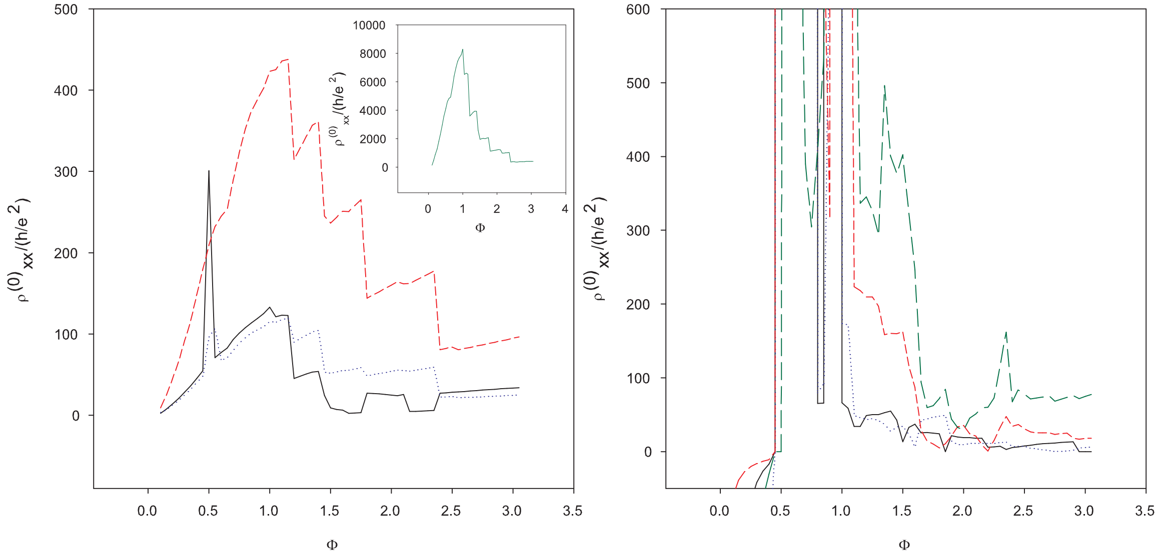

Figure 7.5: Transverse resistivities, ρ_{xx}, for negative values of the 1D modulation potential and different frequencies of the incident radiation field. The solid (black) line corresponds to those values of the frequency for which $\hbar\Omega = 0.25E_F$, the dotted (blue) line corresponds to $\hbar\Omega = 0.5E_F$, the short dashed (red) line corresponds to $\hbar\Omega = E_F$, while the long dashed (green) line is for $\hbar\Omega = 1.5E_F$ (solid green line in the inset on the left). Other parameters used in this Figure are sample size $N_x = N_y = 10$, modulation potential strength $\bar{V} = -0.235$ for (a), and $\bar{V} = -3.235$ for (b). Exponent of the periodic term $N = 10$, $n = 6$, and electron density $n_{2D}a^2 = 0.75$.

In Figure (a) plots of $\rho_{xx}^{(0)}(\Omega)$ for the lowest absolute values of the modulation potential are shown for various values of the incoming radiation's frequency. In the low modulation case the resistivity shows step-like features. The steps become higher and higher as the incident radiation frequency increases. For the highest value of the incident radiation frequency, the transverse resistivity attains a giant maximum for magnetic fields around the value of $\Phi = 1.0$. From this very high value, the transverse resistivity decreases through a series of steps as the magnetic field increases. The situation is different for the larger absolute value of the modulation potential strength shown in Figure 7.5 (b). In this case the resistivity has negative values for small values of the magnetic field, and then it goes through a series of giant positive to zero oscillations for intermediate values of the applied magnetic field. In the high magnetic field portion of the plot, the amplitude of positive oscillations becomes lower. The larger the magnitude of the incident radiation frequency, the larger the amplitude of the oscillations.

7.1.5 1D $\rho_{xy}^{(0)}(\Omega)$ for $\bar{V} < 0$

Numerical results for the Hall resistivity for the negative 1D modulation potential case are shown in Figure 7.6. In plot (a) of this Figure, which corresponds to weak modulation, it can be seen that the Hall resistivity in quenched for magnetic field values lower than $\Phi = 1.0$ for all values of the incident radiation frequency. For the lowest value of this frequency, $\Omega = 0.25E_F/\hbar$, $\rho_{xy}^{(0)}(\Omega)$ goes through negative oscillations for intermediate values of the magnetic field range investigated, while for large values of the magnetic field it becomes positive, and then it decreases again through a number of steps, but it remains positive even for the largest value of the magnetic field investigated. For the other three values of the incident radiation frequency, the Hall resistivity for the low modulation case in also quenched, but it stays negative throughout the investigated magnetic field range. For the frequency values of $\Omega = 0.5E_F/\hbar$ and $\Omega = E_F/\hbar$ it keeps decreasing in the negative, in a step-wise manner, as the applied magnetic field increases. For the highest radiation frequency however, $\rho^{(0)}_{xy}(\Omega)$ decreases to a deep negative minimum first, and then it increases through a series of steps. It never becomes positive for the magnetic field range investigated. For the larger absolute value of the modulation potential strength, the behavior of the Hall resistivity is different. It is also quenched for magnetic field values lower than $\Phi = 1.0$, but it does not show step-like increase as in the low modulation case. Instead, $\rho^{(0)}_{xy}(\Omega)$ shows negative to positive oscillations, some of them of giant amplitude. The Hall resistivity has some positive values for all the incident radiation frequencies but the highest one. For this highest incident frequency case, $\Omega = 1.5E_F/\hbar$, the resistivity is negative all through the range of magnetic fields investigated, except for $\Phi < 1.0$, where it is quenched.

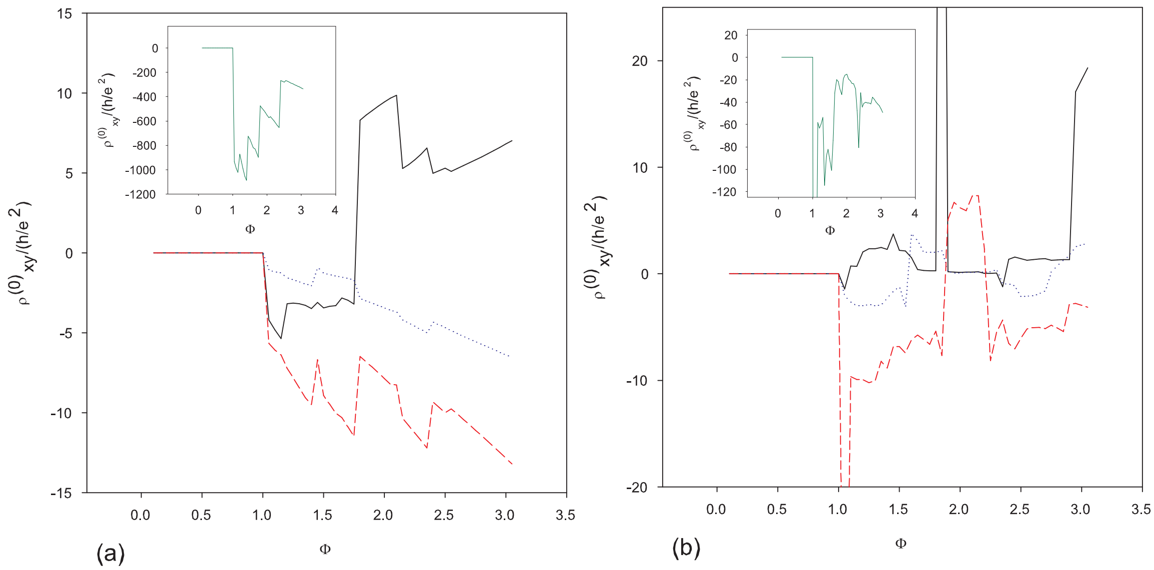

Figure 7.6: Hall resistivities for negative values of the 1D modulation potential and different frequencies of the incident radiation field. The solid (black) line corresponds to those values of the frequency for which $\hbar\Omega = 0.25E_F$, the dotted (blue) line corresponds to $\hbar\Omega = 0.5E_F$, the short dashed (red) line corresponds to $\hbar\Omega = E_F$, while the solid (green) line (inset) is for $\hbar\Omega = 1.5E_F$. Other parameters used in this Figure are sample size $N_x = N_y = 10$, modulation potential strength $\bar{V} = -0.235$ for (a), and $\bar{V} = -3.235$ for (b). Exponent of the periodic term $N = 10$, $n = 6$, and electron density $n_{2D}a^2 = 0.75$.

7.1.6 1D $\rho^{(0)}_{yy}(\Omega)$ for $\bar{V} < 0$

The behavior of the longitudinal resistivity along the quantum conduction channel is displayed in Figure 7.7.

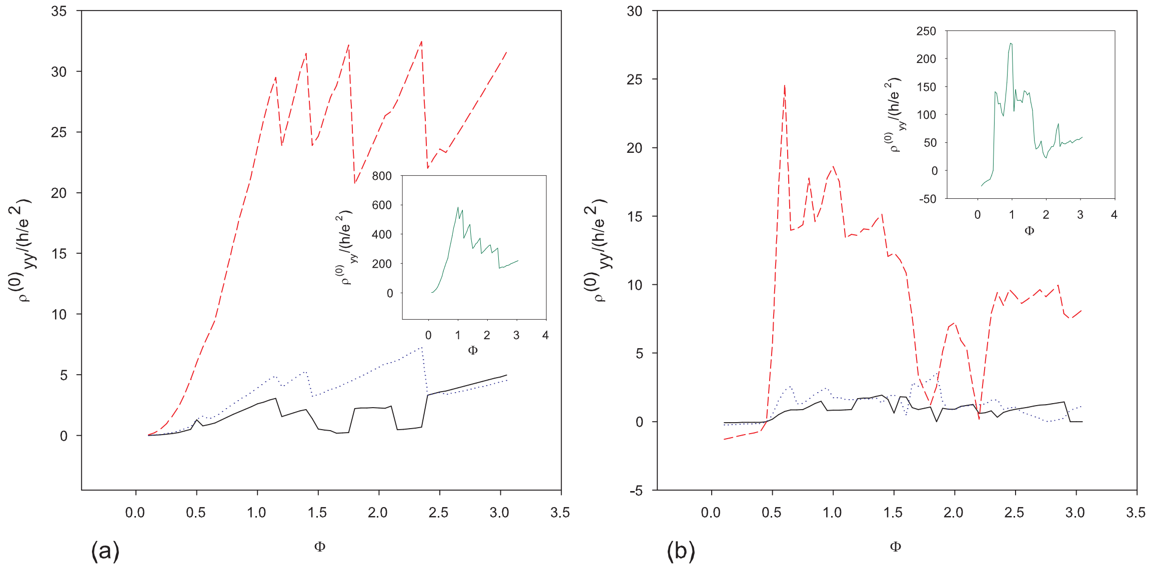

Figure 7.7: Longitudinal resistivities, ρ_{yy}, for negative values of the 1D modulation potential and different frequencies of the incident radiation field. The solid (black) line corresponds to those values of the frequency for which $\hbar\Omega = 0.25E_F$, the dotted (blue) line corresponds to $\hbar\Omega = 0.5E_F$, the short dashed (red) line corresponds to $\hbar\Omega = E_F$, while the solid (green) line (inset) is for $\hbar\Omega = 1.5E_F$. Other parameters used in this Figure are sample size $N_x = N_y = 10$, modulation potential strength $\bar{V} = -0.235$ for (a), and $\bar{V} = -3.235$ for (b). Exponent of the periodic term $N = 10$, $n = 6$, and electron density $n_{2D}a^2 = 0.75$.

Plot (a) corresponds to the low modulation case. With the increase of the magnetic field the longitudinal resistivity increases with and increase of the applied magnetic field, except for the largest value of the applied radiation field frequency. For this frequency of $\Omega = 1.5E_F/\hbar$, the resistivity increases abruptly first, but then it starts decreasing through a series of oscillations, resembling steps, or saw-teeth, of decreasing amplitude. For the rest of the irradiation frequency values, $\rho^{(0)}_{yy}(\Omega)$ shows a series of increasing positive saw-tooth-like oscillations for high values of the magnetic field applied. The larger the frequency of the applied radiation, the larger the magnitude of the corresponding longitudinal resistivity. In the stronger modulation case, shown in plot (b) of Figure 7.7 the behavior of the longitudinal resistivity is somewhat different. The saw-tooth-type oscillations are replaced by positive oscillations of varying amplitude, in general larger in the low magnetic field region. The magnitude of oscillations is larger for larger values of the incident radiation field frequencies.

7.1.7 1D $L_{xx}^{(0)}(\Omega)$ for $\bar{V} > 0$

In the rest of this Chapter we will present numerical results for the magnetotransport coefficients for positive 1D modulation. When the modulation potential is strong, these potentials would correspond to quantum antiwires.

Figure 7.8 is presenting numerical results obtained for the transverse conductivity, along the modulation direction, for 1D positive modulation potentials. Plot (a) corresponds to weak modulation, $\bar{V} = 0.235$, while in the rest of the plots the modulation strength is increased so that it is $\bar{V} = 3.235$ in (b), $\bar{V} = 7.235$ in (c), and $\bar{V} = 10.235$ in (d). Just as in the case of negative modulation, plots corresponding to weak modulation are unlike those obtained for larger values of the modulation potential strength. For the transverse conductivity this means that for the low modulation case the conductivity has large positive values for the various incident frequencies investigated in the low magnetic field limit, while all the stronger modulation plots start from low conductivity values, near zero, for low magnetic fields. After the initial high value, the transverse conductivity decreases, and then it increases again for high magnetic fields, going through a series of steps. As the applied magnetic field increases the height of the steps decreases. Transverse conductivities corresponding to the stronger modulation cases are increasing as the applied magnetic field increases, and they

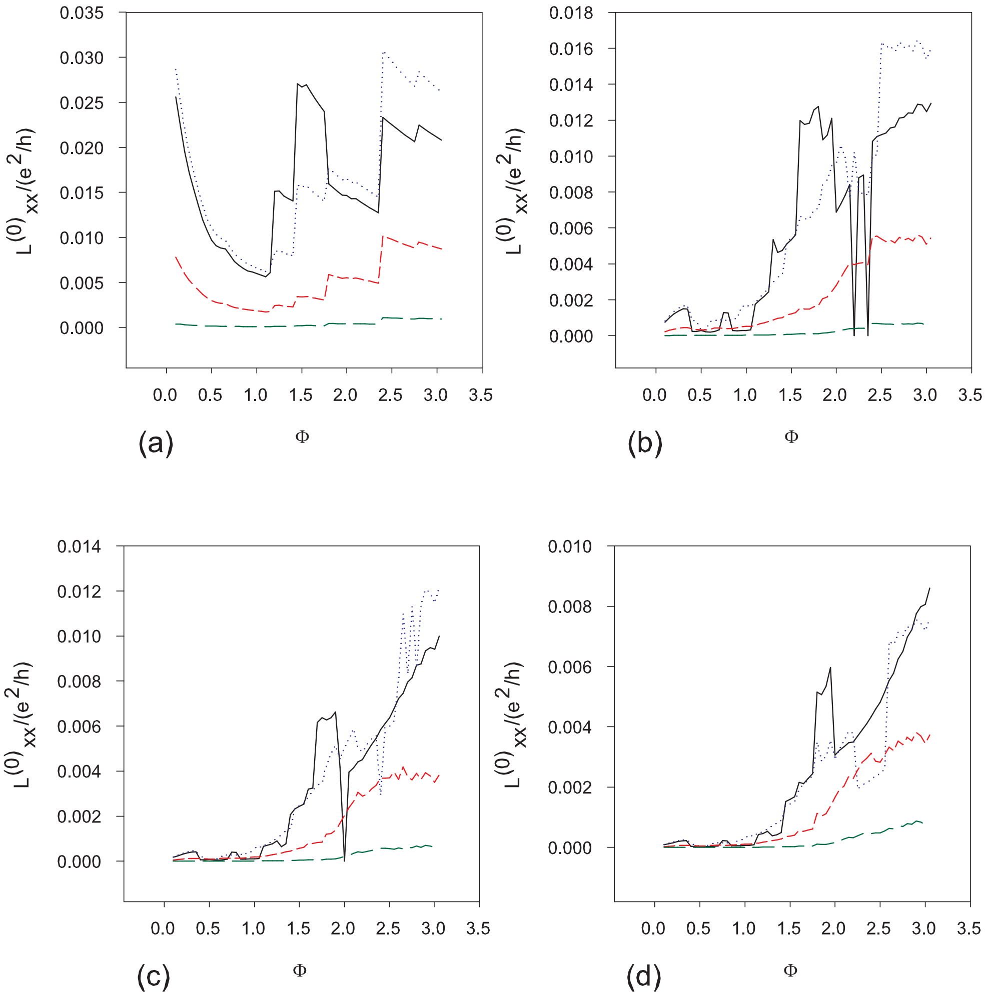

Figure 7.8: Longitudinal conductivities for positive values of the 1D modulation potential and different frequencies of the incident radiation field. The solid (black) line corresponds to those values of the frequency for which $\hbar\Omega = 0.25E_F$, the dotted (blue) line corresponds to $\hbar\Omega = 0.5E_F$, the short dashed (red) line corresponds to $\hbar\Omega = E_F$, while the long dashed (green) line is for $\hbar\Omega = 1.5E_F$. Other parameters used in this Figure are: sample size $N_x = N_y = 10$, modulation potential strength $\bar{V} = 0.235$ for (a), $\bar{V} = 3.235$ for (b), $\bar{V} = 7.235$ for (c), and $\bar{V} = 10.235$ for (d). The exponent of the periodic term $N = 10$; while $n = 6$, and electron density $n_{2D}a^2 = 0.75$.

show some large amplitude oscillations. Unlike in the case of the negative modulation, these oscillations never become negative.

7.1.8 1D $L_{yx}^{(0)}(\Omega)$ for $\bar{V} > 0$

Similar to the negative modulation potential case, the Hall conductivity is quenched for values of the applied magnetic field lower than approximately $\Phi = 1.0$ for all of the values of the incident radiation field frequency, and all of the modulation potential values investigated. For larger values of the magnetic field than this threshold value, the Hall conductivity undergoes large amplitude negative and positive oscillations for the two smaller values of the incident radiation field frequency, $\Omega = 0.25E_F/\hbar$ and $\Omega = 0.5E_F/\hbar$ as shown in Figure 7.9. This Figure also includes plots for the other two values of the incident radiation frequency for reference purposes, but the detail in these two graphs is lost. This is due to the difference in the scale of variation of the Hall conductivity for the two lower ($\Omega = 0.25E_F/\hbar$ and $\Omega = 0.5E_F/\hbar$) and two higher ($\Omega = E_F/\hbar$ and $\Omega = 1.5E_F/\hbar$) values of the incident radiation frequency. Therefore, a separate set of graphs was included in Figure 7.10 for the two larger values of the frequency, and all four values of the positive modulation potential strength investigated. By the comparison of Figure 7.9 and Figure 7.10 the difference becomes obvious. The large amplitude positive and negative oscillations of the Hall conductivity, which are present for the two lower radiation field frequencies, are not present for the two higher values of the frequency. Figure 7.10 illustrates well the difference in the variation of the Hall conductivity with the applied magnetic field for these frequency values. As the magnetic field becomes larger than the threshold value in the plots of Figure 7.10, the Hall conductivity decreases with the increase of Φ, going through a series of steps for the lowest modulation potential strength of $\bar{V} = 0.235$ in plot (a).

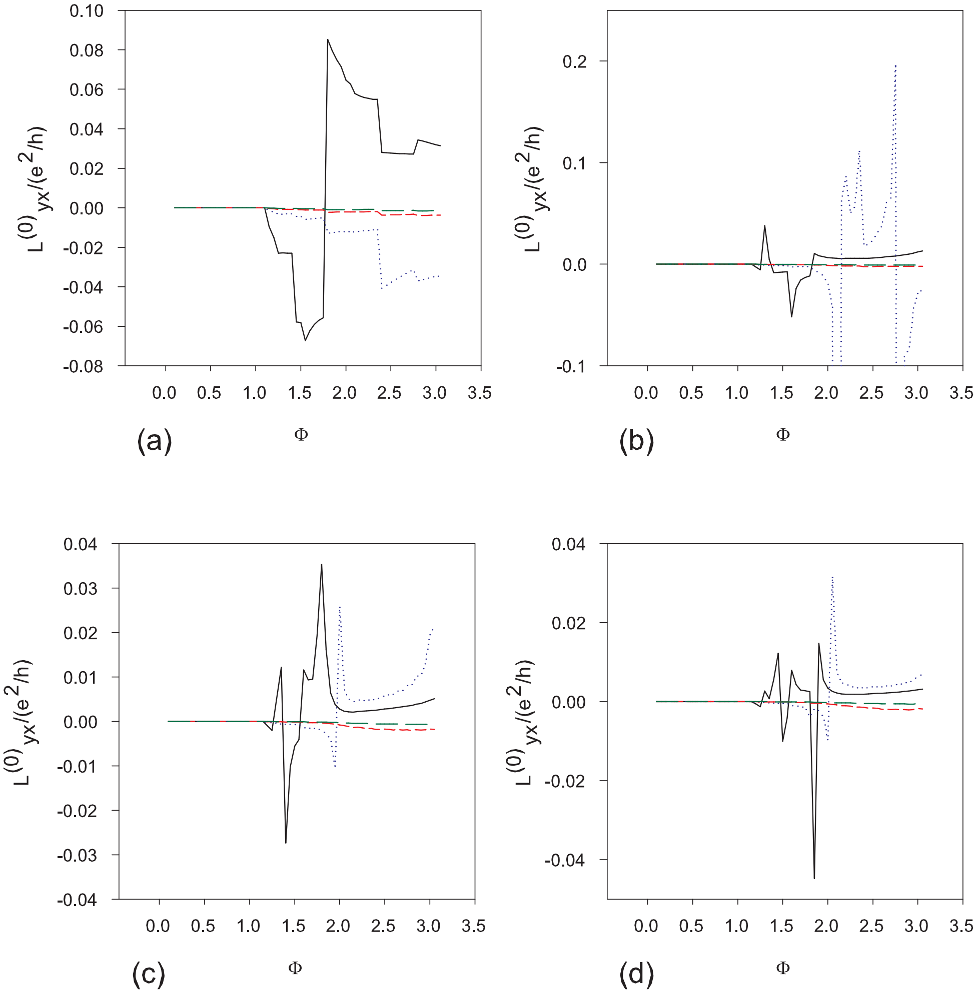

Figure 7.9: Hall conductivities for positive values of the 1D modulation potential and different frequencies of the incident radiation field. The solid (black) line corresponds to those values of the frequency for which $\hbar\Omega = 0.25E_F$, the dotted (blue) line corresponds to $\hbar\Omega = 0.5E_F$, the short dashed (red) line corresponds to $\hbar\Omega = E_F$, while the long dashed (green) line is for $\hbar\Omega = 1.5E_F$. Other parameters used in this Figure are sample size $N_x = N_y = 10$, modulation potential strength $\bar{V} = 0.235$ for (a), $\bar{V} = 3.235$ for (b), $\bar{V} = 7.235$ for (c), and $\bar{V} = 10.235$ for (d). Exponent of the periodic term $N = 10$, $n = 6$, and electron density $n_{2D}a^2 = 0.75$.

For the three higher modulation potential strength values of $\bar{V} = 3.235$ in plot (b), $\bar{V} = 7.235$ in plot (c), and $\bar{V} = 10.235$ in plot (d) the variation of $L_{yx}^{(0)}(\Omega)$ is slightly different than for the low modulation case. Right after the threshold value of the magnetic field is exceeded, the Hall conductivity decreases, going through a series of small steps. Then the decrease becomes monotonic, until the highest magnetic field values investigated are reached, for which values the Hall conductivity undergoes a series of small amplitude negative oscillations. Comparing this again to Figure 7.9, one can see that for small incident radiation frequency values the Hall conductivity takes positive values in the large magnetic field region. Thus there are marked differences between the behavior of the Hall conductivity for 1D positive modulation, which depend on the frequency of the incident radiation.

7.1.9 1D $L_{yy}^{(0)}(\Omega)$ for $\bar{V} > 0$

Now we present our numerical result for the longitudinal conductivity, along the quantum conduction channel for the positive 1D modulation case. Figure 7.11 presence the variation of $L_{yy}^{(0)}(\Omega)$ for the four potential strength values investigated, and for four different values of the incident radiation field frequency. For low modulation strength, corresponding to plot (a) where $\bar{V} = 0.235$, the longitudinal conductivity shows a monotonic decreasing behavior for all four incident radiation frequencies. This behavior resembles that expected of an unmodulated 2DEG. There are no significant oscillations in $L_{yy}^{(0)}(\Omega)$ for any of the incident radiation field frequencies. When the modulation potential strength is increased the behavior of the longitudinal conductivity is changed. After an initial decrease in values taken by the longitudinal conductivity in the low magnetic field portion of the plots, a series of large amplitude oscillations appear. The oscillations are pronounced for the two lowest values of the

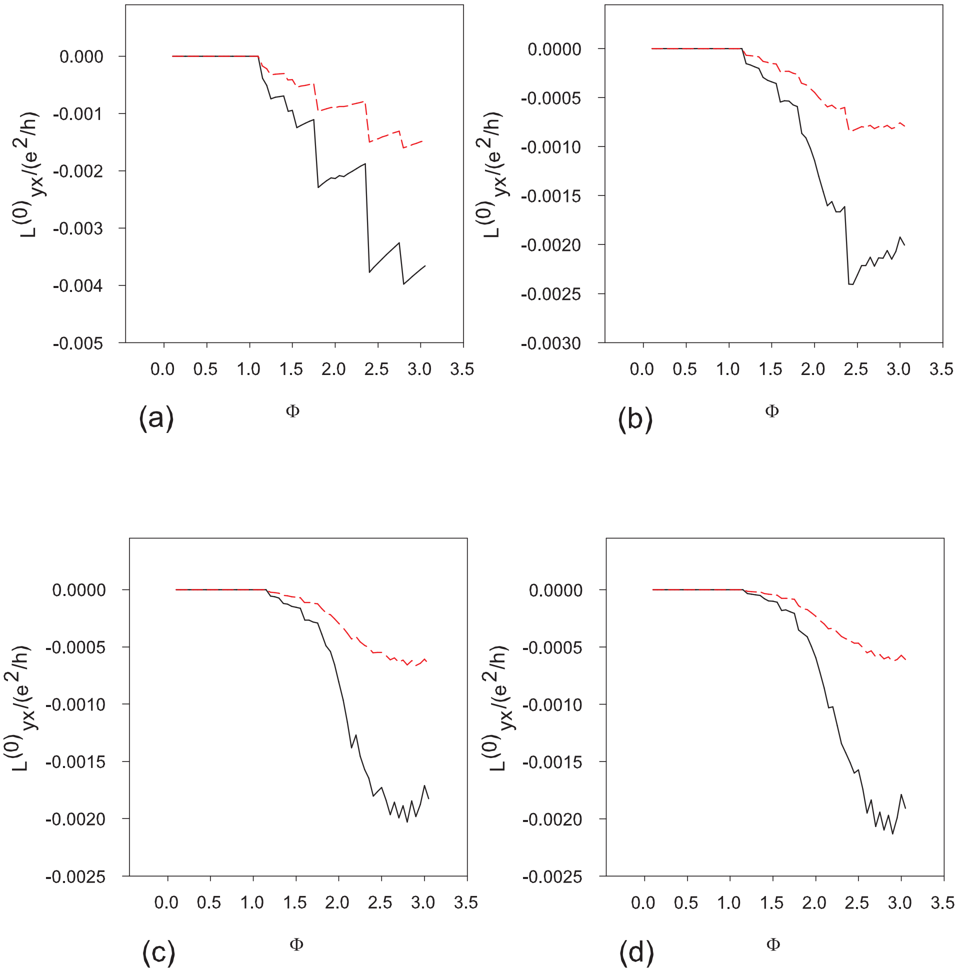

Figure 7.10: Hall conductivities for positive values of the 1D modulation potential and two frequencies of the incident radiation field. The solid (black) line corresponds to those values of the frequency for which $\hbar\Omega = E_F$, while the short dashed (red) line corresponds to $\hbar\Omega = 1.5E_F$. Other parameters used in this Figure are sample size $N_x = N_y = 10$, modulation potential strength $\bar{V} = 0.235$ for (a), $\bar{V} = 3.235$ for (b), $\bar{V} = 7.235$ for (c), and $\bar{V} = 10.235$ for (d). Exponent of the periodic term $N = 10$, $n = 6$, and electron density $n_{2D}a^2 = 0.75$.

incident radiation frequency of $\Omega = 0.25E_F/\hbar$ (solid, black line in the plots), and $\Omega = 0.5E_F/\hbar$ (dotted, blue line in the plots). As the modulation potential increases, the longitudinal conductivity shows and increasing behavior in the high magnetic field portion of the plots. In Figure 7.11 (b), corresponding to $\bar{V} = 3.235$ this behavior is not yet obvious. This is because for some values of the incident radiation the longitudinal conductivity increases (for example $\Omega = E_F/\hbar$, short dashed, red line in Figure 7.11 (b)), but for other values of the frequency, such as $\Omega = 0.25E_F/\hbar$ (solid, black line), and $\Omega = 1.5E_F/\hbar$ (dotted, blue line), after the large amplitude positive oscillations, $L_{yy}^{(0)}(\Omega)$ is still showing a decreasing behavior in the large magnetic field region. In plots (c) and (d) of the same Figure however, corresponding to $\bar{V} = 7.235$, and $\bar{V} = 10.235$ the longitudinal conductivity increases in the large magnetic field portion of the plots for all values of the incident radiation field frequency. There is one more feature of the low magnetic field longitudinal conductivity that can be noticed in Figure 7.11. With the increase of the modulation potential strength, the maximum low-magnetic-field value of the longitudinal conductivity decreases, for the same incident radiation frequency. In Figure 7.11 (a) obtained for $\bar{V} = 0.235$ the low-magnetic-field maximum value corresponding to an incident radiation frequency of $\Omega = 0.25E_F/\hbar$ (solid, black line) is around 12, in plot (b) of the same Figure, but corresponding to $\bar{V} = 7.235$ and $\Omega = 0.5E_F/\hbar$ it is reduced to around 0.35, in plot (c) drawn for modulation potential strength of $\bar{V} = 7.235$ and for the same value of the radiation field frequency it is further reduced to about 0.08, and finally in plot (d) of the same Figure, and for the same parameters it is only around 0.04. This seems counterintuitive at first, because one would expect that a deep quantum antiwire would offer a better conduction channel than a shallow one. But if one takes into account that in low magnetic fields the cyclotron radius is large, it becomes reasonable to think that electrons on large radius cyclotron orbits would undergo more scattering

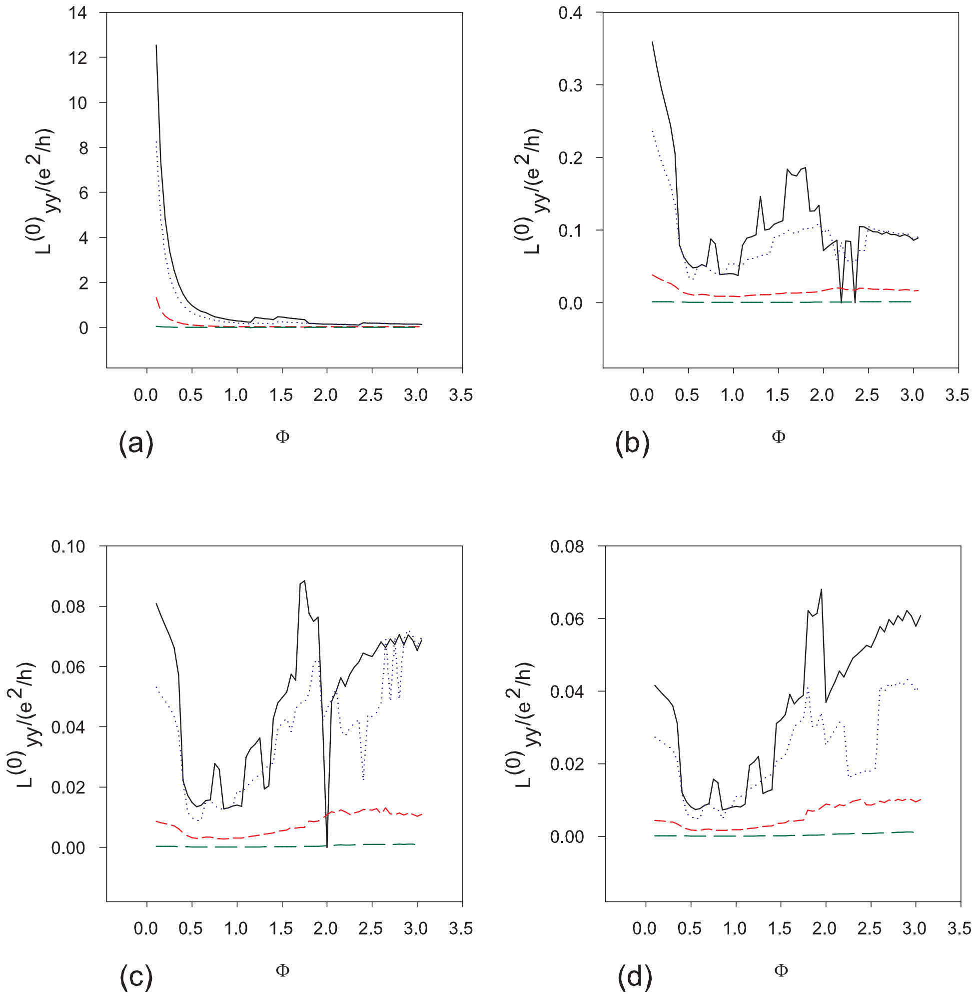

(a) (b) (c) (d)

Figure 7.11: Longitudinal conductivities, L_{yy}, for positive values of the 1D modulation potential and different frequencies of the incident radiation field. The solid (black) line corresponds to those values of the frequency for which $\hbar\Omega = 0.25E_F$, the dotted (blue) line corresponds to $\hbar\Omega = 0.5E_F$, the short dashed (red) line corresponds to $\hbar\Omega = E_F$, while the long dashed (green) line is for $\hbar\Omega = 1.5E_F$. Other parameters used in this Figure are sample size $N_x = N_y = 10$, modulation potential strength $\bar{V} = 0.235$ for (a), $\bar{V} = 3.235$ for (b), $\bar{V} = 7.235$ for (c), and $\bar{V} = 10.235$ for (d). Exponent of the periodic term $N = 10$, $n = 6$, and electron density $n_{2D}a^2 = 0.75$.

when the potential barriers are higher than when shallower. This concludes the sections presenting the conductivities in the 1D positive potential modulation case. We will proceed with the discussion of our numerical results for the resistivities.

7.1.10 1D $\rho_{xx}^{(0)}(\Omega)$ for $\bar{V} > 0$

Figure 7.12 presents transverse resistivity plots for two values of the modulation potential strength and four values of the frequency of the incident radiation.

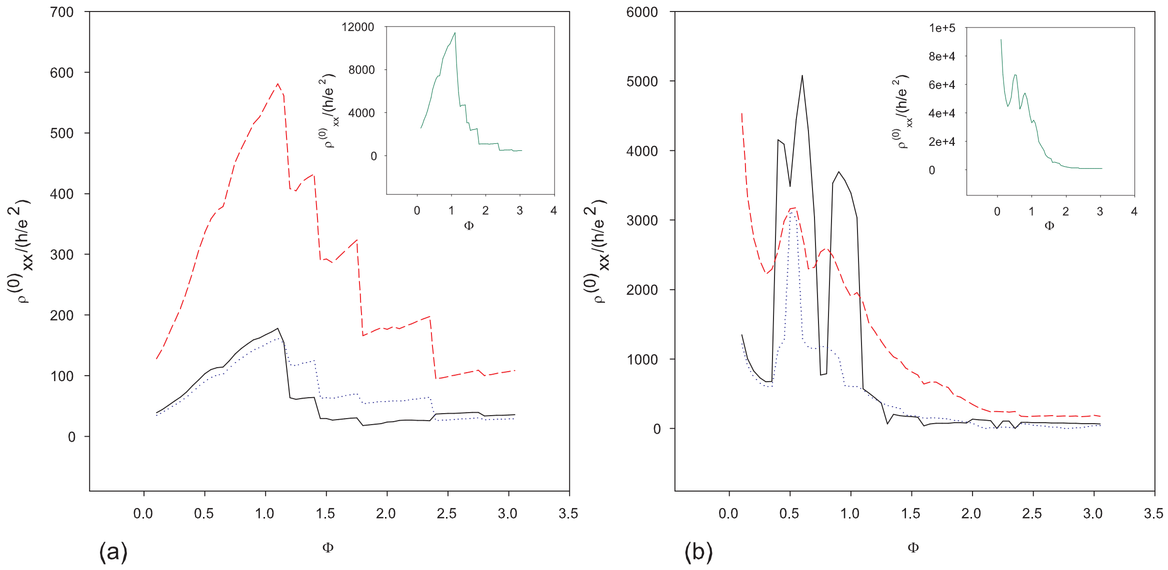

Figure 7.12: Transverse resistivities, ρ_{xx}, for positive values of the 1D modulation potential and different frequencies of the incident radiation field. The solid (black) line corresponds to those values of the frequency for which $\hbar\Omega = 0.25E_F$, the dotted (blue) line corresponds to $\hbar\Omega = 0.5E_F$, the short dashed (red) line corresponds to $\hbar\Omega = E_F$, while the solid (green) line (inset) is for $\hbar\Omega = 1.5E_F$. Other parameters used in this Figure are sample size $N_x = N_y = 10$, modulation potential strength $\bar{V} = 0.235$ for (a), and $\bar{V} = 3.235$ for (b). Exponent of the periodic term $N = 10$, $n = 6$, and electron density $n_{2D}a^2 = 0.75$.

Plot (a) corresponds to weak modulation, with the modulation potential strength equal to $\bar{V} = 0.235$. For this value of the potential, the transverse resistivity takes small, near-zero values in low magnetic field. As the magnetic field increases, the transverse resistivity increases as well, until a maximum value is reached at about

$\Phi = 1.0$. The maximum is located around this value of the magnetic field in each four of the plots corresponding to different incident radiation frequencies. Then, $\rho_{xx}^{(0)}(\Omega)$ starts decreasing, by going through a series of steps. For the larger potential strength in Figure 7.12, plot (b) corresponding to $\bar{V} = 3.235$, the transverse resistivity shows a different behavior. It starts out at large values in the low-magnetic-field region, and it shows a series of giant oscillations in the intermediate magnetic field part, decreasing to low values for large magnetic fields.

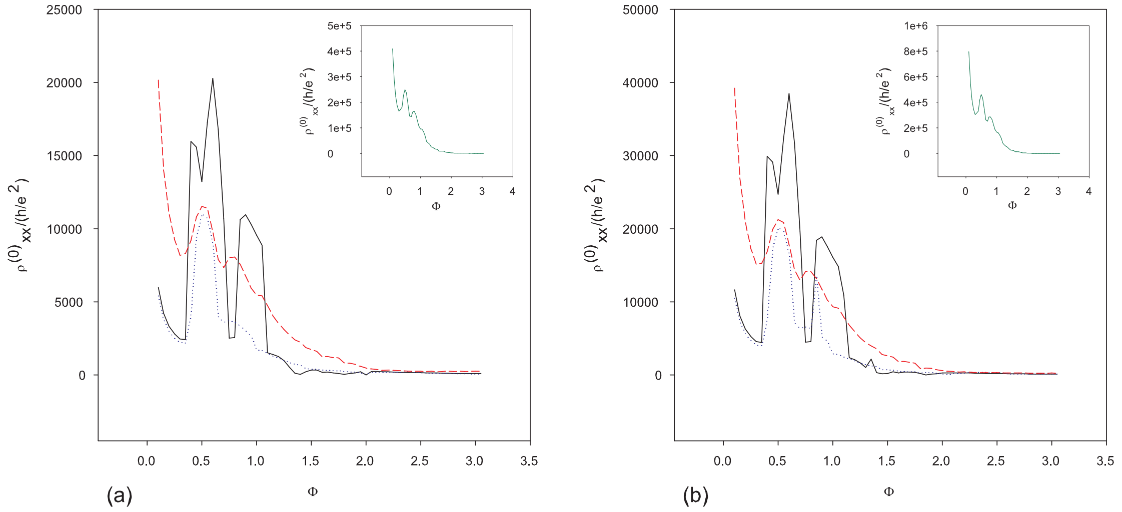

Figure 7.13: Transverse resistivities, ρ_{xx}, for positive values of the 1D modulation potential and different frequencies of the incident radiation field. The solid (black) line corresponds to those values of the frequency for which $\hbar\Omega = 0.25E_F$, the dotted (blue) line corresponds to $\hbar\Omega = 0.5E_F$, the short dashed (red) line corresponds to $\hbar\Omega = E_F$, while the solid (green) line (inset) is for $\hbar\Omega = 1.5E_F$. Other parameters used in this Figure are sample size $N_x = N_y = 10$, modulation potential strength $\bar{V} = 7.235$ for (a), and $\bar{V} = 10.235$ for (b). Exponent of the periodic term $N = 10$, $n = 6$, and electron density $n_{2D}a^2 = 0.75$.

Two higher modulation potential strengths were used to determine the variation of the transverse resistivity in Figure 7.13. Plot (a) corresponds to $\bar{V} = 7.235$, while plot (b) was obtained for $\bar{V} = 10.235$. The shape of the $\rho_{xx}^{(0)}(\Omega)$ versus Φ plots is similar in the strong modulation case to those obtained previously for $\bar{V} = 3.235$. The transverse resistivity starts at high values for the lowest magnetic field strengths, then goes through a series of positive oscillations, and finally decreases in the high magnetic field range.

7.1.11 1D $\rho_{xy}^{(0)}(\Omega)$ for $\bar{V} > 0$

We now present numerical results obtained for the Hall resistivities in the case of positive 1D modulation. For a weak modulation potential strength of $\bar{V} = 0.235$, shown in Figure 7.14 (a), the Hall resistivity is quenched in the lower magnetic field portion, then it decreases to a negative minimum.

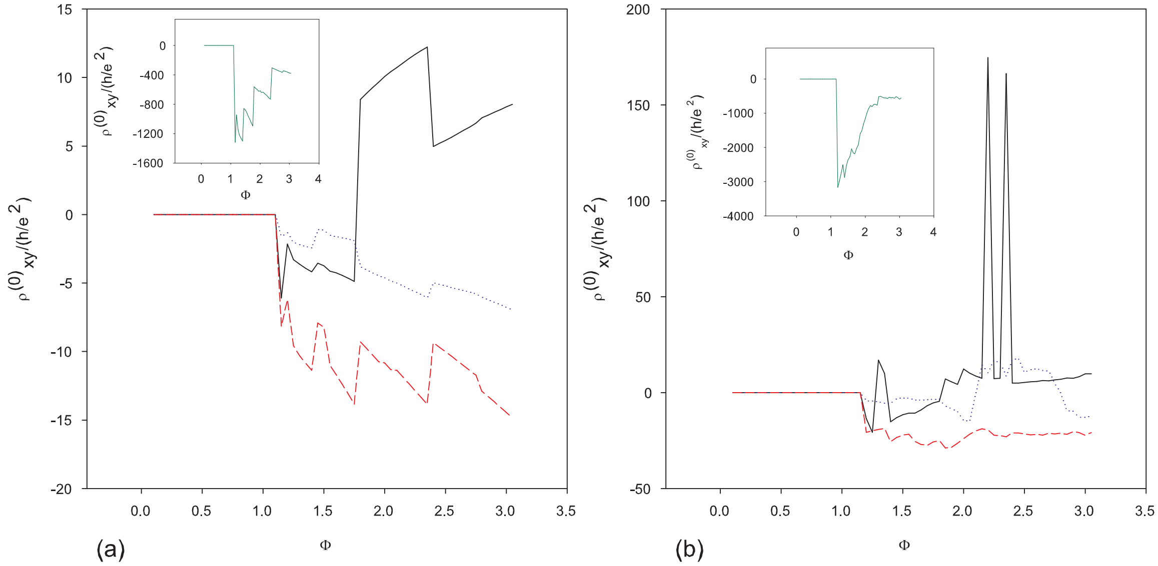

Figure 7.14: Hall resistivities for positive values of the 1D modulation potential and different frequencies of the incident radiation field. The solid (black) line corresponds to those values of the frequency for which $\hbar\Omega = 0.25E_F$, the dotted (blue) line corresponds to $\hbar\Omega = 0.5E_F$, the short dashed (red) line corresponds to $\hbar\Omega = E_F$, while the solid (green) line (inset) is for $\hbar\Omega = 1.5E_F$. Other parameters used in this Figure are sample size $N_x = N_y = 10$, modulation potential strength $\bar{V} = 0.235$ for (a), and $\bar{V} = 3.235$ for (b). Exponent of the periodic term $N = 10$, $n = 6$, and electron density $n_{2D}a^2 = 0.75$.

For the different incident radiation field frequencies the minimum value shows wide variation. The lowest value attained corresponds to the highest incident radiation frequency of $\Omega = 1.5E_F/\hbar$. For this low modulation regime, the variation of the

Hall resistivity for the different radiation field frequencies shows a series of step-like oscillations. For the larger value of the modulation potential strength investigated in Figure 7.14 (b), the behavior of the Hall resistivity is somewhat different. It is still quenched for low magnetic field values, but the step-like oscillations disappear in the intermediate magnetic field range.

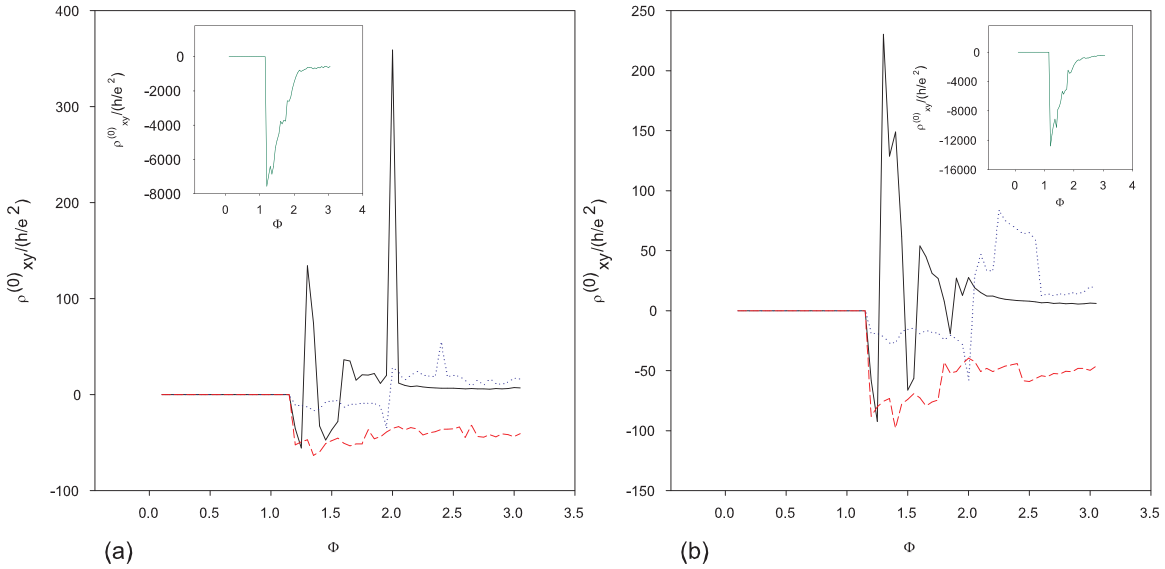

Figure 7.15: Hall resistivities for positive values of the 1D modulation potential and different frequencies of the incident radiation field. The solid (black) line corresponds to those values of the frequency for which $\hbar\Omega = 0.25E_F$, the dotted (blue) line corresponds to $\hbar\Omega = 0.5E_F$, the short dashed (red) line corresponds to $\hbar\Omega = E_F$, while the solid (green) line (inset) is for $\hbar\Omega = 1.5E_F$. Other parameters used in this Figure are sample size $N_x = N_y = 10$, modulation potential strength $\bar{V} = 7.235$ for (a), and $\bar{V} = 10.235$ for (b). Exponent of the periodic term $N = 10$, $n = 6$, and electron density $n_{2D}a^2 = 0.75$.

The step-like variation is replaced by oscillations, which can have giant amplitudes for certain radiation frequencies (such as the solid, black line in plot (b) corresponding to $\Omega = 0.25E_F/\hbar$) and display a double-peak feature. For the largest value of the incident radiation frequency however, (seen in the insets of the two plots of Figure 7.14), the behavior of the Hall resistivity is similar in the two plots. It is quenched for low magnetic fields, then it plunges to a giant negative value, from which it then increases through a series of saw-tooth-like oscillations as the magnetic field increases. For the strong modulation potential case, which is presented in Figure 7.15, the values of $\bar{V} = 7.235$ for (a), and $\bar{V} = 10.235$ were used for the potential strength. The shape of the plots is similar to those obtained for the weaker modulation value of $\bar{V} = 3.235$ in the sense that the Hall resistivity shows large amplitude positive to negative oscillations for magnetic field values above the threshold value for the three lower values of the incident radiation field frequency, $\Omega = 0.25E_F/\hbar$, $\Omega = 0.5E_F/\hbar$, and $\Omega = E_F/\hbar$. For the largest value of the incident radiation field frequency, $\Omega = 1.5E_F/\hbar$, $\rho_{xy}^{(0)}(\Omega)$ behaves just as in the lower modulation cases presented in Figure 7.14. After being quenched, it plunges to a very large negative minimum, and then it increases with the increase of the applied magnetic field through a series of small negative oscillations.

7.1.12 1D $\rho_{yy}^{(0)}(\Omega)$ for $\bar{V} > 0$

In the conclusion of this chapter, we present the numerical data obtained for the longitudinal resistivity for the positive potential modulation. As it can be seen in Figure 7.16 (a), corresponding to the weak modulation case, the longitudinal resistivity increases from a near-zero value taken in the low magnetic field portion of the plots, which is followed by an increase, until a maximum value is attained. Then the longitudinal resistivity oscillates around this maximum value for all of the incident radiation frequencies except the highest one, $\Omega = 1.5E_F/\hbar$. For the latter case, the highest radiation frequency, after attaining the maximum, the longitudinal resistivity decreases, as the magnetic field increases. For all the rest of the modulation potential strengths investigated, $\rho_{yy}^{(0)}(\Omega)$ shows very similar behavior, as just described for $\Omega = 1.5E_F/\hbar$ in the weak modulation case. It starts from a low value in the low magnetic field region, it then increases to a maximum value, and then goes through a series of oscillations. These oscillations take place up to about a value of the magnetic field equal to $\Phi = 1.5$. After this value of the magnetic field, the oscillations become lower in amplitude, and the longitudinal resistivity maintains an almost constant value through the rest of the magnetic field range investigated.

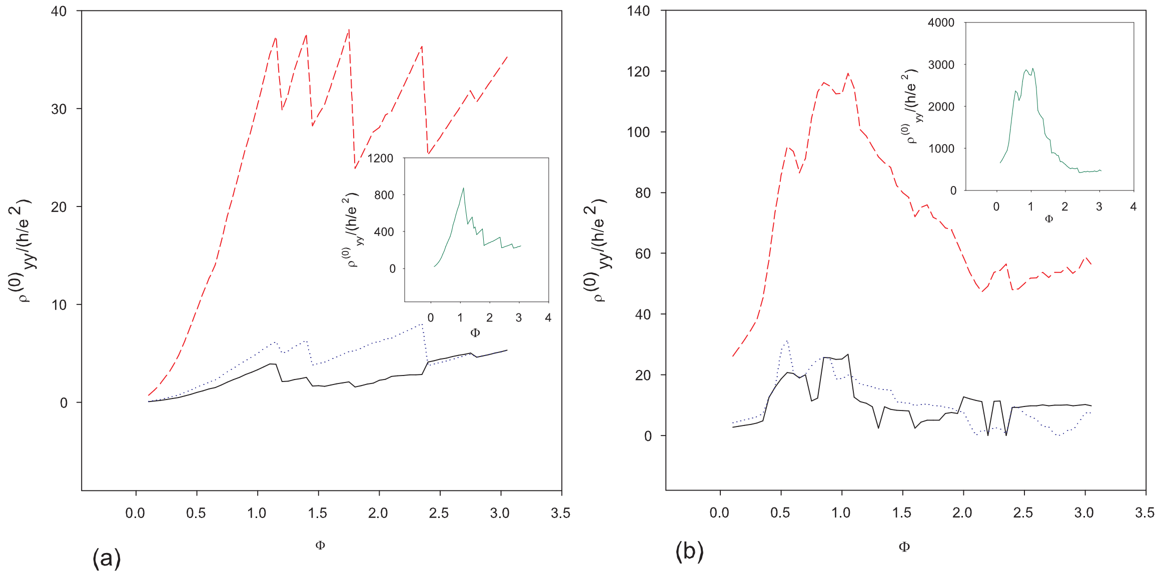

Figure 7.16: Longitudinal resistivities, ρ_{yy}, for positive values of the 1D modulation potential and different frequencies of the incident radiation field. The solid (black) line corresponds to those values of the frequency for which $\hbar\Omega = 0.25E_F$, the dotted (blue) line corresponds to $\hbar\Omega = 0.5E_F$, the short dashed (red) line corresponds to $\hbar\Omega = E_F$, while the solid (green) line (inset) is for $\hbar\Omega = 1.5E_F$. Other parameters used in this Figure are sample size $N_x = N_y = 10$, modulation potential strength $\bar{V} = 0.235$ for (a), and $\bar{V} = 3.235$ for (b). Exponent of the periodic term $N = 10$, $n = 6$, and electron density $n_{2D}a^2 = 0.75$.

This can be accounted for again, by considering the cyclotron motion of the electrons. When the magnetic field is small, the radius of the cyclotron orbit is large, so it is more likely that the electrons are scattered by the potential wall, which would result in and increase in resistivity. For higher magnetic fields however, electrons describe small radius cyclotron orbits. If the width of the quantum antiwire channel is large enough, and the electron cyclotron radius small enough, it is possible that the electron does not undergo numerous scatterings, thus for high magnetic field values the resistivity is lower and it maintains a nearly constant value.

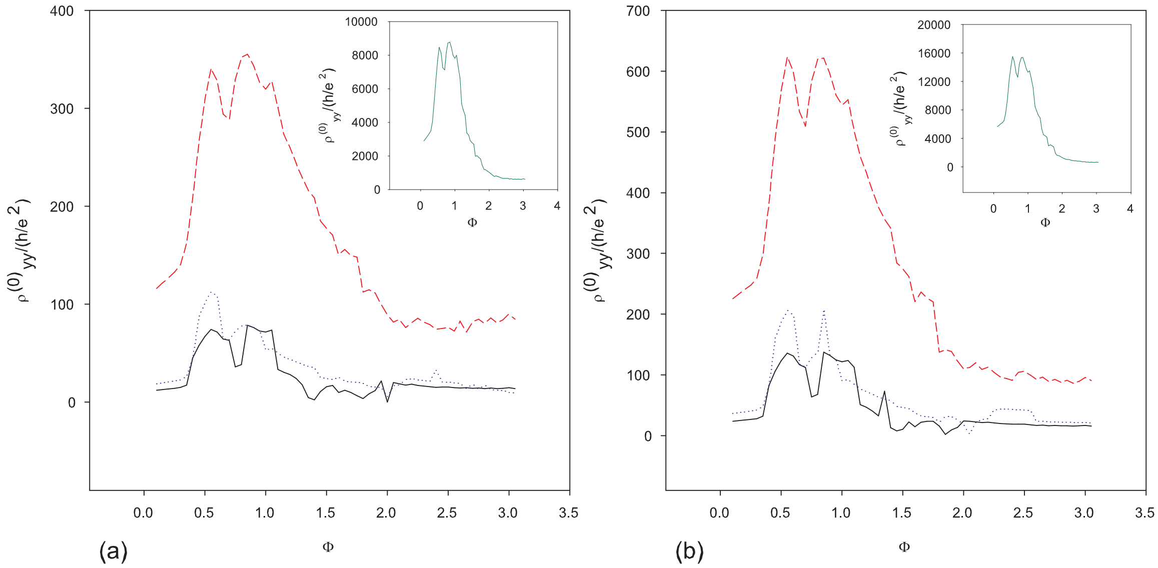

Figure 7.17: Longitudinal resistivities, ρ_{yy}, for positive values of the 1D modulation potential and different frequencies of the incident radiation field. The solid (black) line corresponds to those values of the frequency for which $\hbar\Omega = 0.25E_F$, the dotted (blue) line corresponds to $\hbar\Omega = 0.5E_F$, the short dashed (red) line corresponds to $\hbar\Omega = E_F$, while the solid (green) line (inset) is for $\hbar\Omega = 1.5E_F$. Other parameters used in this Figure are sample size $N_x = N_y = 10$, modulation potential strength $\bar{V} = 7.235$ for (a), and $\bar{V} = 10.235$ for (b). Exponent of the periodic term $N = 10$, $n = 6$, and electron density $n_{2D}a^2 = 0.75$.

By comparing all four plots of longitudinal resistivity, presented for four different potential values in Figures 7.16 (a) and (b), as well as 7.17 (a) and (b), it can be concluded that the lower the modulation potential strength, the lower the longitudinal resistivity. This means that shallower quantum antiwires present less resistance to the passage of charge carriers than deeper ones, which can, again, be explained with the scattering of electrons executing cyclotron motion off the potential walls.

7.1.13 AC versus DC Magnetotransport with 1D Modulation. Comparison of Results.

At the end of this Chapter, similarly to the 2D modulation case, we will compare the results obtained for AC transport to those for DC transport. In his dissertation Tae-ik Park [59], investigated the influence of the steepness and strength of modulation potential on the magnetotransport coefficients. He found step-like features in the transverse conductivities, and giant peaks in the transverse resistivities for strong modulation potential. Also, at low magnetic field, it was found that the transverse resistivities are quenched.

The main features, found by Park, of the magnetoresistivity coefficients for the 1D modulation in the absence of radiation are:

-step-like features in the transverse conductivities

-giant peaks in the transverse resistivities for strong modulation potential

-at low magnetic fields, the Hall resistivities are quenched

-the longitudinal resistivity shows large peaks for low magnetic field, and the shape of the peaks are influenced by the modulation potential strength.

-negative Hall resistivities appear for certain values of the magnetic field

In the AC magnetotransport case, all of the above features of the magnetotransport coefficients are confirmed, and the influence on the QMT coefficients of incident radiation of different frequencies is investigated. The AC transverse conductivities, similarly to the DC case, show the step-like feature. The steepness of the steps is influenced by the frequency of the incident radiation. For certain values of the incident radiation, and the modulation potential strength, the step-like features distort to a saw-tooth-like behavior.

In the case of AC Hall resistivities, the quenching at low magnetic fields is very pronounced. Giant peaks are observed in the Hall resistivity for certain values of the modulation potential strength. The variation of the radiation field frequency, influences the magnitude of the peaks. Negative Hall resistivities are also observed in the AC magnetotransport case.

Chapter 8

Summary and Conclusions

This dissertation investigates the AC magnetotransport of a 2DEG subject to electrostatic modulation using a Green's function method to express the conduction coefficients. Modulation potentials are imposed so that the conduction properties of a 2DEG in the presence of impurity scattering may be modeled. A 1D and 2D modulation potential was examined. When the magnitude of the 1D modulation potential is strong, this potential describes an array of short quantum wires or antiwires, as the electrons are subject to parabolic confinement along one of the propagation directions. The problem is still two-dimensional, as the electrons are able to tunnel between adjacent, parallel wire channels. The 2D modulation potential, for large positive or negative modulation strengths, models quantum dots and antidots, which can scatter or trap charge carriers. As a conclusion we provide a list of the most important results attained after the numerical investigation of 1D and 2D magnetotransport coefficients.

Negative 2D modulation

-The AC longitudinal conductivity for negative 2D modulation shows different behavior than the DC longitudinal conductivity. In the presence of radiation, the longitudinal conductivity shows large amplitude negative oscillations. For large modulation potential strengths the deviation of the AC longitudinal conductivity from its DC counterpart is drastic; the longitudinal conductivity becomes negative except for the lowest applied magnetic fields, while the DC longitudinal conductivity is positive. The amplitude of (negative or positive) oscillations is largest for the lowest frequencies of the incident radiation for the same modulation potential strength.

-The Hall conductivity in the 2D negative modulation potential case shows a series of positive oscillations in the AC case, with only a few negative oscillations. In contrast, the DC Hall conductivity only has negative oscillations in the magnetic field range investigated. With the increase of the modulation potential strength, the negative AC oscillations of the Hall conductivity diminish in the irradiated sample.

-The AC longitudinal resistivity for the negative 2D modulation has a large positive peak at low magnetic fields, then it goes through a series of small amplitude oscillations. Some of these oscillations are negative. The explanation for the appearance of negative longitudinal resistivities is resonant scattering. Resonant scattering occurs for those values of the applied magnetic field for which the scattering force overcomes the Lorentz force.

-The AC Hall resistivity also shows some negative oscillations in the case of 2D negative modulation. The amplitudes of these oscillations are larger for the larger values of the incident radiation frequency.

Positive 2D modulation

-The AC longitudinal conductivity for the positive 2D modulation shows the same general behavior as its DC counterpart. They both take small values for low magnetic fields, and increase as the applied magnetic field increases. The magnitude of the AC longitudinal conductivity, as compared to the DC values, is reduced in the presence of radiation. There are no negative values taken by the AC longitudinal conductivity in the positive 2D modulation case.

-The AC Hall conductivity for the positive 2D modulation is again showing some deviations from the DC case, as it becomes negative for small portions of the applied magnetic field, while the DC Hall conductivity shows only positive oscillations. The negative AC oscillations are due to backscattering caused by commensurability effects between the cyclotron orbit and the potential period. The smaller the frequency of the incident radiation, the larger the amplitude of the negative and positive oscillations.

-The 2D longitudinal resistivity has no negative oscillations in the AC or DC case. When the incident radiation frequency increases, the value of the longitudinal resistivity also increases.

-The 2D AC Hall resistivity for positive modulation potential shows giant low-field magnetoresistance oscillations in the strong modulation potential case. Such giant oscillations were also found in the DC case in previous work. Therefore, the modulation potential strength plays an important role in the behavior of the Hall resistivity for the 2D positive modulation. The magnitude of oscillations is influenced by the frequency of the incident radiation; the larger the applied field frequency, the larger the oscillations.

Negative 1D modulation

-The 1D transverse AC conductivity for negative modulation shows similarities to the unmodulated case for low values of the modulation potential, and high values of the radiation field frequency. For low frequency, the low modulation transverse AC conductivity shows step-like features.

-The 1D Hall AC conductivity is zero for low magnetic field values (below a threshold value) for the entire range of negative modulation potentials investigated. This is also characteristic to the DC Hall conductivity.

-The 1D longitudinal conductivity shows free 2DEG behavior for low strength negative modulations. With the increase of the modulation the longitudinal conductivity becomes negative in the low magnetic field range, and it shows positive to negative oscillations for larger magnetic fields.

-The 1D transverse resistivity shows step-like behavior for low modulation potential strengths. For high modulation strengths the transverse resistivity shows giant oscillations in the low magnetic field region.

-The 1D AC Hall resistivities are quenched in the low magnetic field region. They show step-like behavior in the large magnetic field region, where they take negative values. For the lowest incident radiation frequency, the values become positive for the highest magnetic fields investigated.

-The 1D AC longitudinal resistivity shows step-like behavior in the low modulation case. For higher modulation strengths it shows positive oscillations. The values of the longitudinal resistivity increase as the incident radiation frequency increases.

Positive 1D modulation

-For low modulation potential, the 1D AC transverse conductivity for positive modulation shows step-like behavior. For higher modulation potential strengths the steps disappear and the transverse conductivity increases as the applied magnetic field increases. For certain values of the magnetic field, the transverse conductivity goes through sudden drops or increases due to commensurability effects between the applied modulation potential and magnetic field.

-The 1D AC Hall conductivity is quenched for low magnetic field values. After a threshold magnetic field value is exceeded, the Hall conductivity goes through a series of negative to positive oscillations for certain values of the incident radiation. There are important qualitative and quantitative differences between the behavior of the Hall conductivity for lower and higher incident radiation frequencies. For the lower frequencies, the oscillatory behavior disappears, and the Hall conductivity is negative, and it goes through a series of steps.

-The longitudinal conductivity for positive modulation in the 1D AC case takes a large positive value for low magnetic fields. With the increase of the potential strength and the magnetic field the longitudinal conductivity decreases at first, and then it starts increasing and going through a series of oscillations for larger magnetic fields.

-The 1D transverse resistivity for the positive modulation case shows different behavior in the low modulation case, then for higher modulations strengths. In the low-modulation case the transverse resistivity starts out at low values in the low magnetic field portion, then it increases to a maximum, from which it decreases again through a series of steps. For higher modulation potential strengths, the transverse resistivity takes large values for low magnetic field, and it decreases through a series of positive oscillations as the magnetic field increases. The transverse resistivity takes giant values with the increase of the modulation potential strength and high values of the incident radiation field frequency.

-The 1D Hall resistivity is quenched in the low magnetic field region for the positive 1D modulation. In the low modulation case it shows step-like behavior. In the higher modulation limit it takes a giant negative dip for the largest incident radiation frequency.

-The longitudinal resistivity in the positive 1D modulation case has low values for small applied magnetic fields. It increases for intermediate values of the magnetic field, after which it goes through a series of positive oscillations. The oscillations have giant amplitude for the highest modulation potential and the highest incident radiation frequency.

Appendices

Appendix A

Longitudinal Conductivity Calculation for 2D Modulation

To obtain the longitudinal conductivity we need to calculate the matrix elements v_{μ}^{NM} and v_{ν}^{MN} for the velocity operator between the following states:

$$|N\rangle = \psi_{j',X_0'}\left(\vec{x}'\right) = |j', X_0'\rangle = \sum_{n',m'} C_{n'm'}\left(j', X_0'\right) \phi_{n',X_0'+m'GL_H^2}\left(\vec{x}'\right) \tag{A.1}$$

and

$$|M\rangle = \psi_{j,X_0}\left(\vec{x}\right) = |j, X_0\rangle = \sum_{n,m} C_{n,m}\left(j, X_0\right) \phi_{n,X_0+mGL_H^2}\left(\vec{x}\right) \tag{A.2}$$

In equation (A.1) the notation $\phi_{n',X_0'+m'GL_H^2}\left(\vec{x}'\right)$ stands for:

$$\begin{aligned}\phi_{n',X_0'+m'GL_H^2}\left(\vec{x}'\right) &= \frac{1}{\sqrt{L_y}}\exp\left[-\frac{i\left(X_0'+m'GL_H^2\right)y'}{L_H^2}\right]\sqrt{\frac{1}{\pi^{1/2}L_H2^{n'}n'!}}\\ \cdot\exp&\left[-\frac{\left(x'-X_0'-m'GL_H^2\right)^2}{2L_H^2}\right]H_{n'}\left(\frac{x'-X_0'-m'GL_H^2}{L_H}\right)\end{aligned} \tag{A.3}$$

and in equation (A.2) $\phi_{n,X_0+mGL_H^2}\left(\vec{x}\right)$ can be written as:

$$\begin{aligned}\phi_{n,X_0+mGL_H^2}\left(\vec{x}\right) &= \frac{1}{\sqrt{L_y}}\exp\left[-\frac{i\left(X_0+mGL_H^2\right)y}{L_H^2}\right]\sqrt{\frac{1}{\pi^{1/2}L_H2^{n}n!}}\\ \cdot\exp&\left[-\frac{\left(x-X_0-mGL_H^2\right)^2}{2L_H^2}\right]H_{n}\left(\frac{x-X_0-mGL_H^2}{L_H}\right)\end{aligned} \tag{A.4}$$

Substituting the explicit forms of the wave functions into the expression of the longitudinal conductivity, we arrive to the lengthy expression:

$$
\begin{aligned}
L_{xx}^{(0)}\left(\Omega\right) = {} & \frac{i\hbar e^{2}}{2\hbar\Omega AM^{*2}}\int\limits_{-\infty}^{\infty} d\varepsilon f\left(\varepsilon\right)\sum_{j,j'}\left(\frac{L_y}{2\pi L_H^2}\right)^{2}\int\limits_{-\frac{G}{2}L_H^2}^{\frac{G}{2}L_H^2} dX_0\int\limits_{-\frac{G}{2}L_H^2}^{\frac{G}{2}L_H^2} dX_0' \\
& \cdot\sum_{n,m,n',m'} C_{n'm'}^{*}\left(j',X_0'\right)C_{nm}\left(j,X_0\right)\sqrt{\frac{1}{\pi L_H^2 2^{n+n'}n!n'!}} \\
& \cdot\frac{1}{L_y}\int dy\exp\left[\frac{i\left(X_0'+m'GL_H^2-X_0-mGL_H^2\right)y}{L_H^2}\right] \\
& \cdot\int dx\exp\left[-\frac{\left(x-X_0'-m'GL_H^2\right)^{2}}{2L_H^2}\right]H_n\left(\frac{x-X_0'-m'GL_H^2}{L_H}\right)p_x \\
& \cdot\exp\left[-\frac{\left(x-X_0-mGL_H^2\right)^{2}}{2L_H^2}\right]H_{n'}\left(\frac{x-X_0-mGL_H^2}{L_H}\right) \\
& \cdot\sum_{l,k,l',k'} C_{lk}^{*}\left(j,X_0\right)C_{l'k'}\left(j',X_0'\right)\sqrt{\frac{1}{\pi L_H^2 2^{l+l'}l!l'!}} \\
& \cdot\frac{1}{L_y}\int dy'\exp\left[\frac{i\left(X_0+kGL_H^2-X_0'-k'GL_H^2\right)y'}{L_H^2}\right] \\
& \cdot\int dx'\exp\left[-\frac{\left(x'-X_0-lGL_H^2\right)^{2}}{2L_H^2}\right]H_l\left(\frac{x'-X_0-lGL_H^2}{L_H}\right)p_{x'} \\
& \cdot\exp\left[-\frac{\left(x'-X_0'-l'GL_H^2\right)^{2}}{2L_H^2}\right]H_{l'}\left(\frac{x'-X_0'-l'GL_H^2}{L_H}\right) \\
& \cdot\left\{\left[\frac{\delta\left[\varepsilon-\varepsilon_{j'}\left(X_0'\right)\right]}{\varepsilon+\hbar\Omega-\varepsilon_j\left(X_0\right)+i\eta}-\frac{\delta\left[\varepsilon-\varepsilon_{j'}\left(X_0'\right)\right]}{\varepsilon-\hbar\Omega-\varepsilon_j\left(X_0\right)+i\eta}\right]-\right. \\
& \left.-\left[\frac{\delta\left[\varepsilon-\varepsilon_j\left(X_0\right)\right]}{\varepsilon+\hbar\Omega-\varepsilon_{j'}\left(X_0'\right)-i\eta}-\frac{\delta\left[\varepsilon-\varepsilon_j\left(X_0\right)\right]}{\varepsilon-\hbar\Omega-\varepsilon_{j'}\left(X_0'\right)-i\eta}\right]\right\}
\end{aligned}
\tag{A.5}
$$

We perform the $\int dy$ and $\int dy'$ integrations first, considering only the $m = m'$ (respectively $k = k'$) case. The $\int dy$ integration yields:

$$
\frac{1}{L_y}\int dy\exp\left[\frac{i\left(X_0'+mGL_H^2-X_0-mGL_H^2\right)y}{L_H^2}\right] = \frac{2\pi L_H^2}{L_y}\delta\left(X_0'-X_0\right) \tag{A.6}
$$

The $\int dy'$ integration will have the exact same result as the above expressed in equation (A.6) as we may use the even property of the Dirac delta function. Substituting the results of the y and y' integrations obtained above into equation (A.5) the $\int_{-\frac{G}{2}L_H^2}^{\frac{G}{2}L_H^2} dX_0'$ integration can also be performed using the Dirac delta obtained in (A.6). After we perform this third integration the $\int dx$ and $\int dx'$ integrations in equation (A.5) can also be performed. These two integrals are identical, except that they are written in terms of different variables, so they both have the same result given below for the x–integration:

$$\sqrt{\frac{1}{\pi L_H^2 2^{n+n'} n! n'!}} \int dx \exp\left[-\frac{\left(x - X_0 - mGL_H^2\right)^2}{2L_H^2}\right] H_n\left(\frac{x - X_0 - mGL_H^2}{L_H}\right) p_x$$
$$\cdot \exp\left[-\frac{\left(x - X_0 - mGL_H^2\right)^2}{2L_H^2}\right] H_{n'}\left(\frac{x - X_0 - mGL_H^2}{L_H}\right) = \langle n'| \, p_x \, |n\rangle$$
$$= i\sqrt{\frac{M^*\hbar\omega_c}{2}} \left(-\sqrt{n}\delta_{n',n-1} + \sqrt{n+1}\delta_{n',n+1}\right) = \frac{i\hbar}{\sqrt{2}L_H} \left(-\sqrt{n}\delta_{n',n-1} + \sqrt{n+1}\delta_{n',n+1}\right) \tag{A.7}$$

Using the results obtained thus far in the calculation, the longitudinal conductivity may be written as:

$$\begin{aligned}
&L_{xx}^{(0)}\left(\Omega\right) = \frac{i\hbar e^2 L_y}{4\pi\hbar\Omega A L_H^2 M^{*2}} \int\limits_{-\infty}^{\infty} d\varepsilon f\left(\varepsilon\right) \sum_{j,j'} \int\limits_{-\frac{G}{2}L_H^2}^{\frac{G}{2}L_H^2} dX_0 \\
&\cdot \frac{i\hbar}{\sqrt{2}L_H} \sum_{n,m,n'} C_{n'm}^{*}\left(j', X_0\right) C_{nm}\left(j, X_0\right) \left(-\sqrt{n}\delta_{n',n-1} + \sqrt{n+1}\delta_{n',n+1}\right) \\
&\cdot \frac{i\hbar}{\sqrt{2}L_H} \sum_{l,k,l'} C_{lk}^{*}\left(j, X_0\right) C_{l'k}\left(j', X_0\right) \left(-\sqrt{l}\delta_{l',l-1} + \sqrt{l+1}\delta_{l',l+1}\right) \\
&\cdot \left\{ \left[\frac{\delta\left[\varepsilon - \varepsilon_{j'}\left(X_0\right)\right]}{\varepsilon + \hbar\Omega - \varepsilon_j\left(X_0\right) + i\eta} - \frac{\delta\left[\varepsilon - \varepsilon_{j'}\left(X_0\right)\right]}{\varepsilon - \hbar\Omega - \varepsilon_j\left(X_0\right) + i\eta} \right] \right. \\
&\left. - \left[\frac{\delta\left[\varepsilon - \varepsilon_{j}\left(X_0\right)\right]}{\varepsilon + \hbar\Omega - \varepsilon_{j'}\left(X_0\right) - i\eta} - \frac{\delta\left[\varepsilon - \varepsilon_{j}\left(X_0\right)\right]}{\varepsilon - \hbar\Omega - \varepsilon_{j'}\left(X_0\right) - i\eta} \right] \right\}
\end{aligned} \tag{A.8}$$

The summations over n' and l' in equation (A.8) are now easy to perform using the Kronecker deltas that appeared. Introduce the following notation for one of the structure factors:

$$\begin{aligned}
&F_{j,X_0;j',X_0}^{(2)} = -F_{j',X_0;j,X_0}^{(2)} = \int\limits_{A} d\vec{x} \psi_{j,X_0}^{*}\left(\vec{x}\right) \frac{\partial}{\partial x} \psi_{j',X_0}\left(\vec{x}\right) \\
&= \frac{1}{\sqrt{2}L_H} \sum_{n,m} C_{n,m}\left(j, X_0\right) \left[\sqrt{n+1} C_{n+1,m}^{*}\left(j', X_0\right) - \sqrt{n} C_{n-1,m}^{*}\left(j', X_0\right)\right]
\end{aligned} \tag{A.9}$$

The symmetry property over j and j' of the structure factor indicated above in equation (A.9) can easily be verified as follows:

$$\begin{aligned}
&F_{j,X_0;j',X_0}^{(2)*} = \int\limits_{A} d\vec{x} \psi_{j,X_0}\left(\vec{x}\right) \frac{\partial}{\partial x} \psi_{j',X_0}^{*}\left(\vec{x}\right) = \psi_{j,X_0}\left(\vec{x}\right) \psi_{j',X_0}^{*}\left(\vec{x}\right)\Big|_{-\infty}^{+\infty} \\
&- \int\limits_{A} d\vec{x} \psi_{j',X_0}^{*}\left(\vec{x}\right) \frac{\partial}{\partial y} \psi_{j,X_0}\left(\vec{x}\right) = - \int\limits_{A} d\vec{x} \psi_{j',X_0}^{*}\left(\vec{x}\right) \frac{\partial}{\partial y} \psi_{j,X_0}\left(\vec{x}\right) = -F_{j',X_0;j,X_0}^{(2)}
\end{aligned} \tag{A.10}$$

Using the notation introduced in (A.9), the longitudinal conductivity may be written as:

$$\begin{aligned}
L_{xx}^{(0)}(\Omega) = \frac{i\hbar^3 e^2 L_y}{4\pi\hbar\Omega A L_H^2 M^{*2}} \int\limits_{-\infty}^{\infty} d\varepsilon f(\varepsilon) \sum_{j,j'} \int\limits_{-\frac{G}{2}L_H^2}^{\frac{G}{2}L_H^2} dX_0 \left(F_{j,X_0;j',X_0}^{(2)}\right)^2 \\
\cdot \left\{ \left[\frac{\delta\left[\varepsilon - \varepsilon_{j'}(X_0)\right]}{\varepsilon + \hbar\Omega - \varepsilon_j(X_0) + i\eta} - \frac{\delta\left[\varepsilon - \varepsilon_{j'}(X_0)\right]}{\varepsilon - \hbar\Omega - \varepsilon_j(X_0) + i\eta} \right] \right. \\
\left. - \left[\frac{\delta\left[\varepsilon - \varepsilon_j(X_0)\right]}{\varepsilon + \hbar\Omega - \varepsilon_{j'}(X_0) - i\eta} - \frac{\delta\left[\varepsilon - \varepsilon_j(X_0)\right]}{\varepsilon - \hbar\Omega - \varepsilon_{j'}(X_0) - i\eta} \right] \right\}
\end{aligned} \tag{A.11}$$

This is the equation of the longitudinal conductivity, which is used in section 5.1.

Appendix B

2D Longitudinal Conductivity Formula Used in the Numerical Calculations

In the numerical calculations one would use equation (5.7) in a slightly modified form. First of all one can perform the $\int\limits_{-\infty}^{\infty} d\varepsilon$ integration:

$$\begin{gathered} L_{xx}^{(0)}\left(\Omega\right) = \frac{\pi\hbar^3 e^2 N_y \Phi}{\hbar\Omega A M^{*2}} \sum_{j,j'} \int\limits_{-\frac{G}{2}L_H^2}^{\frac{G}{2}L_H^2} \frac{dX_0}{a} \left(F_{j,X_0;j',X_0}^{(2)}\right)^2 \\ \cdot \left\{\left\{f\left[\varepsilon_{j'}\left(X_0\right) - \hbar\Omega\right] - f\left[\varepsilon_{j'}\left(X_0\right)\right]\right\} \delta\left[\varepsilon_j\left(X_0\right) - \varepsilon_{j'}\left(X_0\right) + \hbar\Omega\right] \right. \\ \left. - \left\{f\left[\varepsilon_{j'}\left(X_0\right) + \hbar\Omega\right] - f\left[\varepsilon_{j'}\left(X_0\right)\right]\right\} \delta\left[\varepsilon_j\left(X_0\right) - \varepsilon_{j'}\left(X_0\right) - \hbar\Omega\right]\right\} \end{gathered} \tag{B.1}$$

In equation (B.1) $f\left[\varepsilon_{j'}\left(X_0\right)\right]$ denotes the Fermi–Dirac distribution function, which can be written explicitly as:

$$f\left[\varepsilon_{j'}\left(X_0\right)\right]=\left\{\exp\frac{\left[\varepsilon_{j'}\left(X_0\right)-\varepsilon_F\right]}{k_BT}+1\right\}^{-1} \tag{B.2}$$

In the low temperature limit, the Fermi–Dirac distribution function reduces to the Heaviside step function. Thus, when $T \to 0$, equation (B.2) may be replaced by:

$$f\left[\varepsilon_{j}\left(X_0\right)\right]=\left\{\exp\frac{\left[\varepsilon_{j}\left(X_0\right)-\varepsilon_F\right]}{k_BT}+1\right\}^{-1}=\theta\left[\varepsilon_F-\varepsilon_j\left(X_0\right)\right] \tag{B.3}$$

Equation (B.3) is the form of the Fermi–Dirac distribution function used in the numerical calculations. The next step in transforming the 2D longitudinal conductivity formula into a form appropriate to numerical calculations is to rewrite variables appearing in equation (B.1) into convenient dimensionless variables. Using the zero temperature Fermi–Dirac distribution function and dimensionless variables, we obtain a modified form of equation (B.1):

$$\begin{aligned}
&L_{xx}^{(0)}\left(\Omega\right)=\frac{\pi^2\hbar^3e^2N_y\Phi}{a^2\hbar^2\omega_c\Omega AM^{*2}}\sum_{j,j'}\int_{-\frac{1}{2}}^{\frac{1}{2}}d\bar{k}_y\\
&\left\{\sum_{n,m}C_{n,m}\left(j,\bar{k}_y\right)\left[\sqrt{n+1}C_{n+1,m}^{*}\left(j',\bar{k}_y\right)-\sqrt{n}C_{n-1,m}^{*}\left(j',\bar{k}_y\right)\right]\right\}^2\\
&\cdot\left\{\left\{\theta\left[\frac{\varepsilon_F-\varepsilon_{j'}\left(\bar{k}_y\right)+\hbar\Omega}{\hbar\omega_c}\right]-\theta\left[\frac{\varepsilon_F-\varepsilon_{j'}\left(\bar{k}_y\right)}{\hbar\omega_c}\right]\right\}\delta\left[\frac{\varepsilon_j\left(\bar{k}_y\right)}{\hbar\omega_c}-\frac{\varepsilon_{j'}\left(\bar{k}_y\right)}{\hbar\omega_c}+\frac{\Omega}{\omega_c}\right]\right.\\
&\left.-\left\{\theta\left[\frac{\varepsilon_F-\varepsilon_{j'}\left(\bar{k}_y\right)-\hbar\Omega}{\hbar\omega_c}\right]-\theta\left[\frac{\varepsilon_F-\varepsilon_{j'}\left(\bar{k}_y\right)}{\hbar\omega_c}\right]\right\}\delta\left[\frac{\varepsilon_j\left(\bar{k}_y\right)}{\hbar\omega_c}-\frac{\varepsilon_{j'}\left(\bar{k}_y\right)}{\hbar\omega_c}-\frac{\Omega}{\omega_c}\right]\right\}
\end{aligned} \tag{B.4}$$

The following is a list of dimensionless variables that will replace the ones used in equation(B.4) and in the Fortran programs:

$$\frac{k_y a}{2\pi} \equiv \bar{k}_y \tag{B.5}$$

$$\bar{\varepsilon}_F = \frac{\varepsilon_F}{\hbar\omega_c} \tag{B.6}$$

$$\bar{\varepsilon}_j\left(\bar{k}_y\right) = \frac{\varepsilon_j\left(\bar{k}_y\right)}{\hbar\omega_c} \tag{B.7}$$

$$\bar{\varepsilon}_{j'}\left(\bar{k}_y\right) = \frac{\varepsilon_{j'}\left(\bar{k}_y\right)}{\hbar\omega_c} \tag{B.8}$$

$$\bar{\Omega} = \frac{\Omega}{\omega_c} \tag{B.9}$$

The multiplying factor which consists of the product of some universal constants and experimental parameters used in the investigation of the problem and which stands in front of the first integral in the expression of the longitudinal conductivity formula (B.4) can also be expressed in terms of dimensionless variables as:

$$\frac{\pi^2\hbar^3 e^2 N_y \Phi}{a^2\hbar^2\omega_c \Omega A M^{*2}} = \frac{e^2}{h} \cdot \frac{\pi}{\Phi\bar{\Omega}N_x} \tag{B.10}$$

Combining all of the above results, the final form of the 2D longitudinal conductivity appropriate for numerical calculation is written as:

$$L_{xx}^{(0)}\left(\Omega\right) = \frac{e^2}{h} \cdot \frac{\pi}{\Phi\bar{\Omega}N_x} \sum_{j,j'} \int\limits_{-\frac{1}{2}}^{\frac{1}{2}} d\bar{k}_y$$

$$\left\{ \sum_{n,m} C_{n,m}\left(j,\bar{k}_y\right) \left[\sqrt{n+1} C^*_{n+1,m}\left(j',\bar{k}_y\right) - \sqrt{n} C^*_{n-1,m}\left(j',\bar{k}_y\right) \right] \right\}^2 \tag{B.11}$$

$$\cdot \left\{ \left\{ \theta\left[\bar{\varepsilon}_F - \bar{\varepsilon}_{j'}\left(\bar{k}_y\right) + \bar{\Omega}\right] - \theta\left[\bar{\varepsilon}_F - \bar{\varepsilon}_{j'}\left(\bar{k}_y\right)\right] \right\} \delta\left[\bar{\varepsilon}_j\left(\bar{k}_y\right) - \bar{\varepsilon}_{j'}\left(\bar{k}_y\right) + \bar{\Omega}\right] \right.$$

$$\left. - \left\{ \theta\left[\bar{\varepsilon}_F - \bar{\varepsilon}_{j'}\left(\bar{k}_y\right) - \bar{\Omega}\right] - \theta\left[\bar{\varepsilon}_F - \bar{\varepsilon}_{j'}\left(\bar{k}_y\right)\right] \right\} \delta\left[\bar{\varepsilon}_j\left(\bar{k}_y\right) - \bar{\varepsilon}_{j'}\left(\bar{k}_y\right) - \bar{\Omega}\right] \right\}$$

Appendix C

Hall Conductivity Calculation for 2D Modulation

We start our calculation from the equation:

$$\begin{gathered}
L^{(0)}_{\mu\nu}\left(\Omega\right)=\frac{i\hbar e^{2}}{2\hbar\Omega A}\int\limits_{-\infty}^{\infty}d\varepsilon f\left(\varepsilon\right)\sum_{M,N}v^{NM}_{\mu}v^{MN}_{\nu}\\
\cdot\left\{\left[G^{(0+)}_{M}\left(\varepsilon+\hbar\Omega\right)-G^{(0+)}_{M}\left(\varepsilon-\hbar\Omega\right)\right]\delta\left(\varepsilon-\varepsilon_{N}\right)\right.\\
\left.-\delta\left(\varepsilon-\varepsilon_{M}\right)\left[G^{(0-)}_{N}\left(\varepsilon+\hbar\Omega\right)-G^{(0-)}_{N}\left(\varepsilon-\hbar\Omega\right)\right]\right\}
\end{gathered}\tag{C.1}$$

Thus to express $L^{(0)}_{yx}\left(\Omega\right)$ we need to calculate the following velocity matrix elements: $\left\langle N\right|v_{y}\left|M\right\rangle$ and $\left\langle M\right|v_{x}\left|N\right\rangle$. Use:

$$\left\langle N\right|v_{y}\left|M\right\rangle=\left\langle N\right|\frac{p_{y}}{M^{*}}\left|M\right\rangle+\left\langle N\right|\frac{eBx}{M^{*}}\left|M\right\rangle\tag{C.2}$$

$$\left\langle M\right|v_{x}\left|N\right\rangle=\left\langle M\right|\frac{p_{x}}{M^{*}}\left|N\right\rangle\tag{C.3}$$

In equations (C.2) and (C.3) above $|N\rangle$ and $|M\rangle$, similarly to the previous calculation of the longitudinal conductivity, stand for:

$$|N\rangle = \psi_{j',X_0'}\left(\vec{x}'\right) = |j', X_0'\rangle = \sum_{n',m'} C_{n'm'}\left(j', X_0'\right) \phi_{n',X_0'+m'GL_H^2}\left(\vec{x}'\right) \tag{C.4}$$

In equation (C.4) the notation $\phi_{n',X_0'+m'GL_H^2}\left(\vec{x}'\right)$ stands for:

$$\begin{aligned} \phi_{n',X_0'+m'GL_H^2}\left(\vec{x}'\right) &= \frac{1}{\sqrt{L_y}} \exp\left[-\frac{i\left(X_0' + m'GL_H^2\right)y'}{L_H^2}\right] \sqrt{\frac{1}{\pi^{1/2}L_H 2^{n'} n'!}} \\ \cdot \exp&\left[-\frac{\left(x' - X_0' - m'GL_H^2\right)^2}{2L_H^2}\right] H_{n'}\left(\frac{x' - X_0' - m'GL_H^2}{L_H}\right) \end{aligned} \tag{C.5}$$

$$|M\rangle = \psi_{j,X_0}\left(\vec{x}\right) = |j, X_0\rangle = \sum_{n,m} C_{n,m}\left(j, X_0\right) \phi_{n,X_0+mGL_H^2}\left(\vec{x}\right) \tag{C.6}$$

and in equation (C.6) $\phi_{n,X_0+mGL_H^2}\left(\vec{x}\right)$ can be written as:

$$\begin{aligned} \phi_{n,X_0+mGL_H^2}\left(\vec{x}\right) &= \frac{1}{\sqrt{L_y}} \exp\left[-\frac{i\left(X_0 + mGL_H^2\right)y}{L_H^2}\right] \sqrt{\frac{1}{\pi^{1/2}L_H 2^{n} n!}} \\ \cdot \exp&\left[-\frac{\left(x - X_0 - mGL_H^2\right)^2}{2L_H^2}\right] H_{n}\left(\frac{x - X_0 - mGL_H^2}{L_H}\right) \end{aligned} \tag{C.7}$$

The Hall conductivity (C.1) can be split into two components:

$$L_{yx}^{(0)}\left(\Omega\right) = L_{yx}^{(0)}\left(\Omega\right)_1 + L_{yx}^{(0)}\left(\Omega\right)_2 \tag{C.8}$$

where the first component can be written as:

$$\begin{aligned} L_{yx}^{(0)}\left(\Omega\right)_1 = \frac{i\hbar e^2}{2\hbar\Omega A}\int\limits_{-\infty}^{\infty} d\varepsilon f\left(\varepsilon\right)\sum_{M,N}\left\langle N\right|\frac{p_y}{M^*}\left|M\right\rangle\left\langle M\right|\frac{p_x}{M^*}\left|N\right\rangle \\ \cdot\left\{\left[G_M^{(0)+}\left(\varepsilon+\hbar\Omega\right)-G_M^{(0)+}\left(\varepsilon-\hbar\Omega\right)\right]\delta\left(\varepsilon-\varepsilon_N\right)\right. \\ \left.-\delta\left(\varepsilon-\varepsilon_M\right)\left[G_N^{(0)-}\left(\varepsilon+\hbar\Omega\right)-G_N^{(0)-}\left(\varepsilon-\hbar\Omega\right)\right]\right\} \end{aligned} \tag{C.9}$$

and the second component is:

$$\begin{aligned} L_{yx}^{(0)}\left(\Omega\right)_2 = \frac{i\hbar e^2}{2\hbar\Omega A}\int\limits_{-\infty}^{\infty} d\varepsilon f\left(\varepsilon\right)\sum_{M,N}\left\langle N\right|\frac{eBx}{M^*}\left|M\right\rangle\left\langle M\right|\frac{p_x}{M^*}\left|N\right\rangle \\ \cdot\left\{\left[G_M^{(0)+}\left(\varepsilon+\hbar\Omega\right)-G_M^{(0)+}\left(\varepsilon-\hbar\Omega\right)\right]\delta\left(\varepsilon-\varepsilon_N\right)\right. \\ \left.-\delta\left(\varepsilon-\varepsilon_M\right)\left[G_N^{(0)-}\left(\varepsilon+\hbar\Omega\right)-G_N^{(0)-}\left(\varepsilon-\hbar\Omega\right)\right]\right\} \end{aligned} \tag{C.10}$$

We have to substitute the explicit forms of the wave functions given above in equations (C.4)-(C.7) into the expression of the two components of the Hall conductivity (C.9) and (C.10). Then we follow the same procedure as indicated in Appendix (A) for the calculation of the longitudinal conductivity. We proceed and perform the indicated integrals. While performing the integrations, we make use of the following well-know relationships involving the matrix elements of the position and momentum operators of the harmonic oscillator, in addition to the ones listed in the longitudinal conductivity calculation:

$$\begin{aligned}\langle n'|\, x\, |n\rangle &= \sqrt{\frac{\hbar}{2M^{*}\omega_c}}\left(\sqrt{n}\delta_{n',n-1}+\sqrt{n+1}\delta_{n',n+1}\right)\\ &= \frac{1}{\sqrt{2}}\sqrt{\frac{\hbar}{eB}}\left(\sqrt{n}\delta_{n',n-1}+\sqrt{n+1}\delta_{n',n+1}\right)=\frac{L_H}{\sqrt{2}}\left(\sqrt{n}\delta_{n',n-1}+\sqrt{n+1}\delta_{n',n+1}\right)\end{aligned} \tag{C.11}$$

and

$$\langle l|\, p_{x'}\, |l'\rangle = i\sqrt{\frac{M^{*}\hbar\omega_c}{2}}\left(-\sqrt{l'}\delta_{l,l'-1}+\sqrt{l'+1}\delta_{l,l'+1}\right)=\frac{i\hbar}{\sqrt{2}L_H}\left(\sqrt{l'+1}\delta_{l,l'+1}-\sqrt{l'}\delta_{l,l'-1}\right) \tag{C.12}$$

After all the integrals are performed and the obtained results substituted into equation (C.8), we get:

$$\begin{aligned}L^{(0)}_{yx}(\Omega) &= -\frac{\hbar^3 e^2 L_y}{4\pi\hbar\Omega A M^{*2} L_H^2}\int\limits_{-\infty}^{\infty} d\varepsilon f(\varepsilon)\sum_{j,j'}\int\limits_{-\frac{G}{2}L_H^2}^{\frac{G}{2}L_H^2} dX_0\\ &\cdot\left[\frac{1}{L_H^2}F^{(1)}_{j',X_0;j,X_0}F^{(2)}_{j,X_0;j',X_0}+F^{(3)}_{j',X_0;j,X_0}F^{(2)}_{j,X_0;j',X_0}\right]\\ &\cdot\left\{\left[\frac{\delta\left[\varepsilon-\varepsilon_{j'}(X_0)\right]}{\varepsilon+\hbar\Omega-\varepsilon_j(X_0)+i\eta}-\frac{\delta\left[\varepsilon-\varepsilon_{j'}(X_0)\right]}{\varepsilon-\hbar\Omega-\varepsilon_j(X_0)+i\eta}\right]\right.\\ &-\left.\left[\frac{\delta\left[\varepsilon-\varepsilon_{j}(X_0)\right]}{\varepsilon+\hbar\Omega-\varepsilon_{j'}(X_0)-i\eta}-\frac{\delta\left[\varepsilon-\varepsilon_{j}(X_0)\right]}{\varepsilon-\hbar\Omega-\varepsilon_{j'}(X_0)-i\eta}\right]\right\}\end{aligned} \tag{C.13}$$

In equation (C.13) the following structure factors are used:

$$\begin{aligned} F^{(1)}_{j',X_0;j,X_0} &= \int\limits_A d\vec{x}\psi^*_{j',X_0}(\vec{x})x\psi_{j,X_0}(\vec{x}) \\ &= \frac{L_H}{\sqrt{2}}\sum_{n,m} C_{n,m}(j,X_0)\left(\sqrt{n+1}C^*_{n+1,m}(j',X_0)+\sqrt{n}C^*_{n-1,m}(j',X_0)\right) \end{aligned} \tag{C.14}$$

This structure factor has the following property:

$$F^{(1)*}_{j,X_0;j',X_0} = F^{(1)}_{j',X_0;j,X_0} \tag{C.15}$$

We can verify the validity of this symmetry property by the following:

$$F^{(1)*}_{j,X_0;j',X_0} = \int\limits_A d\vec{x}\psi_{j,X_0}(\vec{x})x\psi^*_{j',X_0}(\vec{x}) = \int\limits_A d\vec{x}\psi^*_{j',X_0}(\vec{x})\,x\psi_{j,X_0}(\vec{x}) = F^{(1)}_{j',X_0;j,X_0} \tag{C.16}$$

The second structure factor entering equation (C.13) was already introduced in Appendix (A) and its symmetry property was verified there, so we do not repeat the calculation here. We proceed by defining the third structure factor entering the equation of the Hall conductivity:

$$F^{(3)}_{j',X_0;j,X_0} = -i\int\limits_A d\vec{x}\psi^*_{j',X_0}(\vec{x})\frac{\partial}{\partial y}\psi_{j,X_0}(\vec{x}) = -G\sum_{n,m} mC^*_{n,m}(j',X_0)\,C_{n,m}(j,X_0) - \frac{X_0}{L_H^2}\delta_{j',j} \tag{C.17}$$

This structure factor has the symmetry property:

$$F^{(3)*}_{j,X_0;j',X_0} = F^{(3)}_{j',X_0;j,X_0} \tag{C.18}$$

The above property is verified as follows:

$$F^{(3)*}_{j,X_0;j',X_0} = i\int\limits_A d\vec{x}\psi_{j,X_0}(\vec{x})\frac{\partial}{\partial y}\psi^*_{j',X_0}(\vec{x}) = i\,\psi_{j,X_0}(\vec{x})\,\psi^*_{j',X_0}(\vec{x})\big|^{+\infty}_{-\infty} - i\int\limits_A d\vec{x}\psi^*_{j',X_0}(\vec{x})\frac{\partial}{\partial y}\psi_{j,X_0}(\vec{x})$$
$$= -i\int\limits_A d\vec{x}\psi^*_{j',X_0}(\vec{x})\frac{\partial}{\partial y}\psi_{j,X_0}(\vec{x}) = F^{(3)}_{j',X_0;j,X_0} \tag{C.19}$$

Now we would like to write equation (C.13) in a different form. We use the Dirac formula to write the Green's function terms in the Hall conductivity as a sum of a real (principal value integral) part and an imaginary (Dirac delta function) part. Then we use the symmetry properties of the structure factors listed above, and we write the structure factors themselves as a sum of real and imaginary parts. We obtain a very lengthy equation, but all the imaginary terms in that equation cancel, so we end up, as expected, with a real expression for the Hall conductivity. This expression is:

$$\begin{aligned}L^{(0)}_{yx}(\Omega) = &-\frac{\hbar^3 e^2 L_y}{2\pi\hbar\Omega A M^{*2} L_H^2}\int\limits_{-\infty}^{\infty} d\varepsilon f(\varepsilon)\sum_{j,j'}\int\limits_{-\frac{G}{2}L_H^2}^{\frac{G}{2}L_H^2} dX_0\delta\left[\varepsilon-\varepsilon_{j'}(X_0)\right]\\ &\cdot\left\{\frac{1}{L_H^2}\mathrm{Re}\left[F^{(1)}_{j',X_0;j,X_0}F^{(2)}_{j,X_0;j',X_0}\right]+\mathrm{Re}\left[F^{(3)}_{j',X_0;j,X_0}F^{(2)}_{j,X_0;j',X_0}\right]\right\}\\ &\cdot\left\{\frac{1}{\varepsilon+\hbar\Omega-\varepsilon_j(X_0)}-\frac{1}{\varepsilon-\hbar\Omega-\varepsilon_j(X_0)}\right\}\end{aligned} \tag{C.20}$$

We rearrange the equation and combine like terms:

$$
\begin{aligned}
L_{yx}^{(0)}(\Omega) &= \frac{\hbar^3 e^2 L_y}{\pi A M^{*2} L_H^2} \sum_{j,j'}{}^{\prime} f\left[\varepsilon_{j'}(X_0)\right] \int\limits_{-\frac{G}{2}L_H^2}^{\frac{G}{2}L_H^2} dX_0 \\
&\cdot \left\{ \frac{1}{L_H^2} \mathrm{Re}\left[F^{(1)}_{j',X_0;j,X_0} F^{(2)}_{j,X_0;j',X_0}\right] + \mathrm{Re}\left[F^{(3)}_{j',X_0;j,X_0} F^{(2)}_{j,X_0;j',X_0}\right] \right\} \\
&\cdot \frac{1}{\left[\varepsilon_{j'}(X_0) - \varepsilon_j(X_0)\right]^2 - (\hbar\Omega)^2}
\end{aligned}
\tag{C.21}
$$

The prime notation in equation (C.21) over the summation sign means that the summation will be performed only for those values of the indices j and j' for which the denominator is not zero. Thus the final form of the Hall conductivity is written using the partial density of states $D_{j',X_0}(\varepsilon)$ as:

$$
\begin{aligned}
L_{yx}^{(0)}(\Omega) &= \frac{\hbar^3 e^2 L_y}{\pi A M^{*2} L_H^2} \sum_{j,j'}{}^{\prime} \int\limits_{-\frac{G}{2}L_H^2}^{\frac{G}{2}L_H^2} dX_0 \\
&\cdot \left\{ \frac{1}{L_H^2} \mathrm{Re}\left[F^{(1)}_{j',X_0;j,X_0} F^{(2)}_{j,X_0;j',X_0}\right] + \mathrm{Re}\left[F^{(3)}_{j',X_0;j,X_0} F^{(2)}_{j,X_0;j',X_0}\right] \right\} \\
&\cdot \frac{1}{\left[\varepsilon_{j'}(X_0) - \varepsilon_j(X_0)\right]^2 - (\hbar\Omega)^2} \int\limits_{-\infty}^{\infty} d\varepsilon f(\varepsilon) D_{j',X_0}(\varepsilon)
\end{aligned}
\tag{C.22}
$$

Appendix D

2D Hall Conductivity Formula Used in the Numerical Calculations

We start this part by copying over the Hall conductivity formula obtained in the previous Appendix:

$$
\begin{aligned}
& L_{yx}^{(0)}(\Omega) = \frac{\hbar^3 e^2 L_y}{\pi A M^{*2} L_H^2} \sideset{}{'}\sum_{j,j'} \int\limits_{-\frac{G}{2}L_H^2}^{\frac{G}{2}L_H^2} dX_0 \\
& \cdot \left\{ \frac{1}{L_H^2} \mathrm{Re}\left[F^{(1)}_{j',X_0;j,X_0} F^{(2)}_{j,X_0;j',X_0} \right] + \mathrm{Re}\left[F^{(3)}_{j',X_0;j,X_0} F^{(2)}_{j,X_0;j',X_0} \right] \right\} \\
& \cdot \frac{1}{\left[\varepsilon_{j'}(X_0) - \varepsilon_j(X_0)\right]^2 - (\hbar\Omega)^2} \int\limits_{-\infty}^{\infty} d\varepsilon f(\varepsilon) D_{j',X_0}(\varepsilon)
\end{aligned}
\tag{D.1}
$$

We write the integration variable in the first integral in equation (D.1) in a dimensionless form using:

$$
X_0 \to \frac{k_y a}{2\pi} \tag{D.2}
$$

In the new variable, the Hall conductivity (D.1) may be written as:

$$
\begin{aligned}
L_{yx}^{(0)}\left(\Omega\right) = {} & \frac{2\hbar^3 e^2 L_y}{aAM^{*2}} \sum_{j,j'}{}^{\prime} \int\limits_{-\frac{1}{2}}^{\frac{1}{2}} d\left(\frac{k_y a}{2\pi}\right) \\
& \cdot \left\{ \frac{1}{L_H^2} \mathrm{Re}\left[F^{(1)}_{j',\frac{k_y a}{2\pi};j,\frac{k_y a}{2\pi}} F^{(2)}_{j,\frac{k_y a}{2\pi};j',\frac{k_y a}{2\pi}} \right] + \mathrm{Re}\left[F^{(3)}_{j',\frac{k_y a}{2\pi};j,\frac{k_y a}{2\pi}} F^{(2)}_{j,\frac{k_y a}{2\pi}{}_0;j',\frac{k_y a}{2\pi}} \right] \right\} \\
& \cdot \frac{1}{\left[\varepsilon_{j'}\left(\frac{k_y a}{2\pi}\right) - \varepsilon_j\left(\frac{k_y a}{2\pi}\right)\right]^2 - \left(\hbar\Omega\right)^2} \int\limits_{-\infty}^{\infty} d\varepsilon f\left(\varepsilon\right) D_{j',\frac{k_y a}{2\pi}}\left(\varepsilon\right)
\end{aligned}
\tag{D.3}
$$

Introduce the simplifying notation $\frac{k_y a}{2\pi} = L$. Use the rescaled values of the energy variables $\bar{\varepsilon}_j\left(L\right) = \frac{\varepsilon_j(L)}{\hbar\omega_c}$, $\bar{\varepsilon}_{j'}\left(L\right) = \frac{\varepsilon_{j'}(L)}{\hbar\omega_c}^2$, and $\bar{\Omega} = \frac{\Omega}{\omega_c}$. In the new variables the Hall conductivity formula becomes:

$$
\begin{aligned}
L_{yx}^{(0)}\left(\Omega\right) = {} & \frac{2\hbar^3 e^2 L_y}{aAM^{*2}\left(\hbar\omega_c\right)^2 L_H^2} \sum_{j,j'}{}^{\prime} \int\limits_{-\frac{1}{2}}^{\frac{1}{2}} dL \\
& \cdot \left\{ \mathrm{Re}\left[F^{(1)}_{j',L;j,L} F^{(2)}_{j,L;j',L} \right] + \frac{1}{L_H^2} \mathrm{Re}\left[F^{(3)}_{j',L;j,L} F^{(2)}_{j,L;j',L} \right] \right\} \\
& \cdot \frac{1}{\left[\bar{\varepsilon}_{j'}\left(L\right) - \bar{\varepsilon}_j\left(L\right)\right]^2 - \left(\bar{\Omega}\right)^2} \int\limits_{-\infty}^{\infty} d\bar{\varepsilon} f\left(\bar{\varepsilon}\right) D_{j',L}\left(\bar{\varepsilon}\right)
\end{aligned}
\tag{D.4}
$$

The factor in front of the expression on the right-hand side of the above equation can be written in a different form. We arrive to the final form of the Hall conductivity used in numerical calculations for the 2D periodic cosine type modulation case:

$$
\begin{aligned}
L_{yx}^{(0)}\left(\Omega\right) &= \frac{e^2}{h}\frac{2}{N_x\Phi}\sum_{j,j'}{}^{\prime}\int\limits_{-\frac{1}{2}}^{\frac{1}{2}} dL \\
&\cdot\left\{\mathrm{Re}\left[F_{j',L;j,L}^{(1)}F_{j,L;j',L}^{(2)}\right]+2\sqrt{\frac{\pi}{\Phi}}\mathrm{Re}\left[F_{j',L;j,L}^{(3)}F_{j,L;j',L}^{(2)}\right]\right\} \\
&\cdot\frac{1}{\left[\bar{\varepsilon}_{j'}\left(L\right)-\bar{\varepsilon}_{j}\left(L\right)\right]^2-\left(\bar{\Omega}\right)^2}\int\limits_{-\infty}^{\infty} d\bar{\varepsilon} f\left(\bar{\varepsilon}\right)D_{j',L}\left(\bar{\varepsilon}\right)
\end{aligned}
\tag{D.5}
$$

Appendix E

Transverse Conductivity Calculation for 1D Modulation

For the one-dimensional cosine potential modulation problem, we need to calculate the $\langle M| v_x |N\rangle$ and $\langle N| v_x |M\rangle$ matrix elements of the velocity operator for the eigenfunctions of the unperturbed Hamiltonian given by:

$$|N\rangle = \psi_{j,X_0}\left(\vec{x}\right) = |j, X_0\rangle = \sum_n C_n\left(j, X_0\right)\phi_{n,X_0}\left(\vec{x}\right) \tag{E.1}$$

and

$$|M\rangle = \psi_{j',X'_0}\left(\vec{x}'\right) = |j', X'_0\rangle = \sum_{n'} C_{n'}\left(j', X'_0\right)\phi_{n',X'_0}\left(\vec{x}'\right) \tag{E.2}$$

In equations (E.1) $\phi_{n,X_0}\left(\vec{x}\right)$ stands for:

$$\phi_{n,X_0}\left(\vec{x}\right) = \frac{1}{\sqrt{L_y}}\exp\left(-\frac{iX_0 y}{L_H^2}\right)\sqrt{\frac{1}{\pi^{1/2}L_H 2^n n!}}\exp\left[-\frac{\left(x-X_0\right)^2}{2L_H^2}\right]H_n\left(\frac{x-X_0}{L_H}\right) \tag{E.3}$$

and $\phi_{n',X_0'}(\vec{x}')$ has a similar definition.

The initial expression for the transverse conductivity (along the modulation direction) in the 1D case is given by the lengthy expression:

$$
\begin{aligned}
L_{xx}^{(0,1D)}(\Omega) &= \frac{i\hbar e^2}{2\hbar\Omega AM^{*2}} \int_{-\infty}^{\infty} d\varepsilon f(\varepsilon) \sum_{j,j'} \left(\frac{L_y}{2\pi L_H^2}\right)^2 \int_{-\frac{G}{2}L_H^2}^{\frac{G}{2}L_H^2} dX_0 \int_{-\frac{G}{2}L_H^2}^{\frac{G}{2}L_H^2} dX_0' \\
&\cdot \sum_{n,n'} C_{n'}^*(j',X_0') C_n(j,X_0) \sqrt{\frac{1}{\pi L_H^2 2^{n+n'} n! n'!}} \frac{1}{L_y} \int dy \exp\left[\frac{i(X_0'-X_0)y}{L_H^2}\right] \\
&\cdot \int dx \exp\left[-\frac{(x-X_0')^2}{2L_H^2}\right] H_n\left(\frac{x-X_0'}{L_H}\right) p_x \exp\left[-\frac{(x-X_0)^2}{2L_H^2}\right] H_{n'}\left(\frac{x-X_0}{L_H}\right) \\
&\cdot \sum_{l,l'} C_l^*(j,X_0) C_{l'}(j',X_0') \sqrt{\frac{1}{\pi L_H^2 2^{l+l'} l! l'!}} \frac{1}{L_y} \int dy' \exp\left[\frac{i(X_0-X_0')y'}{L_H^2}\right] \\
&\cdot \int dx' \exp\left[-\frac{(x'-X_0)^2}{2L_H^2}\right] H_l\left(\frac{x'-X_0}{L_H}\right) p_{x'} \exp\left[-\frac{(x'-X_0')^2}{2L_H^2}\right] H_{l'}\left(\frac{x'-X_0'}{L_H}\right) \\
&\cdot \left\{\left[\frac{\delta[\varepsilon-\varepsilon_{j'}(X_0')]}{\varepsilon+\hbar\Omega-\varepsilon_j(X_0)+i\eta} - \frac{\delta[\varepsilon-\varepsilon_{j'}(X_0')]}{\varepsilon-\hbar\Omega-\varepsilon_j(X_0)+i\eta}\right] - \right. \\
&\left. - \left[\frac{\delta[\varepsilon-\varepsilon_j(X_0)]}{\varepsilon+\hbar\Omega-\varepsilon_{j'}(X_0')-i\eta} - \frac{\delta[\varepsilon-\varepsilon_j(X_0)]}{\varepsilon-\hbar\Omega-\varepsilon_{j'}(X_0')-i\eta}\right]\right\}
\end{aligned}
\tag{E.4}
$$

First we perform the $\int dy$ and $\int dy'$ integrations.

$$
\frac{1}{L_y} \int dy \exp\left[\frac{i(X_0'-X_0)y}{L_H^2}\right] = \frac{2\pi L_H^2}{L_y} \delta(X_0'-X_0) \tag{E.5}
$$

Similarly to the integration performed above, the $\int dy'$ integration yields $2\pi L_H^2 \delta(X_0-X_0')/L_y$, but using the even property of the Dirac delta function this also reduces to the above result $2\pi L_H^2 \delta(X_0'-X_0)/L_y$. When the result of the $\int dy$ and $\int dy'$ integrations is substituted back into the equation of the 1D transverse conductivity (E.4), the

$\int\limits_{-\frac{G}{2}L_H^2}^{\frac{G}{2}L_H^2} dX_0'$ integration can easily be performed over the Dirac delta function. After this integration is done, the $\int dx$ and $\int dx'$ integrations can be performed. These integrals are in fact the matrix elements of the orthonormalized harmonic oscillator momentum operator, which are well known:

$$\langle n'|\, p_x \,|n\rangle = i\sqrt{\frac{M^*\hbar\omega_c}{2}}\left(-\sqrt{n}\delta_{n',n-1} + \sqrt{n+1}\delta_{n',n+1}\right) = \frac{i\hbar}{\sqrt{2}L_H}\left(\sqrt{n+1}\delta_{n',n+1} - \sqrt{n}\delta_{n',n-1}\right) \tag{E.6}$$

and

$$\langle l'|\, p_{x'} \,|l\rangle = i\sqrt{\frac{M^*\hbar\omega_c}{2}}\left(-\sqrt{l}\delta_{l',l-1} + \sqrt{l+1}\delta_{l',l+1}\right) = \frac{i\hbar}{\sqrt{2}L_H}\left(\sqrt{k+1}\delta_{l',l+1} - \sqrt{l}\delta_{l',l-1}\right) \tag{E.7}$$

Therefore $L_{xx}^{(0,1D)}(\Omega)$ of equation (E.4) becomes, using the above two results (E.6) and (E.7)):

$$\begin{aligned}
L_{xx}^{(0,1D)}(\Omega) = {} & \frac{i\hbar e^2 L_y}{4\pi\hbar\Omega A M^{*2} L_H^2}\int\limits_{-\infty}^{\infty} d\varepsilon f(\varepsilon)\sum_{j,j'}\int\limits_{-\frac{G}{2}L_H^2}^{\frac{G}{2}L_H^2} dX_0 \\
& \cdot \sum_{n,n'} C_{n'}^*(j', X_0)\, C_n(j, X_0)\frac{i\hbar}{\sqrt{2}L_H}\left(\sqrt{n+1}\delta_{n',n+1} - \sqrt{n}\delta_{n',n-1}\right) \\
& \cdot \sum_{l,l'} C_l^*(j, X_0)\, C_{l'}(j', X_0)\frac{i\hbar}{\sqrt{2}L_H}\left(\sqrt{k+1}\delta_{l',l+1} - \sqrt{l}\delta_{l',l-1}\right) \\
& \cdot \left\{\left[\frac{\delta[\varepsilon - \varepsilon_{j'}(X_0)]}{\varepsilon + \hbar\Omega - \varepsilon_j(X_0) + i\eta} - \frac{\delta[\varepsilon - \varepsilon_{j'}(X_0)]}{\varepsilon - \hbar\Omega - \varepsilon_j(X_0) + i\eta}\right]\right. \\
& \left. - \left[\frac{\delta[\varepsilon - \varepsilon_j(X_0)]}{\varepsilon + \hbar\Omega - \varepsilon_{j'}(X_0) - i\eta} - \frac{\delta[\varepsilon - \varepsilon_j(X_0)]}{\varepsilon - \hbar\Omega - \varepsilon_{j'}(X_0) - i\eta}\right]\right\}
\end{aligned} \tag{E.8}$$

The summations over n' and l' are now easily performed using the Kronecker deltas. Similar to the 2D case we introduce the following notation for one of the structure factors:

$$\begin{gathered}
F^{(2,1D)}_{j,X_0;j',X_0} = \int\limits_A d\vec{x}\psi^*_{j,X_0}\left(\vec{x}\right)\frac{\partial}{\partial x}\psi_{j',X_0}\left(\vec{x}\right) \\
= \frac{1}{\sqrt{2}L_H}\sum_n C_n\left(j,X_0\right)\left[\sqrt{n+1}C^*_{n+1}\left(j',X_0\right)-\sqrt{n}C^*_{n-1}\left(j',X_0\right)\right]
\end{gathered} \tag{E.9}$$

The structure factor defined in equation (E.9) has the same property upon exchanging indices j and j' as the corresponding structure factor defined in the 2D modulation case:

$$F^{(2,1D)*}_{j,X_0;j',X_0} = -F^{(2,1D)}_{j',X_0;j,X_0} \tag{E.10}$$

This property was already verified in the 2D case, but for the sake of completeness it is listed here again:

$$\begin{gathered}
F^{(2,1D)*}_{j,X_0;j',X_0} = \int\limits_A d\vec{x}\psi_{j,X_0}\left(\vec{x}\right)\frac{\partial}{\partial x}\psi^*_{j',X_0}\left(\vec{x}\right) = \psi_{j,X_0}\left(\vec{x}\right)\psi^*_{j',X_0}\left(\vec{x}\right)\Big|^{+\infty}_{-\infty} \\
-\int\limits_A d\vec{x}\psi^*_{j',X_0}\left(\vec{x}\right)\frac{\partial}{\partial y}\psi_{j,X_0}\left(\vec{x}\right) = -\int\limits_A d\vec{x}\psi^*_{j',X_0}\left(\vec{x}\right)\frac{\partial}{\partial y}\psi_{j,X_0}\left(\vec{x}\right) = -F^{(2,1D)}_{j',X_0;j,X_0}
\end{gathered} \tag{E.11}$$

Using the form factor defined in equation (E.9) above, the transverse conductivity (E.8) may be written as:

$$
\begin{aligned}
L_{xx}^{(0,1D)}\left(\Omega\right) = {} & \frac{i\hbar^3 e^2 L_y}{4\pi\hbar\Omega A M^{*2} L_H^2} \int\limits_{-\infty}^{\infty} d\varepsilon f\left(\varepsilon\right) \sum_{j,j'} \int\limits_{-\frac{G}{2}L_H^2}^{\frac{G}{2}L_H^2} dX_0 \left(F_{j,X_0;j',X_0}^{(2,1D)}\right)^2 \\
& \cdot \left\{ \left[\frac{\delta\left[\varepsilon - \varepsilon_{j'}\left(X_0\right)\right]}{\varepsilon + \hbar\Omega - \varepsilon_j\left(X_0\right) + i\eta} - \frac{\delta\left[\varepsilon - \varepsilon_{j'}\left(X_0\right)\right]}{\varepsilon - \hbar\Omega - \varepsilon_j\left(X_0\right) + i\eta} \right] \right. \\
& \left. - \left[\frac{\delta\left[\varepsilon - \varepsilon_j\left(X_0\right)\right]}{\varepsilon + \hbar\Omega - \varepsilon_{j'}\left(X_0\right) - i\eta} - \frac{\delta\left[\varepsilon - \varepsilon_j\left(X_0\right)\right]}{\varepsilon - \hbar\Omega - \varepsilon_{j'}\left(X_0\right) - i\eta} \right] \right\}
\end{aligned}
\tag{E.12}
$$

This concludes the derivation of the transverse conductivity for the 1D case.

Appendix F

1D Transverse Conductivity Formula Used in the Numerical Calculations

In the numerical calculations one would use equation (5.30) for the conductivity along the modulation direction in a slightly modified form. First of all the partial density of states, $D_{j',X_0}(\varepsilon)$, in this equation can be replaced by its explicit form:

$$D_{j',X_0}(\varepsilon) = \delta\left[\varepsilon - \varepsilon_{j'}(X_0)\right] \tag{F.1}$$

Then one can perform the $\int\limits_{-\infty}^{\infty} d\varepsilon$ integration:

$$L_{xx}^{(0,1D)}(\Omega) = \frac{\pi\hbar^3 e^2 N_y \Phi}{\hbar\Omega A M^{*2}} \sum_{j,j'} \int\limits_{-\frac{G}{2}L_H^2}^{\frac{G}{2}L_H^2} \frac{dX_0}{a} \left(F_{j,X_0;j',X_0}^{(2,1D)}\right)^2$$
$$\cdot \left\{\left\{f\left[\varepsilon_{j'}(X_0) - \hbar\Omega\right] - f\left[\varepsilon_{j'}(X_0)\right]\right\} \delta\left[\varepsilon_j(X_0) - \varepsilon_{j'}(X_0) + \hbar\Omega\right]\right.$$
$$\left. - \left\{f\left[\varepsilon_{j'}(X_0) + \hbar\Omega\right] - f\left[\varepsilon_{j'}(X_0)\right]\right\} \delta\left[\varepsilon_j(X_0) - \varepsilon_{j'}(X_0) - \hbar\Omega\right]\right\} \tag{F.2}$$

In equation (F.2) $f\left[\varepsilon_{j'}(X_0)\right]$ denotes the Fermi–Dirac distribution function, which can be written explicitly as:

$$f\left[\varepsilon_{j'}(X_0)\right] = \left\{\exp\frac{\left[\varepsilon_{j'}(X_0) - \varepsilon_F\right]}{k_B T} + 1\right\}^{-1} \tag{F.3}$$

The low temperature limit of the Fermi–Dirac distribution function, which is the Heaviside step function, may be used in equation (F.3). Thus, when $T \to 0$, equation (F.3) may be replaced by:

$$f\left[\varepsilon_j(X_0)\right] = \left\{\exp\frac{\left[\varepsilon_j(X_0) - \varepsilon_F\right]}{k_B T} + 1\right\}^{-1} = \theta\left[\varepsilon_F - \varepsilon_j(X_0)\right] \tag{F.4}$$

The next step in transforming the 1D transverse conductivity formula into a form convenient in doing numerical calculations is rewriting variables appearing in equation (F.2) into convenient dimensionless variables. Using the zero temperature Fermi–Dirac distribution function and dimensionless variables, we obtain a modified form of equation (F.2):

$$
\begin{aligned}
L_{xx}^{(0,1D)}(\Omega) = {} & \frac{\pi^2\hbar^3 e^2 N_y \Phi}{a^2\hbar^2\omega_c\Omega A M^{*2}} \sum_{j,j'} \int_{-\frac{1}{2}}^{\frac{1}{2}} d\bar{k}_y \\
& \cdot \left\{ \sum_n C_n\left(j,\bar{k}_y\right)\left[\sqrt{n+1}C_{n+1}^{*}\left(j',\bar{k}_y\right) - \sqrt{n}C_{n-1}^{*}\left(j',\bar{k}_y\right)\right] \right\}^2 \\
& \cdot \left\{ \left\{ \theta\left[\frac{\varepsilon_F - \varepsilon_{j'}\left(\bar{k}_y\right)}{\hbar\omega_c} + \frac{\Omega}{\omega_c}\right] - \theta\left[\frac{\varepsilon_F - \varepsilon_{j'}\left(\bar{k}_y\right)}{\hbar\omega_c}\right] \right\} \delta\left[\frac{\varepsilon_j\left(\bar{k}_y\right) - \varepsilon_{j'}\left(\bar{k}_y\right)}{\hbar\omega_c} + \frac{\Omega}{\omega_c}\right] \right. \\
& \left. - \left\{ \theta\left[\frac{\varepsilon_F - \varepsilon_{j'}\left(\bar{k}_y\right)}{\hbar\omega_c} - \frac{\Omega}{\omega_c}\right] - \theta\left[\frac{\varepsilon_F - \varepsilon_{j'}\left(\bar{k}_y\right)}{\hbar\omega_c}\right] \right\} \delta\left[\frac{\varepsilon_j\left(\bar{k}_y\right) - \varepsilon_{j'}\left(\bar{k}_y\right)}{\hbar\omega_c} - \frac{\Omega}{\omega_c}\right] \right\}
\end{aligned}
\tag{F.5}
$$

The following is a list of dimensionless variables that will be used in equation(F.5) and in the Fortran programming:

$$\frac{k_y a}{2\pi} = \bar{k}_y \tag{F.6}$$

$$\bar{\varepsilon}_F = \frac{\varepsilon_F}{\hbar\omega_c} \tag{F.7}$$

$$\bar{\varepsilon}_j\left(\bar{k}_y\right) = \frac{\varepsilon_j\left(\bar{k}_y\right)}{\hbar\omega_c} \tag{F.8}$$

$$\bar{\varepsilon}_{j'}\left(\bar{k}_y\right) = \frac{\varepsilon_{j'}\left(\bar{k}_y\right)}{\hbar\omega_c} \tag{F.9}$$

$$\bar{\Omega} = \frac{\Omega}{\omega_c} \tag{F.10}$$

The constant factor in front of the integral sign in the expression of the transverse conductivity formula (F.5), consisting of the product of some universal constants and experimental parameters can also be expressed in terms of dimensionless variables as:

$$\frac{\pi^2\hbar^3 e^2 N_y \Phi}{a^2\hbar^2\omega_c \Omega A M^{*2}} = \frac{e^2}{h}\cdot\frac{\pi}{\Phi\bar{\Omega}N_x} \tag{F.11}$$

Combining all of the above results, the final form of the 1D transverse conductivity, appropriate for numerical calculation, is written as:

$$\begin{aligned}
L_{xx}^{(0,1D)}(\Omega) &= \frac{e^2}{h}\cdot\frac{\pi}{\Phi\bar{\Omega}N_x}\sum_{j,j'}\int_{-\frac{1}{2}}^{\frac{1}{2}} d\bar{k}_y \\
&\cdot\left\{\sum_n C_n\left(j,\bar{k}_y\right)\left[\sqrt{n+1}C_{n+1}^{*}\left(j',\bar{k}_y\right)-\sqrt{n}C_{n-1}^{*}\left(j',\bar{k}_y\right)\right]\right\}^2 \\
&\cdot\left\{\left\{\theta\left[\bar{\varepsilon}_F-\bar{\varepsilon}_{j'}\left(\bar{k}_y\right)+\bar{\Omega}\right]-\theta\left[\bar{\varepsilon}_F-\bar{\varepsilon}_{j'}\left(\bar{k}_y\right)\right]\right\}\delta\left[\bar{\varepsilon}_j\left(\bar{k}_y\right)-\bar{\varepsilon}_{j'}\left(\bar{k}_y\right)+\bar{\Omega}\right]\right. \\
&\left.-\left\{\theta\left[\bar{\varepsilon}_F-\bar{\varepsilon}_{j'}\left(\bar{k}_y\right)-\bar{\Omega}\right]-\theta\left[\bar{\varepsilon}_F-\bar{\varepsilon}_{j'}\left(\bar{k}_y\right)\right]\right\}\delta\left[\bar{\varepsilon}_j\left(\bar{k}_y\right)-\bar{\varepsilon}_{j'}\left(\bar{k}_y\right)-\bar{\Omega}\right]\right\}
\end{aligned} \tag{F.12}$$

Appendix G

Hall Conductivity Calculation for 1D Modulation

The Hall conductivity can be expressed as the yx element of the linear response tensor, calculated in Chapter . It can be obtained following a very similar method such as used in the 2D case. One has to express the x and y component of the velocity operators:

$$v_x = \frac{p_x}{M^*} \tag{G.1}$$

and

$$v_y = \frac{p_y}{M^*} + \frac{eBx}{M^*} \tag{G.2}$$

and calculate the matrix element of these operators in terms of the following states:

$$|N\rangle = \psi_{j,X_0}\left(\vec{x}\right) = |j, X_0\rangle = \sum_n C_n\left(j, X_0\right)\phi_{n,X_0}\left(\vec{x}\right) \tag{G.3}$$

$$|M\rangle = \psi_{j',X_0'}\left(\vec{x}'\right) = |j', X_0'\rangle = \sum_{n'} C_{n'}\left(j', X_0'\right)\phi_{n',X_0'}\left(\vec{x}'\right) \tag{G.4}$$

Thus the equation that leads to expression of the Hall conductivity that we are seeking is:

$$\begin{aligned} L_{yx}^{(0,1D)}\left(\Omega\right) &= \frac{i\hbar e^2}{2\hbar\Omega A}\int\limits_{-\infty}^{\infty} d\varepsilon f\left(\varepsilon\right)\sum_{M,N} v_y^{NM} v_x^{MN} \\ &\cdot\left\{\left[G_M^{(0+)}\left(\varepsilon+\hbar\Omega\right) - G_M^{(0+)}\left(\varepsilon-\hbar\Omega\right)\right]\delta\left(\varepsilon-\varepsilon_N\right)\right. \\ &\left.-\delta\left(\varepsilon-\varepsilon_M\right)\left[G_N^{(0-)}\left(\varepsilon+\hbar\Omega\right) - G_N^{(0-)}\left(\varepsilon-\hbar\Omega\right)\right]\right\} \end{aligned} \tag{G.5}$$

After a lengthy calculation, in which integrations associated with the calculation of velocity matrix elements indicated in equation (G.5) above are performed, we arrive to the following formula for the Hall conductivity:

$$\begin{aligned} L_{yx}^{(0,1D)}\left(\Omega\right) &= -\frac{\hbar^3 e^2 L_y}{4\pi\hbar\Omega A M^{*2} L_H^2}\int\limits_{-\infty}^{\infty} d\varepsilon f\left(\varepsilon\right)\sum_{j,j'}\int\limits_{-\frac{G}{2}L_H^2}^{\frac{G}{2}L_H^2} dX_0 \\ &\cdot\left[\frac{1}{L_H^2}F^{(1)}_{j',X_0;j,X_0}F^{(2)}_{j,X_0;j',X_0} + F^{(3)}_{j',X_0;j,X_0}F^{(2)}_{j,X_0;j',X_0}\right] \\ &\cdot\left\{\left[\frac{\delta\left[\varepsilon-\varepsilon_{j'}\left(X_0\right)\right]}{\varepsilon+\hbar\Omega-\varepsilon_j\left(X_0\right)+i\eta} - \frac{\delta\left[\varepsilon-\varepsilon_{j'}\left(X_0\right)\right]}{\varepsilon-\hbar\Omega-\varepsilon_j\left(X_0\right)+i\eta}\right] - \right. \\ &\left. - \left[\frac{\delta\left[\varepsilon-\varepsilon_{j}\left(X_0\right)\right]}{\varepsilon+\hbar\Omega-\varepsilon_{j'}\left(X_0\right)-i\eta} - \frac{\delta\left[\varepsilon-\varepsilon_{j}\left(X_0\right)\right]}{\varepsilon-\hbar\Omega-\varepsilon_{j'}\left(X_0\right)-i\eta}\right]\right\} \end{aligned} \tag{G.6}$$

In equation (G.6) above, the following notations are used for the structure factors:

$$F^{(1,1D)}_{j',X_0;j,X_0} = \frac{L_H}{\sqrt{2}} \sum_n C_n\left(j, X_0\right) \left(\sqrt{n+1} C^*_{n+1}\left(j', X_0\right) + \sqrt{n} C^*_{n-1}\left(j', X_0\right)\right) \tag{G.7}$$

$$F^{(2,1D)}_{j',X_0;j,X_0} = \frac{1}{\sqrt{2} L_H} \sum_n C_n\left(j, X_0\right) \left[\sqrt{n+1} C_{n+1}\left(j', X_0\right) - \sqrt{n} C_{n-1}\left(j', X_0\right)\right] \tag{G.8}$$

$$F^{(3,1D)}_{j,X_0;j',X_0'} = -k_y \sum_n C_n\left(j, X_0\right) C_n\left(j', X_0\right) = -\frac{X_0}{L_H^2} \delta_{j,j'} \tag{G.9}$$

In the above equation the orthonormality property of the expansion coefficients has been used.

Now the Green's function terms in the denominators of the last curly bracket in equation G.6 can be written in a different form using the Dirac formula. Taking into account the symmetry properties of the delta function and principal value terms that arise, some terms will be eliminated in the Hall conductivity formula, which becomes:

$$\begin{aligned} L^{(0,1D)}_{yx}\left(\Omega\right) = {} & \frac{\hbar^3 e^2 L_y}{\pi A M^{*2} L_H^2} \sum_{j,j'}{}' f\left[\varepsilon_{j'}\left(X_0\right)\right] \int\limits_{-\frac{G}{2} L_H^2}^{\frac{G}{2} L_H^2} dX_0 \\ & \cdot \left\{ \frac{1}{L_H^2} \mathrm{Re}\left[F^{(1)}_{j',X_0;j,X_0} F^{(2)}_{j,X_0;j',X_0}\right] + \mathrm{Re}\left[F^{(3)}_{j',X_0;j,X_0} F^{(2)}_{j,X_0;j',X_0}\right] \right\} \\ & \cdot \frac{1}{\left[\varepsilon_{j'}\left(X_0\right) - \varepsilon_j\left(X_0\right)\right]^2 - \left(\hbar\Omega\right)^2} \end{aligned} \tag{G.10}$$

The prime notation in equation (G.10) over the summation sign means that the summation will be performed only for those values of the indices for which the denominator is not zero. In terms of the partial density of states, the Hall conductivity may be written as:

$$\begin{aligned} L_{yx}^{(0,1D)}\left(\Omega\right) &= \frac{\hbar^3 e^2 L_y}{\pi A M^{*2} L_H^2} \sum_{j,j'}{}^{\prime} \int\limits_{-\frac{G}{2}L_H^2}^{\frac{G}{2}L_H^2} dX_0 \\ &\cdot \left\{ \frac{1}{L_H^2} \mathrm{Re}\left[F_{j',X_0;j,X_0}^{(1)} F_{j,X_0;j',X_0}^{(2)} \right] + \mathrm{Re}\left[F_{j',X_0;j,X_0}^{(3)} F_{j,X_0;j',X_0}^{(2)} \right] \right\} \\ &\cdot \frac{1}{\left[\varepsilon_{j'}\left(X_0\right) - \varepsilon_j\left(X_0\right)\right]^2 - \left(\hbar\Omega\right)^2} \int\limits_{-\infty}^{\infty} d\varepsilon f\left(\varepsilon\right) D_{j',X_0}\left(\varepsilon\right) \end{aligned} \tag{G.11}$$

This is the final form of the Hall conductivity formula for the 1D case.

Appendix H

1D Hall Conductivity Formula Used in the Numerical Calculations

We need to modify the form of the Hall conductivity equation (5.36) listed in Chapter 5 and obtained in Appendix G for the 1D case, and put it into a dimensionless form that is convenient for numerical calculations. First we change the integration variable in the dX_0 integration, and introduce the notation $k_y a/2\pi = \bar{k}_y$. Then we use the following rescaled variables for the energies and frequency of radiation field:

$$\bar{\varepsilon}_j\left(\bar{k}_y\right) = \frac{\varepsilon_j\left(\bar{k}_y\right)}{\hbar\omega_c} \tag{H.1}$$

$$\bar{\varepsilon}_{j'}\left(\bar{k}_y\right) = \frac{\varepsilon_{j'}\left(\bar{k}_y\right)^2}{\hbar\omega_c} \tag{H.2}$$

$$\bar{\Omega} = \frac{\Omega}{\omega_c} \tag{H.3}$$

In the above-defined dimensionless variables, the Hall conductivity can be written as:

$$L_{yx}^{(0,1D)}\left(\Omega\right)=\frac{2\hbar^{3}e^{2}L_{y}}{aAM^{*2}\left(\hbar\omega_{c}\right)^{2}L_{H}^{2}}\sum_{j,j'}{}^{\prime}\int\limits_{-\frac{1}{2}}^{\frac{1}{2}}d\bar{k}_{y}$$
$$\cdot\left\{\mathrm{Re}\left[F_{j',\bar{k}_{y};j,\bar{k}_{y}}^{(1,1D)}F_{j,\bar{k}_{y};j',\bar{k}_{y}}^{(2,1D)}\right]+\frac{1}{L_{H}^{2}}\mathrm{Re}\left[F_{j',\bar{k}_{y};j,\bar{k}_{y}}^{(3,1D)}F_{j,\bar{k}_{y};j',\bar{k}_{y}}^{(2,1D)}\right]\right\} \tag{H.4}$$
$$\cdot\frac{1}{\left[\bar{\varepsilon}_{j'}\left(\bar{k}_{y}\right)-\bar{\varepsilon}_{j}\left(\bar{k}_{y}\right)\right]^{2}-\left(\bar{\Omega}\right)^{2}}\int\limits_{-\infty}^{\infty}d\bar{\varepsilon}f\left(\bar{\varepsilon}\right)D_{j',\bar{k}_{y}}\left(\bar{\varepsilon}\right)$$

The coefficient in front of the summation in equation (H.4) can be written in a more convenient form:

$$\frac{2\hbar^{3}e^{2}L_{y}}{aAM^{*2}\left(\hbar\omega_{c}\right)^{2}L_{H}^{2}}=\frac{e^{2}}{h}\frac{2}{N_{x}\Phi} \tag{H.5}$$

Writing the partial density of states explicitly, we may perform the last integration in equation (H.4). We also substitute all of the form factors:

$$F_{j',\bar{k}_{y};j,\bar{k}_{y}}^{(1,1D)}=\frac{L_{H}}{\sqrt{2}}\sum_{n}C_{n}\left(j,\bar{k}_{y}\right)\left(\sqrt{n+1}C_{n+1}^{*}\left(j',\bar{k}_{y}\right)+\sqrt{n}C_{n-1}^{*}\left(j',\bar{k}_{y}\right)\right) \tag{H.6}$$

$$F_{j,\bar{k}_{y};j',\bar{k}_{y}}^{(2,1D)}=\frac{1}{\sqrt{2}L_{H}}\sum_{n}C_{n}\left(j',\bar{k}_{y}\right)\left[\sqrt{n+1}C_{n+1}^{*}\left(j,\bar{k}_{y}\right)-\sqrt{l}C_{n-1}^{*}\left(j,\bar{k}_{y}\right)\right] \tag{H.7}$$

$$F_{j',\bar{k}_{y};j,\bar{k}_{y}}^{(3,1D)}=-\frac{\bar{k}_{y}}{L_{H}^{2}}\delta_{j',j} \tag{H.8}$$

The final form of the dimensionless Hall conductivity for the 1D modulation potential used in the numerical calculations is:

$$
\begin{aligned}
&L_{yx}^{(0,1D)}\left(\Omega\right) = \frac{e^2}{h}\frac{2}{N_x\Phi}\sum_{j,j'}\int\limits_{-\frac{1}{2}}^{\frac{1}{2}} d\bar{k}_y \frac{\theta\left[\bar{\varepsilon}_F - \bar{\varepsilon}_j\left(\bar{k}_y\right)\right]}{\left[\bar{\varepsilon}_j\left(\bar{k}_y\right) - \bar{\varepsilon}_{j'}\left(\bar{k}_y\right)\right]^2 - \left(\bar{\Omega}\right)^2} \\
&\cdot\Bigg\{\sum_n C_n\left(j,\bar{k}_y\right)\left[\sqrt{n+1}C^*_{n+1}\left(j',\bar{k}_y\right) + \sqrt{n}C^*_{n-1}\left(j',\bar{k}_y\right)\right] \\
&\cdot\sum_l C_l\left(j',\bar{k}_y\right)\left[\sqrt{l+1}C^*_{l+1}\left(j,\bar{k}_y\right) - \sqrt{l}C^*_{l-1}\left(j,\bar{k}_y\right)\right] \\
&-\sqrt{\frac{\pi}{\Phi}}\bar{k}_y\delta_{j',j}\sum_l C_l\left(j',\bar{k}_y\right)\left[\sqrt{l+1}C^*_{l+1}\left(j,\bar{k}_y\right) - \sqrt{l}C^*_{l-1}\left(j,\bar{k}_y\right)\right]\Bigg\}
\end{aligned}
\tag{H.9}
$$

Appendix I

Longitudinal Conductivity Calculation for 1D Modulation

The yy element of the frequency-dependent linear response tensor, $L_{yy}^{(0)}(\Omega)$, along the quantum wire channel, can be obtained by calculating the matrix element of the following velocity operator:

$$v_y = \frac{p_y}{M^*} + \frac{eBx}{M^*} \tag{I.1}$$

This velocity operator is substituted in the general conductivity equation:

$$\begin{aligned} L_{yy}^{(0,1D)}(\Omega) = \frac{i\hbar e^2}{2\hbar\Omega A} \int\limits_{-\infty}^{\infty} d\varepsilon f(\varepsilon) \sum_{M,N} v_y^{NM} v_y^{MN} \\ \cdot \Big\{ \Big[G_M^{(0+)}(\varepsilon + \hbar\Omega) - G_M^{(0+)}(\varepsilon - \hbar\Omega) \Big] \delta(\varepsilon - \varepsilon_N) \\ - \delta(\varepsilon - \varepsilon_M) \Big[G_N^{(0-)}(\varepsilon + \hbar\Omega) - G_N^{(0-)}(\varepsilon - \hbar\Omega) \Big] \Big\} \end{aligned} \tag{I.2}$$

We calculate the matrix elements between the following two states:

$$|N\rangle = \psi_{j',X_0'}\left(\vec{x}'\right) = |j', X_0'\rangle = \sum_{n'} C_{n'}\left(j', X_0'\right)\phi_{n'}\left(\vec{x}'\right) \tag{I.3}$$

and

$$|M\rangle = \psi_{j,X_0}\left(\vec{x}\right) = |j, X_0\rangle = \sum_{n} C_{n}\left(j, X_0\right)\phi_{n,X_0}\left(\vec{x}\right) \tag{I.4}$$

After performing the integrations involved in calculating the matrix elements contained in equation (I.2), we have obtained:

$$\begin{aligned}
L_{yy}^{(0,1D)}\left(\Omega\right) &= \frac{i\hbar^3 e^2 L_y}{4\pi\hbar\Omega A M^{*2} L_H^2} \int\limits_{-\infty}^{\infty} d\varepsilon f\left(\varepsilon\right) \sum_{j,j'} \int\limits_{-\frac{G}{2}L_H^2}^{\frac{G}{2}L_H^2} \frac{dX_0}{a} \\
&\cdot \left[\left(F_{j',X_0;j,X_0}^{(1,1D)}\right)^2 + 2eBF_{j',X_0;j,X_0}^{(1,1D)} F_{j',X_0;j,X_0}^{(3,1D)} + e^2B^2\left(F_{j',X_0;j,X_0}^{(3,1D)}\right)^2\right] \\
&\cdot \left\{\left[\frac{\delta\left[\varepsilon - \varepsilon_{j'}\left(X_0\right)\right]}{\varepsilon + \hbar\Omega - \varepsilon_j\left(X_0\right) + i\eta} - \frac{\delta\left[\varepsilon - \varepsilon_{j'}\left(X_0\right)\right]}{\varepsilon - \hbar\Omega - \varepsilon_j\left(X_0\right) + i\eta}\right] - \right. \\
&- \left. \left[\frac{\delta\left[\varepsilon - \varepsilon_{j}\left(X_0\right)\right]}{\varepsilon + \hbar\Omega - \varepsilon_{j'}\left(X_0\right) - i\eta} - \frac{\delta\left[\varepsilon - \varepsilon_{j}\left(X_0\right)\right]}{\varepsilon - \hbar\Omega - \varepsilon_{j'}\left(X_0\right) - i\eta}\right]\right\}
\end{aligned} \tag{I.5}$$

Now we use the Dirac formula to express the Green's function terms in the last curly brackets in equation (I.5). Using the symmetry property of the delta functions and principal value terms with respect to the summations over indices j and j', only the delta function parts contribute to the yy conductivity. We may write the longitudinal conductivity as:

$$L_{yy}^{(0,1D)}\left(\Omega\right)=\frac{\hbar^{3}e^{2}L_{y}}{4\hbar\Omega AM^{*2}L_{H}^{2}}\int\limits_{-\infty}^{\infty}d\varepsilon\sum_{j,j'}\int\limits_{-\frac{G}{2}L_{H}^{2}}^{\frac{G}{2}L_{H}^{2}}\frac{dX_{0}}{a}$$

$$\cdot\left[\left(F_{j',X_{0};j,X_{0}}^{(1,1D)}\right)^{2}+2eBF_{j',X_{0};j,X_{0}}^{(1,1D)}F_{j',X_{0};j,X_{0}}^{(3,1D)}+e^{2}B^{2}\left(F_{j',X_{0};j,X_{0}}^{(3,1D)}\right)^{2}\right] \tag{I.6}$$

$$\cdot\,\delta\left[\varepsilon-\varepsilon_{j'}\left(X_{0}\right)\right]\left\{\left[f\left(\varepsilon\right)-f\left(\varepsilon+\hbar\Omega\right)\right]\delta\left[\varepsilon+\hbar\Omega-\varepsilon_{j}\left(X_{0}\right)\right]\right.$$

$$\left.-\left[f\left(\varepsilon\right)-f\left(\varepsilon-\hbar\Omega\right)\right]\delta\left[\varepsilon-\hbar\Omega-\varepsilon_{j}\left(X_{0}\right)\right]\right\}$$

We rearrange some of the constants and introduce the following notations for the partial densities of states:

$$D_{j',X_{0}}\left(\varepsilon\right)=\delta\left[\varepsilon-\varepsilon_{j'}\left(X_{0}\right)\right] \tag{I.7}$$

$$D_{j,X_{0}}\left(\varepsilon-\hbar\Omega\right)=\delta\left[\varepsilon-\hbar\Omega-\varepsilon_{j}\left(X_{0}\right)\right] \tag{I.8}$$

$$D_{j,X_{0}}\left(\varepsilon+\hbar\Omega\right)=\delta\left[\varepsilon+\hbar\Omega-\varepsilon_{j}\left(X_{0}\right)\right] \tag{I.9}$$

Using equations (I.7)-(I.9), the longitudinal conductivity equation becomes:

$$L_{yy}^{(0,1D)}\left(\Omega\right)=\frac{\hbar^{3}e^{2}N_{y}\Phi}{2\Omega AM^{*2}}\int\limits_{-\infty}^{\infty}d\varepsilon\sum_{j,j'}\int\limits_{-\frac{G}{2}L_{H}^{2}}^{\frac{G}{2}L_{H}^{2}}\frac{dX_{0}}{a}$$

$$\cdot\left[\frac{1}{L_{H}^{4}}\left(F_{j',X_{0};j,X_{0}}^{(1,1D)}\right)^{2}+\frac{2}{L_{H}^{2}}F_{j',X_{0};j,X_{0}}^{(1,1D)}F_{j',X_{0};j,X_{0}}^{(3,1D)}+\left(F_{j',X_{0};j,X_{0}}^{(3,1D)}\right)^{2}\right]$$

$$\cdot\,D_{j',X_{0}}\left(\varepsilon\right)\left\{\left[f\left(\varepsilon-\hbar\Omega\right)-f\left(\varepsilon\right)\right]D_{j,X_{0}}\left(\varepsilon-\hbar\Omega\right)-\left[f\left(\varepsilon+\hbar\Omega\right)-f\left(\varepsilon\right)\right]D_{j,X_{0}}\left(\varepsilon-\hbar\Omega\right)\right\} \tag{I.10}$$

Appendix J

1D Longitudinal Conductivity Formula Used in the Numerical Calculations

Now we would like to write the longitudinal conductivity formula (along the quantum wire channel) given in equation (5.33) of Chapter 5 in a modified form, which is appropriate for numerical calculations. First we change the integration variable in the dX_0 integration, and introduce the notation $k_y a/2\pi = \bar{k}_y$. Then we use the rescaled variables for the energies and frequency of radiation field:

$$\bar{\varepsilon}_j\left(\bar{k}_y\right) = \frac{\varepsilon_j\left(\bar{k}_y\right)}{\hbar\omega_c} \tag{J.1}$$

$$\bar{\varepsilon}_{j'}\left(\bar{k}_y\right) = \frac{\varepsilon_{j'}\left(\bar{k}_y\right)^2}{\hbar\omega_c} \tag{J.2}$$

$$\bar{\Omega} = \frac{\Omega}{\omega_c} \tag{J.3}$$

Then we write the partial densities of states in their explicit form, using equations (I.7)-(I.7). The longitudinal conductivity can then be written as:

$$\begin{aligned} L_{yy}^{(0,1D)}\left(\Omega\right) = &\frac{\pi\hbar^3 e^2 L_y}{2\hbar\Omega a A M^{*2}\hbar\omega_c}\sum_{j,j'}\int\limits_{-\frac{1}{2}}^{\frac{1}{2}} d\bar{k}_y \\ &\cdot\left[\left(F_{j',\bar{k}_y;j,\bar{k}_y}^{(1,1D)}\right)^2 + 2eBF_{j',\bar{k}_y;j,\bar{k}_y}^{(1,1D)}F_{j',\bar{k}_y;j,\bar{k}_y}^{(3,1D)} + e^2B^2\left(F_{j',\bar{k}_y;j,\bar{k}_y}^{(3,1D)}\right)^2\right] \\ &\cdot\left\{\left[f\left(\bar{\varepsilon}_{j'}\left(\bar{k}_y\right)-\bar{\Omega}\right)-f\left(\bar{\varepsilon}_{j'}\left(\bar{k}_y\right)\right)\right]\delta\left[\bar{\varepsilon}_{j'}\left(\bar{k}_y\right)-\bar{\Omega}-\bar{\varepsilon}_j\left(\bar{k}_y\right)\right]\right. \\ &\left.-\left[f\left(\bar{\varepsilon}_{j'}\left(\bar{k}_y\right)+\bar{\Omega}\right)-f\left(\bar{\varepsilon}_{j'}\left(\bar{k}_y\right)\right)\right]\delta\left[\bar{\varepsilon}_{j'}\left(\bar{k}_y\right)+\bar{\Omega}-\bar{\varepsilon}_j\left(\bar{k}_y\right)\right]\right\} \end{aligned} \tag{J.4}$$

Now we write the form factors in their explicit forms:

$$F_{j',\bar{k}_y;j,\bar{k}_y}^{(1,1D)} = \frac{L_H}{\sqrt{2}}\sum_n C_n\left(j,\bar{k}_y\right)\left(\sqrt{n+1}C_{n+1}^*\left(j',\bar{k}_y\right)+\sqrt{n}C_{n-1}^*\left(j',\bar{k}_y\right)\right) \tag{J.5}$$

$$F_{j',\bar{k}_y;j,\bar{k}_y}^{(3,1D)} = -\frac{\bar{k}_y}{L_H^2}\delta_{j',j} \tag{J.6}$$

Transform the multiplying factor on the right-hand side of equation (J.4) in front of the summation:

$$\frac{\pi\hbar^3 e^2 L_y}{2\hbar\Omega a A M^{*2}\hbar\omega_c} = \frac{e^2}{h}\frac{\pi}{\bar{\Omega}N_x\Phi} \tag{J.7}$$

The final form of the longitudinal conductivity formula used in the numerical calculations is:

$$
\begin{aligned}
&L_{yy}^{(0,1D)}\left(\Omega\right)=\frac{e^2}{h}\cdot\frac{1}{\bar{\Omega}N_x\Phi}\sum_{j,j'}\int\limits_{-\frac{1}{2}}^{\frac{1}{2}}d\bar{k}_y\\
&\cdot\left\{\left[\sum_n C_n\left(j,\bar{k}_y\right)\left(\sqrt{n+1}C_{n+1}^{*}\left(j',\bar{k}_y\right)+\sqrt{n}C_{n-1}^{*}\left(j',\bar{k}_y\right)\right)\right]^2\right.\\
&\left.+4\sqrt{\frac{\pi}{\Phi}}\delta_{j',j}\sum_n C_n\left(j,\bar{k}_y\right)\left(\sqrt{n+1}C_{n+1}^{*}\left(j',\bar{k}_y\right)+\sqrt{n}C_{n-1}^{*}\left(j',\bar{k}_y\right)\right)+4\frac{\pi}{\Phi}\left(\delta_{j',j}\right)^2\right\}\\
&\cdot\left\{\left[f\left(\bar{\varepsilon}_{j'}\left(\bar{k}_y\right)-\bar{\Omega}\right)-f\left(\bar{\varepsilon}_{j'}\left(\bar{k}_y\right)\right)\right]\delta\left[\bar{\varepsilon}_{j'}\left(\bar{k}_y\right)-\bar{\Omega}-\bar{\varepsilon}_j\left(\bar{k}_y\right)\right]\right.\\
&\left.-\left[f\left(\bar{\varepsilon}_{j'}\left(\bar{k}_y\right)+\bar{\Omega}\right)-f\left(\bar{\varepsilon}_{j'}\left(\bar{k}_y\right)\right)\right]\delta\left[\bar{\varepsilon}_{j'}\left(\bar{k}_y\right)+\bar{\Omega}-\bar{\varepsilon}_j\left(\bar{k}_y\right)\right]\right\}
\end{aligned}
\tag{J.8}
$$

Appendix K

List of Abbreviations

$2DEG$ two-dimensional electron gas

QW quantum wire(s)

AW quantum antiwire(s)

QD quantum dot(s)

QA quantum antidot(s)

QMT quantum magneto-transport

ρ_{xx} longitudinal resistivity

ρ_{xy} transverse resistivity

Ω frequency of the external time-dependent radiation field

$1D$ one-dimensional

R resistance

G conductance

I current

V voltage

L length

A area

ρ resistivity

σ conductivity

n carrier density

μ carrier mobility

e elementary charge

h Planck's constant

λ_{dB} de Broglie wavelength

λ_F Fermi wavelength

k_F Fermi wavevector

E_F Fermi energy

l mean free path

l_c coherence length

p momentum

k_B Boltzmann's constant

T absolute temperature

$GaAs - AlGaAs$ gallium arsenide - aluminum gallium arsenide

Si silicon

QHE quantum Hall effect

SdH Shubnikov - de Haas

WO Weiss oscillations

B magnetic flux density

ω_c cyclotron frequency

m_c cyclotron mass

M^* electron effective mass

MBE molecular beam epitaxy

LL Landau levels

N_{2D} number of electrons in two dimensions

L_x is the sample length in the x-direction

L_y is the sample length in the y-direction

N_x number of unit cells in the x direction

N_y number of unit cells in the y direction

Φ flux ratio, number of flux quanta per unit cell

τ_m momentum relaxation time

H_0 unperturbed single-electron Hamiltonian for our one- or two-dimensional scattering array

q charge of current carriers

N exponent in the expression of the modulation potential

U_L modulating potential

$\vec{G}$ reciprocal lattice vector

$\vec{k}_x$ reciprocal lattice vectors in the x direction

$\vec{k}_y$ reciprocal lattice vectors in the y direction

a_x lattice constants in the x direction

a_y lattice constants in the y direction

V_0 amplitude of modulating potential

$\phi\left(\vec{r}\right)$ scalar potential

$\vec{A}$ vector potential

TBA tight binding approximation

LRT linear response tensor

L_H magnetic length

n Landau level index

m umklapp scattering index

$C_{n,m}\left(j, X_0\right)$ expansion coefficients in expression of eigenvalues

j energy eigenvalue subband index

X_0 guiding center of the cyclotron orbits

$H_n(x)$ the n-th Hermite polynomial

$E_j(X_0)$ j-th eigenenergy

r_c cyclotron orbit

RF radio frequency

IR infrared

$ZRSs$ zero resistance states

$NRSs$ negative resistance states

SAW surface acoustic wave

AC alternating current

DC direct current

Bibliography

[1] F. Bloch, "Über die Quantenmechanik der Elektronen in Kristallgittern", *Z. Phys.*, **52**, 555 (1928).

[2] L.D. Landau, "The Theory of a Fermi Liquid", *Zh. Eksp. Teor. Fiz.*, **30**, 1058 (1956), *Sov. Phys. JETP*, **3**, 920 (1957).

[3] L.D. Landau, "Oscillations in a Fermi Liquid" *Zh. Eksp. Teor. Fiz.*, **32**, 920 (1957), *Sov. Phys. JETP*, **5**, 101 (1957).

[4] R. Kubo, "Statistical-Mechanical Theory of Irreversible Processes. I. General Theory and Simple Applications to Magnetic and Conduction Problems" *J. Phys. Soc. Jpn.*, **12**, 570 (1957).

[5] R. Landauer, "Spatial Variation of Currents and Fields Due to Localized Scatterers in Metallic Conduction" *IBM J. Res. Dev.*, **1**, 223 (1957).

[6] M. Büttiker, "Four-Terminal Phase-Coherent Conductance" *Phys. Rev. Lett.*, **57**, 1761 (1986).

[7] L. Esaki, R. Tsu, "Superlattice and Negative Differential Conductivity in Semiconductors", *IBM J. Res. Dev.*, **14**, 61 (1970).

[8] L. L. Chang, L. Esaki, R. Tsu, "Resonant Tunneling in Semiconductor Double Barriers", *Appl. Phys. Lett.*, **24**, 593 (1974).

[9] R. Dingle, H. L. Störmer, A. C. Gossard, W. Wiegmann, "Electron Mobilities in Modulation-Doped Semiconductor Heterojunction Superlattices", *Appl. Phys. Lett.*, **33**, 665 (1978).

[10] M. A. Paalanen, D. C. Tsui, A. C. Gossard, "Quantum Hall Effect at Low Temperatures", *Phys. Rev. B*, **25**, 5566 (1982).

[11] D. R. Hofstadter, "Energy Levels and Wave Functions of Bloch Electrons in Rational and Irrational Magnetic Fields", *Phys. Rev. B*, **14**, 2239 (1976).

[12] R. B. Laughlin "Quantized Hall Conductivity in Two Dimensions", *Phys. Rev. B*, **23**, 5632 (1981).

[13] M. A. Zudov, R. R. Du, J. A. Simmons, J. L. Reno "Shubnikov-de Haas-Like Oscillations in Millimeterwave Photoconductivity in a High-Mobility Two-Dimensional Electron Gas", *Phys. Rev. B*, **64**, 201311(R) (2001).

[14] R.G. Mani, J. H. Smet, K. von Klitzing, V. Narayanamurti, W. B. Johnson, V. Umansky "Demonstration of a 1/4-Cycle Phase Shift in the Radiation-Induced Oscillatory Magnetoresistance in $GaAs/AlGaAs$ Devices", *Phys. Rev. Lett.*, **92**, 146801 (2004).

[15] V. Ryzhii, R. Suris "Nonlinear Effects in Microwave Photoconductivity of Two-Dimensional Electron Systems", *J. Phys.: Condens. Matter*, **15**, 6855 (2003).

[16] R. G. Mani, J. H. Smet, K. von Klitzing, V. Narayanamurti, W. B. Johnson, V. Umanskyk "Zero-Resistance States Induced by Electromagnetic-Wave Excitation in $GaAs/AlGaAs$ Heterostructures", *Nature*, **420**, 646 (2002).

[17] M. A. Paalanen, R. L. Willett, P. B. Littlewood, R. R. Ruel, K. W. West, L. N. Pfeiffer, D. J. Bishop "RF Conductivity of a Two-Dimensional Electron System at Small Landau-Level Filling Factors", *Phys. Rev. B*, **45**, 11342 (1992).

[18] S. H. Simon "Coupling of Surface Acoustic Waves to a Two-Dimensional Electron Gas", *Phys. Rev. B*, **54**, 13878 (1996).

[19] B. I. Halperin, P. A. Lee, N. Read "Theory of the Half-Filled Landau Level", *Phys. Rev. B*, **47**, 7312 (1993).

[20] V. I. Talyanskii, D. R. Mace, M. Y. Simmons, M. Pepper, A. C. Churchill, J. E. F. Frost, D. A. Ritchie, G. A. C. Jones "The Propagation of Low-Frequency Edge Excitations in a Two-Dimensional Electron Gas in the IQHE Regime", *J. Phys.: Condens. Matter*, **7**, L435 (1995).

[21] V. I. Talyanskii, J. E. F. Frost, M. Pepper, D. A. Ritchie, M. Grimshaw, G. A. C. Jones "Low-Frequency Edge Excitations in an Electrostatically Confined *GaAs/AlGaAs* Two-Dimensional Electron Gas", *J. Phys.: Condens. Matter*, **5**, 7643 (1993).

[22] E. Vasiliadou, G. Müller, D. Heitmann, D. Weiss, K. von Klitzing, H. Nickel, W. Schlapp, R. Losch "Collective Response in the Microwave Photoconductivity of Hall Bar Structures", *Phys. Rev. B*, **48**, 17145 (1993).

[23] S. A. Mikhailov, N. A. Savostianova, "Microwave Response of a Two-Dimensional Electron Stripe", *Phys. Rev. B*, **71**, 035320 (2005).

[24] J. H. Smet, B. Gorshunov, C. Jiang, L. Pfeiffer, K. West, V. Umanksy, M. Dressel, R. Meisels, F. Kuchar, K. von Klitzing "Circular-Polarization-Dependent

Study of the Microwave Photoconductivity in a Two-Dimensional Electron System", *Phys. Rev. Lett*, **95**, 116804 (2005).

[25] I. V. Kukushkin, J. H. Smet, S. A. Mikhailov, D. V. Kulakovskii, K. von Klitzing, W. Wegscheider "Observation of Retardation Effects in the Spectrum of Two-Dimensional Plasmons", *Phys. Rev. Lett*, **90**, 156801 (2003).

[26] H. Silberbauer, U. Rössler "Quantum Study of Magnetotransport in Antidot Superlattices", *Phys. Rev. B*, **50**, 11911 (1994).

[27] D. Weiss, K. Richter, A. Menschig, R. Bergmann, H. Schweizer, K. von Klitzing, G. Weimann "Quantum Study of Magnetotransport in Antidot Superlattices", *Phys. Rev. Lett*, **70**, 4118 (1993).

[28] E. Vasiliadou, R. Fleischmann, D. Weiss, D. Heitmann, K. von Klitzing, T. Geisel, R. Bergmann, H. Schweizer, C. T. Foxon "Cyclotron-Resonance Anomalies in an Antidot Array Measured by Microwave Photoconductivity", *Phys. Rev. B*, **52**, R8658 (1995).

[29] G. S. Vieira, J. M. Villas-Bôas, P. S. S. Guimarães, N. Studart, J. Kono, S. J. Allen, K. L. Campman, A. C. Gossard "Magnetically Tuned Resonant Photon-Assisted Tunneling", *Phys. Rev. B*, **70**, 035316 (2004).

[30] D. Langbein, "The Tight-Binding and the Nearly-Free-Electron Approach to Lattice Electrons in External Magnetic Field", *Phys. Rev.*, **180**, 633 (1969).

[31] A. Rauch, "On the Broadening of Landau Levels in Crystals", *Phys. Status Solidi B*, **69**, K9 (1975).

[32] Y. Hasegawa, Y. Hatsugai, M. Kohmoto, "Stabilization of Flux States on Two-Dimensional Lattices", *Phys. Rev. B*, **41**, 9174 (1990).

[33] G. Gumbs, P. Fekete, “Hofstadter Butterfly for the Hexagonal Lattice” *Phys. Rev. B*, **56**, 3787 (1997).

[34] P. Fekete, G. Gumbs, “Magnetic Subband Structure of Bloch Electrons in a Two-Dimensional Lattice Under Magnetic Modulation”, *J. Phys.: Condens. Matter*, **11**, 5475 (1999).

[35] G. Y. Oh, M. H. Lee, “Energy Spectrum of Two-Dimensional Tight-Binding Electrons in a Spatially Varying Magnetic Field”, *Phys. Rev. B*, **53**, 1225 (1996).

[36] R. Taboryski, B. Brosh, M. Y. Simmons, D. A. Ritchie, C. J. B. Ford, M. Pepper, “Magnetothermopower Oscillations in a Lateral Superlattice”, *Phys. Rev. B*, **51**, 17243 (1995).

[37] G.-Y. Oh, “Effects of Field Modulation on the Hofstadter Spectrum”, *Phys. Rev. B*, **60**, 1939 (1999).

[38] D. Weiss, M. L. Roukes, A. Menschig, P. Grambow, K. von Klitzing, G. Weimann, “Electron Pinball and Commensurate Orbits in a Periodic Array of Scatterers”, *Phys. Rev. Lett.*, **66**, 2790 (1991).

[39] D. Huang, G. Gumbs, “Quenching of the Hall Effect in Strongly Modulated Two-Dimensional Electronic Systems”, *Phys. Rev. B*, **48**, 2835 (1993).

[40] R. R. Gerhardts, D. Weiss, K. v. Klitzing, “Novel Magnetoresistance Oscillations in a Periodically Modulated Two-Dimensional Electron Gas”, *Phys. Rev. Lett.*, **62**, 1173 (1989).

[41] R.W. Winkler, J.P. Kotthaus, K. Ploog, “Landau Band Conductivity in a Two-Dimensional Electron System Modulated by an Artificial One-Dimensional Superlattice Potential”, *Phys. Rev. Lett.*, **62**, 1177 (1989).

[42] R.R. Gerhardts, D. Weiss, U. Wulf, "Magnetoresistance Oscillations in a Grid Potential: Indication of a Hofstadter-Type Energy Spectrum" *Phys. Rev. B*, **43**, 5192 (1991).

[43] A. Lorke, J. Kotthaus, K. Ploog, "Magnetotransport in Two-Dimensional Lateral Superlattices" *Phys. Rev. B*, **44**, 3447 (1991).

[44] H. Fang, P.J. Stiles, "Novel Magnetoresistance Oscillations in a Two-Dimensional Superlattice Potential" *Phys. Rev. B*, **41**, 10171 (1990).

[45] D. Pfannkuche, R.R. Gerhardts, "Theory of Magnetotransport in Two-Dimensional Electron Systems Subjected to Weak Two-Dimensional Superlattice Potentials" *Phys. Rev. B*, **46**, 12606 (1992).

[46] C. Zhang, R.R. Gerhardts, "Theory of Magnetotransport in Two-Dimensional Electron Systems with Unidirectional Periodic Modulation" *Phys. Rev. B*, **41**, 12850 (1990).

[47] T.-i. Park, G. Gumbs, M. Pepper, "Quantum Magnetotransport Properties of Short Quantum Wires", *Phys. Rev. B*, **56**, 6758 (1997).

[48] G. Gumbs, D. Huang, "Quantum Magnetotransport in a Two-Dimensional Square Array of Scatterers", *Superl. Microstr.*, **14**, 1 (1993).

[49] G. Gumbs, D. Huang, A. H. MacDonald, "Comparison of Magnetotransport in Two-Dimensional Arrays of Quantum Dots and Antidots", *Phys. Rev B*, **48**, 2843 (1993).

[50] M. Torres, A. Kunold "Photoconductivity in AC-Driven Modulated Two-Dimensional Electron Gas in a Perpendicular Magnetic Field", *J. Phys.: Condens. Matter*, **18**, 4029 (2006).

[51] H. U. Baranger, A. D. Stone, "Electrical Liner-Response Theory in an Arbitrary Magnetic Field: A New Fermi-Surface Formation", *Phys. Rev B*, **40**, 8169 (1989).

[52] A. Bastin, C. Lewiner, O. Betbeder-Matibet, P. Nozieres, "Quantum Oscillations of the Hall Effect of a Fermion Gas with Random Impurity Scattering", *J. Phys. Chem. Solids*, **32**, 1811 (1971).

[53] L. Smrčka, P. Streda, "Transport Coefficients in Strong Magnetic Fields", *J. Phys. C: Solid State Phys.*, **10**, 2153 (1977).

[54] D. Huang, G. Gumbs, "Quantum Magnetotransport Theory for Bound-State Electrons in Lateral Surface Superlattices", *Phys. Rev. B*, **51**, 5558 (1995).

[55] G. Gumbs, D. Huang, J. P. Loehr, "Temperature Dependence of the Intersubband Transitions of Doped Quantum Wells", *Phys. Rev. B*, **51**, 4321 (1995).

[56] G. Gumbs, D. Huang, H. Qiang, F. H. Pollak, P. D. Wang, C. M. Sotomayor Torres, M. C. Holland, "Electromodulation Spectroscopy of an Array of Modulation-Doped Quantum Dots: Experiment and Theory", *Phys. Rev. B*, **50**, 10962 (1994).

[57] R. Fleischmann, T. Geisel, R. Ketzmerick, "Magnetoresistance Due to Chaos and Nonlinear Resonance in Lateral Surface Superlattices", *Phys. Rev. Lett.*, **68**, 1367 (1992).

[58] G. Gumbs, "Dynamic Resistivity of a Two-Dimensional Electron Gas with Electric Modulation", *Phys. Rev. B*, **72**, 125342 (2005).

[59] T. Park, "Modulation Potential Effects on the Quantum Magnetotransport in a Two-Dimensional Electron Gas", *Dissertation*, (published by the Graduate Center of CUNY), (1998).

[60] C. Weisbuch, B. Vinter, “Quantum Semiconductor Structures”, (Academic Press, New York, 1998), pp. 109-199.

[61] C. J. B. Ford, S. Washburn, M. Büttiker, C. M. Knoedler, J. M. Hong “Influence of Geometry on the Hall Effect in Ballistic Wires”, *Phys. Rev. Lett.*, **62**, 2724 (1989).

[62] C. J. B. Ford, S. Washburn, R. Newbury, C. M. Knoedler, J. M. Hong, “Resonant Suppression of the Quantized Hall Effect in Ballistic Junctions”, *Phys. Rev. B*, **43**, 7339 (1991).

[63] J. E. F. Frost, C.-T. Liang, D. R. Mace, M. Y. Simmons, D. A. Ritchie, M. Pepper “Ballistic Composite Fermions in Semiconductor Nanostructures”, *Phys. Rev. B*, **53**, 9602 (1996).

[64] G. Kirczenow, E. Castaño, “Diffraction, Phase Breaking, and Hall Anomalies in Quantum Dots ”, *Phys. Rev. B*, **43**, 7343 (1991).

[65] C. J. B. Ford, T. J. Thornton, R. Newbury, M. Pepper, H. Ahmed, D. C. Peacock, D. A. Ritchie, J. E. F. Frost, G. A. C. Jones “Vanishing Hall Voltage in a Quasi-One-Dimensional $GaAs-Al_xGa_{1-x}As$ Heterojunction”, *Phys. Rev. B*, **38**, 8518 (1988).

[66] M. Büttiker “Negative Resistance Fluctuations at Resistance Minima in Narrow Quantum Hall Conductors”, *Phys. Rev. B*, **38**, 12 724 (1988).